THE UNIVERSITY of ADELAIDE

Development of Mid-infrared Fluoroindate Glasses

by

Jiafang Bei

Supervisors:
Prof. Heike Ebendorff-Heidepriem
Prof. Tanya. M. Monro

A thesis submitted in fulfilment of the
Degree of Doctor of Philosophy

in the
Faculty of Sciences
School of Physical Sciences

OCT, 2017

DECLARATION OF AUTHORSHIP

I, Jiafang Bei, herely declare that:

- this thesis presents my own work and does not incorporate without acknowledgement any material previously submitted for a degree or diploma in any university;
- to the best of my knowledge it does not contain any materials previously published or written by another party in fulfilment, partial or otherwise, of any other degree or diploma at another Univeristy or institute of higher learning, except where due reference is made in the text; and all substantive contributions by others to the work presented, including jointly authored publications, is clearly acknowledged.
- I give consent to this copy of my thesis, when deposited in the University Library, being made available for loan and photocopying, subject to the provisions of the Copyright Act 1968.
- I also give permission for the digital version of my theis to be made available on the web, via the University's digital research repository, the Library catalogue and also through web search engines, unless permission has been granted by the University to restrict access for a period of time.

Signature: __ Printed: Jiafang Bei Date: 06/02/2018

UNIVERSITY OF ADELAIDE

ABSTRACT

Faculty of Sciences

School of Chemistry & Physics

Doctor of Philosophy

By Jiafang Bei

Heavy metal fluoride glasses are promising materials for active optical fibres. The initial systems reported in the literatures were fluorozirconate glasses. However, new materials are required to achieve higher and extended transmission in the IR spectrum (or equivalently lower phonon energies). This motivates the investigation of fluoroindate glasses in this project, as their lower phonon energies relative to fluorozirconate glasses extends their infrared transmission up to 8 μm (~3 mm thickness). In addition, fluoroindate glasses offer higher fibre drawing ability and resistance against devitrification.

A fluoroindate glass with the specific composition of $32InF_3$-$20ZnF_2$-$20SrF_2$-$18BaF_2$-$8GaF_3$-$2CaF_2$ (IZSBGC) has been developed in this project. This material demonstrates high transmission in the IR and high thermal stability against crystallisation. This thesis presents an approach for reducing the loss of optical fiber made using this material by optimising glass melting, preform extrusion and fiber drawing conditions. The optimised fibre fabrication procedures enable us to produce fibres with reduced surface crystallization, fibre loss and enhanced fibre bending strain. Glass flow analysis provides insights into the glass temperature-viscosity behaviour and the relationship between preform surface roughness and extrusion temperature, which enables the fabrication of preforms with low surface roughnesses and eventually reduced fiber scattering loss.

This thesis also presents an investigation into the chemical durability of the IZSBGC

fluoroindate glass, by comparing its leaching behaviour (in deionized water) against that of the widely studied fluorozirconate (ZBLAN) system. The work presented in this thesis advances our understanding of the corrosion behaviour between the two types of fluoride glasses in deionized water and demonstrates the introduction of Na reduces the chemical stability of fluoride glasses.

Based on IZSBGC glass composition, work has also been carried out in the preparation of rare earth elements doped fluoroindate glass and step index (core/clad) optical fibre for the development of a fibre laser at ~4 μm. We investigated the feasibility of techniques for fabrication including stacked billet and rod-in-tube methods. While further optimisation of fabrication procedure is required to enhance transmission, preliminary results suggest that core and clad glasses with similar fibre drawing temperature/viscosity are desirable for step-index fibre fabrication.

ACKNOWLEDGEMENTS

I would like to express my gratitude to all those who gave me the possibility to complete my PhD thesis.

First and foremost I would like to express my sincere appreciation to my Principal Supervisor, Prof. Heike Ebendorff-Heidepriem, and Co-supervisor, Prof. Tanya Monro, who have supported me throughout my PhD study and thesis writing with their constant guidance, patience, invaluable advices and knowledge. Without their endless support and encouragement, this PhD work would not have been possible.

I would like to acknowledge Defence Science and Technology Group in Australia for the funding support to my PhD project. Special thanks go to Dr Alexander Hemming who commented on all my published/unpublished papers/reports and discussed my experimental work with me.

I would also like to thank staff members at Adelaide Microscopy Centre: Mr Angus Netting, Dr Benjamin Wade, Mr Ken Neubauer, and Ms. Aoife McFadden (ex staff) for their assistance in using FESEM, EPMA, and Solution ICP-MS. Dr Jonathan Campbell at Flinders University is thanked for the DSC analysis.

I am also indebted to my friends and colleagues at The University of Adelaide for their moral support and help which made my studies in Adelaide more enjoyable and unique.

Finally, I would especially like to thank my husband Gujie Qian for his encouragement and help; my lovely daughter Becca for your born; my parents for their support over many years. Thank you all indeed for your endless love and understanding.

CONTENTS

DECLARATION OF AUTHORSHIP ..... **I**

ABSTRACT ..... **III**

ACKNOWLEDGEMENTS ..... **V**

LIST OF FIGURES ..... **XI**

LIST OF TABLES ..... **XV**

CHAPTER 1 **INTRODUCTION** **1**

1.1. Overview 1

1.2. Literature review 2
1.2.1. Mid infrared glasses 2
1.2.2. Fluoride glasses 4
1.2.2.1. Fluorozirconate glasses 4
1.2.2.2. Fluoroaluminate glasses 5
1.2.2.3. Indium fluoride based glasses 7
1.2.3. Loss mechanisms in fluoride glasses 9
1.2.3.1. Intrinsic losses in glasses 9
1.2.3.2. Extrinsic loss in glasses 11
1.2.4. Evaluation of glass stabilities 15
1.2.5. Fluoride glass, preform and fibre fabrication 16
1.2.5.1. Fluoride glass preparation 17
1.2.5.2. Preform preparation 19
1.2.5.3. Fibre drawing 23
1.2.6. Methods for reduction of fibre scattering loss 23
1.2.6.1. Chemical etching and mechanical polishing 23
1.2.6.2. Heating zone optimisation 24
1.2.6.3. Application of additional weight 25
1.2.7. Chemical durability of (bulk) fluoride glasses 25
1.2.8. Fluoride fibre laser in mid-infrared region 26

1.3. A gap in the literature regarding fluoroindate glass fibres 28

1.4. Outline of the thesis 29

CHAPTER 2 **FABRICATION AND CHARACTERISATION METHODOLOGY** **31**

2.1. Commercial raw materials 31

2.2. Equipment for glass/fibre preparation 33

2.3. Analytical techniques 36
2.3.1. Thermal properties 36
2.3.1.1. Differential Scanning Calorimetry 36
2.3.1.2. Dilatometer 37
2.3.1.3. Thermal Gravimetric Analysis (TGA) 37
2.3.2. Optical properties 38
2.3.2.1. FTIR spectroscopic analysis 38
2.3.2.2. Refractive index spectrum 39
2.3.2.3. Raman spectrum 41
2.3.2.4. Fibre loss measurement 41
2.3.3. Surface properties 42
2.3.3.1. Scanning electron microscopic analysis 42
2.3.3.2. Electron probe micro-analysis 43
2.3.3.3. Characterization of surface roughness 44
2.3.3.4. X-ray photoelectron Spectroscopy (XPS) 45
2.3.4. Other properties 46
2.3.4.1. X-ray powder diffraction analysis 46
2.3.4.2. Micro X-ray diffraction analysis 47
2.3.4.3. Solution inductively coupled plasma mass spectrometry and flame atomic absorption spectrometry 47
2.3.4.4. Mechanical strength measurement of fibres 48

CHAPTER 3 **GLASS PREPARATION (BASE GLASS ONLY) 51**

3.1. Characterization of indium fluoride raw materials from different suppliers 52

3.2. Glass fabrication of IZSBGC glass 55
3.2.1. Optimisation of IZSBGC glass melting with 30g batch size 55
3.2.1.1. Investigation of melting and casting temperatures 56
3.2.1.2. Choice of crucible material 58
3.2.1.3. Reduction of extrinsic loss via fluorination method during glass melting 59
3.2.2. Up-scaling of the glass batch size 65

3.3. Conclusion 68

CHAPTER 4 **UNSTRUCTURED PREFORM FABRICATION 69**

4.1. Preform fabrication by casting method 69

4.2. Preform fabrication by extrusion 72
4.2.1. Annealing tests 72
4.2.2. Preliminary extrusion trials 74
4.2.3. Glass flow analysis 75
4.2.4. Surface quality analysis 82

4.3. Conclusions 83

CHAPTER 5 **UNSTRUCTURED FIBRE FABRICATION 85**

5.1. Experimental details of fibre drawing 85

5.2. Results and Discussion 86
5.2.1. Preliminary fibres drawing from preforms prepared by casting and exrusion methods 86
5.2.2. Reduction of scattering loss of fibres drawn from extruded preforms 88

5.3. Conclusions 100

CHAPTER 6 **EXPERIMENTAL STUDY OF THE CHEMICAL DURABILITY OF FLUOROZIRCONATE AND FLUOROINDATE GLASSES IN DEIONIZED WATER.. 103**

6.1. Experimental details of leaching in deionized water 104

6.2. Results and Discussion 105
6.2.1. Infrared spectroscopic studies 105
6.2.2. pH study of corrosion solution 106
6.2.3. Scanning electron microscopy study 107
6.2.4. X-ray photoelectron spectroscopic study 111
6.2.5. ZBLAN and IZSGBG fibre strain and SEM study before and after corrosion 113
6.2.6. SEM study on cleaved fibre surface before and after corrosion 114

6.3. Conclusion 115

CHAPTER 7 **STEP INDEX FIBRE FABRICATION 117**

7.1. Experimental procedures 117

7.2. Results and discussion 118
7.2.1. Selection of rare earth ions for 4 μm laser application 118
7.2.1.1. The composition of rare earth doped glasses 118
7.2.1.2. Judd-Ofelt calculation 119
7.2.2. Selection of core and cladding glasse 128
7.2.2.1. Refractive index and density 130
7.2.2.2. Phonon energy 132
7.2.2.3. Thermal properties 133
7.2.3. Fabrication of core/clad structures 134
7.2.3.1. Overview of methods 134
7.2.3.2. Annealing tests 135
7.2.3.3. Extrusion of core/clad preform 137
7.2.3.4. Fibre fabrication 147

7.3. Conclusion 154

CHAPTER 8 **CONCLUSIONS AND FUTURE WORK 157**

8.1. Conclusions 157

8.2. Future work 159

APPENDIX A **AN EXPERIMENTAL STUDY OF DIRECTLY CAST CORE/CLAD GLASS BILLETS 161**

I. Experimental details 161

II. Results and discussion 162

APPENDIX B **TEMPERATURE PROFILE STUDY OF A DRAWING TOWER FURNACE 167**

I. Experimental details 168

II. Results and discussion 169

BIBLIOGRAPHY 177

PUBLISHED PAPERS 191

CONFERENCE PUBLICATIONS 237

LIST OF FIGURES

Figure 1. 1. Absorbance spectra of fluorozirconate (ZBLAN) and fluoroindate glass (IZBS) with 3 mm thickness 8
Figure 1. 2. "built-in casting" process. 20
Figure 1. 3. Rotational casting process. 20
Figure 1. 4. A stack of glass tubes and rods. 21
Figure 1. 5. Sketch of extrusion process. 22
Figure 1. 6. Transmittance spectra of the 1.0 mm thick AYF2 ($40AlF_3$-$15YF_3$-$15CaF_2$-$10BaF_2$-$10SrF_2$-$10MgF_2$-$1ErF_3$) and ZBLAN samples ($53ZrF_4$-$20BaF_2$-$4LaF_3$-$3AlF_3$-20NaF). 27
Figure 1. 7. The optical transmission curve for SiO_2 glasses, BeF_2 glasses and two types of heavy metal fluoride glasses; one is ZrF_4 based, the other one is a multicomponent glass, for example InF_3, based glass. 27

Figure 2. 1. Glovebox for glass fabrication. 34
Figure 2. 2. Extrusion machine for preform fabrication at IPAS, The University of Adelaide. 35
Figure 2. 3. 4m soft glass drawing tower. 36
Figure 2. 4. PerkinElmer STA6000. 38
Figure 2. 5. PerkinElmer Spectrum 400 FT-IR Spectrometer. 39
Figure 2. 6. (a) J.A. Woollam Co., Inc. VASE Ellipsometer HS-190) and (b) J. A. Woollam Co., Inc. VASE Ellipsometer VB-400 40
Figure 2. 7. The Philips XL 30 Field emission scanning electron microscope at Adelaide Microscopy Centre. 43
Figure 2. 8. The CAMECA SX51 electron microprobe. 43
Figure 2. 9. The optical ContourGT-K1 profiler from Brucker. 45
Figure 2. 10. The HUBER Guinier Imaging Plate Camera G670 for X-ray powder diffraction. 46
Figure 2. 11. The laboratory-based Rigaku D/MAX Rapid II micro-diffractometer. 47
Figure 2. 12. Solution ICP-MS instrument at Adelaide Microscopy Centre. 48
Figure 2. 13. Bending strength measurement approach. 49

Figure 3. 1. XRD result of InF_3 from Astron. 52
Figure 3. 2. XRD results of InF_3 from Synquest for different batch numbers. 53
Figure 3. 3. XRD result of InF_3 from Testbourne. 53
Figure 3. 4. TGA result of InF_3 raw materials from three different suppliers. 54
Figure 3. 5. FTIR results of $CuSO_4 \cdot 5H_2O$ (left) and InF_3 raw material sample from Testbourne ($InF_3 \cdot 3H_2O$) (right) at different temperatures. 55
Figure 3. 6. Defects obserbed in glass: (a) Defects with a haze appearance look a very fine film of dust or coating on the glass that cannot be removed; (b) Striae are mainly generated due to the unfinished homogenization melt. 56
Figure 3. 7. Absorption coefficient for the glass samples prepared under the three different fabrication conditions (a) 2.75-6.00 μm; (b) 5.00-8.75μm. 63

Figure 3. 8. DSC curves for the glass samples (IM37-39) prepared under the three different fabrication conditions (A-C), respectively.....64
Figure 3. 9. DSC curves for glasses prepared under three different conditions.....65
Figure 3. 10. Absorption coefficient and images for the glass sample IM90 (batch size: 150g). 66

Figure 4. 1. Photographs of rods IM4 of 12 mm in diameter (a), and IM6 of10 mm in diameter (b).....70
Figure 4. 2. Glass surface images: (a) before annealing at 330 ˚C less than 8 hours; (b) the edge of the glass after annealing at 330 ˚C less than 8 hours; (c) before annealing at 322 ˚C for 24 hours; (d) after annealing at 322 ˚C for 24 hours. 74
Figure 4. 3. Fluoroindate glass preforms extrude from billets. 75
Figure 4. 4. Extrusion force profile for a fluoroindate extrusion trial using die (c) at 320 ˚C. 79
Figure 4. 5. Calculated viscosity values as a function of extrusion temperature. 81
Figure 4. 6. Linear thermal expansion curve of IZSBGC sample obtained using 5˚C/min heating rate. 82
Figure 4. 7. Surface roughness of extruded preforms as a function of extrusion temperature. 83

Figure 5. 1. Microscope image of the fibre drawn from the preform IE1 extruded at 322 ˚C. 87
Figure 5. 2. Loss measurements at 1550 nm for fibres made using different methods. Linear fittings of the data are also shown in the figure. 87
Figure 5. 3. AFM morphology of IE3 surface (a) before etching; (b) surface without white precipitate after etching by 15 wt% $HCl_{(aq)}$. Insets are optical microscope images of the IE3 surfaces before and after etching. 91
Figure 5. 4. (a) SEM secondary electron image and (b) EDS analysis of the white precipitate formed after 15 wt% $HCl_{(aq)}$ etch. 91
Figure 5. 5. XRD result of the white precipitate after 15 wt% $HCl_{(aq)}$.....91
Figure 5. 6. Optical interferometric profiler images (colored images) of preform surface for IF12 fibre drawing (a) before chemo-mechanical treatment; the data in (a) is one of the measurements used for the surface roughness calculation of IE9 preform, Table 5.2; (b) after chemo-mechanical treatment. Images in grey scales in (a) and (b) are optical microscope images of the preform surfaces before and after chemo-mechanical treatment. 93
Figure 5. 7. Surface images of the fibre drop neckdown of IF13, 12, 17 and 18.....93
Figure 5. 8. Scanning electron microscopy images of fibre surfaces and cross-sections (IF13, 12, 17, 18, 15 and 19). 94
Figure 5. 9. Fibre loss spectra and spot loss measurement results at 1550 nm of IF12-6. 98
Figure 5. 10. FTIR loss spectrum of IF19 in the wavelength range of 2 – 5.5 μm. 98
Figure 5. 11. Breaking strain of IF13, 12, 17, 18, 15 and19. 99
Figure 5. 12. Fibre loss and bend strain as a function of the surface roughness of the fibres.....99

Figure 6. 1. Absorption coefficient of (a) IZSBGC and (b) ZBLAN after leaching in deionized water at 25±2˚C. Change of absorption coefficients for both glass types at (c) 2.9 μm and (d) 6.1 μm..... 106
Figure 6. 2. pH values of deionized water solutions after different leaching time (error bars are smaller than data symbols). 107
Figure 6. 3. Formation of multiple hydrated layers on ZBLAN glass during corrosion tests in deionized water. 109
Figure 6. 4. Formation of multiple and hydrated layers of IZSBGC glass during corrosion test in deionized water. 109
Figure 6. 5. EDS analysis for line scan (red line in Fig. 6.4) of the IZSBGC glass after leaching for 6 days in deionized water. 110
Figure 6. 6. Thickness of the hydrated layer of IZSBGC, ZBLA and ZBLAN versus corrosion time in deionized water. 111
Figure 6. 7. High resolution Zr 3*d* spectra for a fresh fracture surface (bottom) and a hydrated surface (top). 112
Figure 6. 8. High resolution In $3d_{5/2}$ spectra for a fresh fracture surface (bottom) and a hydrated surface (top). 112
Figure 6. 9. Fibre breaking strains before and after leaching in deionized water for ZBLAN (left) and IZSBGC (right) fibres. 113
Figure 6. 10. Scanning electron microscopy images of fibre surfaces and cross-sections: (a) ZBLAN fibre before leaching in deionized water; (b) ZBLAN fibre after leaching in deionized water; (c) IZSBGC fibre before leaching in deionized water; (d) IZSBGC fibre after leaching in deionized water. ... 114

Figure 7. 1. Photographs of IM47-50 glass samples..... 119
Figure 7. 2. Photographs IM47-50 glass samples under intense white light source (from left to right: IM47, IM48, IM49 and IM50). 119
Figure 7. 3. Procedure of Judd-Ofelt analysis. 120
Figure 7. 4. Absorption cross-section spectrum and oscillator strengths for the various bands of Pr^{3+} in fluoroindate IZSBGC glass. 123
Figure 7. 5. Absorption cross-section spectrum and oscillator strengths for the various bands of Dy^{3+} in fluoroindate IZSBGC glass.. 123
Figure 7. 6. Absorption cross-section spectrum and oscillator strengths for the various bands of Ho^{3+} in fluoroindate IZSBGC glass. 124
Figure 7. 7. Absorption cross-section spectrum and oscillator strengths for the various bands of Er^{3+} in fluoroindate IZSBGC glass. 124
Figure 7. 8. Refractive index results for (left) 0.4-2.0 μm and (right) 3-12 μm wavelength range. 131
Figure 7. 9. Raman spectra for base and doped glasses..... 133
Figure 7. 10. DSC results of base, core and cladding glasses (experimental errors of ±2˚C). 133
Figure 7. 11. A schematic diagram of stacked extrusion process for producing a simple core-clad structure. 135
Figure 7. 12. Schematic of rod/cane-in-tube process for producing a simple core-clad structure. 135
Figure 7. 13. IM127 glass surface images (core glass): (a) before annealing at 318 ˚C for 10 hours; (b) after annealing at 318 ˚C for 10 hours; (c) before annealing at 315 ˚C for 10 hours; (d) after annealing at 315 ˚C for 10 hours. 136

Figure 7. 14. IM128 glass surface images (cladding glass): (a) before annealing at 322 ˚C for 10 hours; (b) after annealing at 322 ˚C for 10 hours; (c) before annealing at 318 ˚C for 10 hours; (d) after annealing at 318 ˚C for 10 hours 136
Figure 7. 15. Photographs of extruded preforms IE24 and IE25 made using stacked billets. Note the green glass is the core glass and the colourless glass is the cladding glass (SOE: start of extrusion; EOE: end of extrusion). 140
Figure 7. 16. Photographs of extruded rods IE24 and IE25. Note that the orientation and lighting of these preforms is different compared with the preforms shown in Figure 7.15 (Both extrusions started from left to right in the Figure). 140
Figure 7. 17. Cross-sectional photographs of IE24 and IE25 preforms. 141
Figure 7. 18. Photograph of IE27 preform and the ratio of core/cladding in IE27. 142
Figure 7. 19. Refractive index of core/cladding in IE27 and comparison with original core (IM127) and clad (IM128) glass. 143
Figure 7. 20. SEM image of IF31 fibre drawn from IE35.....147
Figure 7. 21. Micro-XRD results of IF31 fibre drawn from IE35: (a) microscope image of the IF31 surface; (b) XRD pattern collected from a clear part in (a); and (c) XRD pattern collected from a white area in (a).....148
Figure 7. 22. Loss of IF31 at 980 nm using cutback measurement.....148
Figure 7. 23. Photograph of IF23 cane.....149
Figure 7. 24. Loss of IF23 cane using the cutback measurement. The high loss peaks are Pr^{3+} absorption bands. 149
Figure 7. 25. Surface roughness measurement of cane IF23 cane using an optical profiler.....150
Figure 7. 26. SEM image of IF27 fibre drawn from IE25 core/clad preform: (a) fibre cross-section, (b) interface of core and clad region, (c) side view showing fibre surface roughness. 153
Figure 7. 27. Micro-XRD results of IF25 and 27 fibre drawn from IE24 and 25: (a) Crystallisation peaks found in micro-XRD spectrum collected from white areas on the surfaces from IF25 and 27 (b) white pattern on IF25 collected Micro-XRD measurement; and (c) white pattern on IF27 collected Micro-XRD measurement.....153

Figure A. 1. Photographs of directly cast core/clad glass billets. 164

Figure B. 1. Sketch of fibre drawing furnace. 168
Figure B. 2. Measured glass temperature as a function of furnace temperature for static and dynamic measurement method using IZSBGC glass tube.....171
Figure B. 3. Glass temperature profile for dynamic (1.4mm/min) measurement method using IZSBGC glass tube and 4.5 cm and 2 cm susceptor. The axial positions L=0 and L=45mm coincide approximately with the top and bottom of the susceptor. 172
Figure B. 4. Peak glass temperature as a function of furnace temperature for dynamic and static measurements of IZSBGC glass using 4.5 cm and 2 cm graphite susceptors.. 174

LIST OF TABLES

Table 1. 1. Typical optical parameters of selected IR glasses 3
Table 1. 2. The properties of ABCYS glass ($40AlF_3$-$12BaF_2$-$22CaF_2$-$16YF_3$-$10SrF_2$) compared with ZBLAN glass ($53ZrF_4$-$20BaF_2$-$4LaF_3$-$3AlF_3$-$20NaF$) (Bulk glasses)..... 6

Table 2. 1. Different fluoride raw materials supplied by different commercial suppliers. 32
Table 2. 2. The relationship between the water temperature and density..... 50

Table 3. 1. Fabrication details of 30g block melts..... 57
Table 3. 2. 30g glass blocks melted using different crucibles 59
Table 3. 3. 30g glass blocks melting conditions. 60
Table 3. 4. Electron probe microanalysis of block glass sample IM 39 (melted under fluorination condition C). 61
Table 3. 5. Optimised base glass melting condition for different batch size. 67

Table 4. 1. Fabrication results of cast IZSBGC glass rod..... 71
Table 4. 2. Temperature effects on annealing test. 73
Table 4. 3. Extrusion Parameters: Preform surface roughness, S_a and S_q, Extrusion temperature, T, Die Channel Diameter, D_1, Die Channel Length, L_1, Ram Speed, V_0, Ram Force, F, Slip coefficient, α, Glass viscosity η.. 77

Table 5. 1. Glass rod / preform preparation conditions and results of the fibre loss. 87
Table 5. 2. Fibre drawing conditions, results of spot loss measurements and surface roughness of fibres IF4, IF13, 12, 17, 18, 15 and 19. 89
Table 5. 3. Etching solution studied for fluoroindate glass. 92
Table 5. 4. Fibre strain of Trial IF13, 12, 17, 18, 15 and 19..... 98

Table 6. 1. Semi-quantitative analysis measured using EDS for multi-layer compositions for ZBLAN glass after 6 days corrosion in deionized water (in at.%) 108
Table 6. 2. Comparison of fibre breaking strains before and after leaching in deionized water for ZBLAN and IZSBGC fibres. 114

Table 7. 1. RE ion doped IZSBGC glass blocks (30 g). 119
Table 7. 2. Judd-Ofelt parameters for IZSBGC fluoroindate glass. 122
Table 7. 3. Radiative decay rates, A_{ba}, branching ratios, β_{ba}, radiative lifetime, $\tau_{rad,}$ and emission peak for the main emitting states of rare earth ions in IZSBGC glass. 127
Table 7. 4. Properties of 30 g glasses with modified glass composition. 129
Table 7. 5. Comparison of refractive indices for IM127/IM128 and IE27 core/clad glass combination at 1550 nm (using J.A. Woollam Co., Inc. VASE Ellipsometer HS-190) and 3000~5500 nm (using J. A. Woollam Co., Inc. VASE Ellipsometer VB-400). 132
Table 7. 6. Melting condition for different batch size. 138
Table 7. 7. Extrusion condition for core and cladding glass..... 145
Table 7. 8. Surface roughness and fibre loss at 980 nm of fibres or canes. 151

Table A. 1. Results for IZSBGC clad glass melts. 165
Table A. 2. Results for IZSBGC Pr-doped glass melts including core glass melts. 166

Table B. 1. Experimental details of IZSBGC glass profiling. 175
Table B. 2. Summary of peak glass temperature at different furnace temperatures for 4.5 cm susceptor. 176
Table B. 3. Summary of peak glass temperature at different furnace temperatures for 2cm susceptor. 176

Chapter 1

INTRODUCTION

1.1. Overview

Low-loss silica fibres, one of the greatest inventions in the last century, have become a fundamental element of our communication systems, and are vital for medical science, sensor technology and laser manufacturing. Since Kao and Hockham first put forward their new concept of using silica glass optical fibres as a data transmission medium in 1966 [1], great efforts have been spent on making or improving optical fibre performance. After the first fibre with a loss of 20 dB/km was developed by the Corning glass research group in 1970 [2], researchers have been focusing on how to reduce the transmission loss which has been reduced greatly in the following 10–20 years, e.g., 0.5 dB/km (1.2 μm) in 1976 [3], 0.157 dB/km (1.55 μm) in 1984 [4], and 0.154 dB/km (1.55 μm) in 1986 [5]. The 0.154 dB/km fibre loss has already approached its theoretical minimum value. The achievements in low loss and low attenuation enabled the development of telecommunication and internet in 1980's.

The widespread use of optical fibres has been driven by growing demands in the telecommunication, medical and defence industries. With the transmission losses of silica- based optical fibres approaching the theoretical limits and the increasing demand for high transmission bandwidth, research in optical fibre technology has been directed towards new materials or approaches that might enable even lower losses. In particular, new approaches to the realisation of infrared transmitting fibres have been intensively explored since 1980's [6-8]. Mid-infrared optical fibres can be defined as fibre optics that

transmit electromagnetic radiation with wavelengths greater than approximately 2 μm [9]. The transmission window of mid-IR optical fibres for guiding light is in the range of 2.5-25 μm. The mid-IR spectral region is of great importance because of its specific sensitivity to numerous molecular rotational and vibrational states of gases, toxic agents, air water, soil pollutants, the building blocks of life, and several explosive agents. All of these occur in the infrared 'fingerprint' region of the electromagnetic spectrum – between approximately 2.5 and 25 μm. Therefore, low-loss mid-IR optical fibres will ultimately become indispensable tools for a variety of applications in environmental monitoring (e.g., pollution control), detection of water quality, soil contaminants, life sciences, atmospheric chemistry, non-invasive disease diagnosis, and public safety.

Nowadays, fibre materials, especially for mid-IR fibres, are commonly made from glasses. Several mid-IR glass systems have been widely studied. For example, ZBLAN glasses have high transmittance up to 4–5 μm, but they have poor mechanical properties and chemical durability. Chalcogenide glasses have wide transmission regions (from near infrared to far infrared region) but their transmittances are lower than other glasses principally due to their higher Fresnel loss. In comparison, indium fluoride-based glasses have longer cut-off transmission wavelengths than fluorozirconate glasses, and present good optical quality, stability against atmospheric moisture, and mechanical stability [10]. The research presented in this thesis investigates the fabrication of indium fluoride-based mid-IR glasses and fibres, and aims to advance the research underpinning low-loss fluoroindate glass fibres using the extrusion technique for preform fabrication.

1.2. Literature review

1.2.1. Mid infrared glasses

There are three broad classes of IR transmitting glass materials for fibre fabrication: (1) heavy-metal oxide glasses (e.g., TeO_2- and GeO_2-based systems with heavy-metal oxides); (2) heavy-metal fluoride (HMF) glasses, including indium fluoride-based glasses; and (3) chalcogenide glasses which contain one or more of the chalcogen elements (8S, Se or Te). Table 1.1 shows the transmission range and refractive index at 1.55 μm of several infrared glasses, including oxide (e.g., TeO_2 glass), HMF (e.g., ZBLAN) and chalcogenide glasses (e.g., sulfide, selenide, and telluride glasses).

Table 1. 1. Typical optical parameters of selected IR glasses

Glass type	*n* (refractive index @ 1.55 μm	Wavelength range of transparency (μm)	Sample thickness (mm)	Bibliography
Tellurite glass	1.98	0.4-5.5	~2	[11]
Germanate glass	1.85	0.26-5	~2	[12]
InF_3 based fluoride glass	1.44	0.3-8.5	~3	[13]
ZBLAN fluoride glass	1.49	0.3-7.5	~2	[14, 15]
As_2Se_3 chalcogenide glass	2.90	1.0-15	~10	[16]
Te-based chalcogenide glass	~3.20	1.5-20	~3	[17]

Both tellurite and germanate based heavy metal oxide glasses have high rare earth solubilities, which makes them promising for application as laser and amplifier materials [12, 18]. TeO_2 glasses have reasonably wide transmission regions (up to 6 μm with a glass thickness of 2-3 mm [19]), due to their relatively low phonon energies in oxide glass network formers (> 600 cm^{-1}) [20-22], and high refractive and nonlinear refractive indices (about 2) [23, 24]. Germanate-based heavy metal oxide glasses can transmit visible to infrared lights, ranging from 0.3 to 5 μm [25]. Germanate glasses generally have higher glass transition temperatures (>380 ˚C) than tellurite (e.g. ~290 ˚C for ZnO-containing tellurite glasses) and fluoride glasses (typically around 300 ˚C) [26, 27], and possess better thermal and mechanical stabilities than other IR transmitting glasses due to the stronger Ge-O bond between Ge^{4+} and O^{2-} ions. Hence, germanate glasses have higher glass transition temperature and higher laser-damage thresholds [28]. This makes germanate glasses promising fibre materials for 3 μm laser power delivery [29]. Compared with tellurite and germanate glasses, chalcogenide glasses (e.g., $Ge_{15}Te_{75}Ga_{10}$) have wide transmission up to 27 μm for a glass thickness of 2 mm, low glass transition temperatures (<200 ˚C) [30] and high nonlinearity [31]. However, chalcogenide glasses are generally less robust due to their weaker bonds than those of most oxide glasses [32]. The preparation of chalcogenide glasses also involves rather sophisticated processes (e.g., raw materials requiring sealed in silica ampoules under vacuum, application of a rocking furnace for melting) [33]. In addition, the solubility of rare earth elements in chalcogenide glasses is typically lower than that in oxide and fluoride glass systems [34].

Fluoride glasses have attracted much research interest over the past few decades. They have theoretically lower losses than silica glass [35] and can transmit light in the IR wavelength region due to the shift of the multi-phonon edge to longer wavelengths in the presence of heavier metal ions. Similar to TeO_2- and GeO_2-based glasses, fluoride glasses can also be prepared by the relatively easy direct-casting process with high solubility of rare earth elements [13, 36], much simpler than that for preparing chalcogenide glasses. Fluoride glasses have high transmission in mid IR regions up to 9 μm with a glass thickness of 3 mm [15], wider than those of TeO_2- (~6 μm [24]) and GeO_2- (~5.5 μm [25]) based glasses. Fluoride glasses also exhibit lower refractive index and optical nonlinearity than chalcogenide, TeO_2-, and GeO_2-based glasses, and therefore they are suitable matrices for high-power laser application [34] Although the mid IR transmission window of fluoride glasses are narrower than those of chalcogenide glasses, the preparation of the former glass systems can be carried out using the relatively straightforward direct-casting technique. More detailed introduction of fluoride glasses will be covered in the next section which also includes InF_3 based glasses – the focus of this PhD thesis.

1.2.2. Fluoride glasses

Fluoride glasses can be divided into four types: fluoroaluminate glasses based on AlF_3, fluorozirconate glasses based on ZrF_4, fluoroindate glasses based on InF_3, and fluoride glasses based on divalent fluorides [37]. Most previous studies in relation to fluoride glasses were focused on fluorozirconate and fluoroaluminate matrices. Since the last decade, indium fluoride glasses have attracted more and more attentions.

1.2.2.1. Fluorozirconate glasses

Fluorozirconate glasses mainly contain ZrF_4 and can transmit light of up to 7.5 μm (50% transmission including Fresnel reflection) through the glass with thickness of around 4 mm [38]. Poulain et al. [39] first prepared ZrF_4-BaF_2 glasses, and found that the likelihood of glass crystallisation decreases when AlF_3 was added into the glass matrix, and that the glass thermal stability can be further improved by introducing NaF. Poulain et al. concluded that the introduction of these additional components added into fluoride glasses can improve the glass thermal stability. Qiu et al. [40] found that the substitution of MgF_2, CaF_2 or SrF_2 for BaF_2 in the ZrF_4-AlF_3 based system resulted in decreases in density and refractive index, glass-forming ability and thermal stability, and that substitution of PbF_2

for ZnF_2, on the contrary, gave rise to an opposite trend. Similar results were obtained previously when ZnF_2 was replaced by PbF_2 [40]. The increase in glass stability (low devitrification rate) due to mixed alkali effect [40] (mixed effect due to the presence of two or more either alkaline or alkaline earth elements) was observed only when BaF_2 was replaced by SrF_2. These phenomena can be explained from the viewpoint of the glass structure as well as from the mutual obstruction effect of ions [40].

Ko and Doremus [41] suggested that fluorozirconate glass structures are based on zirconium fluoride units in eightfold coordinations. Ignatieva and Bouznik [42] investigated the structures of fluorozirconate and oxyfluoroniobate glasses by quantum chemical DV-X_α method together with spectroscopic analysis. The isolated ZrF_6^{2-} molecular ions are dissociated to remain stable, while ZrF_7^{3-} and ZrF_8^{4-} are unstable and dissociated into ZrF_6^{2-} and F^-, primarily because a change of the ZrF_7^{3-} charge state from 3 to 2 from dissociation energies (assuming chain-like ZrF_7 polyhedra) stabilises the seven-coordinated polyhedra. Therefore, ZrF_7^{3-} and ZrF_8^{4-} have to join by Zr–F–Zr bridging bonds and form networks from ZrF_7 and ZrF_8 polyhedra to increase their stability.

Among all fluorozirconate glasses, ZBLAN glass ($53ZrF_4$-$20BaF_2$-$4LaF_3$-$3AlF_3$-$20NaF$ (in mol %) is the most stable fluorozirconate glass. ZBLAN optical fibres are widely used in various mid-IR applications such as high laser power delivery and fibre lasers and amplifiers [43].

1.2.2.2. Fluoroaluminate glasses

Compared with ZrF_4-based glasses (Table 1.2), AlF_3-based fluoride glasses exhibit similar optical features (e.g., extended IR transmission up to 6 μm for a thickness of 3 mm) [44]), with better thermal stability, higher glass transition temperature, and better chemical durability and mechanical strength [38]. However, glass compositions (glass-forming regions) of fluoroaluminate glasses are small and limited [45]. Hence, multi-component glass compositions have been adopted to improve the glass-forming region. For example, Hu and Lin [46] studied the effect of addition of YF_3, LaF_3 and YbF_3 on the kinetics of glass crystallisation and change of crystalline phases, and found that the addition of suitable amounts of YF_3 and/or YbF_3 improved the glass-forming region of RF_3-AlF_3 systems (R=Ca+Mg+Sr+Ba).

Table 1. 2. The properties of ABCYS glass ($40AlF_3$-$12BaF_2$-$22CaF_2$-$16YF_3$-$10SrF_2$) compared with ZBLAN glass ($53ZrF_4$-$20BaF_2$-$4LaF_3$-$3AlF_3$-20NaF) (Bulk glasses) [38]

Properties		ABCYS	ZBLAN
Optical properties			
Cut off wavelength (μm) (thickness=4 mm)	UV (T=50%)	0.29	0.20
	IR (T=50%)	6.84	7.57
Chemical properties			
Water solubility (23 ˚C) weight loss%		0.01	29.2
Thermal properties			
Glass transition T_g (˚C)		432	256
The onset of crystallisation T_x (˚C)		556	349
Melting point T_m (˚C)		726	450
Mechanical properties			
Young's Modulus E (kg/mm^2)		5720	5380
Knoop Hardness H (kg/mm^2)		370	225
Poisson's Ratio		0.31	0.31

Glass network structure affects optical properties, chemical stability and mechanical strength [47]. In contrast to fluorozirconate glasses, relatively little is known about the glass network structures of fluoroaluminate glass systems. Videan and Kawamoto [48, 49] studied the structures of AlF_3-CaF_2-BaF_2 glasses by Raman spectroscopy, and suggested that these glasses only consist of both $[AlF_6]$ and $[AlF_4]$ or $[AlF_6]$. Chen and Gan [50] investigated AlF_3-YF_3-MF_3 (M=Ca+Mg+Sr+Ba) glasses by Raman and infrared spectroscopic techniques and observed that (1) a significant variation in AlF_3 to YF_3 molar ratio could change the vibrational spectra indicating that there are both tetrahedral $[AlF_4]$ and octahedral $[AlF_6]$ units in the $50AlF_3$-$50MF_2$ (M=Ca+Mg+Sr+Ba) glasses; (2) when AlF_3 was replaced by YF_3, the number of tetrahedral $[AlF_4]$ units decreased and YF_n polyhedral appeared; and (3) almost all the tetrahedral $[AlF_4]$ units were substituted by YF_n polyhedral and there were mainly $[AlF_4]$ and $[AlF_6]$ polyhedral units in the glass network of $20AlF_3$-$30YF_3$-$50MF_3$. Akasaka and Nanba [51] studied the structure of a ternary $40AlF_3$-$20YF_3$-$40CaF_2$ glass (AYC glass) by a combination of X-ray diffraction,

neutron diffraction and molecular dynamic simulations. Compared with $40AlF_3$-$20BaF_2$-$40CaF_2$ glass (ABC), the AYC glass has a similar structure, with AlF_6 octahedra connected by their corners to form chains with branches. Although AlF_7 polyhedra were not found in the ABC glass, they exist in the AYC glass (one-third of the AlF_6 octahedra) but are distorted due to the presence of Y^{3+}.

1.2.2.3. Indium fluoride based glasses

Due to low maximum phonon energy (~510 cm^{-1}) of fluoroindate glass, they are characterised by transmittance further into the IR region, and significantly lower non-radiative decay rates in comparison with fluorozirconate and fluoroaluminate glasses [52-54]. They also present better optical quality, stability against atmospheric moisture, and mechanical stability than fluorozirconate glasses [10].

ZBLAN fibres (1m length) can only transmit up to ~ 4 μm, which restricts laser and fibre applications in the mid IR range. As a new fluoride glass candidate, indium fluoride glass system attracted more and more attention in the mid IR application, due to its wide transmittance up to 5.5 μm (1 m fibre length) [55], since Videau [56], for the first time, investigated indium fluoride glasses (InF_3-BaF_2-YF_3) in 1983. Since then, more studies have been focused on the characteristics and advantages of fluoroindate glasses, especially in ternary and multi-component (more than three components) InF_3-based glasses.

It is generally accepted that InF_3-based glasses have similar structures to those of fluoroaluminate glasses and consist of InF_6 octahedra [57]. GaF_3 is normally added to increase the stability of InF_3 glasses and form In/Ga glasses which are called BIG glasses. BIG glasses (e.g. $30BaF_2$-$18InF_3$-$12GaF_3$-$20ZnF_2$-$10YbF_3$-$6ThF_4$-$4ZrF_4$) have equivalent thermal stability as ZBLAN ($53ZrF_4$-$20BaF_2$-$4LaF_3$-$3AlF_3$-$20NaF$) glasses. To date many types of InF_3 glasses have been synthesised such as InF_3-BaF_2-ZnF_2-SrF_2 and PbF_2-InF_2-GaF_3 glass systems [36]. Furthermore, extended transparency of InF_3 glasses in the infrared wavelength region as shown in Figure 1.1 is very promising for active optical fibre applications.

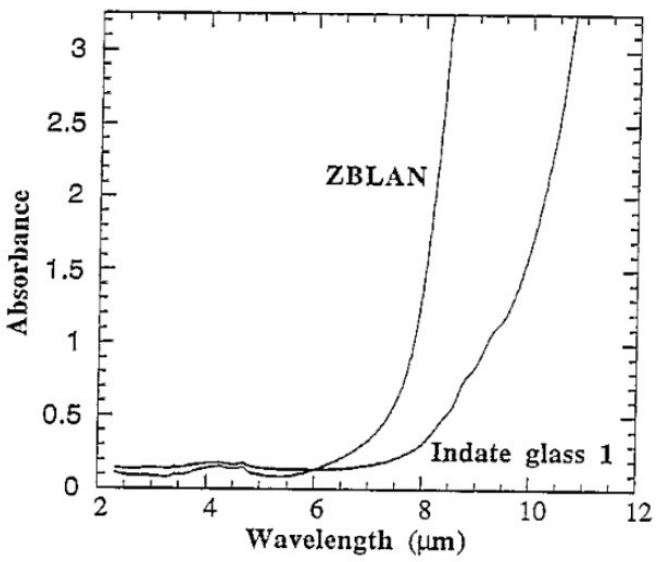

Figure 1. 1. Absorbance spectra of fluorozirconate (ZBLAN) and fluoroindate glass (IZBS) with 3 mm thickness [13].

Messaddeq et al. [36] prepared InF_3- ZnF_2-SrF_2-BaF_2-X (X= PbF_2, CdF_2, NaF, CaF_2; IZSBX) glasses, and found that the glass forming ability increases with increasing content of CaF_2 and PbF_2. The preparation of large bulk samples were limited by crystallsation stability. It was found that this could only be overcome by the addition of small quantities of GdF_3 (less than 4 wt%). Boutarfaia et al. [58] investigated the glass formation of InF_3-BaF_2-SrF_2-YF_3 systems and, pointed out that the quaternary system is more stable due to the presence of YF_3 acting as a stabiliser with the optimum concentration from 5 to 10 mol%. Later on, Boutarfaia et al. [59] also investigated the glass-forming ability and crystallisation kinetics of multi-component In/Ga fluoride based glasses according to the 'confusion effect' and found that the glass forming ability increases when NaF is replaced by LiF and decreases when KF and CsF is substituted for NaF.

An earlier study [15] has shown that the glass composition of $32InF_3$-$20ZnF_2$-$20SrF_2$-$18BaF_2$-$8GaF_3$-$2CaF_2$ (IZSBGC) with high InF_3 content is particularly promising for mid-infrared application due to its high transmission and low rate of crystallisation. This is an advantage for fabricating high power delivery fibre in the mid infrared region. Therefore, this research project chose to focus on IZSBGC glass system for fibre applications.

1.2.3. Loss mechanisms in fluoride glasses

The loss characteristics of glasses are determined by two main factors: intrinsic and extrinsic losses. Two dominant intrinsic loss contributions in fluoride glasses are Rayleigh scattering and IR edge absorption while extrinsic losses arise from the absorption and scattering of impurities such as crystals, transition metals, bubbles and OH^- stretch vibration [60].

1.2.3.1. Intrinsic losses in glasses

(a) IR absorption edge

Optical transparency in the infrared region is dependent on phonon absorptions, which are associated with molecular vibration energy.

Considering any particular anion-cation pair, the fundamental stretching vibration frequency can be calculated by the Szigeti equation [61]:

$$V_0 = \frac{1}{2\pi}\sqrt{\frac{F}{\mu}} \tag{1-1}$$

Where F is related to the bond strength, and μ is the reduced mass of the pair $[m_c * m_a/(m_a+m_c)]$. The infrared cut-off frequency depends on the largest vibration frequency of the glass network formers. The principle of designing infrared transmitting glasses is that the weakly-bound compounds should be selected as glass network formers to ensure a low basic vibration frequency. Therefore to obtain good infrared light transmitting glasses, metal compounds with high reduced masses and low force constants are preferred [62]. Phonon energy decreases with decreasing frequency; hence, low phonon energy materials with heavy elements and weak bonding are needed in order to obtain long-wavelength transparency.

(b) Rayleigh scattering

Rayleigh scattering is caused by microscopic variations in the local dielectric constant on a scale much smaller than the wavelength of light [63]. The magnitude of the optical scattering coefficient due to this effect can be calculated using electromagnetic theory and thermodynamics [64]:

$$\alpha_{scatt,\rho} = \frac{8}{3}\frac{\pi^3}{\lambda_4}\left(n^8 p^2\right)\left(kT_f\right)\beta_T \tag{1-2}$$

where λ is the optical wavelength, n is the refractive index, p is the photoelastic coefficient, k is Boltzmann's constant, T_f is the fictive temperature corresponding approximately to the glass transition temperature, T_g , and β_T is the isothermal compressibility of the material. The term kT_f presents the driving energy for density fluctuations. Glasses with lower T_g often have greater driving energies. The ZrF_4-based fluoride glasses have T_g typically around 550 K, which are much lower than the T_g of vitreous silica (1400 K), and hence fluoride glasses have potentially lower scattering due to density fluctuations.

Multi-component homogeneous glasses, however, have additional scattering losses associated with compositional fluctuations (if the size of scattering centers is smaller than the wavelength of light [65]). An expression for the mean composition fluctuation in the glass can be derived by [60, 66]:

$$\left\langle \Delta C^2 \right\rangle T = \rho_0 / C_0 \,(kT_f / V)\left(\frac{\partial \mu}{\partial G}\right)^{-1} C_0, T_f \tag{1-3}$$

where C is the mole fraction of one of the components in the glass composition C_0, ρ_0 is the density of the glass with the composition C_0, μ is the chemical potential difference between the major and minor constituents, and V is the molar volume. In Eq. (1-3), the compositional fluctuations are minimised when T_g is low and the chemical potential for a small compositional variation is large. It appears that glasses with low T_g such as ZrF_4-based glasses indeed have low compositional and density fluctuations, and hence low Rayleigh scattering [60].

Theoretical calculations of Rayleigh scattering due to the density fluctuations for ZrF_4-based glasses have been carried out by Poignant using Eq. (1-2) [64]. Their calculations indicated that the theoretical limit of Rayleigh scattering for the ZrF_4-based glasses (0.4 dB/km at 1 μm, 0.06 dB/km at 1.6 μm and 0.0015 dB/km at 4 μm) is about half that for vitreous silica (the most widely used fibre material) (0.8 dB/km at 1 μm, 0.12 dB/km at 1.6 μm and 0.003 dB/km at 4 μm), if the influence of the compositional fluctuations is

ignored. Up to date, there have been a number of reports on the scattering measurements for both bulk fluoride glasses and fibres [67-72]. The scattering data are Rayleigh in character, exhibiting a λ^{-4} dependence. Tran et al. [67] directly measured the scattering in the mid-infrared spectral region for homogeneous ZrF_4-based glass samples with relatively large sizes and showed that the total scattering coefficients were near the theoretical limit. Indeed, the measured and theoretical Rayleigh scattering of ZrF_4-based glasses are both lower than those of silica glasses in the mid-infrared region. Although silica glasses have low Rayleigh scattering in both near and mid-infrared regions, they have high multiphonon absorption. In comparison, fluoride systems (i.e., ZrF_4-based glasses) have both low multiphonon absorption and Rayleigh scattering, which make potentially good candidates for low-loss fibres.

1.2.3.2. Extrinsic loss in glasses

Compared with intrinsic loss which determines the absorption edges, the extrinsic loss is more important as it dominates the glass fibre loss in the transmission window especially for fluoride glasses. The losses of fabricated fibres are always higher than the theoretically estimated values. It is important to note that Rayleigh scattering, which ultimately determines the attainable loss, represents only a small contribution to the fibre loss for fibres, and elimination of many other extrinsic losses caused by absorptions and scatterings is important and challenging. For example, Shibata et al. estimated the theoretical minimum fluoride fibre loss to be $<10^{-2}$ dB/km at 2-3 μm, one magnitude lower than that of the conventional silica fibres that underpin our telecommunications systems. This estimate was based on losses due to Rayleigh scattering and IR edge absorption which are the dominant intrinsic loss factors in fluoride glasses [7]. However, the lowest fluoride fibre loss reported so far is 0.7 dB/km at 2.6 μm measured by Kanamori and Sakaguchi on a 30 m long fluorozirconate fibre [73], which is still significantly higher than the theoretical loss. Since fluoride glasses have significantly lower crystallisation stability than oxide glasses, impurities in the raw materials and moisture in the atmosphere during preparation of fluoride glasses can easily induce crystallisation which leads to scattering centers and increases the loss [74]. Absorption of impurities such as transition metals and rare earth ions in the raw materials also contributes to the loss of the glass, resulting in absorption losses in the fibres [75]. In summary, extrinsic losses come from several sources but can be broadly categorised into two groups: extrinsic absorption and extrinsic scattering.

(a) Extrinsic absorption

Extrinsic absorption is caused by the presence of impurities in glass. It may result from the impurity metal ions, hydroxyl ions, molecular ions and gases in the glass [62] which can be introduced from raw material itself or glass/fibre fabrication process (e.g., metal ions dissolved from crucible or casting mould during melting or casting). Hence, it is essential to use raw materials with high purities during glass fabrications to reduce impurity metal ions content and optimise glass fabrication (e.g., fluorination, selection of suitable crucible materials for melting).

(1) Transition metals and rare earth elements

Absorption due to 3*d* transition from transition metals (e.g., Ti^{4+}, Fe^{2+}, Fe^{3+}, Co^{2+}, Ni^{2+}, Cu^{+} and Cu^{3+}) introduced from raw material impurities and fabrication procedures (casting mould) and rare earth ions is one of the key factors that prevents the further reduction of present fibre losses. The 3*d* transition of metal impurities and absorption from some rare earth elements due to their narrow width of the energy level splitting in the mid-IR region can cause significant fibre losses.

(2) Hydroxyl groups

Hydroxyl impurities can cause absorption and optical loss, which is one of the major problems to be overcome during the preparation of glass fibres. In silica fibres operating at 1.3 or 1.55 μm, a combination band of the fundamental OH stretching vibrations at 2.72 μm have been found [76]. The most intense absorption peak in many fluoride fibres due to the fundamental OH resonance is around 2.9 μm.

(3) Molecular ions and gases

Molecular ions such as NH^{4+}, CO_3^{2-}, SO_4^{2-} and PO_4^{3-} have their fundamental absorptions in the infrared region. Therefore, contamination by these complex ions can reduce the infrared transmission of fluoride glass fibres [77].

(4) Fluorine deficiency

ZrF_4-based glasses synthesised under reducing conditions are often found to contain black substances within a transparent glass block; these black substances are sometimes even found in glasses prepared under inert atmosphere conditions. Robinson et al. [78] found these black substances in glasses prepared under an HF atmosphere, and identified them

as fluorine-deficient phases produced from the dissociation of ZrF_4 (Eq. 1-4). These species have a broad absorption band around 0.5 μm [79].

$$ZrF_4\left(white\right) \rightarrow ZrF_2\left(black\right) + F_2 \tag{1-4}$$

In order to suppress this absorption completely, glass synthesis must be conducted under oxidizing conditions [79].

(b) Extrinsic scattering

The extrinsic scattering in glasses is related to impurities in glass. It is a major cause of loss in glass and strongly affected by the technological process of glass fabrications. Present fluoride fibres have some extrinsic scattering centres such as microcrystallites, oxide, non-oxide particles, and bubbles.

(1) Crystals

In general, fluoride glasses have lower stability against crystallisation than silica-based systems. Hence fluoride glasses are more likely to have crystallisation during fibre fabrication processes such as casting of glasses and fibre drawing. Since crystals have different refractive indices from those of the glass hosts, they can scatter light in the glasses and can, therefore, increase the scattering loss. The degree of additional scattering loss depends on the crystal sizes and the differences in refractive index between the crystals and the glass matrix.

The crystallisation tendency of glasses depends largely on the basic glass compositions and dopants. In addition, impurities in the glass such as hydroxyl ions, different complex ions, oxides, and metal particles can significantly increase the likelihood of crystallisation. The most deleterious and ubiquitous impurity is water/moisture that may exist in the processing environmental atmosphere and in the raw materials, resulting in crystallisation in the final glass products. The presence of water/moisture in the drawing atmosphere can also facilitate surface crystallisation of preforms and fibres, and hence fibre drawings require to be carried out under dry atmosphere.

(2) Phase separation

Phase separation is a phenomenon whereby the glass matrix separates into two different amorphous phases at elevated temperatures. Since the separated phases generally have different refractive indices, the occurrence of phase separation can cause excess scattering. Phase separation has been found in some fluoride glass systems (e.g., ZBLAN) [80, 81]. Although this problem can be minimised by optimising the glass compositions, it is still a concern for fluorozirconate glasses [82].

Previous studies on oxide glasses [83, 84] suggested that a small amount of certain substance added to glasses (e.g., impurities in raw materials) may cause a substantial change in the interfacial tension of the phase in which the additives concentrate, or glass structure. Such changes may cause lower viscosities and higher diffusion rates of mobile ions so that phase separation can proceed. This accounts for the influence that water incorporated into the glass structure causes the phase separation behaviour of glasses according to the studies by Kreidl [84]. It seems that a small glass compositional change may result in phase separation. The best way to avoid phase separation is to optimise glass compositions or prevent glass compositional change resulting from impurities/contamination ions during melting.

(3) Bubbles

Bubbles are often found in preforms fabricated by various techniques including built-in casting [85], rotational casting [68], double crucible technique [86], and extrusion [87, 88].

The presence of bubbles in fibres also contributes to excess scattering. For example, according to the calculations by Moore et al. [89], a spherical bubble of 10 μm in diameter would contribute 0.1 dB of essentially wavelength-independent scattering. As the bubbles become smaller, the scattering starts to show wavelength dependence and the transition due to Rayleigh λ^{-4} scattering occurring when bubbles are smaller than 0.3 μm in radius.

McNamara and MacFarlan [90] investigated the shrinking behaviour of bubbles, and found that there are three types of bubbles in the glasses (1) bubbles that collapse completely during heat treatment; (2) bubbles that shrink to a minimum size and then go no further, (3) and bubbles that collapse into a dispersed group of smaller bubbles.

Studies [91] [92] have shown that crystals and bubbles are significant sources of scattering loss and therefore a further lowering of loss could be expected if these could be eliminated.

1.2.4. Evaluation of glass stabilities

Some glass characteristic temperatures can be measured by differential thermal analysis (e.g., differential scanning calorimetry – DSC). Glass thermal stability is usually evaluated, based on some indicators containing these characteristic temperatures. The most commonly used indicator is ΔT, which is the difference between the glass transition temperature (T_g) and the onset of crystallisation (T_x):

$$\Delta T = T_x - T_g \tag{1-5}$$

Glasses with good glass-forming abilities should have large ΔT. However, this criterion only gives a general estimate of glass stability, limiting its application. It is largely known that heavy metal fluoride glasses are more likely to have phase separation. Fluoride glasses often have two or more T_g temperatures which are rather difficult to characterise; thus the use of ΔT is limited in practical applications. Hruby [93] suggested that T_g, T_x and T_m (melting point) should be taken into account at the same time, and that a new parameter H_r can be expressed as:

$$H_r = \frac{T_x - T_g}{T_m - T_x} \tag{1-6}$$

In addition, other parameters used to evaluate the glass thermal stability are weighted thermal stability range and Saad-Poulain parameter S [94]:

$$H' = \frac{T_x - T_g}{T_g} \tag{1-7}$$

$$S = \frac{\left(T_p - T_x\right)(T_x - T_g)}{T_g} \tag{1-8}$$

Iqbal [95] also defined a new parameter by taking into account the critical cooling rate R_c:

$$ST = \left(T_x - T_g \,/\, R_c\right) \tag{1-9}$$

However, these terms are not always accurate because of the complex glass systems. For example, the errors of S indices can be very large due to the following two reasons: (1) the glass crystallisation peak temperature (T_p) is largely dependent on the sample particle sizes for e.g., DSC analysis; (2) and melting temperature (T_m) cannot be accurately measured as Tm is normally higher than the highest working temperature of DSC. Hu and Jiang [96] suggested that the crystallisation kinetic factor (K_{TP}) is a more reasonable method to characterise the glass thermal stability. The new equation can be defined as:

$$K_{T_p} = \upsilon \cdot \exp\left(-E \,/\, RT_p\right) \tag{1-10}$$

in which E is the activation energy of crystallisation process and υ is the frequency factor.

1.2.5. Fluoride glass, preform and fibre fabrication

IZSBGC glasses, which possess absorption edges at longer wavelengths than fluorozirconate glasses (e.g., ZBLAN glass) [15], were chosen as a potential glass for glass and fibre fabrication research within this project. A series of glasses were required being prepared by optimising the glass and fibre qualities.

Several research studies have been published on the subject of fluoroindate glass fibres with low losses. Among these fluoroindate glass matrices, PbF_2-InF_3 based fluoride glass has high thermal stability against crystallisation, and has been fabricated into a fibre with a minimum transmission loss of 0.043 dB/m at 3.33 μm [97]. In comparison, Itoh et al. have developed a single-mode fibre, using InF_3/GaF_3 glass as a core glass and ZBLAN glass as a cladding glass, with a low loss around 0.2 dB/m at 1.2 μm [98]. Nishida et al. systematically studied InF_3/GaF_3 glass fibres and obtained a minimum loss of 0.025 dB/m at 3.3 μm [99]. Recently a multimode fibre with an optical loss of 0.85 dB/m at 1.3 μm was obtained from a preform made by rotational casting method, where the importance of fluorination with HF during glass melting was also discussed [100]. However, all these fibres have comparatively low InF_3 (~28 mol%) and high GaF_3 contents, which limits their IR transmittance.

Commercial fluoroindate glass fibres are now available with low loss in a wide spectrum (<1 dB/m for 1.5-5 μm) [55], but the glass composition is not available in the open literature. An earlier study [15] reported the successful preparation of $32InF_3$-$20ZnF_2$-$20SrF_2$-$18BaF_2$-$8GaF_3$-$2CaF_2$ (IZSBGC) fibres, but the resulting fibre loss was unknown.

To understand and investigate fabrications of fluoroindate glass fibres, state-of-the-art progress on the fabrication processes of fluoride optical fibres is reviewed in this section.

1.2.5.1. Fluoride glass preparation

In contrast to molten oxides, molten fluorides are less viscous but more likely to have crystallisation and are highly corrosive to crucible materials. In the synthesis of a fluoride glass, there are different problems when glass melting progresses in crucibles, such as corrosions to melting equipment (including crucibles), the reactions with oxygen and moistures in the atmosphere, evaporations and phase separations. Since fluoride glass preparation is sensitive to the melting atmosphere, it is crucial to strictly control the melting conditions for minimising the problem metioned above.

(1) Melt-quench method

The melting procedure for the melt-quench method is as follows: (1) firstly, fluorides are carefully and thoroughly mixed in appropriate proportions and melted in the temperature range of 800 to 1000˚C; (2) after melting, glass melts are poured into preheated stainless steel or brass moulds; (3) finally, glasses are annealed at a certain temperature below T_g to reduce thermal strains formed during quenching. To avoid the reactions between fluorides and H_2O, moisture levels are strictly controlled during melting, achieved by melting glasses in an atmosphere-controlled glove box.

High-purity raw materials are critical to successful glass preparation as impurities such as oxgyen, low transition metals and rare earth elements contained in the raw materials can result in colour centres, IR absorption and fluorescence quenching. The use of high-purity raw materials will help to minimise the number of scattering centers in glasses.

Apart from the purity of raw materials, the melting atmosphere is of paramount importance for preparation of fluoride glasses. Fluoride glasses must be prepared under strictly-controlled melting atmospheres (e.g., under dry N_2, use of ammonium bifluoride for fluorination of oxidised raw materials) to prevent hydrolysis, surface crystallisation,

etc. Gold, platinum and vitreous carbons are normally used as crucible materials at temperatures above 400 ˚C as molten fluorides will react with oxide-based crucibles [74].

(2) Ammonium bifluoride processing (ABP)

The first use of ABP for fluoride glass synthesis can be traced back to Sun [101] for fluoroberyllates, where it was used to prevent melt hydrolysis. However, NH_4HF_2 had later been found to have another capability of converting oxides into fluorides; this was then utilised for preparing fluoride glasses from oxide materials. The chemical reaction between oxides and NH_4FHF can be written as:

$$MO_n + (n + \frac{x}{2})NH_4HF_2 \Leftrightarrow MF_{2n} \cdot xNH_4F + nH_2O + (n - \frac{x}{2})NH_3 \qquad (1\text{-}11)$$

This reaction can usually occur at a low temperature: for example, mixing ZrO_2 and NH_4HF produces an exothermic reaction. Metallic ammonium fluoride complexes further decomposes upon heating, and the residual traces of volatile NH_4F are mostly removed during melting.

In practice, the glass batch is first heated to a temperature between 200 and 400 ˚C and held at this temperature for a short period which may vary from a few minutes to several hours. The optimum temperature and duration depend on many factors:

- Water content of starting materials, including ammonium bifluoride
- Water concentration in working atmosphere in the glove box
- Batch size
- Batch composition
- Residual concentration of carbonates, nitrates, and oxysalts
- Crucible geometry
- Pressure
- Content of hydroxyl group in glasses

There are some limitations in application of ABP. Firstly, the preparation of ABP glasses requires large time scales. Secondly, ammonium may induce some chemical reduction and trace level of impurities from itself may still remain in the final glass. Lastly, some possible impurities (including moistures) in NH_4FHF can remain in glasses which can significantly affect purity of the final glass fibres.

(3) Reactive atmosphere processing (RAP)

Reactive atmosphere processing has been utilised to obtain clear and low OH content glasses. Robinson [78] has successfully applied reactive atmospheric processing using CCl_4 for fluoride glasses melting for the first time. In RAP, glass-melting reagents are melted under an atmosphere with a chemical component that is capable of removing anionic impurities such as oxygen and hydroxyl groups.

The removal of oxygen and hydroxyl groups by CCl_4 can be expressed as:

Deoxygenation $$O^{2-} + CCl_4 \Leftrightarrow 2Cl^- + COCl_2 \quad (1\text{-}12)$$

Dehydroxylation $$OH^- + CCl_4 \Leftrightarrow Cl^- + COCl_2 + HCl \quad (1\text{-}13)$$

At the same time, the following reaction occurs at higher temperatures than T_g:

$$OH^- + F^- \Leftrightarrow O^{2-} + HF \quad (1\text{-}14)$$

As CCl_4 results in chlorine incorporation, other reactive atmospheres are suggested e.g., SF_6, CF_4 [78], NF_3 [102]. RAP is not only an effective way to remove OH^- and H_2O but also can form a strong oxidative atmosphere in furnaces, so that some elements are transformed into higher valence states. However, RAP cannot remove oxides such as PO_3^- and SO_4^{2-}.

1.2.5.2. Preform preparation

Silica-based optical fibre preforms are fabricated by chemical vapor deposition (CVD) techniques such as outside vapor deposition (OVD) and modified chemical vapor deposition (MCVD). A suitable CVD method for fluoride glass is, however, yet to be developed. Here, other methods suitable for the fabrication of fluoride glass preforms are reviewed.

(1) Preform fabrications by casting

Glass fibre preforms can be prepared by glass melting in crucibles, followed by casting process using metal moulds. Techniques specifically adapted to fluoride glass have been developed to obtain a core-cladding structure in the preform. In Fig. 1.2 and 1.3, preforms fabricated by the build-in casting and a rotational casting process method have been achieved by Mitachi et al. [103] and Tran [68]. Both these casting methods have been used successfully for preparation of fluoride glass preform and fluoroindate glass fibres [97, 99, 100].

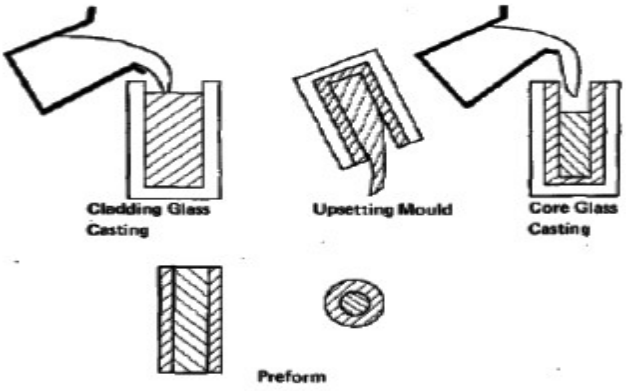

Figure 1. 2. “built-in casting” process [103].

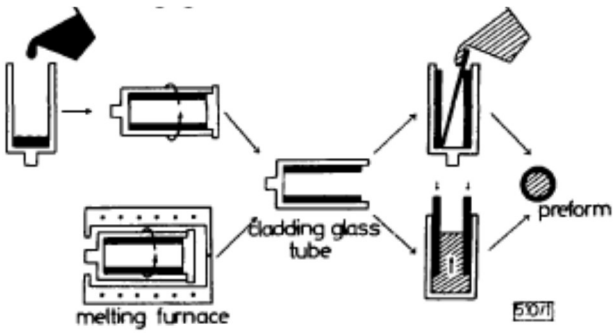

Figure 1. 3. Rotational casting process [68].

Another preparation technique called suction casting has been developed for single-mode fibre preforms. In a suction casting, a specifically designed cylindrical mould with a reservoir at the bottom is normally used. However, the casting method for preform preparation is current restricted to fabricate fibres with simple structures. Explores of new methods for the complexity of preform fabrication were required.

(2) The stack-and-draw procedure

Stack-and-draw method was first introduced by Knight and Birks et al in 1996 for silica photonic crystal fibres (PCFs) [104]. This method is widely used for preparation of most silica microstructured fibres, and recently has also been demonstrated in fabrication of ZBLAN fibres [105, 106]. During the process, the PCF preform can be fabricated by stacking a number of capillary silica tubes and rods manually to form the desired air-silica structure. Solid, hollow, or doped glass regions can be easily incorporated by inserting glass rods in the middle. After the stack is prepared, it is usually fitted inside a silica tube in order to secure the stack and to add silica to the structure [107] and then silica capillaries (and tube) are fused together, and drawn successfully down to PCFs (Fig. 1.4) [108]. The stack-and-draw procedure has proven to be highly versatile, allowing complex lattices to be assembled from individual typically stackable capillaries units.

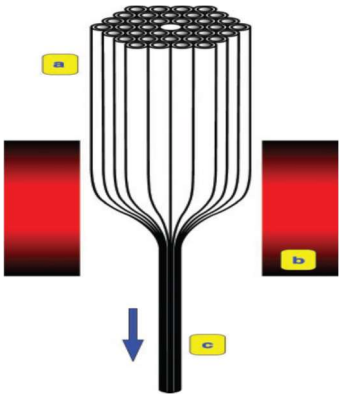

Figure 1. 4. A stack of glass tubes and rods (a) constructed as a macroscopic “preform” with the required photonic crystal structure. It is then fused together and drawn down to fibre (c) in two stages using a standard fibre drawing tower. To soften the silica glass, the furnace (b) runs at 1800 to 2000 ˚C.

One of the biggest disadvantages of the stack-and-draw technique is contamination by surrounding atmosphere. For example, even small amounts of dust on the glass surface could result in a significant increase in fibre attenuation. Therefore, this technique needs to be fabricated under clean and dust-free conditions. Other disadvantages are the fragility of capillaries for soft glasses and that soft glass capillaries can be scratched easily. This is the principal obstacle for chalcogenide glass microstructured optical fibres. Another main obstacle is insufficient fusion of capillaries, and thus some possible defects (e.g., tiny bubbles, voids and other contamination) likely appearing at the capillary/capillary interfaces may result in high loss in microstructured optical fibres [109].

(3) Billet extrusions

During billet extrusion, molten glass is forced through a die containing predetermined flow channels to achieve a target preform cross-sectional structure during an extrusion procedure, which allows bulk glass to be extruded into a preform with almost every desired structure. The extrusion speeds need to be slow enough to ensure that the material strands linger for adequate time within the die and thus can fuse together completely [110]. The extrusion method also works for many materials, including chalcogenides, polymers, and compound glasses (Fig. 1.5). For detailed advantages of extrusion over other preform preparation methods, please refer to Chapter 4 and 5.

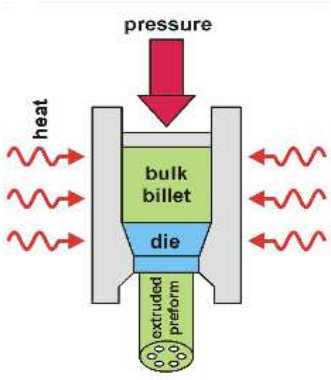

Figure 1. 5. Sketch of extrusion process.

Billet extrusion can be used to form long preforms of a desired diameter as well as a range of internal structures [111, 112]. Compared with the casting method, the extrusion technique is a versatile method for the production of low-loss microstructured optical fibres with various shapes produced from different types of glasses [110, 113, 114].

(4) Drilling

Preform drilling is a straightforward approach to enable rapid fabrication of general microstructured preform without further steps [115-117]. This technique is available for a variety of glasses, including soft glasses [115-118]. Although drilling appears to be a simple and immediate way to prepare a preform, it is limited to circular hole sizes and relatively short preforms [110]. A large mode area MOF made from fluorozircoaluminate glass has been demonstrated using the drilling technique for preform fabrication with a loss of 2.75 dB/m at 4000 nm [119]. However, surface and subsurface damage was caused during drill process, resulting in a poor fibre strength.

1.2.5.3. Fibre drawing

The fundamental knowledge and skills for drawing preforms into fibres (e.g., diameter control, capstan driving, and plastic coating) have been developed for oxide glass fibres. However, drawing of fluoride fibre preforms is more sensitive to temperature fluctuation and variation in atmosphere, thus requiring more precise control of drawing conditions. The optimum temperature depends on parameters such as furnace temperature distribution, drawing speed, preform diameter, heat transfer coefficient, specific heat, and density of the glass. For example, for drawing a fluorozirconate glass preform with 7 mm diameter, the furnace temperature distribution needs to be within 335-345 ˚C for a heating zone (40 mm long) from top to bottom to achieve a fixed tension [120]. A dry inert atmosphere or a reactive fluorination atmosphere (e.g., N_2 and NF_3) is effective in suppressing surface crystallisation. Surface treatment of preforms by chemical etching before the drawing process also helps to eliminate mechanical drawbacks at the surface that would otherwise cause crystallisation in preforms.

1.2.6. Methods for reduction of fibre scattering loss

Extrinsic loss from scattering such as bubbles and poor surface quality (caused by e.g., surface crystallisation) will cause an increase in fibre loss. Hence, it is critical to reduce loss in fluoride fibres by improving fibre fabrication conditions. Both casting and extrusion methods unavoidably introduce surface defects (i.e., metallic particles and graphite particles) and surface scratches (leading to high roughness) generated during contact with molds or dies [121]. Reheating during fibre drawing may lead to surface crystallisation. Other surface contaminations may generate from the reaction of glass surfaces with moisture in the atmosphere during fibre fabrication or storage. Poor surface quality associated with surface contamination and scratches will cause low fibre strength and high loss in air-clad (i.e., unstructured) fibres and air/glass microstructured fibres unless the contaminated layer can be removed [122].

1.2.6.1. Chemical etching and mechanical polishing

Methods to improve surface quality include chemical etching and mechanical polishing. Chemical etching allows a uniform and rapid dissolution of surface regions in fluoride glasses. The etching method was also found to smooth the fibre surface (i.e., reduce the

surface roughness), which enabled the preparation of fluoride fibres with low transmission loss and high fibre strength [123].

For fluorozirconate glasses, chemical etching of preforms was observed to prevent surface crystallisation during fibre drawing due to the removal of pre-existing surface defects and top atomic surface layer with different composition as compared to that of the bulk glass [58], thereby reducing the loss and increasing the mechanical strength of fluorozirconate fibres [124]. HCl has been widely used as an etchant for soft glasses as it is a corrosive acid which can remove a surface layer from matrice [173, 174].

1.2.6.2. Heating zone optimisation

Since the viscosity of fluoride glasses shows a strong temperature dependence and sensitivity to surrounding atmosphere, an accurate control of the drawing temperature and atmosphere is critical to the preparation of long-length, low-loss and high-strength fibres [171, 177].

Sakaguchi et al. [93] successfully minimised surface crystallisation in the neck-down region of a fluorozirconate glass by extending the heating zone of the furnace used for fibre drawing. As fluoride glass has a steep temperature-viscosity dependence, small temperature fluctuations may cause large variations in the glass viscosity. Thus, temperature dependence of glass viscosity are caused by a shorter heating zone with a higher maximum preform temperature and steeper preform temperature gradient along the drawing axis [93, 178]. The steeper temperature gradient requires higher maximum glass temperature to form a preform drop, which may lead to an increase in surface crystallisation. In contrast, for a longer heating zone, the reduced temperature gradient and larger heat spread in axial direction allows the preform to drop at a lower maximum temperature, reducing the probability of surface crystallisation during fibre drawing. The neck-down shape using a longer heating zone is elongated, indicating that the dwell time for glass in the heating zone is increased in comparison with that in a shorter heating zone. The reduction of surface crystallisation for a longer heating zone indicates that the impact of temperature on crystallisation is more significant than the time the glass dwells in the hot zone [93]. In addition, the reduced temperature gradient using a longer heating zone resulted in an improved drawing stability (e.g., constant/uniform fibre diameter).

1.2.6.3. Application of additional weight

Optical fibres are drawn by heating a short region close to the preform end and allowing it to flow downward from an initial diameter of the order of centimeters to the desired final diameter using a fibre drawing tower [86]. However, in the case of fluoride glasses, their viscosity decreases very rapidly with increasing temperature. The consequence of this rapid viscosity change with temperature is that the usable viscosity range for fibre drawing is narrow and the risk of devitrificaion of fluoride glass is increased. To reduce the crystallisation of the glass during fibre drawing process, fibres can be produced by applying an additional weight at the bottom of a preform to obtain tension in addition to gravity from the additional weight to pull a fibre at a lower furnace temperature (i.e., at a temperature where no glass crystallisation occurs).

1.2.7. Chemical durability of (bulk) fluoride glasses

Fluoride glasses have relatively poor chemical durability when compared to oxide glasses (e.g., silicate [125] and tellurite glasses [126]), as they are reactive in aqueous environments. The presence of water or an acidic solution leads to dissolution of the fluoride glasses and subsequent formation of surface layers. In general, the corrosion of heavy metal fluoride (HMF) glasses in un-buffered water is extremely rapid compared to silicate glasses, with dissolution reactions more than 10-100 times faster than those for silicate glasses [127]. This is not surprising since the structure of fluoride glasses is quite different from that of the silicates. Chemical corrosion can result in high transmission losses in fluoride fibres as well as have a significant negative impact on fibre strength [128, 129], posing potential limitations to the application of fluoride fibres. Therefore, it is essential to understand the corrosion process and chemical durability of these glasses to guide the development of improved materials or methods for the protection of these materials.

To date many types of HMF glasses have been synthesised, of which the fluorozirconate glasses are most widely studied [55]. Leaching behaviors of HMF glasses (e.g., fluorozirconate) have been studied in earlier published work [130-132]. The chemical durability of these NaF-containing fluorozirconate glasses (e.g., ZBLAN) in aqueous environments was, however, found to be extremely poor and rather sensitive to water, while other fluoride glasses without NaF (e.g., ZBL and ZBLA [125, 133]) are relatively

stable in aqueous solutions. Similarly, Moynihan et al. [131] compared two fluorozirconate glasses (ZBLAN and ZBLA) and found that the ZBLA glass without NaF has better chemical durability in deionized water than the ZBLAN glass containing 20 mol% NaF.

Compared with the fluorozirconate glasses, fluoroindate glasses are considered relatively stable against atmospheric moisture [36, 134], possibly due to lower solubility of InF_3 (0.04 g/100 ml in water at room temperature) [135] compared to ZrF_4 (1.32-1.39 g/100 ml in water at room temperature) [136]. However, no experimental details are given in refs [15,16] regarding the stability of the fluoroindate glasses under atmospheric moisture conditions. Indeed, no research studies have been reported on the chemical durability of fluoroindate glasses, which prompted us to carry out this project to advance our knowledge in this aspect and explore the possibility of practical application from the viewpoint of chemical durability.

1.2.8. Fluoride fibre laser in mid-infrared region

Mid-infrared (mid-IR) light sources, owing to their numerous applications and potential applications in areas such as spectroscopy, microscopy or chemical sensing [137-139], have been the object of extensive research over the past decade. Especially, generating emission wavelengths longer than 2 μm from fibre lasers is a task which tests the limits of current glass technology. It is because fibre lasers operating on laser transitions which have wavelengths > 2 μm will need to use glasses that have very low phonon energies. The maximum phonon energy of the glass sets the overall infrared transparency range of the fibre and the multiphonon relaxation rates which influence the quantum efficiency. The need for lower phonon energies has to be balanced with acceptable optical, mechanical, chemical, and thermal properties of glasses.

Germanate glasses [140] have robust mechanical qualities, maximum phonon energies [141] of 900 cm^{-1} and large rare-earth cation solubilities, which allow cluster-reduced Tm^{3+} concentrations in fibres for high-efficiency 1.9 μm emission [142] and short-length devices providing narrow-line width output [143]. However, the practicality of germanate glasses for emission beyond 2 μm depends upon the effective removal of OH^- impurity from the glass, which is difficult to achieve. Similarly, although tellurite glass fibre [144] is a type of promising alternative, the presence of insufficiently low concentration of OH^-

is a common issue for the tellurite glass fibres. For example, a loss of 50 dB/m at 3 μm is sufficient to suppress 3 μm lasing in state-of-the-art Er^{3+}-doped tellurite glass [145]. The presence of OH in tellurite glass fibre has somwhat limited its application.

In comparison, fluoride glasses have wide transmission range and low phonon energies which result in improved quantum efficiencies for a number of rare-earth (RE) transitions [146], enabling observation of rare-earth emission lines, especially at wavelengths beyond 2 μm (Fig.1.6 and 1.7). Among many fluoride compositions investigated, it is known that fluoroaluminate or fluorozirconate glasses have been employed as the host glass for the rare-earth ions [147-151], because such glasses are thermally stable against crystallisation and can be easily prepared compared to most other fluoride glasses. Most of the realised mid-infrared fibre lasers used ZBLAN as the host material [152-159].

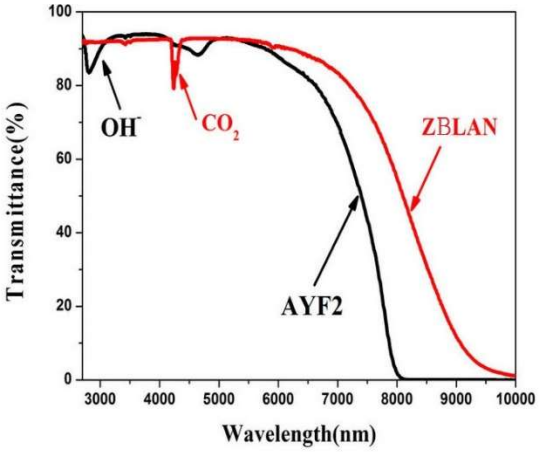

Figure 1. 6. Transmittance spectra of the 1.0 mm thick AYF2 ($40AlF_3$-$15YF_3$-$15CaF_2$-$10BaF_2$-$10SrF_2$-$10MgF_2$-$1ErF_3$) and ZBLAN samples ($53ZrF_4$-$20BaF_2$-$4LaF_3$-$3AlF_3$-$20NaF$) [160].

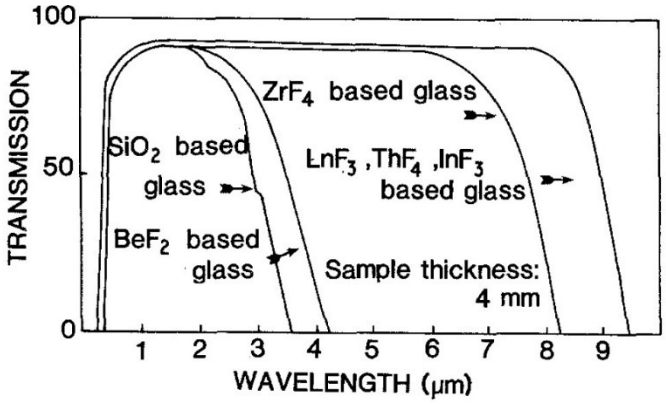

Figure 1. 7. The optical transmission curve for SiO_2 glasses, BeF_2 glasses and two types of heavy metal fluoride glasses; one is ZrF_4 based, the other one is a multicomponent glass, for example InF_3, based glass [74].

Recently new fluoroindate glasses have been shown to be more thermally stable than the conventional fluorozirconate and fluoroaluminate glasses [134]. Fluoroindate glasses were also found to be a better matrix for rare earth ions doping, resulting in a longer fluorescence lifetime, compared to its doping in fluorozirconate and fluoroaluminate glasses [161]. Fibre made from this glass can provide an efficient method to realise high power laser [152, 162, 163], which is possibly due to higher luminescence efficiency (much lower multiphonon emission rates) of fluoroindate glass for photonics applications in the mid-infrared region than those of most other fluoride glasses (e.g., fluorozirconate glasses). Active applications utilising fluorescence from rare earth ions such as fibre laser and amplifiers are therefore expected to be efficient in fluoride glasses [164].

1.3. A gap in the literature regarding fluoroindate glass fibres

The IR range is an important region for chemical analysis, imaging and sensing [165, 166], and current fibre application require a wider MIR window than oxide glasses (e.g., tellurite and germanate glasses) up to 5 μm. The general aim of this research project is to achieve low loss fluoroindate glass fibre fabrication for high power delivery application in mid-infrared region. The glass composition $32InF_3$-$20ZnF_2$-$20SrF_2$-$18BaF_2$-$8GaF_3$-$2CaF_2$ (IZSBGC) was demonstrated as a high transmission and low rate of crystallisation glass for mid infrared applications [15]. Although short unstructured fibres (up to 5 m in length) were successfully drawn from a glass rod with a diameter of 9 mm from this IZSBGC glass, neither the approach used for glass rod fabrication (or preform preparation) nor the resulting fibre loss is given in this paper. In addition, Itoh et al. have successfully made their InF_3/GaF_3 core and ZBLAN cladding preform by stacked extrusion (using vertically stacked billets to extrude a preform with a core and cladding structure) and drawn it into single mode fibres [98]. However, they only focused on the progress in Pr^{3+} doped InF_3/GaF_3 fibre with a high gain coefficient, high power delivery and no details of the fabrication of fluoroindate glass preform using the extrusion technique have been reported.

Furthermore, fluoride glasses are reactive in aqueous environments when compared to oxide glasses [167] (e.g., silicate [125] and tellurite glasses [126]). However, there are no research studies reported on the chemical durability of fluoroindate glasses.

1.4. Outline of the thesis

This thesis will advances the fabrication of fluoroindate glasses, and to the best of my knowledge, for the first time, the extrusion of fluoroindate glass and drawing of fibres from extruded preforms. It will also showcase the step-by-step reduction of the resulting fibre loss, and investigate the chemical durability of the as-prepared fluoroindate glass samples.

Chapter 2 shows various methodologies including instrumental analysis employed in the project. The main body of this thesis comprises five parts. Chapter 3 includes the glass melting conditions for different batch sizes. Chapter 4, building on the work in Chapter 3, contains discussions on the different preform fabrication methods and the extrusion conditions for unstructured preform preparation. Chapter 5 explores the possible temperature for fluoroindate glass fibre fabrications and introduces potential methods to reduce the fibre scattering loss. Chapter 6 reports the durability comparison between fluoroindate glass and fluorozirconate. Chapter 7 preliminarily demonstrated the possible method for fabricating step-index fluorindate fibres using extrusion technique. In Chapter 8, the main outcomes of this research project are presented and the possible research directions for future work are also discussed.

Chapter 2

FABRICATION AND CHARACTERISATION METHODOLOGY

This chapter first summarises commercial raw materials used for making glasses, and then introduces facilities for preparation of glasses, preforms and fibres. The experimental details of various analytical methods utilised to study the thermal, optical and other properties of fluoroindate glasses are also briefly discussed.

2.1. Commercial raw materials

Different fluoride raw materials available from commercial suppliers were used in this project. Their suppliers and purities are shown in Table 2.1. During glass melting, ammonium bifluoride processing (ABP) as described in Chapter 1 was applied to fluorinate oxide impurities in $InF_3 \cdot 3H_2O$ (Testbourne, 4N) and low metal purity of GaF_3 (Synquest, 1N). If oxide impurities are not fluorinated and introduced into the final glass fibre, they will result in extrinsic losses (Introduction, Chapter 1). A higher amount of excess NH_4HF_2 was used to compensate for the loss of fluorine due to the formation and loss of HF (refer to the details in the Chapters 3).

Table 2. 1. Different fluoride raw materials supplied by different commercial suppliers.

Raw material	Supplier	Metal% (fluorine %)	Glass melting
InF_3	Astron	99.999%	IM1-15,17-18, 20, 22, 37-39, 47-50, 154
InF_3	Synquest	99.9% (95.87%)	IM70, 72, 91, 98-153, 155-160
$InF_3 \cdot 3H_2O$	Testbourne	99.99%	IM16, 19, 21, 23-36,40-46, 51-69, 71, 73-90, 92-97
ZnF_2	Astron	99.999%	IM61
ZnF_2	Cerac	99.9%	IM1-59, 67-81, 98-104
ZnF_2	Alfa	99.995%	IM60, 62-66
ZnF_2	Synquest	99.9%	IM82-97, 105-160
SrF_2	Astron	99.999%	IM61, 75-84, 86-94
SrF_2	Cerac	99.9%	IM1-59, 67-73
SrF_2	Materion	99.9% (99.0%)	IM97-160
SrF_2	Sigma	99.99%	IM60, 62-66, 74, 85, 95-96
BaF_2	Astron	99.999%	IM67-96, 157
BaF_2	Alfa	99.99%	IM1-35 97-157
BaF_2	Sigma	99.999%	IM35-66
BaF_2	Cerac	99.9%	IM157-160
GaF_3	Cerac	99.95%	IM1-40
GaF_3	American Element	99.99%	IM41-62
GaF_3	Synquest	96.3% (99.3%)	IM63-100, 105-160
Ga_2O_3	Cerac	99.995%	IM101-104
CaF_2	Astron	99.999%	IM57-59, 61,67-149
CaF_2	Cerac	99.995%	IM1-57
CaF_2	Cerac	99. 95%	IM150-160
CaF_2	Sigma	99.99%	IM60, 62-66
NH_4HF_2	Cerac	99.9%	IM21, 23-36, 39-46, 51-69, 71-97, 101-160
PbF_2	Sigma	99.9%	IM95, 120, 127, 131, 134-139, 141, 143-144, 148-149, 151, 153, 156, 158, 160

Table 2.1 (continued)

LaF_3	Alfa	99.9%	IM96, 128, 130, 132-133, 142, 145-147, 150, 152, 155, 157, 159
ErF_3	Alfa	99.99%	IM42-43, 45,47
PrF_3	Alfa	99.9%	IM48, 79-81, 120, 127, 131, 134-139, 141, 143-144, 148-149,151, 153, 156, 158, 160
DyF_3	Alfa	99.9%	IM49, 76-78
HoF_3	Alfa	99.99%	IM50

Note that 99.999%, 99.99%, 99.9%, 99%,96.3% were called as 5N, 4N, 3N, 2N, 1N, respectively in the text. "IM" stands for "indium fluoride glass melt" and is used to number all glass samples after melting in this thesis.

2.2. Equipment for glass/fibre preparation

All fluoroindate glass fibres in this study were prepared from starting fluoride raw materials through a three-step process including glass melting, extrusion and fibre drawing. All steps for glass/fibre fabrication were carried out under strictly controlled atmosphere (e.g. glove box purged with N_2 for glass melting; extrusion machine and fibre drawing tower purged with N_2 for preform and fibre fabrication; see text below). This section generally introduces the main fabrication equipment used in this project including glovebox with a controlled-atmosphere glass melting capability, extrusion machine, and fibre drawing tower.

Fluoride glasses were produced in a controlled-atmosphere glass melting facility purged with 99.999% N_2. This equipment enables production of fluoroindate glasses in this study including undoped and doped glass through the controlled batching, melting, casting and annealing. The controlled-atmosphere glass melting capability consists of a 5-port glove box with integrated melting furnace with a maximum temperature of 800-900 ˚C, and a 350 mm long and vertical barrel-shaped annealing furnace with a maximum furnace temperature of 500 ˚C (Fig. 2.1). Note that the annealing furnace and real glass annealing temperatures are different due to the fact that the furnace temperature is measured away from where the glass is located. For the annealing (furnace) temperature of 340 ˚C, the real temperature was measured as 310 ˚C.

Figure 2. 1. Glovebox for glass fabrication.

An extrusion machine developed in-house can extrude a preform at a temperature of up to 700 ˚C and a force of up to 100 kN (Fig. 2.2). Preforms can be made from glasses made in-house and commercially sourced glasses. The structures can include rods of 1-20mm diameter, tubes of 10-20mm outer diameter and 0.5-8mm inner diameter, wagon-wheel structures (suspended core), hexagonal arrays of 1 to 7 rings of air holes and spider-web like structures with large air filling fractions [114, 168, 169]. All fluoroindate glasses in this project were extruded under N_2 (99.999%) conditions, with the N_2 gas flowing upwards from the bottom of extrusion machine. “IE” stands for “indium fluoride glass extrusion” and is used to number all glass preform samples after extrusion in this thesis.

Figure 2. 2. Extrusion machine for preform fabrication at IPAS, The University of Adelaide.

A 4 m soft glass drawing tower (Fig. 2.3) was used to draw the fluoride glass preforms in this project. This tower can draw preforms of 8-15 mm in diameter and up to 180 mm long into canes of approximately 1 mm or fibres of 100-400 μm in outer diameter. The temperature range that can be reached in the centre of the hot zone of the RF furnace is approximately 200-900 ˚C. Pressure, vacuum and dry gas can be applied to the preform during caning and fibre drawing.

It should be noted that glass science background knowledge and expertise/skills in preform and/or fibre fabrication using this equipment is critical to fabricate glass fibres with high performances (i.e., low loss and high mechanical strength). In this thesis, “IF” stands for “indium fluoride glass fibre” and is used to number all glass fibre samples after fibre drawing.

Figure 2. 3. 4m soft glass drawing tower.

2.3. Analytical techniques

2.3.1. Thermal properties

2.3.1.1. Differential Scanning Calorimetry

Differential scanning calorimetry (DSC) is one of the most widely used of the thermal techniques available to the analyst, and provides the basic properties of materials. A DSC analyser measures the heat flow changes that occur as one sample is heated, cooled or held isothermally, together with the temperature at which these changes occur. The energy changes enable the user to find and measure the transitions that occur in the sample quantitatively, and to record the temperature where they occur, and then to characterise a material for melting processes, glass transition temperatures and a range of more complex events. Typical resultant graphs of the heat flow versus temperature or time can be easily used to identify a number of endothermal or exothermal transitions occurring in materials, from which parameters can be identified such as glass transition temperature (T_g), crystallisation temperature (T_c), and melting temperature (T_m).

In this project, the characteristic temperatures, i.e., glass transition temperature (T_g), glass crystallisation temperature (T_x) and peak of crystallisation temperature (T_p), of samples were measured using a differential scanning calorimetry (DSC) TA Q20 (sample No ≤ IM116) or 2930 (sample No > IM116) equipment with experimental errors of ± 2 ˚C. The DSC measurements were conducted from room temperature to up to 530 ˚C at a heating rate of 10 ˚C /min under N_2 atmosphere.

2.3.1.2. Dilatometer

Dilatometer is a traditional thermoanalytical apparatus designed to measure volume changes caused by its thermal environment. Linear thermal expansion coefficient, annealing characteristics and other physical or chemical changes manifesting themselves in a change of linear dimension can be precisely determined. A dilatometer permits the thermal expansion of a long rod of glass to be compared to that of a standard, typically vitreous silica, heated slowly in a large furnace with a long and even hot zone. The principle of operation is to determine dimensional changes versus temperature or time while the sample undergoes a controlled temperature program. The degree of expansion divided by the change in temperature is called the material's coefficient of linear thermal expansion (α), which can be demonstrated as the following equation [170]:

$$\alpha_T = \left[1/l(T)\right]\left[dl\left(T\right)/dT\right] \tag{2-1}$$

where α_T is coefficient of linear thermal expansion, and $l(T)$ is the length of the sample at the temperature T.

For the thermal dilatometric measurement, we used a piece of rod of 5 mm in diameter that was extruded at 320 ˚C (IE16). This measurement was conducted from room temperature to up to 500 ˚C at a heating rate of 5 ˚C/min using a Dilatometer (Netzsch DIL 402, Germany), with experimental errors of ± 0.01 ˚C.

2.3.1.3. Thermal Gravimetric Analysis (TGA)

TGA is a method of thermal analysis which uses heat to find chemical and physical property changes in materials. TGA provides quantitative measurement of mass change in materials associated with transition and thermal degradation. It records change in mass from dehydration, decomposition, and oxidation of a sample with time and temperature

in an atmosphere of nitrogen, helium, air, other gas, or in vacuum. This method is commonly used in inorganic materials, metals, polymers and plastics, ceramics and glasses.

TGA was conducted in simultaneous thermal analyzer (PerkinElmer STA 6000) (Fig. 2.4) which is allowed for operation from 15 ˚C to 1000 ˚C. It is also equipped with the FTIR spectrometer (PerkinElmer Spectrum 400) in Fig. 2.5). Combining a thermogravimetric Analyzer (TGA) and a FTIR Spectrometer allows to collect and detect chemical change in IR region.

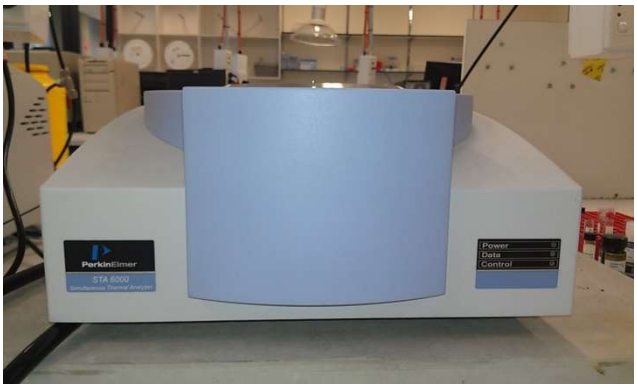

Figure 2. 4. PerkinElmer STA6000.

2.3.2. Optical properties

2.3.2.1. FTIR spectroscopic analysis

Fourier transform infrared (FTIR) spectrometry provides detailed information about vibrations of a molecule. Since molecular vibrations readily reflect chemical features of a molecule, such as an arrangement of nuclei and chemical bonds within the molecule, infrared spectroscopy contributes considerably not only to identification of the molecule but also to study of the molecular structure. Furthermore, an interaction with a surrounding environment also causes a change in molecule vibrations, and hence, infrared spectroscopy is also useful in studying the interaction. In this project, FTIR is mainly used for determination of OH content and IR cut-off edge position.

FTIR spectroscopy is applicable to samples in various states, e.g., solid, crystal, fibre, film, liquid, solution and gas. Furthermore, measurements of infrared spectra of a sample

in a solution and in a solid state allow us to compare its structure in the solution with that in the solid.

IR transmission measurements in this project were conducted using a commercial Fourier transform infra-red (FTIR) spectrometer (PerkinElmer Spectrum 400; Fig.2.5). The absorption coefficients in the thesis were calculated from the transmission data by subtracting background absorbance from measured absorbance and normalizing to sample thickness. After subtraction, the absorption coefficients calculated from FTIR measurements can be used to compare the transmission cut-off wavelength (transmission window) and OH absorption (which affects extrinsic loss) located at 3 μm among different samples.

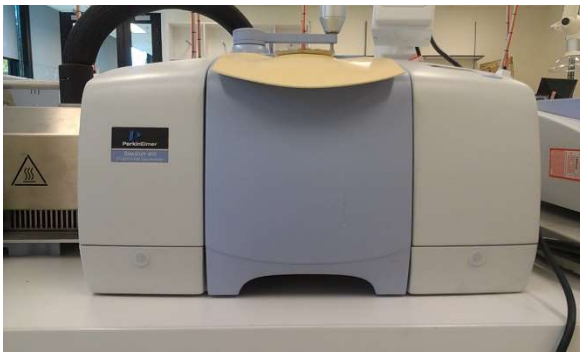

Figure 2. 5. PerkinElmer Spectrum 400 FT-IR Spectrometer.

2.3.2.2. Refractive index spectrum

Ellipsometry is an optical technique for investigating the refractive index properties. As an optical technique, ellipsometry is a sensitive and non-destructive and contactless measurement technique [171]. It measures a change in polarization as light reflects or transmits from a material structure. The polarization change is represented by an amplitude ratio, Ψ, and the phase difference, Δ. The measured response depends on optical properties and thickness of any given sample. Thus, ellipsometry is primarily used to determine film thickness and optical constants. However, it is also applied to characterise composition, crystallinity, roughness, doping concentration, and other material properties associated with changes in optical responses of an incident radiation that is made to interact with the material being investigated.

Ellipsometry can also be used to characterise composition, roughness, thickness (depth), crystalline nature, doping concentration, electrical conductivity and other material properties.

In this project, a VASE Ellipsometr (J. A. Woollam Co.) were used to study the glass refractive index for step-index fibre investigation. As our fluoroindate glass has an infrared absorption edge at 8.7μm for 1 cm sample thickness, the wavelength was scanned across the spectral range from 450 to 8000 nm. The refractive indices over the wavelength range of 0.45-2.20 μm and 2.20-10.00 μm were measured using a spectroscopic ellipsometer (J.A. Woollam Co., Inc. VASE Ellipsometer HS-190) and (J. A. Woollam Co., Inc. VASE Ellipsometer VB-400), respectively (Fig. 2.6).

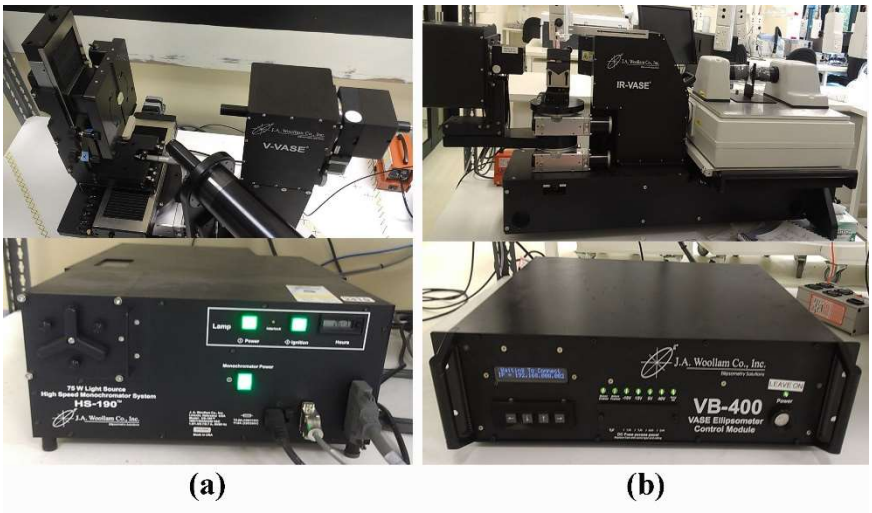

Figure 2. 6. (a) J.A. Woollam Co., Inc. VASE Ellipsometer HS-190) and (b) J. A. Woollam Co., Inc. VASE Ellipsometer VB-400.

For a typical measurement, at lease five incidence angels were measured within a range of ±10 degrees. In this study, the preliminary set of optical constants for core and clad fluoroindate glasses were modeled as a general oscillator (GENOSC) layer, which was developed to simplify modeling of the optical constant of unknown materials in WVASE32® software. The GENOSC model allows us to use the same or different types of oscillators together at the same time to describe the dispersion of optical parameters for materials. As the surface roughness of the sample influenced the ellipsometric measurements, surface roughness tends to cause depolarisation [172, 173]. Depolarisation occurs when a portion of polarised light becomes randomly polarised during the measurement and the regression analysis of the ellipsometric data will have errors owing

to depolarisation. In the present study, surface roughness should be modeled using the surface roughness (SROUGH) layer. To evaluate the quality of fitting, the mean-squared-error (MSE) varies after each fitting until it reaches the lowest value (<1). Each sample was measured for three times within a refractive index error below ±0.006.

2.3.2.3. Raman spectrum

Raman spectroscopy provides information about molecular vibrations that can be used for sample identification and quantification. The technique involves shining a monochromatic light source (e.g., laser) on a sample and detecting the scattered light. The majority of the scattered light will remain at the incident frequency, the process of which is known as (elastic) Rayleigh scattering. A very small amount of the scattered light (ca. 10-5% of the incident light intensity) is shifted in energy from the laser frequency due to interactions between the incident electromagnetic waves and the vibrational energy levels of the molecules in the sample. Plotting the intensity of this "shifted" light versus frequency results in a Raman spectrum of the sample. Generally, Raman spectra are plotted with respect to the laser frequency such that the Rayleigh band lies at 0 cm^{-1}. On this scale, the band positions will lie at frequencies that correspond to the energy levels of different functional group vibrations. The Raman spectrum can thus be interpreted similar to the infrared absorption spectrum.

For the step-index fibre study in this project, Raman spectra were measured to understand the relationship between glass composition and the resultant glass structure (and metal-fluorine bond vibrations). The spectra were measured using a confocal Raman microscope (Renishaw, inVia, British) excited at 785nm.

2.3.2.4. Fibre loss measurement

To investigate the impact of fabrication conditions on fibre loss, 1550 nm was selected as a wavelength for spot loss measurements and broadband spectral range of 500-1750 nm for white light source measurements. The fibre losses were measured based on the cutback method using a 1550 nm laser (spot loss measurement) and a bulb (broadband loss measurement) as the light sources. The output power of the fibre under test during spot loss measurement at 1550 nm was recorded by a power meter and for broadband loss measurement with an optical spectrum analyser. The relative errors for spot loss

measurements varied from 2.2% to 5.9% of the average value. The uncertainties of the broadband loss measurements were up to 10% of the measured values.

The mid-IR fibre transmission was measured from 2 to 8 μm using a fibre-coupled Bruker Vertex 70 FTIR spectrometer with a liquid nitrogen cooled HgCdTe detector. The fibre loss was determined via a cut-back measurement.

The recording of attenuation spectrum is based on the cutback method. Measurements were taken using the same fibre with different lengths, L_1 and L_2 (L_1>L_2). Attenuation α is measured in dB/m and is calculated by the following equation:

$$\alpha = \frac{10}{L_1 - L_2} Log \frac{I_2}{I_1} \tag{2-2}$$

2.3.3. Surface properties

2.3.3.1. Scanning electron microscopic analysis

Scanning electron microscopic (SEM) analyses were conducted on a Philips XL30 field emission scanning electron microscope (FESEM; Fig. 2.7) at the Adelaide Microscopy Centre. The FESEM is equipped with an energy dispersive X-ray spectrometer (EDS), a secondary electron (SE) and a back scattered electron (BSE) detector. FESEM was used for surface morphology, sample texture (by examining cross-sections of glass or fibre samples) and elemental distribution analysis (e.g., black particles in swan neck linear). Samples were carbon coated to minimise surface charging during FESEM study. Accelerating voltage was normally set at 15 or 20 KV to obtain the best contrast and resolution, and was also provided for excitation of relevant element lines in EDS spectra.

In this study, FESEM was employed to study the microstructures and compositions of black particles on the crucible wall after melting and the white precipitate on the glass surface after etching. It was also applied to study the cross-section and surface quality of fibres.

Figure 2. 7. The Philips XL 30 Field emission scanning electron microscope at Adelaide Microscopy Centre.

2.3.3.2. Electron probe micro-analysis

Electron probe micro-analysis (EPMA) was carried out on a CAMECA SX51 at Adelaide Microscopy Centre (Fig.2.8). The EPMA instrument was equipped with four wavelength dispersive X-ray Spectrometers (WDS), an energy dispersive X-ray spectrometer (EDS) and a reflected-light optical microscope. The polished samples were all carbon coated before EPMA measurement of minerals compositions or elemental distribution (mapping). The EPMA spot measurement were conducted at an accelerating voltage of 15 KV and a specimen current of ~ 20 nA with wavelength-dispersive X-ray spectrometers (WDS) and counting times of 20 s for the elements and their backgrounds, respectively. Quantitative elemental analysis was carried out via calibration of X-ray data against reference standard materials.

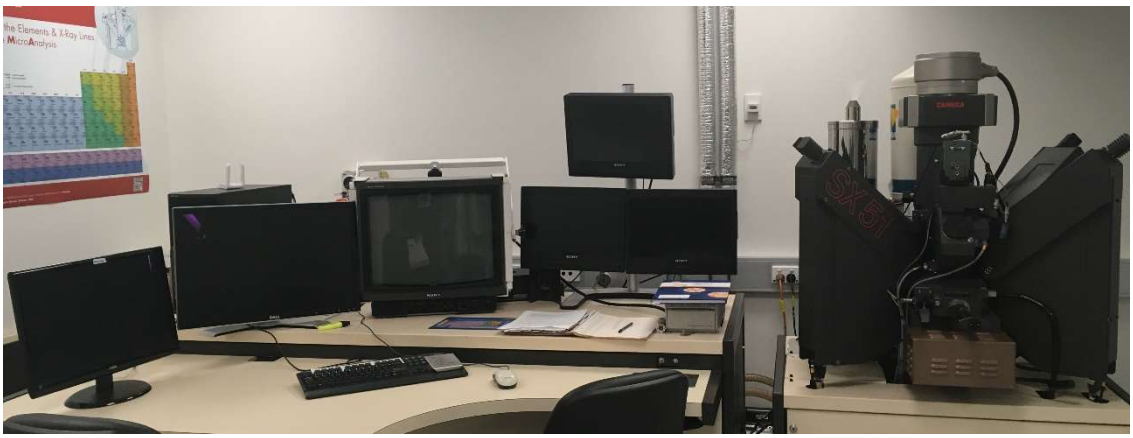

Figure 2. 8. The CAMECA SX51 electron microprobe.

2.3.3.3. Characterization of surface roughness

The Atomic Force Microscope (AFM) is primarily used to measure and analyse surface topography and morphology, providing nanoscale height measurements. The AFM is used for relatively small and flat samples - the maximum scan area is 100 × 100 μm and it can scan features of up to 10μm in height. Data collected provided information on the height of surface features, allowing both 2D and 3D imaging of sample surfaces. In this project, surface roughnesses of some samples were measured using the NT-MDT Ntegra Solaris Atomic Force Microscope at Adelaide Microscopy Centre. In this project, the glass surfaces before and after etching were probed using this AFM instrument, which allowed quantification of the etching quality.

AFM images of 50×50 μm^2 preform area were processed to determine the roughness parameters, S_a (Average Roughness), and S_q (Root mean square (RMS) Roughness) defined in Eqs. (2-3) and (2-4), respectively [174]:

$$S_a = \frac{1}{MN}\sum_{k=0}^{M-1}\sum_{l=0}^{N-1}\left|z(x_k, y_l)\right| \tag{2-3}$$

$$S_a = \sqrt{\frac{1}{MN}\sum_{k=0}^{M-1}\sum_{l=0}^{N-1}\left[z(x_k, y_l)\right]^2} \tag{2-4}$$

Where M and N are the numbers of the measured points and $Z(x_k, y_l)$ is the distance from each measured point to the central plane on the surface of the tested preform sample. S_p is the maximum peak height.

As an alternative to AFM, an optical interferometric profiler (model Contour GT-K1 profiler from Brucker) was also used to measure the surface roughness. This technique is a non-contact, non-destructive measurement of the surface profile using interference of broadband light and special objectives with built-in reference mirrors. It can measure surface topography from nanometer-scale roughness through millimeter-scale steps with sub-nanometer resolution. AFM and optical profiler could achieve same level of subnanometer surface roughness. Compared with AFM, automatic imaging optimisation of an optical profiler results in faster and more consistent results, without the size limitation of the scan area. The surface roughness of preforms and fibres were measured using an optical interferometric profiler (model Contour GT-K1 Optical Profiler Stitching

System from Veeco) (Fig. 2.9). From the optical profiler images, roughness parameters, S_a (average roughness), and S_q (root mean square (RMS) roughness) defined the same as Eqs. (2-3) and (2-4), respectively [174].

Where M and N are the numbers of the measured points and $Z(x_k, y_l)$ is the distance from each measured point to the central plane on the surface of the tested preform sample. Three surfaces areas, each being ~120×160 μm^2, were probed in the preforms, while five areas, each being ~25×160 μm^2, were measured in the fibres.

Figure 2. 9. The optical ContourGT-K1 profiler from Brucker.

2.3.3.4. X-ray photoelectron Spectroscopy (XPS)

XPS is now a widely used analytical technique for investigating the chemical composition of solid surfaces. Surface analysis using XPS involves irradiation of the solid in vacuum with monoenergetic soft x-rays and analyzing the emitted electrons by energy. MgKα X-ray source (1253.6 eV) or AlKα X-ray source (1486.6 eV) are ordinarily used. These photons have limited penetrating power in a solid, of the order of 1-10μm. They interact with atoms in this surface region by the photoelectric effect, causing electrons to be emitted. The spectrum obtained is a plot of the number of emitted electrons per energy interval versus their kinetic energy. Each element has a unique elemental spectrum, and the spectral peaks from a mixture are approximately the sum of the elemental peaks from the individual constituents.

XPS measurements in this project were performed in an ultra high vacuum apparatus built by SPECS (Berlin, Germany) using a non-monochromatic MgKα X-ray source (1253.6 eV) and a hemispherical Phoibo100 energy analyser from SPECS. Charge compensation was performed by an electron flood gun SPECS FG20 at 1 eV and 1 μA. Calibrations of the XPS binding energies were made against adventitious carbon (284.8 eV).

2.3.4. Other properties

2.3.4.1. X-ray powder diffraction analysis

X-ray powder diffraction (XRD) is a rapid and powerful analytical technique primarily for phase identification and quantification of crystalline materials. The basic principle is that when X-ray penetrates through or reflects from the (crystalline) sample, it is diffracted by the crystal lattice planes according to the Bragg law:

$$n\lambda = 2d\sin\theta \tag{2-5}$$

in which λ is the wavelength of X-ray, d is the spacing of the crystal planes, θ is the angle of incidence on a crystal, and n is the reflection order (an integer; 1,2,3, etc.). Details concerning the principle for XRD can be found in [175].

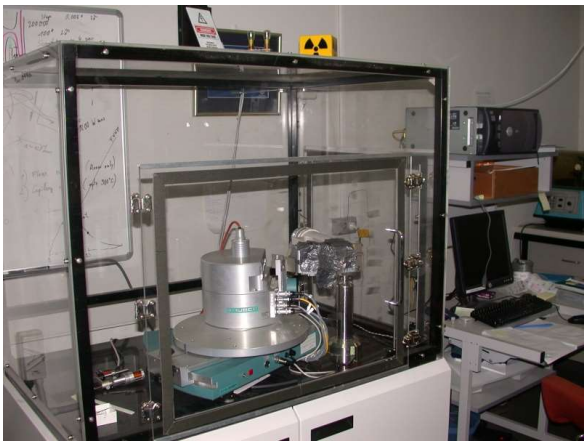

Figure 2. 10. The HUBER Guinier Imaging Plate Camera G670 for X-ray powder diffraction.

In this project, room-temperature XRD patterns of post-quenched products were obtained on a Huber Guinier Imaging Plate Camera G670 (Fig. 2.10) with Co $K\alpha_1$ radiation (λ = 1.78892 Å). Details about the Huber Guinier camera G670 and its read out system can be found in [176]. A schematic digram of the Guinier image plate camera is shown

in [177]. The samples were ground in acetone under air, spread uniformly on a MYLAR (polyethylene terephthalate) or film, and then mounted onto the sample oscillation unit for data collection. The phase identification was performed with the aid of Diffrac.Eva 3.0.

2.3.4.2. Micro X-ray diffraction analysis

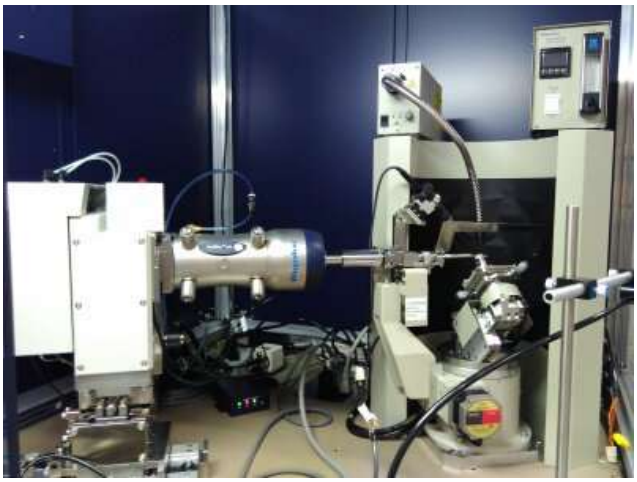

Figure 2. 11. The laboratory-based Rigaku D/MAX Rapid II micro-diffractometer.

Micro X-ray diffraction (Micro-XRD) measurement allows for small volumes of material to be probed. In this project, Micro-XRD was carried out using a laboratory-based Rigaku D/MAX Rapid II micro-diffractometer (Fig. 2.11) with Co Kα radiation (wavelength 1.7902 Å; accelerating voltage and filament current: 40 kV and 15 mA) at a fixed incident angle of 10 degrees. A 0.1 mm collimator, equivalent to an X-ray beam size of approximately 150 × 150 μm, was used during XRD analysis. Exposure time (on the imaging plate) for each analysis was 10 min. 2D data (Debye-Scherrer rings) collected from the imaging plate were converted to 1D profile (i.e., intensity vs. 2 theta) using the computer software 2DP.

2.3.4.3. Solution inductively coupled plasma mass spectrometry and flame atomic absorption spectrometry

Solution inductively coupled plasma mass spectrometry (solution ICP-MS) (Fig. 2.12) was utilised to measure the metals concentrations in solutions. Standard solutions were prepared at different concentrations for calibration purpose; diluted sample solutions were used for analyses. For measurements of Ca, Zn, Ga, Sr, In and Ba concentrations, the

corresponding ^{43}Ca, ^{66}Zn, ^{71}Ga, ^{88}Sr, ^{115}In and ^{138}Ba isotopes were chosen and analysed during ICP-MS analysis. 200 ppb indium solutions were used as internal standards during solution ICP-MS analysis.

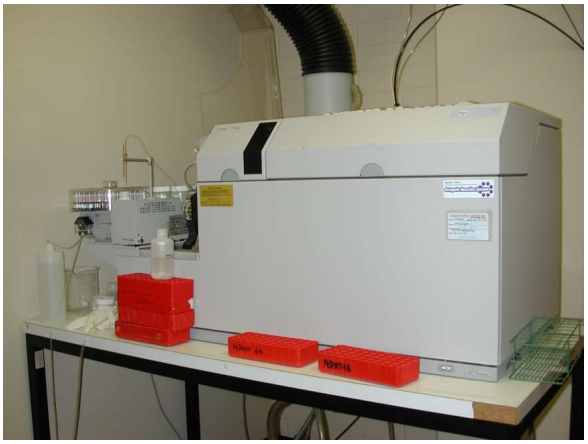

Figure 2. 12. Solution ICP-MS instrument at Adelaide Microscopy Centre.

2.3.4.4. Mechanical strength measurement of fibres

The mechanical strength of the fibres is determined by flaws or defects in the material, structure, and the way in which these flaws grow. The mechanical behavior of optical fibre is described by parameters such as fatigue, which is the measure of how fast a flaw grows under an extra stress. In this project, mechanical fibre strength was characterised by measuring the fibre bending radius at fibre breakage (minimum bending radius) [178]. Fibre pieces of approximately 15 cm length were bent and held between two vertically parallel plates as shown in Fig. 2.13. One of the plates was held stationary, while the other was mounted to a movable rail driven by a stepper motor. The latter plate was set to move at a speed of 0.3 mm/s towards the fixed plate until fibre breakage. Measurements were repeated to estimate the minimum bending radius at least 10 times. The calculation of the strain was based on Eq. (2-6):

$$\tau_s = r/0.42D \tag{2-6}$$

where τ_s is the breaking strain which can be measured from D, the minimum distance between the plates when the fibre fractures, and r is the fibre diameter.

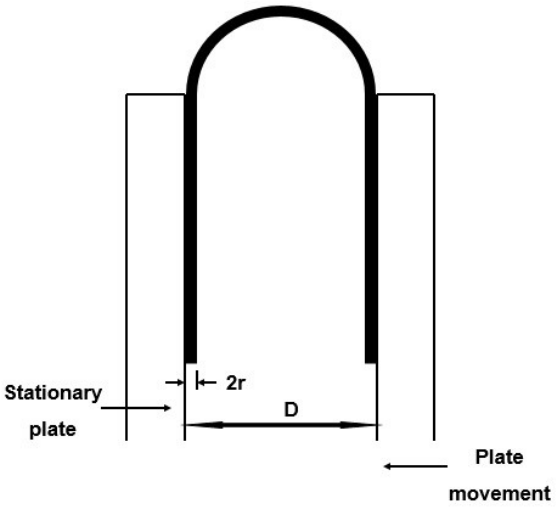

Figure 2. 13. Bending strength measurement approach.

The glass density is calculated by Archimedean's principle using water, H_2O [179]. This method consists of weighing the sample in the air, m_{air} and then in H_2O, m_{H_2O}. The density, ρ, is calculated according to equation (2-7) with ρ_{H_2O}, the density of H_2O:

$$\rho = \frac{m_{air}}{m_{air-m_{H_2O}}} \times \rho_{H_2O} \tag{2-7}$$

Benzene and coal oil can also be used as immersion fluids. The relationship between the water temperature and its density is listed in Table 2.2 [178].

Table 2. 2. The relationship between the water temperature and density.

Temp (˚C)	**+0**	**+1**	**+2**	**+3**	**+4**	**+5**	**+6**	**+7**	**+8**	**+9**
0	0.99984	0.99990	0.99994	0.99996	0.99997	0.99996	0.99994	0.99990	0.99985	0.99978
10	0.99970	0.99961	0.99949	0.99938	0.99924	0.99910	0.99894	0.99877	0.99860	0.99841
20	0.99820	0.99799	0.99777	0.99754	0.99730	0.99704	0.99678	0.99651	0.99623	0.99594
30	0.99565	0.99534	0.99503	0.99470	0.99437	0.99403	0.99368	0.99333	0.99297	0.99259
40	0.99222	0.99183	0.99144	0.99104	0.99063	0.99021	0.98979	0.98936	0.98893	0.98849

Chapter 3

GLASS PREPARATION (BASE GLASS ONLY)[1]

Several studies have investigated the preparation of fluoroindate glass fibers. Among all fluoroindate glass matrices examined, PbF_2-InF_3 based fluoride glass has good durability, high thermal stability against crystallization, and has been fabricated into a fiber with a minimum transmission loss of 0.043 dB/m at 3.33 μm [97]. In comparison, Itoh et al. developed a single-mode fiber, using InF_3/GaF_3 glass as a core glass and ZBLAN glass as a cladding glass, with a low loss round 0.2 dB/m at 1.2 μm [98]. Nishida et al. systematically studied InF_3/GaF_3 glass fibers and obtained the minimum loss of 0.025 dB/m at 3.3 μm [99]. In addition, a multi-mode fiber with an optical loss of 0.85 dB/m at 1.3 μm has been obtained from a preform made using the rotational casting method [100]; the importance of fluorination with HF during glass melting was also discussed in this published work. However, all these fibers have comparatively low InF3 (~28 mol%) and high GaF_3 contents, limiting their IR transmittance. An earlier research study [180] showed that the glass composition $32InF_3$-$20ZnF_2$-$20SrF_2$-$18BaF_2$-$8GaF_3$-$2CaF_2$ (IZSBGC) with high InF_3 content was promising for mid-infrared applications due to its high transmission and low rate of crystallization. Therefore, this composition was chosen as the base glass for this work.

To develop low-loss fluoride glass fibres, it is important to reduce sources of extrinsic absorption and scattering in glasses. In this chapter, the reduction of defects (e.g., crystals, bubble, oxide and hydroxyl (OH) group contents) in IZSBGC glass (hereafter referred to as base glass) is reported. The major aim was to optimise the glass melting conditions and

[1] Half of this Chapter has been published in journal paper I and II in "Published papers".

to explore the feasibility of fabricating glass billets, which have a size that is sufficient for fibre fabrication, and have with good thermal stability and optical quality.

3.1. Characterization of indium fluoride raw materials from different suppliers

Three indium fluoride raw material types with different purities from different suppliers (Astron, Testbourne and Synquest) were used in this project due to changing availability of raw materials. For example, InF_3 from Testbourne was ordered to replace InF_3 from Astron which was no longer available from the supplier after a few melts. Hence it is important to examine the effect of raw materials on the resulting glasses. XRD and TGA measurements were carried out to examine the quality of the indium fluoride raw materials.

XRD results indicate that the indium fluoride raw material from Astron (~99.999% metal content) is anhydrous indium fluoride (Fig. 3.1), and that the indium fluoride from Synquest (~99.9% metal content) contained indium fluoride and oxide (Fig. 3.2). In comparison, the indium fluoride from Testbourne (~99.99% metal content) was identified by XRD as indium fluoride hydrate ($InF_3 \cdot 3H_2O$; Fig. 3.3). Although the Synquest indium fluoride raw materials contained indium oxide, the oxide impurity can be fluorinated into indium fluoride at 450 ˚C within a short time, based on Boutarfaia and Poulain [181].

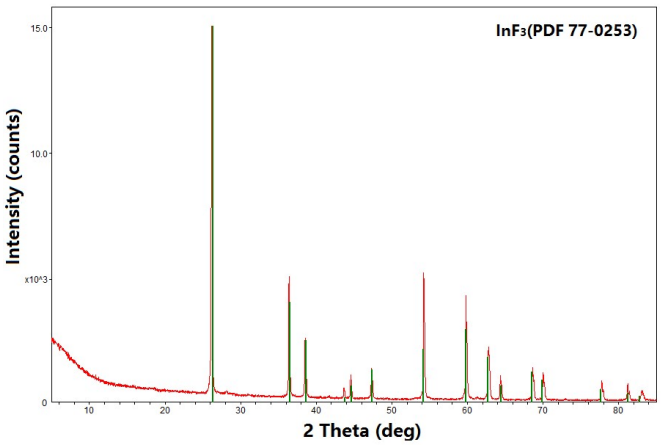

Figure 3. 1. XRD result of InF_3 from Astron.

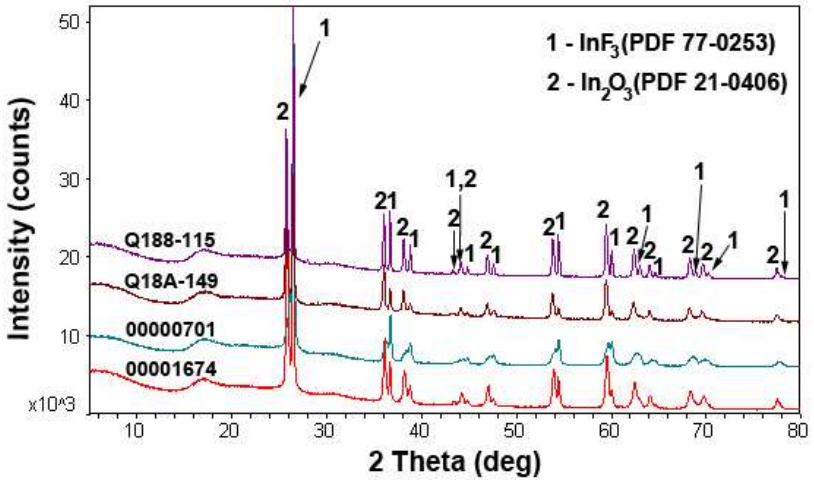

Figure 3. 2. XRD results of InF_3 from Synquest for different batch numbers.

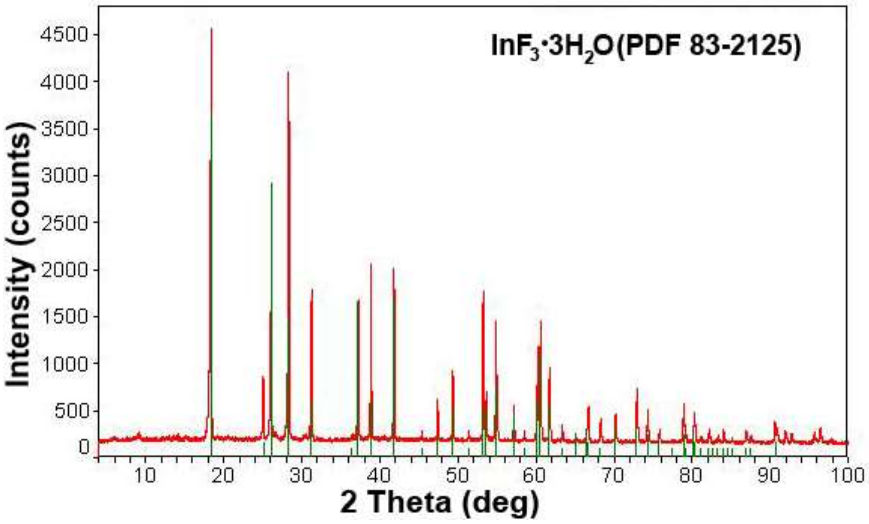

Figure 3. 3. XRD result of InF_3 from Testbourne.

To confirm the water content in the InF_3 raw materials from Testbourne, thermogravimetric analysis (TGA) was conducted using a commercial Simultaneous Thermal Analyzer (PerkinElmer STA 6000) connected to an FTIR spectrometer (PerkinElmer Spectrum 400). The experimental error of the temperature measurement was ± 2 ˚C. The STA-FTIR measurements were conducted from room temperature to up to 350 ˚C at a heating rate of 10 ˚C /min under N_2 atmosphere.

$CuSO_4 \cdot 5H_2O$ (containing 36 wt% crystal water) was used as a reference sample. TGA result (Fig. 3.4) for $CuSO_4 \cdot 5H_2O$ demonstrated that 27 wt% was lost from 75 ˚C to 150 ˚C. It was also found that around 24 wt% was lost from 120 ˚C to 200 ˚C for the InF_3 raw

material from Testbourne. The weight loss in both $CuSO_4 \cdot 5H_2O$ and InF_3 raw material sample from Testbourne was due to loss of the crystal water contained in both chemicals.

Simultaneous FTIR results of $CuSO_4 \cdot 5H_2O$ and InF_3 raw material sample from Testboure are shown in Fig. 3.5. From the FTIR results of $CuSO_4 \cdot 5H_2O$ (Fig. 5a), the absorbance at about 3550, 3700 and 3950 cm^{-1} started to increase after 75 ˚C and decrease after 130 ˚C. The change of absorbance corresponded to the weight loss from 75 ˚C to 150 ˚C in TGA. Therefore, the absorbance changes at about 3550, 3700 and 3950 cm^{-1} were attributed to water released during the TGA measurements. At the same wavenumber positions (at about 3550, 3700 and 3950 cm^{-1}), it was - found that InF_3 raw material sample from Testbourne (Fig. 3.5b) had similar absorbance change corresponding to the weight loss from 120 ˚C to 200 ˚C in TGA results due to the presence of water.

In addition, the TGA results showing 24 wt% loss in InF_3 raw material from Testbourne were due to the water loss during heating, in agreement with the 23.9 wt% of water content in $InF_3 \cdot 3H_2O$ calculated based on its stoichiometry. The presence of water of crystallisation in $InF_3 \cdot 3H_2O$ is also in agreement with the XRD result.

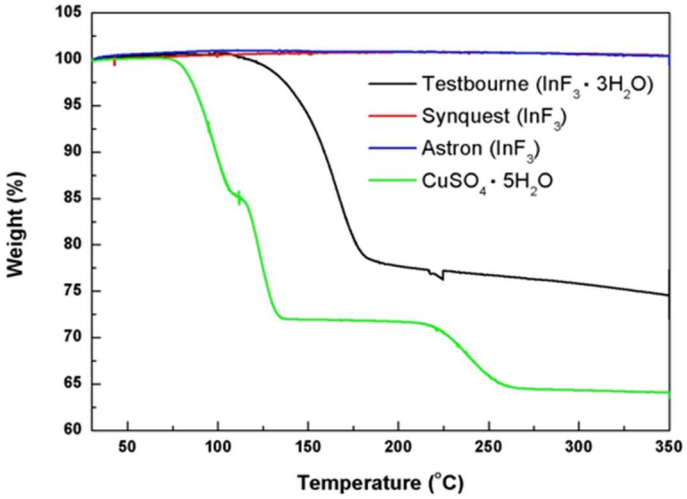

Figure 3. 4. TGA result of InF_3 raw materials from three different suppliers.

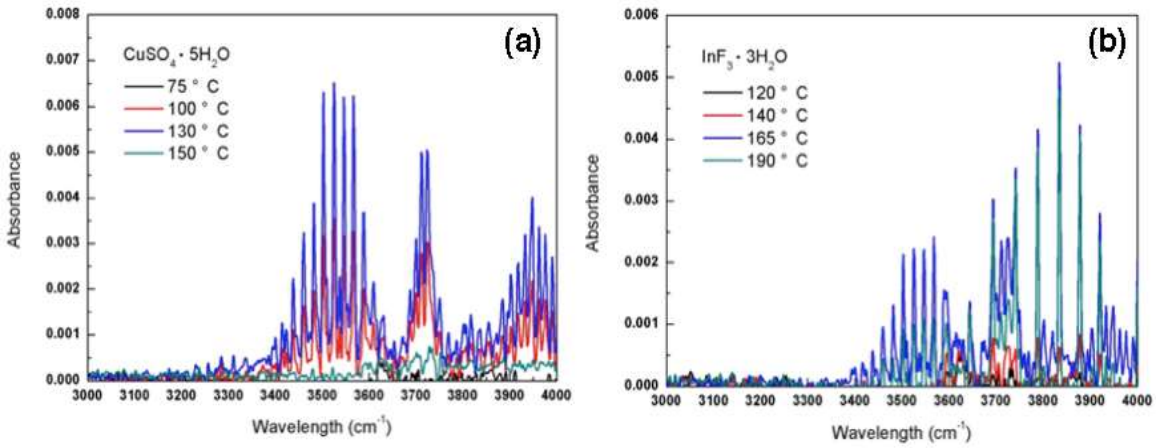

Figure 3. 5. FTIR results of $CuSO_4 \cdot 5H_2O$ (left) and InF_3 raw material sample from Testbourne ($InF_3 \cdot 3H_2O$) (right) at different temperatures.

3.2. Glass fabrication of IZSBGC glass

Fluoride glasses must be prepared under strictly-controlled melting atmospheres (e.g., under dry N_2, use of ammonium bifluoride for fluorination of oxidised raw materials) to prevent hydrolysis and crystallisation. Hence, the traditional melting techniques developed for oxide glasses in open air furnaces are generally unsuitable for fluoride systems. In this work, glass preparation procedures were conducted under a dry N_2 atmosphere controlled furnace (described in Chapter 2.2) to prevent oxdiation and reudce OH content in glass melting.

3.2.1. Optimisation of IZSBGC glass melting with 30g batch size

Small batch size with 30 g was used for investigation of a variety of melting conditions (such as melting and cast temperatures, crucible materials and fluorination methods) for the specific purpose of reducing the content of defects (e.g., haze and striae in Fig. 3.6) in IZSBGC glass made with various InF_3 from different suppliers. All 30 g glass melts were cast into a 30 cm long and 15 cm wide brass mould with different thickness (depending on glass casting viscosity during different melting procedure), which was called block sample hereafter.

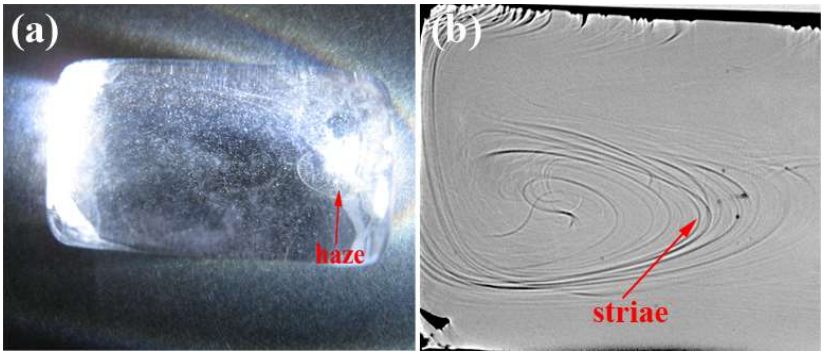

Figure 3. 6. Defects obserbed in glass: (a) Defects with a haze appearance look a very fine film of dust or coating on the glass that cannot be removed [182]; (b) Striae are mainly generated due to the unfinished homogenization melt [183].

3.2.1.1. Investigation of melting and casting temperatures

In contrast to many oxide glasses, the melting temperature for fluoride is relatively low and temperatures over 1100 ˚C are rarely encountered [180]. For IZSBGC glass in this study, most glass samples were melted ≤ 900 ˚C to avoid high fluorine loss from the batch above 900 ˚C. The temperature ramp speed was set to 5 ˚C/min.

Preliminary melting trials were conducted using 99.999% metal content InF_3 from Astron and other fluoride raw materials with purity ≥99.9% metal content for 30 g glass batches. Some of the glass fabrication details are shown in Table 3.1. Best results were obtained for melting at 900 ˚C for ~3h (IM3, IM18, IM20, and IM22); these glasses were free of crystals and black particles, except two black dots on the surface of IM3 glass and faint haze-like striaes in IM3 and IM20 glasses. A lower melting temperature of 800 ˚C (IM5) led to significant amounts of black particles forming on the top of glass. Short melting times of only 1 h at 900 ˚C (IM10) resulted in crystals in the glasses. The use of increased temperature of 950 ˚C after melting at 900 ˚C (IM12 and IM17) also produced crystals in the glass due to the high fluorine loss. However, when the temperature was slightly increased to 910-920 ˚C after the 900 ˚C melting step (IM20, IM22), the amount of bubbles was decreased.

Table 3. 1. Fabrication details of 30g block melts. (+) [#]

Melt no.	Crucible material	Cast weight	Yield	evaporative loss (%)	Melting temp. / time	Fining time / temp.	Time before casting	Pre-heated mould / Anneal. temp.	Defects		
									Black particles	Haze[$]	Bubbles
IM3	Pure Pt	24.1g	80%	2.5%	900 ˚C / 3:00h	800 ˚C / 0:30h	65s	290 ˚C / 340 ˚C	+		
IM5	Pure Pt	19.6g	65%	2.2%	800 ˚C / 3:00h	--	75s	290 ˚C / 340 ˚C	+		+
IM10	Pt95Au5	11.2g	37%	1.8%	900 ˚C / 1:00h	750 ˚C / 3:00h	72s	290 ˚C / 340 ˚C		crystals	
IM12	Pt95Au5	18.6g	62%	2.3%	900 ˚C / 3:00h 900 ˚C / 0:30h	800 ˚C / 1:30h	68s	290 ˚C / 340 ˚C		++	
IM17	Pure Pt	23.4g	78%	2.2%	900 ˚C / 2:00h 900 ˚C / 0:50h	800 ˚C / 0:50h	67s	290 ˚C / 340 ˚C		+++	
IM18	Pt95Au5	20.3g	68%	2.2%	900 ˚C / 3:00h	800 ˚C / 0:30h	68s	290 ˚C / 340 ˚C			++
IM20	Pt95Au5	23.6g	79%	2.2%	900 ˚C / 3:00h 920 ˚C / 0:30h	800 ˚C / 0:30h	65s	290 ˚C / 340 ˚C		+	+
IM22	Pt95Au5	20.6g	69%	2.4%	900 ˚C / 3:00h 910 ˚C / 0:30h	780 ˚C / 0:30h	64s	290 ˚C / 340 ˚C			+

(+) Note that Pre-heated mould / Anneal. temp. is the furnace temperature (described in Chapter 2.2).

All glass blocks prepared by raw material InF_3 from Astron with~99.999% metal content and other fluorides with ≥99.9% metal content. No fluorination was used except for IM17 (fluorination: 0.12 L/min SF_6 at 800 ˚C for 15min). [$]

The formation of crystals during casting is strongly dependent upon the cooling rate (e.g., on average ~4K/s and ~9K/s in the beginning 30 sec of casting procedure for 30g glass melt) for glass melts during casting, which is hard to measure and in turn is affected by the casting temperature, waiting time before casting, and mould temperature. The glass melts needed to cool down sufficiently fast through the nucleation and crystal growth temperature region between the melting and glass transition temperature to avoid crystal formation. For IZSBGC glass, good glass quality was obtained with casting at 900 ˚C (casting temperature) and a mould temperature of 290 ˚C for 30 g sample. 290 ˚C was cold enough to cool down glass melt quickly without crystallization and cracking when glass melt was taken out from furnace at 900 ˚C.

3.2.1.2. Choice of crucible material

Platinum and vitreous carbon crucibles have been extensively used for fluoride glass melting [15]. An earlier study [114] suggested that platinum crucible is safe for fluoride glass melting without contamination or corrosion of the crucible material at glass melting temperatures. In comparison, vitreous carbon crucibles have been widely used with good results [13, 184], owing to the fact that carbon is inert, relatively pure, and not wetted or reactive with fluoride melts. In this project, glass melting was carried out using both platinum and vitreous carbon crucibles for comparison purpose.

Table 3.2 compares the results of three samples melted using crucibles made from different materials and using InF_3 from Astron. Pure platinum and platinum alloy with 5% gold can produce glasses with similar qualities (IM1 and IM12 in Table 3.2). However the platinum alloy crucibles (Pt95Au5) can be cleaned more easily without residual glass due to the lower degree of glass wetting for this alloy compared to pure platinum crucibles. Glass melting using platinum and vitreous carbon crucibles was also compared. Both IM12 and IM13 melts were conducted using the same melting procedure, but platinum alloy (Pt95Au5) was used for IM12 and vitreous carbon crucible was used for IM13. Both glasses contain striaes and tiny crystals. The glass melted in platinum alloy crucible did not show any black particles, whereas the glass melted in a vitreous carbon crucible contained a layer of black particles on the surface, indicating that vitreous carbon fosters the formation of black particles due to the reduction of In^{3+} under reducing condition. Black particles are detrimental to glass optical properties as they cause high loss. In conclusion, the platinum alloy Pt95Au5 was found to be the optimum crucible material

with respect to wetting/cleaning and occurrence of black particles compared with the other two crucibles. Hence, Pt95Au5 crucibles were used for further glass fabrications.

Table 3. 2. 30g glass blocks melted using different crucibles ***#.**

Melt No	Crucible	Defects		
		Black particles	Haze	Bubbles
IM1	Pure Pt		+	+
IM12	Pt95Au5		++	
IM13	Vitreous carbon	++	+	

***** No fluorination was used for these three samples.

All glass blocks prepared by raw material InF_3 (99.999% metal content from Astron), other fluorides with ≥99.9% metal content.

3.2.1.3. Reduction of extrinsic loss via fluorination method during glass melting

As discussed above, an important step in reducing extrinsic losses in glasses is to reduce oxide impurities in the starting materials used for melting. Three small glass blocks (Table 3.3) were initially fabricated to optimise the melting conditions using InF_3 from Astron with ~99.999% metal content (Table 2.1 in Chapter 2) and investigate the effect of different fluorination techniques on the OH content in the glass blocks. Two approaches were considered, use of ammonium bifluoride (NH_4HF_2) in the melting process as a fluorination reagent [185], and SF_6 being used as a secondary atmosphere to study the reduction of oxide impurities (e.g., In_2O_3 and H_2O content in the raw material) of the fluoride glasses [186]. The glass batches with excess NH_4HF_2 (1.6 wt% of the batch weight) were first heat-treated at 235 ˚C, and then melted at 900 ˚C. The SF_6 procedure included application of an SF_6 reactive atmosphere at 700 ˚C for 15 minutes, followed by the melting process at 900 ˚C. SF_6 was introduced at 700 ˚C, rather than 900 ˚C, because we have observed that SF_6 can corrode the Pt crucible and/or Pt liner, resulting in the incorporation/formation of Pt particles in the melt. Table 3.3 summarises the processes used to fabricate the glasses.

Table 3. 3. 30g glass blocks melting conditions (+).

Melt No.	Fluorination Conditions		Dwell	Dwell Time @ 700 ˚C	Dwell Time @ 900 ˚C	Absorption co-efficient at ~2.9 μm (cm^{-1})	T_g (˚C)	T_x (˚C)	T_p (˚C)
	Trial	method							
IM37#	(A)	---	@ **235** ˚C/45 min	15 min	3 h	0.00106(±0.0012)	318	389	415
IM38#	(B)	SF_6	@ **235** ˚C/45 min	15 min with SF_6	3 h	0.0042(±0.0004)	318	389	413
IM39#	(C)	NH_4HF_2	@ **235** ˚C/45 min	15 min	3 h	0.0023(±0.0002)	310	389	419
IM25*	(C)	NH_4HF_2	@ **235** ˚C/45 min	---	3 h	---	307	385	409
IM129**	(C)	NH_4HF_2	@ **235** ˚C/45 min	---	3 h	---	307	389	409
IM111**	(D)	NH_4HF_2	@ **450** ˚C/1h	---	2 h	---	308	389	407

(+): The temperature ramp speed was set to 5 ˚C/min. All glass melts were prepared with N_2.
#: raw material InF_3 (99.999% metal content from Astron), other fluorides with ≥99.9% metal content.
*:raw material $InF_3 \cdot 3H_2O$ (99.99% metal content from Testbourne) (i.e., needs 31.4 wt% compensation to provide the same amount of InF3) other fluorides ≥ 99.9% metal content.
**:raw material InF_3 (99. 9% metal content from Synquest), , GaF_3 (96.3% metal content from Synquest), other fluorides ≥99% metal content.

Table 3. 4. Electron probe microanalysis of block glass sample IM 39 (melted under fluorination condition C).

	In	**Zn**	**Sr**	**Ba**	**Ga**	**Ca**	**F**
EMPA results (mol %)	9.74±0.19	5.97±0.28	6.05±0.18	5.37±0.32	2.88±0.21	0.58±0.09	67.74±0.21
Glass batch composition (mol %)	9.41	5.88	5.88	5.29	2.35	0.59	70.60

Sample IM39, which was prepared with the anhydrous InF_3 raw (Table 2.1 in Chapter 2) and melted under C condition (N_2+NH_4HF_2), was selected for EMPA analysis to determine the glass chemical composition after melting (Table 3.4). Although 3 hours were used for glass melting at 900 ˚C, there was no significant difference between measured and calculated concentrations for each element, suggesting that evaporation loss (3.7 wt.%) during glass melting is negligible.

Fig. 3.7 shows the absorption coefficient spectra of three glasses prepared under different fluorination conditions (Table 3.3). It is clear that fluorination of the raw materials using NH_4HF_2 significantly reduced the absorption of OH groups (at ~2.9 μm) from 0.00106 (± 0.0012) to 0.0023 (± 0.0002) cm^{-1} (Fig. 3.7a). As the OH content increases, relatively strong hydrogen bonds between OH and fluorine ions can form, which shifts the OH resonance (~2.9 μm) to longer wavelengths [187]. In Fig. 3.7b, the infrared absorption edges of our glass samples are at about 8.7 μm where the absorption coefficient is 2.3 cm^{-1} (corresponds to ~10 % transmission for 1cm sample thickness). In addition, in our IZBSGC glasses (Fig. 3.7b), additional absorption >7.5 μm is observed for samples IM37 and 38 (melted under A and B conditions in Table 3.3), which were made without NH_4HF_2. In particular, a shoulder at 7.8 μm and a shift of the IR edge to the shorter wavelengths were observed. Similar IR absorption features were observed in ZrF_4-BaF_2-LaF_3 (7.1 μm) and BaF_2-ZrF_4-YbF_3-ThF_4 (9.1 μm) glasses due to oxide impurities in the glasses [60, 188]. Therefore, the shoulder at 7.8 μm in the absorption spectra for samples IM37 and 38 (melted under A (N_2) and B conditions (N_2+SF_6)) is attributed to the oxide impurities in the glasses caused by lack of fluorination under A condition and incomplete fluorination without NH_4HF_2 under B condition. The absorption at 7.8 μm was suppressed using NH_4HF_2 for a sample (melted under C condition (N_2+NH_4HF_2)), indicating an effective reduction of oxide and OH impurities. Drexhage [189] found that an incomplete conversion of the starting oxide materials by the fluorinating agent (NH_4HF_2) during glass melting could alter the slope of the IR multi-phonon edge, which corresponds to a shift of the IR absorption edge. Hence, the significant shift of the IR absorption edge to shorter wavelengths for samples IM37 and 38 (melted under A (N_2) and B conditions (N_2+SF_6)), when compared with sample IM39 (melted under C condition, N_2+NH_4HF_2; Fig. 3.7b), is also attributed to the incomplete conversion of oxides to fluorides due to the lack of fluorination with NH_4HF_2 for preparing samples IM37 and 38.

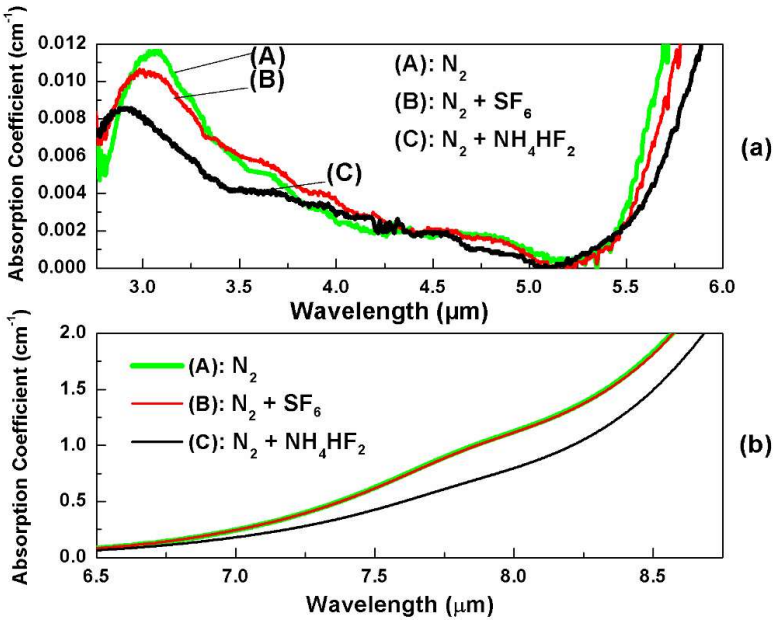

Figure 3. 7. Absorption coefficient for the glass samples prepared under the three different fabrication conditions (a) 2.75-6.00 μm; (b) 5.00-8.75μm.

DSC measurements showed that melting with NH_4HF_2 for sample IM39 increased ΔT (T_x-T_g) which is usually used as an assessment of glass stability compared with other evaluation of glass stabilities as described in Chapter 1.2.4. IM39 also show a flattened crystallisation peak, suggesting a lower crystallisation rate [15] compared with samples IM37 and 38 (Table 3.3 and Fig. 3.8). The crystallisation peak of sample IM39 shows a small shoulder at ~400 ºC. Based on the crystallisation theory by [190, 191], the shoulder indicates a slight change in the crystallisation behavior at this temperature.

It was found that oxide inclusions stimulated crystallisation in zirconium fluoride-based glasses [192]. Therefore, we attribute the enhanced crystallisation stability (reflected by increased ΔT and reduced crystallisation rate) for sample IM39 to a lower amount of oxide impurities in this sample, as a result of the fluorination with NH_4HF_2. Sample IM39 has a slightly lower glass transition temperature than the other two samples IM37 and 38, which we also attribute to the lower oxide impurity content of sample IM39. Similar results were observed when oxide impurities were present in ZrF_4-based ternary glasses [122, 193].

The comparison of the melting conditions for these three samples (IM37-39) shows that the absorption of OH groups at 2.9 μm in $32InF_3$-$20ZnF_2$-$20SrF_2$-$18BaF_2$-$8GaF_3$-$2CaF_2$ (IZSBGC) glasses can be reduced by employing a fluorination method with NH_4HF_2.

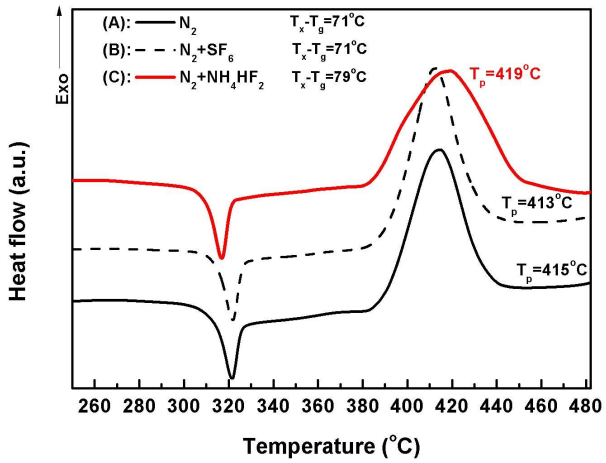

Figure 3. 8. DSC curves for the glass samples (IM37-39) prepared under the three different fabrication conditions (A-C), respectively.

Apart from the InF_3 from Astron, two other InF_3 raw materials i.e., 99.99% (metal purity) $InF_3{\cdot}3H_2O$ from Testbourne (labeled with a star '*' in Table 3.3), and anhydrous 99.9% (metal purity) InF_3 from Synquest (labeled with double star '**' in Table 3.3) were also used for glass melting with slightly adjusted melting procedures (e.g., addition of excess $InF_3{\cdot}3H_2O$ as compensation for loss of water). The water in $InF_3{\cdot}3H_2O$ reacts with InF_3, resulting in the formation of $In(OH)_3$ and gaseous HF. Hence, for glass batches using $InF_3{\cdot}3H_2O$, a higher amount of excess NH_4HF_2 (6.7 wt% of the batch weight) was used to compensate for the loss of fluorine due to the formation and loss of HF, while for glass batches containing anhydrous InF_3 from Synquest a lower amount of NH_4HF_2 was used (2.4 wt% of the batch weight) due to the absence of water in the raw material. For the glasses prepared using $InF_3{\cdot}3H_2O$, excessive amounts of InF_3 were also needed due to water/hydroxide impurities in the raw material.

The glass batches were first fluorinated at 235 ˚C or 450 ˚C, followed by melting at 900 ˚C. Table 3.3 lists the fluorination and melting conditions, and characteristic temperatures (T_g, T_x, and T_p) of samples (IM25, 129 and 111) fluorinated under C and D.

DSC measurements (Fig. 3.9, Table 3.3) show that different fluorination methods (C and D) and melting conditions had negligible impact on T_g; the variations were within the temperature error of the DSC measurements. However, it was found that Sample IM129 fluorinated under C condition contained a few un-dissolved particles. Mohammed [194] introduced 500 ˚C for elimination of NH_4HF_2 products prior to melting of their fluoride glasses. Fluorination at 450 ˚C prior to melting in this work for Sample IM111 fluorinated

under C condition effectively reduced the remaining (i.e., non-reacted) NH_4HF_2 in the final glass. The un-dissolved particles in Sample B are attributed to possible residual products (from NH_4HF_2) in the glass, which could not be eliminated by fluorination at 235 ˚C.

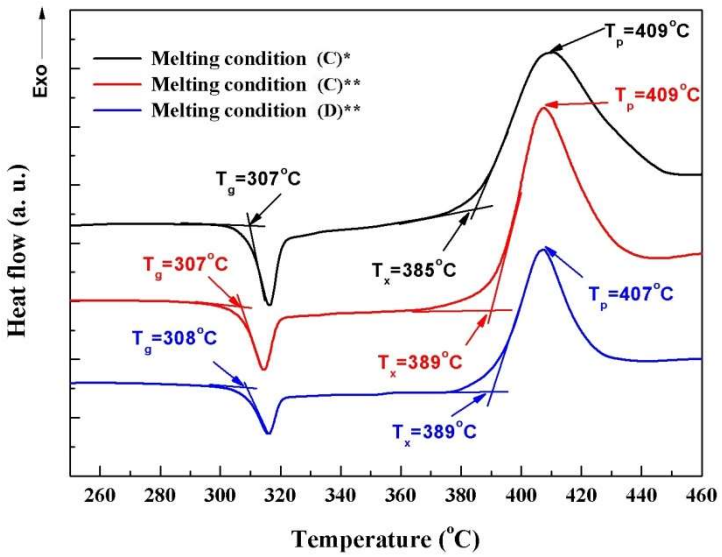

Figure 3. 9. DSC curves for glasses prepared under three different conditions.

3.2.2. Up-scaling of the glass batch size

For preform extrusion, larger glass melts (up to 150 g) were required and they were cast into cylindrical mould with 30 mm in diameter and 20-30 mm long, resulting in glass samples referred to as “billets”. The melting procedures for larger melts were based on those for the melting of 30 g samples. Melting conditions for different batch size samples using different raw materials are listed in Table 3.5. The challenges for up-scaling from 30 g to 150 g glass melts are discussed below.

If larger glass melts are cast under the same conditions as those for small glass melts, larger glasses would have slower cooling rate which would result in crystals in glasses. Hence, quicker cooling rate is needed to pass the glass crystallisation temperature to avoid the formation of crystals in glasses (i.e., depending on wait time before casting and pre-heating mould temperature). A low glass casting temperature can prevent crystal formation, but may result in a highly viscous melt when casting and favour the formation of bubbles [9] by the trapping of gases from the atmosphere into the glass melts during casting. In addition, a highly viscous large-size melt leads to low yield of cast glass since

the glass already solidifies during casting, and thus not all of the glass in the crucible can be cast out. Furthermore, a low mould temperature may also result in glass cracking within the mould.

In this study, the glass mould temperatures for casting large glass batch sizes were adjusted to achieve crystal-free glass without cracks and bubbles and with high yield. For example, the mould temperature was reduced when the batch size increased due to lower cooling speed compared with smaller size (e.g., from 220 ˚C for 30 g batch size (IM111) to 180 ˚C for 100 g batch size (IM122). By optimising glass melting conditions, large batch size with 150 g (i.e., IM90) was successfully fabricated into a clear glass billet. The resulting low absorption coefficient at about 3 μm (Fig. 3.10) is similar to that of IM39 with a smaller batch size of 30 g (Fig. 3.7a).

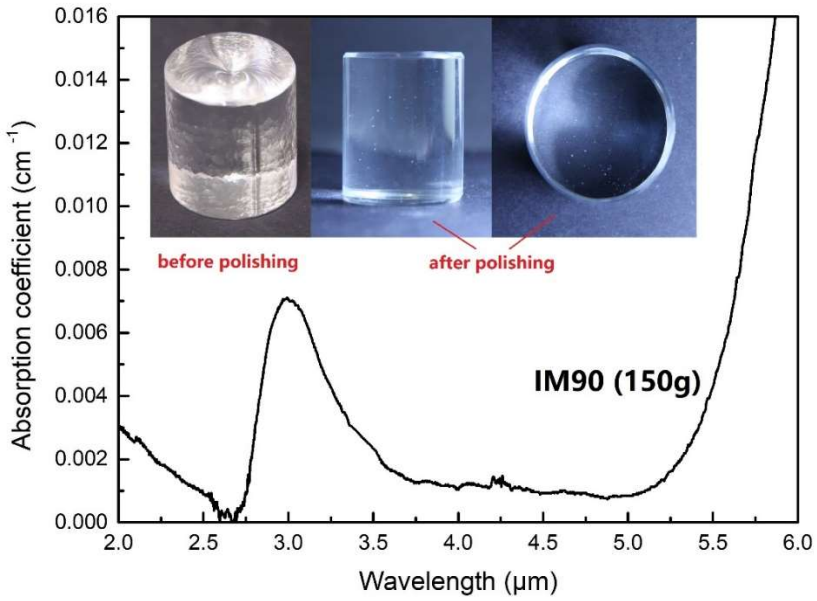

Figure 3. 10. Absorption coefficient and images for the glass sample IM90 (batch size: 150g).

Table 3. 5. Optimised base glass melting condition for different batch size.

Raw materials	Melt No.	Batch weight (g)	NH_4HF_2/batch weight (wt %)	Fluorination		Melting temp./time	Time before casting (s)	Mould / Anneal temp. (˚C)
				Temp. (˚C)	Time (min)			
#	IM39	30	1.6	235	45	900˚C/3h	66	290/340
*	IM75	30	6.8	235	45	900˚C/3h	79	270/340
	IM68/69	60/80	6.7	235	45	900˚C/3h	84/98	250/340
	IM71	100	6.7	235	52	900˚C/3h	103	250/340
	IM90	150	6.7	235	75	900˚C/3.25h	108	245/340
**	IM111	30	2.4	450	60	900˚C/2h	70	220/335
	IM113	65	2.4	450	70	900˚C/3h	93	200/335
	IM122	100	2.4	450	80	900˚C/3.5h	112	180/335

#: raw material InF_3 (99.999% metal content from Astron), other fluorides ≥ 99.9% metal content.

*: raw material $InF_3 \cdot 3H_2O$ (99.99% metal content from Testbourne), GaF_3 (96.3% metal content from Synquest), other fluorides ≥ 99% metal content.

**: raw material InF_3 (99.99% metal content from synquest), GaF_3 (96.3% metal content from Synquest), other fluorides ≥99% metal content.

3.3. Conclusion

In summary, it was found that Pt alloy crucible containing 5% gold and 95% platinum is more suitable than pure platinum and vitreous carbon crucibles for fluoroindate glass melting, as Pt alloy crucible is easier to clean for further use than pure platinum crucible and the use of Pt alloy crucible does not result in the formation of black particles which were found in IM13 melted in vitreous carbon crucible. The absorption at 2.9 μm due to OH groups in $32InF_3$-$20ZnF_2$-$20SrF_2$-$18BaF_2$-$8GaF_3$-$2CaF_2$ (IZSBGC) glasses was successfully reduced by employing a fluorination method with NH_4HF_2. Sample IM111 prepared using the anhydrous InF_3 raw material from Synquest with ~99.99% metal content demonstrated a higher glass crystallisation stability, as compared to IM25 melted using the $InF_3 \cdot 3H_2O$ raw material from Testbourne. A high fluorination temperature of 450 ˚C for IM111 enabled successful preparation of a crystal-free glass and eliminated the remaining NH_4HF_2 in the glass. Glass samples were successfully scaled up to 150g with minimum defects found in the glasses, which are suitable for extrusion.

Chapter 4

UNSTRUCTURED PREFORM FABRICATION[2]

The major thrust of work into the development of fluoride infrared fibres has been directed towards developing optical fibres with low loss. The chemical vapor deposition (CVD) technique has been demonstrated as a means of producing low-loss silica glass fibres [195, 196]. Unlike silica-based glasses, there has been no CVD method developed yet for fabrication of fluoride glass preforms. Most fluoride glass fibre preforms are prepared by a melt-quench technique using a metal mould. Billet extrusion technique is another possible method for fluoride glass preform preparation.

In this chapter, both casting and extrusion methods were compared for application to IZSBGC glass preform fabrication. To the best of my knowledge, it is the first time extrusion of fluoroindate glass and drawing of fibers from extruded preforms has been demonstrated. Glass flow analysis was carried out to provide insights into the glass temperature-viscosity behavior and the relationship between preform surface roughness and extrusion temperature, which enabled fabrication of preforms with low surface roughness and eventually reduced the fiber scattering loss.

4.1. Preform fabrication by casting method

Casting techniques (e.g., rotational casting and suction casting methods) are widely used for fluoride glass preform fabrication, and have been used for making fluoroindate glass

[2] The majority of this Chapter has been published in journal paper I and II in "Published papers".

fibers [97, 99, 100]. It is a direct way to produce glass preforms that are directly drawn into a fibre instead of elongating cast glasses into preforms via extrusion.

Glass rods were prepared by directly casting melts into rod-shape moulds (10 or 12 mm in diameter; Table 4.1). Fining process was applied by reducing the temperature (to 800 ˚C) to dissolve the bubbles into molten glass prior to casting [197]. However, casting into rod-shape moulds is challenging as it is prone to produce large bubbles (up to 1 mm in diameter) in the middle of the cast rods (Fig. 4.1). The formation of bubbles can probably be explained by the more turbulent flow of molten glasses with gases (e.g., N_2 or gases from decomposition reaction of impurities) when they are poured into long and thin moulds, which generates and traps bubbles in the cast glass. In addition to bubbles, the cast rods also exhibited an orange-peel-like surface, which has a high surface roughness and needs to be removed before fibre drawing. Another problem with the casting technique is inflexibility for complex structured fibre fabrications due to the resulting orange-peel-like rough surface finish and difficulties in casting operation and mould fabrication.

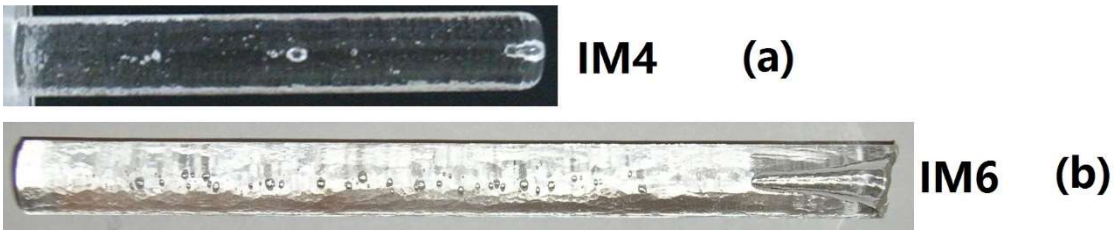

Figure 4. 1. Photographs of rods IM4 of 12 mm in diameter (a), and IM6 of10 mm in diameter (b).

Table 4. 1. Fabrication results of cast IZSBGC glass rod.

Melt no.	**Batch weight (g)**	**Cast weight (g)**	**Yield (%)**	**Evaporative loss (%)**	**Melting Temp. (˚C) /time (h)**	**Fining Temp. (˚C) / time (h)**	**Time before casting (s)**	**Mould / Anneal. temp. (˚C)**
IM4	40	24.1	81	2.5	900 / 3	800 / 0.5	71	290 / 340
IM6	80	40.9	51	2.5	900 / 3	800 / 0.5	85	290 / 340
IM8	50	40.9	82	2.4	900 / 3	800 / 0.5	84	290 / 340

4.2. Preform fabrication by extrusion

Conventional fabrication techniques using the casting method for the preparation of fluoride fibre preforms are not suitable for making rods with various shapes and long lengths. Billet extrusion technique has been demonstrated as a suitable method for fluoride glass preform fabrication [114]. Extrusion conditions for fluoroindate glasses were based on a previously published study on fluorozirconate glass extrusion [114]. Graphite has been used as a die material for fluorozirconate glass extrusion due to the relatively low friction between the die and glass surfaces. Using a graphite die, rather than a stainless steel die, fluorozirconate glass could be extruded at higher viscosities (~10^8 Pa·s), i.e., lower temperatures. Extrusion with a graphite die allowed fluorozirconate preforms to be extruded below the onset of glass surface crystallisation temperature (290 ˚C [114]) which is 62 ˚C lower than the glass crystallisation temperature determined by DSC (T_x = 352 ˚C [15]]). In this work, graphite was also used as the die material for the extrusion of IZSBGC glass at a temperature below the onset of glass crystallisation temperature [114].

4.2.1. Annealing tests

To achieve a good surface quality for glass items extruded through graphite dies, the extrusion temperature needs to be high enough (but not too high to trigger glass crystallisation) to allow low extrusion force which can prevent the die cracking and achieve good surface roughness. [114]. A low extrusion force minimises shedding of graphite particles from the die onto the glass and reduces the chance of die breakage. Shedding can degrade the surface quality of extruded rods, whereas die breakage can lead to premature stopping of an extrusion trial. While higher temperatures decrease the extrusion force, they can increase the probability of undesired surface crystallisation. Therefore, the maximum temperature that can be used for extrusion of preforms with good surface quality will be limited by the onset of glass surface crystallisation temperature.

Thin polished glass slides made from the fluoroindate glass IM25 melted under (C)* condition using InF_3 from Testbourne, fluorination at 235 ˚C and melting at 900 ˚C (Table

3.3 in Chapter 3) were used for annealing tests to explore whether surface crystallisation could occur under extrusion conditions. The glass slides polished using 1 μm Al_2O_3 powders had lower surface roughness and thickness than the extruded preforms. Therefore, any sign of crystallisation on the glass slide would be easily identified on the smooth surfaces under an optical microscope. This information was then used to predict suitable extrusion conditions. As the glass transition temperature (T_g) is ~310 ˚C and extrusion is conducted above T_g, temperatures in the range of 315-350 ˚C were used for annealing tests. The results are demonstrated in Table 4.2. It can be found that glass slide No. 2 became opaque after annealing for certain times at different temperatures while the other sample annealed ≤ 330 ˚C was still fully transparent. As high temperatures enable extrusion at low forces, temperatures within 320-330 ˚C were selected for further annealing tests.

Table 4. 2. Temperature effects on annealing test.

Sample No	**315 ˚C/2h**	**320 ˚C/2h**	**330 ˚C/2h**	**340 ˚C/2h**	**350 ˚C/2h**
Slide 1	Fully transparent				
Slide 2		Fully transparent	Fully transparent	Translucent/slight opaque	Fully opaque
Slide 3		Fully transparent			
Slide 4				Fully transparent	
Slide 5					Fully opaque

Two more identical glass slides were treated at elevated temperatures comparable to those used for extrusion (within 24 h). There was no observable change before or after annealing at 322 ˚C, while a surface layer in the form of wrinkles occurred on the edge of the glass sample after annealing at 330 ˚C (Fig. 4. 2). Variation in surface composition during re-heating (e.g., annealing) causes the formation of the wrinkles [198] which are not crystals but may act as seeds to facilitate crystallisation. Both surface wrinkle patterns and surface crystallisation should be avoided during extrusion for making a low loss fibre. This annealing test suggests that a temperature of 330 ˚C for preform extrusion can cause surface wrinkle patterns. By contrast, the extrusion temperature at 322 ˚C is sufficiently low to avoid surface wrinkle patterns.

Note that the surface wrinkle patterns possibly lead to surface crystallisation at a temperature lower than T_x (385-389 ˚C as measured by DSC; Table 3.3 in Chapter 3), due to the different thermal treatment during annealing in comparison with the DSC measurement. In the annealing process, the glass was kept at elevated temperatures for less than 8h, whereas during the DSC measurement the glass was heated at a rate of 10 ˚C/min. The long dwell time during annealing can result in surface wrinkle patterns which facilitate crystallisation at temperatures below T_x.

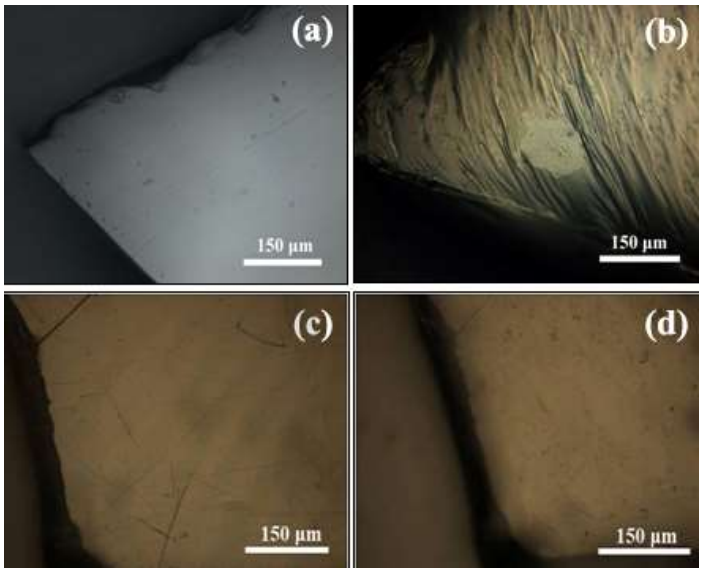

Figure 4. 2. Glass surface images: (a) before annealing at 330 ˚C less than 8 hours; (b) the edge of the glass after annealing at 330 ˚C less than 8 hours; (c) before annealing at 322 ˚C for 24 hours; (d) after annealing at 322 ˚C for 24 hours.

4.2.2. Preliminary extrusion trials

The glass melts were cast into a billet mould with an inner diameter of 30 mm and a length of 30 mm, which was used for preform extrusions. Prior to extrusion, the cylindrical billets were polished using 1 µm Al_2O_3 powders which were also used for polished the slides used for the annealing tests. The billets were then extruded into rod-shape (cylindrical) preforms of 8 mm in diameter at temperatures within 20 ˚C above the glass transition temperature (T_g =310 ˚C) using graphite dies.

The preliminary extrusions were conducted at 317 (IE9), 322 (IE1) or 330 ˚C (IE3), requiring at least 8 h. The higher viscosity at the relatively low temperature of 317 ˚C required higher extrusion force (~35 kN) and caused the graphite die to crack, as compared to the other two trials at higher temperatures. The extrusion force was greatly

reduced by increasing the extrusion temperature. More specifically, the force decreased to ~10 kN at 322 ˚C and 7-8 kN at 330 ˚C, respectively. The reduced extrusion force successfully prevented the graphite die from cracking and decreased the friction between the glass surface and graphite die.

The results show that the extrusion method is suitable for the preparation of bubble-free preforms, and that extruded rods typically exhibit a better surface finish than cast rods. The different surface finish between the extruded and cast rods can be understood by their different fabrication techniques: extruded preforms have a fire polished surface as the hot glass cools down in free space [199], whereas the hot cast glass rod during the casting procedure is in contact with the mold when cooling down (Fig. 4. 3).

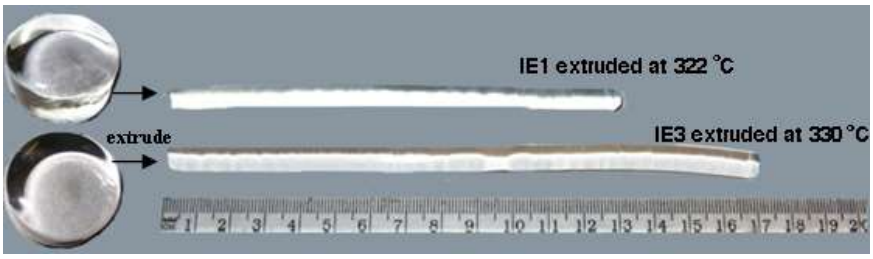

Figure 4. 3. Fluoroindate glass preforms extrude from billets.

Although no obvious surface wrinkle pattern and crystallisation were observed on the rods extruded at temperatures in the range of 322 to 330 ˚C under the optical microscope, the annealing test showed that a surface layer in the form of wrinkles most likely occurred at 330 ˚C (IE3). One possible reason for the difference between annealing and extrusion results is that the slides have a large free space and thus evaporation can occur, resulting in changes in surface composition and thus possibly facilitating surface wrinkle patterns. During extrusion, the majority of the bulk glass is encased in the sleeve, so evaporation at high temperature can only occur for the glass coming out of the die for only a short period of time, minimising the chance of surface crystallisation.

4.2.3. Glass flow analysis

For the IZSBGC fluoroindate glass, characteristic temperatures are around 307-308 ˚C for T_g and 385-389 ˚C for T_x (Table 3.3 in Chapter 3) depending on the melting conditions. In the previous work [200], preliminary extrusion trials were conducted at

317, 322 and 330 ˚C. Here, to identify the best die design and advance the understanding of temperature-viscosity behaviour and the impact of temperature on extrusion force and rod surface quality, extrusion trials were performed using different die designs and temperatures between 317 and 330 ˚C, which is ~60 ˚C lower than T_x = 389 ˚C determined by DSC in the previous work [200]. Therefore, after polishing or chemo-mechanical treatment (refer to 5.2.2.1 in Chapter 5) the cylindrical billets were extruded into rod-shape (cylindrical) preforms of 5-10 mm in diameter at temperatures in the range of the glass transition temperature (T_g = 307 ˚C) (Table 3.3 in Chapter 3) to T_g+23 ˚C under N_2 controlled atmosphere. Four types of graphite dies (a-d) with different die channel lengths and diameters (Table 4.3) were used to extrude unstructured rods. Die types (a) (8 mm die channel diameter) and (d) (5 mm die channel diameter) were used for extrusions of 65 g (batch weight) glass billets, whereas die types (b) and (c) were used for extrusions of ≥100 g (batch weight) glass billets.

Table 4. 3. Extrusion Parameters: Preform surface roughness, S_a and S_q, Extrusion temperature, T, Die Channel Diameter, D_1, Die Channel Length, L_1, Ram Speed, V_0, Ram Force, F, Slip coefficient, α, Glass viscosity η.[§].

Extrusion No	Melt No	Preform surface roughness		Die Type	T (˚C)	D_1 (mm)	L_1 (mm)	V_0 (μm/s)	F (kN)	α (mm)	log η (log Pa·s)
		S_a (nm)	S_q (nm)								
IE1	IM28	—	—	a	322	8	8	0.60	10.85	5.08	9.44 (± 0.06)
IE2	IM26	—	—	a	325	8	8	0.60	7.15	5.08	9.26 (± 0.04)
IE3	IM30	—	—	a	330	8	8	0.60	2.24	5.08	8.76 (± 0.03)
IE5	IM35	49.47 (± 5.68)	59.46 (± 10.83)	b	330	10	7	0.60	1.41	4.51	8.88 (± 0.04)
IE15	IM93	—	—	b	324	10	7	0.33	4.01	4.51	9.59 (± 0.05)
IE9	IM68	—	—	c	317	10	2	0.33	19.00	1.69	10.52 (± 0.03)
IE10	IM71	141.96 (± 14.22)	162.62 (± 6.96)	c	318	10	2	0.33	18.10	1.69	10.50 (± 0.03)
IE11	IM73	190.50 (± 10.90)	234.35 (± 21.65)	c	316	10	2	0.33	22.05	1.69	10.58 (± 0.03)
IE12	IM90	67.11 (± 7.20)	84.33 (± 7.61)	c	320	10	2	0.33	8.34	1.69	10.16 (± 0.05)

Table 4.3 (continued)

IE14	IM94	64.29 (± 1.88)	78.86 (± 0.96)	c	324	10	2	0.33	3.58	1.69	9.79 (± 0.04)
IE16	IM113	—	—	d	320	5	2	0.33	34.25	1.69	9.76 (± 0.06)

§: Note that only glass for IE16 was melted under condition (D)** and the glasses for the rest preforms were all melted under condition (C)*; For glass melting conditions please refer to Table 3.3; the surface roughness S_a and S_q are the average values by repeating measurements 3 times.

The extrusion trials were conducted at a fixed temperature and ram speed, while the extrusion force was adjusted by an automatic control loop to maintain the fixed ram speed. The extrusion force measured after the die was completely filled with glass (i.e., when the rod started to emerge from the extrusion die; Fig. 4.4) was used for calculations presented in Table 4.3. Other details of the extrusion set-up, die types and error analysis used in this work can be found in [200]. For analysis of the extrusion data in Table 4.3, errors for the viscosity values were obtained based on relative errors for the temperature measurements (0.90-0.95%) and ram force, F (3-17% in the region when a rod emerged from a die).

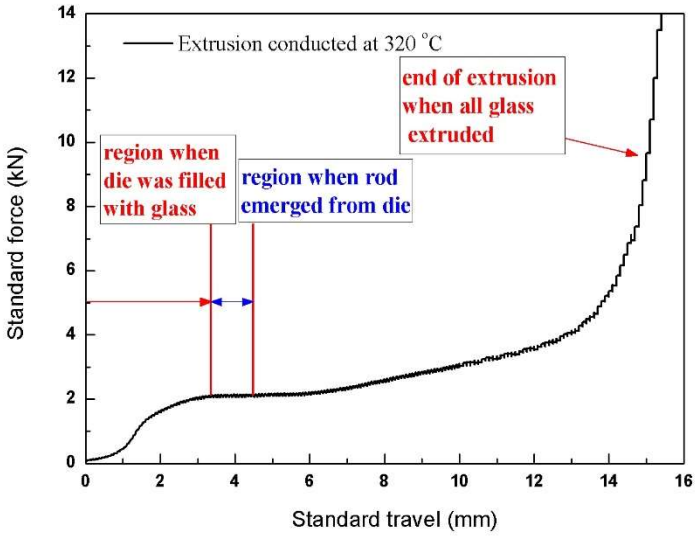

Figure 4. 4. Extrusion force profile for a fluoroindate extrusion trial using die (c) at 320 ˚C.

According to previously published results [200-202], it can be assumed that the extrusion flow of fluoroindate glass follows the Poiseuille law, and that the glass is a Newtonian fluid. Hence, the force or pressure required to extrude a glass through a circular die channel can be approximated by the following equation [200]:

$$P = \frac{128L_1}{\pi D_1^3 (D_1 + 8\alpha)} A_0 V_0 \eta \tag{4-1}$$

where subscript '0' and '1' refer to the billet and die, respectively, $P = F/A_0$ is the pressure P calculated from the measured force F and billet cross section area A_0, L_1 is the die channel length, D_1 is the die channel diameter, V_o is the ram speed, η is the glass viscosity, and α is the slip coefficient at the glass/die boundary.

According to Eq. (4-1) and assuming a constant slip coefficient, the extrusion pressure is proportional to the die channel length and the inverse of the fourth exponent of the channel diameter. Metal dies made from stainless steel or nickel alloys were found to have no slip ($\alpha = 0$, i.e. constant slip coefficient) when they were used for the majority of oxide glass extrusions [200, 202]. By contrast, graphite is a non-wetting material [202]. A slip at the glass/die boundary was observed previously by using graphite as an extrusion die material [200]. For extrusion of fluoroindate glass through graphite dies, it was found that with the shorter die channel in die (c), as compared to dies (a) and (b), the extrusion force did not decrease linearly with the die channel length, L_1, which cannot be explained by Eq. (4-1) assuming a constant slip coefficient. Analysis of published data on extrusion of silicate glasses through graphite dies with different die channel length [200] revealed that the slip coefficient decreased linearly with decreasing die channel length, and can be approximated by:

$$\alpha(mm) = 0.5557 + 0.5652 L_1(mm) \quad (R^2 = 0.950) \tag{4-2}$$

Equation 4-2 indicates that α decreases with L_1. Therefore, the extrusion force decreases with L_1 in a nonlinear manner in Eq. (4-1), which explains the nonlinear decrease of the extrusion force with L_1 in the extrusion of fluoroindate glasses. Assuming that the dependence of die channel length on the slip coefficient for IZSBGC glass/graphite die interface is equivalent to that for silicate glass/graphite die interface, Eq. 4-2 was used to calculate the slip coefficients for different die channel length for the extrusion trials (Table 4.3).

Once the slip coefficient α is known, Eq. (4-1) can be used to calculate the viscosity from the measured extrusion force and other parameters in the extrusion trials conducted using different temperatures and graphite die geometries [19]. Table 4.3 shows the experimental parameters used for this calculation and the calculated viscosities. In Fig. 4.5, the calculated viscosity values are plotted as a function of the inverse of the glass temperature for fluoroindate glass extrusion trials, assuming die temperature is equivalent to glass temperature.

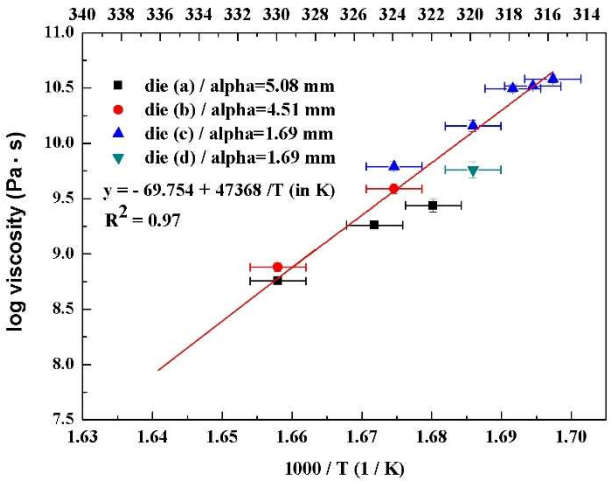

Figure 4. 5. Calculated viscosity values as a function of extrusion temperature.

The experimental viscosity data can be well fitted with a two-parameter Arrhenius equation in the temperature range of 317 and 330 ˚C [201] as shown in Fig. 4.5:

$$log\eta = A + B / T \tag{4-3}$$

where η is the viscosity (in Pa·s), T is the temperature (in K) and A and B are empirical constants. For the fluoroindate glass reported in this work, the Arrhenius equation of the temperature viscosity curve was determined from glass viscosity calculated from extrusion trials. The linear fitting of Arrhenius equation for the fluoroindate glass (IZSBGC) studied in this project yielded log η (in Pa·s) = -69.754 + 47368/T (in K) (Fig. 4.5).

To further confirm the calculation in Fig. 4.5, a thermal dilatometer was used to measure the deformation point of fluoroindate glass (Fig. 4.6) using 5 mm diameter rod piece which was melted under the same conditions as those for (D)** (using the InF_3 from Synquest, fluorination at 450 ˚C and melting at 900 ˚C) in Table 3.3. In Fig. 4.6, the dilatometric softening temperature (i.e. the temperature, at which a sample reaches maximum expansion in a length versus temperature curve during heating of the sample [203]) was measured to be 330 ˚C for fluoroindate glass (IZSBGC). Note that the viscosity at this dilatometric softening temperature corresponds to 10^8-10^9 Pa·s [203], which is in agreement with the viscosity at 330 ˚C in Fig. 4.5, determined using the extrusion trials. This suggests the calculated viscosities in Fig. 4.5 are reliable.

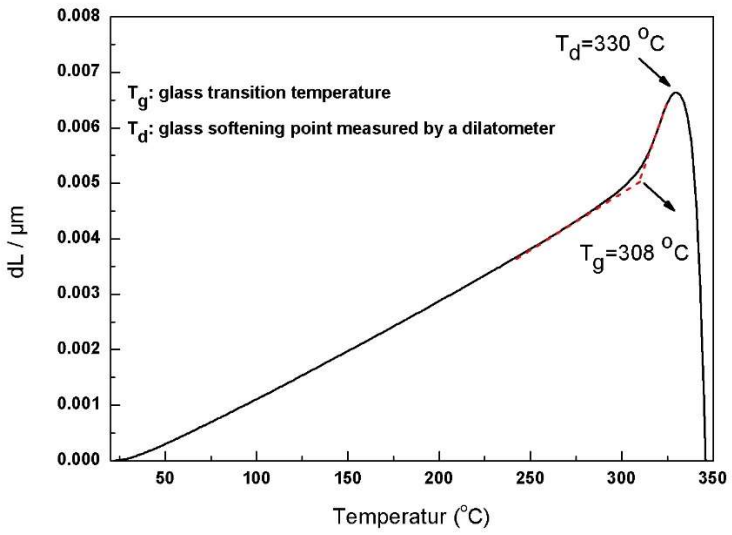

Figure 4. 6. Linear thermal expansion curve of IZSBGC sample obtained using 5 ˚C/min heating rate.

4.2.4. Surface quality analysis

The surface roughness results for extruded preforms (Table 4.3 and Fig. 4.7) demonstrate that the roughness decreases with increasing extrusion temperature, which was also reported for extruded polymer preforms [204]. There are several reasons that possibly account for this observation. Firstly, the surface is smoothened by fire-polishing at elevated temperatures during extrusion, i.e. at low glass viscosities [205]. The glass preform was still hot when it emerged from the die exit and moved slowly out of the hot zone, leading to fire-polishing of the preform surface. The fire-polishing process softened or melted the surface, which then deliquesced and rounded sharp edges, and also filled pits (e.g., scratches) due to lower viscosity [206]. Consequently, the fire-polishing resulted in a smoothed preform surface with reduced surface roughness. The effects of fire-polishing will become more prominent with increasing temperature, thus leading to a smoother preform surface as the extrusion temperature increases.

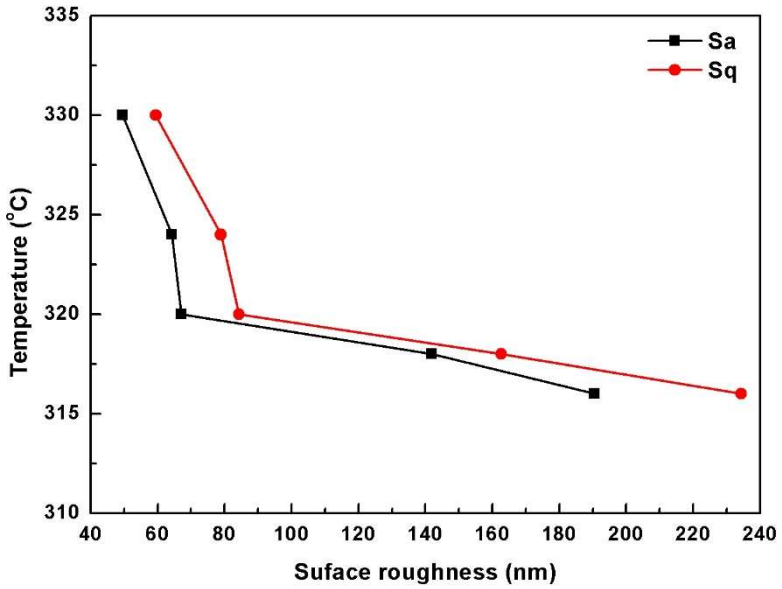

Figure 4. 7. Surface roughness of extruded preforms as a function of extrusion temperature.

Secondly, a certain degree of slip occurred at the fluid/solid interface for a partly wetted interface. For a Newtonian fluid, there exists a general nonlinear relationship between the amount of slip and the local shear rate at a solid surface [207]. The velocity gradient (shear rate) in viscous fluid flow generates a tangential force (mechanical shear stress) which is proportional to the viscosity when the fluid is under shearing [208]. When the temperature increases, the extrusion can be achieved at a lower viscosity with a lower shear stress. The lower shear stress, therefore, reduced the shearing at the graphite die surface, leading to reduced surface roughness and improved glass surface finish (e.g., less extrusion stripes). It also reduced the shearing of the graphite particles that could contaminate the glass surface, thereby improving the glass surface quality. Furthermore, higher extrusion forces can lead to changes in the slip behaviour at the fluid/die interface, which can result in melt fracture extrusion instabilities and increase the extruded preform's surface roughness [209]. Low extrusion forces at high extrusion temperatures are therefore desired to improve the surface roughness of extruded glass preforms.

4.3. Conclusions

The annealing tests on fluoroindate glass demonstrated that a temperature of 330 ˚C for preform extrusion could cause potential surface crystallisation, whereas 322 ˚C for

extrusion was sufficiently low to avoid potential surface crystallisation. The preform surface properties including surface roughness and crystallisation of extruded fluoroindate glass rods essentially depended upon the extrusion temperature. A relatively high temperature reduced the extrusion force, which minimised graphite shedding, cracking of dies and slip instabilities between glass and die surface. The fire-polishing effect became prominent with increasing temperature, thus leading to a smoother preform surface as the extrusion temperature increased. Both these effects were found to be essential to minimization of rod surface roughness. However, even for rods with good surface finish, sufficiently high temperature eventually resulted in surface crystallisation. In this study, the optimum temperature for extrusion was found to be around 322 ˚C. Therefore, to achieve a low extrusion force and eliminate shear-induced surface roughness with no glass surface crystallisation, the extrusion temperatures of 320-322 ˚C were chosen for fiber drawing trials in the next chapter.

Chapter 5

UNSTRUCTURED FIBRE FABRICATION [3]

The presence of surface crystallisation (e.g., white precipitates) and roughness on preforms and fibres, which are major scattering centers, caused high fibre loss and low fibre strength. The aims of the study in this chapter are therefore to investigate the impacts of fibre drawing conditions and surface treatment on the fibre scattering loss, and to improve mechanical strength of unstructured fluoroindate glass fibres.

5.1. Experimental details of fibre drawing

The cast rod (IM6; Table 3.3) was polished using 1 μm Al_2O_3 powders to remove the orange peel surface formed during casting.

Compared with previous publications [210, 211], 15 wt% $HCl_{(aq)}$ solution (vs. 37% in the literature) was used on IE3 (Fig. 4.3) for preliminary chemical etching for about 25 min (stirring applied) at a reasonable etching rate at room temperature to remove a ~0.5 mm thick outer layer, followed by a short rinse with methanol in an ultrasonic bath. However, this method resulted in a significant white layer giving rise to a high loss.

To further improve the surface quality of the cast billets and extruded preforms and compare with the previous method used on IE3, mechanical polishing and/or a new chemical etching methodology specifically for IZSBGC glass surface treatments were applied. More specifically, after glass melting, cylindrical billets were polished using 3

[3] The majority of this Chapter has been published in journal paper I and II in "Published papers".

μm diamond pastes and then suspension of 40 nm colloidal silica, which can produce scratch-free surfaces [212, 213]. For comparison purposes, some of the billets and/or preforms for chemical etching were suspended in a 1.36 M $ZrOCl_{2(aq)}$ solution (with stirring applied) at room temperature for about 30 min to remove a ~0.5 mm thick outer layer, followed by a rinse in methanol in an ultrasonic bath for 30 min and final hand polishing with 40nm colloidal silica solution (hereafter referred to as chemo-mechanical treatment). After etching, the preform was rinsed with methanol for 30 min and then dried using a N_2 gas gun.

All preforms (including surface treated and non-surface treated) were cleaned by isopropyl alcohol in an ultrasonic bath for 30 min prior to fibre drawing then pulled into unstructured fibres with diameters ranging from 130 to 180 μm under N_2 controlled atmosphere at feeding rate of 1.4 mm/min which is also used for ZBLAN glass fibre fabrications. The induction heating furnace used in the fibre drawing tower comprises a cylindrical graphite ring, which acts as the susceptor and therefore the heat source of the furnace. In this study, two types of graphite susceptors with the same inner and outer diameters but different heights (2 cm or 4.5 cm-long) were used to explore the impact of the furnace working temperature and the maximum preform temperature for fluoroindate glass fibre fabrications. For some preforms, an additional weight of ~190 g was applied to the bottom of the preforms during fibre drawing to decrease the temperature at which a drop is formed.

5.2. Results and Discussion

5.2.1. Preliminary fibres drawing from preforms prepared by casting and exrusion methods

The unstructured optical fibre drawn from IE1, extruded at 322 ˚C, was successfully obtained with a diameter of approximately 140 μm and without any evidence of crystallisation (Fig. 5.1). This unstructured fibre exhibited lower fibre loss of ~1.9 dB/m at 1550 nm (Fig. 5.2) compared with the fibre made from the cast rod (Table 5.1). This can be explained by reference to the improved surface finish and the lack of larger bubbles

in the extruded preform, although the loss was still higher than other reported fluoroindate glass fibres (e.g., step index fibre fabricated by rotational casting [100]).

Table 5. 1. Glass rod / preform preparation conditions and results of the fibre loss.

Sample	Diameter of rod/preform (mm)	Glass melting condition§	Fabrication Method	Surface Treatment	Fibre Loss at 1550 nm (dB/m)
IM6	10	(A)*	Direct Casting	Mechanical Polishing	42.3
IE1 (extruded from IM28)	8	(C)*	Extruded @ 322 ˚C (±1 ˚C)	Clean by Isopropyl Alcohol Ultrasonic Bath for 30 min	1.9

§: For glass melting conditions please refer to Table 3.3.

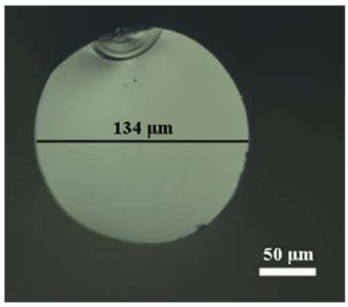

Figure 5. 1. Microscope image of the fibre drawn from the preform IE1 extruded at 322 ˚C.

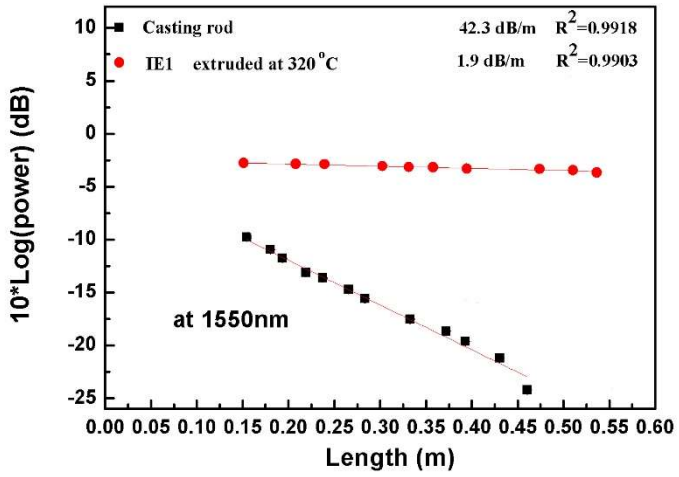

Figure 5. 2. Loss measurements at 1550 nm for fibres made using different methods. Linear fittings of the data are also shown in the figure.

5.2.2. Reduction of scattering loss of fibres drawn from extruded preforms

In order to reduce the loss of extruded preforms, the impact of a range of surface treatment and fibre drawing conditions was investigated (including chemo-mechanical treatment, expansion of heating zone length to decrease the maximum preform temperature, use of additional weight, and the extrusion temperature). During fluoride fibre drawing, one of the most important aims is to minimise surface crystallisation of the preform neck-down, because experiments have shown that this surface crystallisation significantly correlates to degraded mechanical strength in the drawn fibres and increases fibre loss for air-clad (i.e., unstructured) fibres and air/glass microstructured fibres [120]. Table 5.2 summarises the experimental details of fibres IF4, 13, 12, 17, 18, 15 and 19 drawn from extruded preforms under different conditions, and presents results of fibre surface roughness and fibre spot loss measurements at 1550 nm. To investigate the correlation between fibre loss and surface roughness, the surface roughness and loss of an unstructured fibre (made from commercial F2 lead-silicate glass; Table 5.2) without surface crystallisation were also measured as a benchmark for comparison purpose.

Table 5. 2. Fibre drawing conditions, results of spot loss measurements and surface roughness of fibres IF4, IF13, 12, 17, 18, 15 and 19.

Fibre No	Extrusion No	Melt No	Glass melting condition §	Extrusion Temperature (˚C)	Surface treatment	Susceptor (cm)	Additional weight (g)	Preform roughness		Fibre surface roughness		Spot loss at 1550 nm (dB/m)
								S_a (nm)	S_q (nm)	S_a (nm)	S_q (nm)	
IF4	IE3	IM30	(C)*	330	15 wt% HCl	4	0	---	---	---	---	31.2 (R^2=0.948)
IF13	IE12	IM90	(C)*	320	none	2	0	67.1 (± 7.2)	84.3 (± 7.6)	172.0 (± 77.0)	223.0 (± 103.0)	27.8 (R^2=0.962)
IF12	IE12	IM90	(C)*	320	Preform	2	0	67.1 (± 7.2)	84.3 (± 7.6)	149.0 (± 29.0)	205.0 (± 38.0)	20.1 (R^2=0.996)
IF17	IE19	IM118	(D)**	320	Preform	4.5	0	71.6 (± 7.9)	90.4 (± 8.6)	13.8 (± 4.1)	15.9 (± 4.4)	7.8 (R^2=0.972)
IF18	IE20	IM121	(D)**	320	Preform	4.5	190	66.2 (± 5.9)	80.8 (± 6.8)	10.5 (± 1.1)	15.2 (± 3.8)	4.1 (R^2=0.993)
IF15	IE17	IM114	(D)**	320	Billet/preform	4.5	190	20.5 (± 4.1)	33.7 (± 5.3)	9.3 (± 1.8)	12.9 (± 2.3)	3.6 (R^2=0.958)
IF19	IE21	IM122	(D)**	322	Billet/preform	4.5	190	14.7 (± 2.2)	18.8 (± 3.4)	9.1 (± 0.4)	12.8 (± 1.9)	2.3 (R^2=0.999)
F2† fibre			—	560	—	4.5	0			8.0 (± 0.8)	12.0 (± 1.2)	—

§: For glass melting conditions please refer to Table 3.3.

†: Commercial F2 glass billet (outer diameter: 30 mm) was used to fabricate extruded preform and unstructured fibre.

Chemical etching has been demonstrated to improve fluorozirconate glass surface quality and hence reduce surface crystallisation [214]. Thus, the impact of etching on fluoroindate glass surface crystallisation was investigated during fibre drawing.

The surface layer for IE3 extruded at 330 ˚C (prone to form wrinkle patterns at this temperature, which is discussed in Chapters 4.2.1) would result in increasing amounts of crystals at elevated temperatures during the fibre drawing procedure, which would ultimately increase loss and decrease mechanical strength of the fibre made from this rod. This can be explained by the increasing amount of surface defects or the slightly different composition between the surface layer and volume glass after extrusion [198], resulting in different thermal expansion coefficients of the surface and volume glasses, and thus creating surface wrinkle patterns or crystals during fibre drawing. Thus, chemical etching was applied to IE3 to remove the surface layer on the preform surface. To evaluate the efficacy of preform etching, the surface roughness of the preform before and after etching were determined using AFM (Fig. 5.3). During the extrusion procedure, extrusion stripes, which can be seen on the preform surfaces (shown in inset optical micrograph of Fig. 5.3a), were most likely caused by the friction between the glass surface and graphite die. On the preform surface without white precipitate, the maximum roughness in the stripe regions dramatically decreased after etching, while the average roughness did not change obviously after etching (Fig. 5.3). SEM-EDS analysis (Fig. 5.4) showed that the white precipitate was composed of metal halides (F^- and Cl^-). EDS analysis also suggested that the chlorine ions from the etchant (i.e., $HCl_{(aq)}$) can co-precipitate with ions leached out from the glass matrix. XRD indicated that the white precipitate contained crystalline $(Sr_{0.19}Ba_{0.81})FCl$ (Fig. 5.5). It is clear that etching using solely 15 wt% $HCl_{(aq)}$ solution is not an effective way to improve the surface quality. However, the reduction of the surface roughness in the stripe regions (when no precipitate was present) indicates that etching will improve the surface quality and remove defects associated with preform extrusion once the etchant is further optimised, overcoming the issue of precipitate formation.

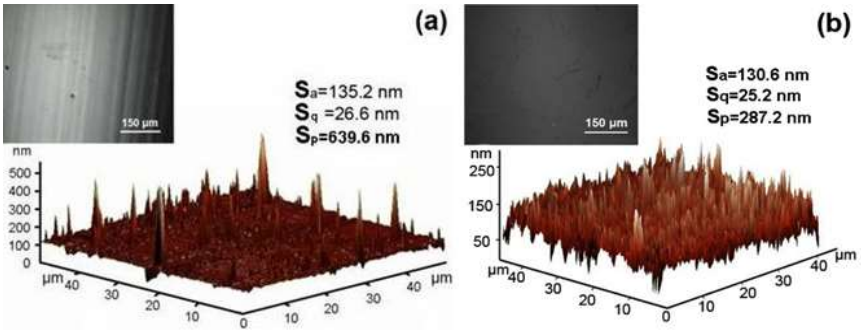

Figure 5. 3. AFM morphology of IE3 surface (a) before etching; (b) surface without white precipitate after etching by 15 wt% $HCl_{(aq)}$. Insets are optical microscope images of the IE3 surfaces before and after etching.

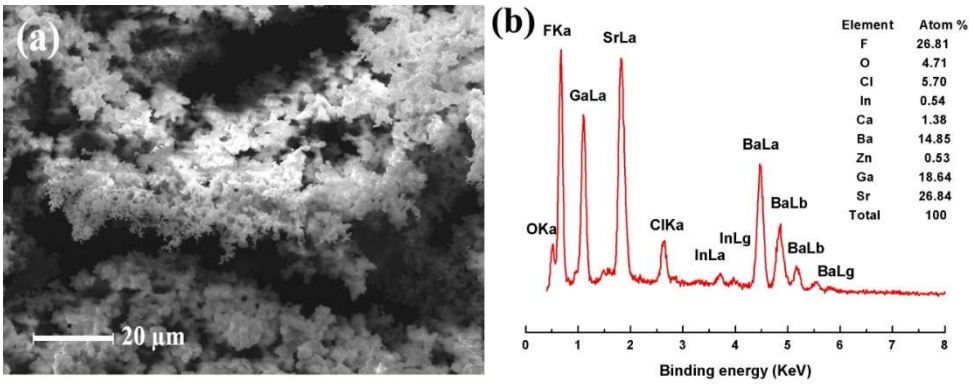

Figure 5. 4. (a) SEM secondary electron image and (b) EDS analysis of the white precipitate formed after 15 wt% $HCl_{(aq)}$ etch.

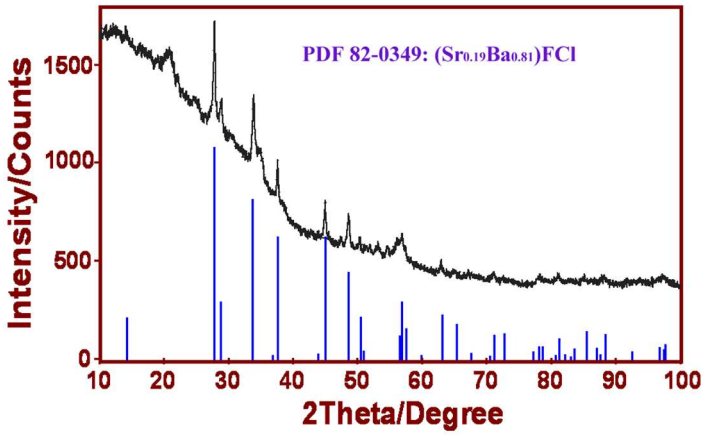

Figure 5. 5. XRD result of the white precipitate after 15 wt% $HCl_{(aq)}$.

Although chemical etching was applied to IE3 extruded at 330 ˚C, the resultant fibre (IF4) exhibited a relatively high loss (Table 5.2), which is attributed to the occurrence of the white precipitate on the etched preform. The precipitate resulted in surface crystallisation

during fibre drawing, which caused scattering centers on the fibre surface and is reflected by the relatively poor linear regression (R^2=0.96).

To further study surface treatment effects on fibre drawing, the published etching solution recipe, i.e., 0.4 mol $ZrOCl_2 \cdot 8H_2O$ in 1L 1N HCl for ZBLAN glasses [129] was used for IE10 (Table 4.3). It resulted in the formation of a white layer on a glass preform during etching; however, when the new etching solution (1.36 M $ZrOCl_{2(aq)}$) specifically developed for IZSBGC glass (Table 5.3) was used, white layers were not observed on the preform (immersed in etching solution) during the etching process. A few regions of light white layers were, however, found on the dried and etched billet or preform surface. Hence, etched billets or preforms were polished with a 40 nm colloidal silica suspension to remove white layer formed during etching. This chemo-mechanical treatment was applied to some glass billets and preforms before fibre drawing. A preform extruded at 320 ˚C was cut into two pieces that were used for IF13 and IF12 fibre drawing trials using 2 cm heating zone. The difference between the two fibre drawing trials was that the IF12 preform was etched with 1.36 M $ZrOCl_{2(aq)}$ to remove a ~0.5 mm thick outer layer and then polished with 40 nm colloidal silica suspension, while the IF13 preform remained unetched. Surface roughness measurements of the IF12 preform before and after chemo-mechanical treatment revealed that the average roughness dramatically decreased from 70 to 7 nm (Fig. 5.6).

Table 5. 3. Etching solution studied for fluoroindate glass.

No.	Etching solution	White layer during etching
1	15 wt% $HCl_{(aq)}$ (4.86 M $HCl_{(aq)}$)	++++++++++
2	0.4 mol $ZrOCl_2 \cdot 8H_2O$ in 1L 1N HCl	++++++++
3	0.4 mol $ZrOCl_2 \cdot 8H_2O$ in 1L 1.5 N HCl	++++++++++
4	0.4 mol $ZrOCl_2 \cdot 8H_2O$ in 1L 0.5 N HCl	+++++++
5	0.8 mol $ZrOCl_2 \cdot 8H_2O$ in 1L 1N HCl	+++++++
6	0.8 mol $ZrOCl_2 \cdot 8H_2O$ in 1L 0.5N HCl	++++++
7	0.8 mol $ZrOCl_2 \cdot 8H_2O$ in DI water, 1L solution (0.8 M $ZrOCl_{2(aq)}$)	++++
8	1 mol $ZrOCl_2 \cdot 8H_2O$ in DI water, 1L solution (1 M $ZrOCl_{2(aq)}$)	++
9	1.36 mol $ZrOCl_2 \cdot 8H_2O$ in DI water, 1L solution(1.36 M $ZrOCl_{2(aq)}$)	Not found

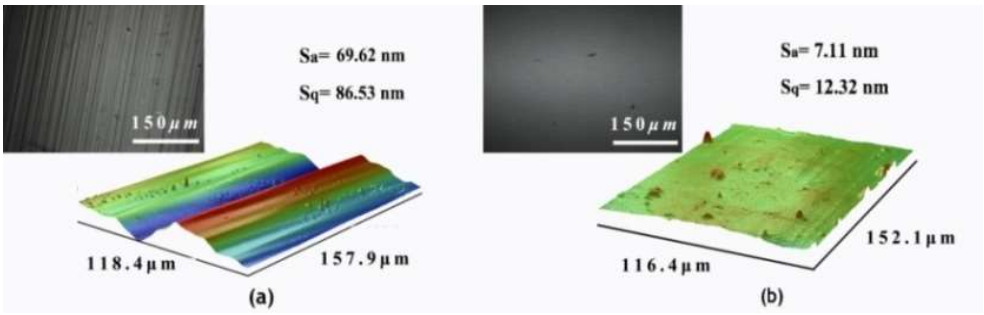

Figure 5. 6. Optical interferometric profiler images (colored images) of preform surface for IF12 fibre drawing (a) before chemo-mechanical treatment; the data in (a) is one of the measurements used for the surface roughness calculation of IE9 preform, Table 5.2; (b) after chemo-mechanical treatment. Images in grey scales in (a) and (b) are optical microscope images of the preform surfaces before and after chemo-mechanical treatment.

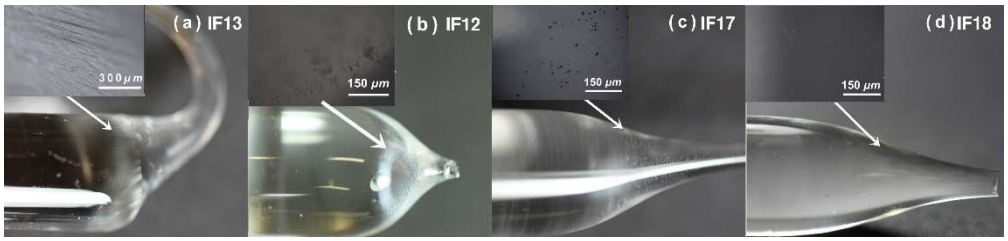

Figure 5. 7. Surface images of the fibre drop neckdown of IF13, 12, 17 and 18.

To investigate the effect of the chemo-mechanical treatment on the preform during fibre drawing, IF13 and IF12 preform neck-down surfaces were examined under an optical microscope (Fig. 5.7). During fibre drawing, re-heating of the IF13 preform resulted in the formation of corrugation patterns on the surface of the preform neck-down (Fig. 5.7(a)). This corrugation pattern is attributed to surface crystallisation during glass re-heating. In contrast, no corrugation patterns were observed on the IF12 preform neck-down (Fig. 5.7(b)) except for several small crystal spots on the surface. The fibre surface roughness of IF12 was reduced to 149 ± 29 nm (S_a), as compared to 172 ± 77 nm (S_a) for IF13 (Table 5.2). This clearly indicates that the chemo-mechanical treatment applied to IF12 preform effectively reduced surface crystallisation during fibre drawing.

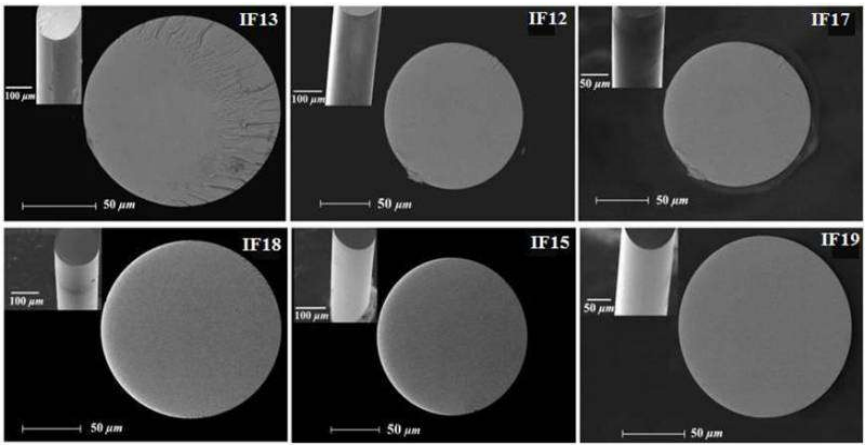

Figure 5. 8. Scanning electron microscopy images of fibre surfaces and cross-sections (IF13, 12, 17, 18, 15 and 19).

In Fig. 5.8, SEM analysis shows the features of the cross-sections and the surface of fibres IF13, 12, 17, 18, 15 and19. All these fibres were cleaved at a tension as low as possible to prevent a surface wrinkle pattern, which was otherwise observed to occur at high tensions. In addition, each fibre was cleaved at least 20 times to ensure that fibre surfaces (Fig. 5.8) were reproducible and representative. For all the cleaved surfaces of IF13, the fibre cross-section shows fracture patterns that resemble a surface wrinkle pattern (Fig. 5.8(a)). It is likely that this fracture pattern arises from surface crystallisation and propagated rapidly when the fibre is fractured [214]. For IF12 fibre, the chemo-mechanical treatment of the preforms before fibre drawing resulted in significantly reduced surface wrinkle patterns (Fig. 5.8(b)).

For the IF12 fibre, surface crystallisation was reduced but not completely suppressed, as demonstrated by observation of crystal spots on the preform neck-down. To further reduce surface crystals, longer heating zone was applied as described in chapter 5.2.

In a fibre-drawing furnace, the temperature that controls the furnace temperature is usually measured at a point close to the heat source (in this thesis, the heat source is called as “susceptor”). For a fibre drawing furnace, the susceptor length correlates with the length of the heating zone according to the temperature profiling results in Appendix II. To investigate the impact of increased heating zone length on surface crystallisation for fluoroindate glass fibres (IZSBGC) a larger susceptor length of 4.5 cm for IF17 was used to compare with 2 cm-long susceptor for IF12. IF17 was drawn at a furnace temperature being ~75 ˚C lower than that of IF12. This confirms that, for a longer heating zone, a

lower maximum temperature can be used to form a preform drop. The length of neck-down of IF17 was observed to be elongated compared to that of IF12 (Fig. 5.7), consistent with results by Sakaguchi et al. [120], indicating lower maximum glass temperature. Although the neck-down surface of IF17 contained similar small crystal spots compared with those of IF12 (Fig. 5.7), the number of spots was significantly reduced. SEM images revealed that the surface wrinkle patterns of IF17 were greatly suppressed (Fig. 5.8c). In addition, the fibre surface roughness (S_a) was reduced from 149 ± 29 nm for IF12 to 13.7 ± 4.1 nm for IF17 (Table 5.2). These results demonstrate a decrease in surface crystallisation for IF17, due to the reduced maximum preform temperature of IF17 combined with reduced temperature gradient along the drawing axis as a result of the longer heating zone used for IF17 than that for IF12.

For IF18, an additional weight was applied at the bottom of its preform to decrease the glass temperature required to form a drop during fibre drawing. The decreased glass temperature also reduced the surface crystallisation rate (without wasting a significant length of the preform). The fibre drop temperature for IF18 decreased by 15 ˚C in comparison with IF17. No crystallisation was found on the neck-down of IF18 on inspection with an optical microscope (Fig. 5.7 (d)). Both surface roughness of IF18 (Table 5.2) and surface wrinkle patterns of cleaved fibre cross-section (Fig. 5.8) were reduced due to the reduced crystallisation of the fibre surface. Note that all billets for IF13, 12, 17 and 18 were polished mechanically.

For comparison, chemo-mechanical treatment was applied to IF15 and IF19 billets before extrusion. The only difference between IF15 and IF19 was that the preforms for these two fibre drawing trials were extruded at different temperatures (320 ˚C for IF15 and 322 ˚C for IF19). Compared with the fibre surface roughness of IF18 and IF15, the chemo-mechanical treatment of IF15 billet before extrusion slightly improved the IF15 fibre surface quality and resulted in a reduced surface roughness relative to IF18 (Table 5.2). The improved fibre surface quality of IF15 is attributed to an improved billet surface quality after chemo-mechanical treatment, superior to use of only mechanical billet polishing before extrusion (for IF13, 12, 17 and 18). Chemo-mechanical treatment of the billet for IF15 removed surface micro-cracks and micro-scratches before extrusion, thereby enabling IF15 to have a lower fibre surface roughness. IF19, which was fabricated from a preform extruded at 322 ˚C, exhibits the lowest surface roughness (Table 5.2) of all fluoroindate fibres fabricated, and no surface wrinkle patterns were found on this fibre

cross-section (Fig. 5.8f). It is also the longest fibre obtained in this work with a length of 38 m. These results are attributed to the better surface quality of the IF19 preform by extruding the preform at 2 ˚C higher than those used for extrusion of IF13, 12, 17, 18 and 15, resulting in a lower force for extrusion of IF19 preform. As discussed above, lower force results in an improved preform surface quality, which finally leads to improved fibre surface quality.

The spot loss measurement results at 1550 nm shown in Table 5.2 and Fig. 5.9 are consistent with the broadband fibre loss measurement results (Fig. 5.9). Note that no fibre of IF13 with adequate length was available for broadband loss measurements to be performed after spot loss measurement, due to low production yield of this fibre. The broad absorption band at 1000 nm of IF12 (Fig. 5.9) is thought to be due to absorptions from 3d transition metals (e.g., Fe^{2+}, Co^{2+}, Cu^{2+}) from the raw materials used for IF12. Both spot loss and broadband fibre loss results demonstrate that the loss is remarkably decreased from IF13, 12, 17, 18, 15 to 19, which correlates with reduction of the fibre surface roughness. As IF13 and IF12 were made from the same billet and preform, the lower loss of IF12 compared with IF13 demonstrates that the loss is determined by surface scattering due to surface roughness caused by surface crystallisation. Similar correlation is observed for IF17, 18, 15 to 19 made from glass using melting condition (D)** (InF_3 from Testbourne, fluorination at 235 ˚C and melting at 900 ˚C as shown in Table 3.3). The reduction of surface crystallisation from IF13, 12, 17, 18, 15 to 19 resulted in a smooth fibre surface with low surface roughness, which effectively reduced light scattering and thus fibre loss.

IF19, which has the lowest loss in the near-infrared region of all fibres investigated in this work, also exhibited low loss in the mid-infrared region; the fibre loss of IF19 at 2, 4, 5 μm was measured to be 2.0, 1.5 and 2.2 dB/m, respectively (Fig. 5.10). The lowest loss of 1.3 dB/m was located at 2.7 μm. In comparison, an unstructured ZBLAN fibre, which was made using commercial raw materials with comparable purity, fluorination with NH_4HF_2 at 235 ˚C, identical controlled atmosphere melting facility and the extrusion technique for preform fabrication, demonstrated a similar fibre loss of 1.1 ± 0.5 dB/m at 4.0 μm [114].

A 2 m-long fibre with 1.9 dB/m (R^2=0.992) fibre loss at 1550 nm was drawn from an un-etched preform (IE3), while IF19 with 2.3 dB/m (R^2=0.999) was obtained with a length

of 38 m. The significantly larger fibre yield for IF19 is attributed to the higher fibre drawing stability achieved. This is believed to be due to the improvements in the fibre fabrication conditions, resulting in the suppression of fibre surface crystallisation during fibre drawing. Although chemical etching and additional weight were applied to prevent crystallisation during fibre drawing in this work, IF19 exhibited a slightly higher fibre loss of 2.3 dB/m compared to the previously obtained fibre with 1.9 dB/m. This can be explained by the relatively high levels of impurities in the raw materials used for IF19 (ZnF_2: 99%; BaF_2: 99.99%) in comparison with IF1 (ZnF_2: 99.9%; BaF_2:99.999%). Those high purity raw materials used in the previous work for this project are no longer available for purchase.

To further study the correlation between fibre loss and surface roughness, the fibre surface roughness of an unstructured F2 soft glass fibre was measured. Ref [113] demonstrated that the loss of air-clad and air/glass microstructured fibres was dominated by surface scattering associated with surface roughness compared with the loss of the bulk material, and that extruded F2 glass fibres showed the same loss as that of the F2 bulk glass within the measurement errors. This indicates that the surface roughness of unstructured F2 fibre is so low that it does not contribute to fibre loss. The indium fluoride fibre IF19 shows a surface roughness of 9.1 ± 0.4 nm (S_a), which is very close to the F2 fibre surface roughness of 8.0 ± 0.8 nm (S_a). This result confirms that the reduced surface roughness from IF13, 12, 17, 18, 15 to 19, due to reduced surface crystallisation, leads to a decrease in light scattering and hence reduces fibre loss both in spot loss and broadband fibre loss measurements. The decreased surface roughnesses of fibres probably result from the improved surface quality of preforms (Table 5.2) using optimum extrusion temperature.

The fibre breaking strains gradually increased from IF13, 12, 17, 18, 15 to 19 (Table 5.4 and Fig. 5.11), which correlates with the observed decrease in fibre surface roughness (Table 5.2). A smooth fibre surface without defects (e.g. crystals) is, unsurprisingly, an important characteristic of high strength fibres [120]. The enhanced breaking strain of the fibres from trial IF13, 12, 17, 18, 15 to 19 is attributed to the reduced surface roughness due to the reduced crystallisation on the fibre surfaces during fibre drawing via improvement of the preform and fibre fabrication conditions.

Table 5. 4. Fibre strain of Trial IF13, 12, 17, 18, 15 and 19.

	IF13	IF12	IF17	IF18	IF15	IF19
Mean of measured radius (μm)	62.34	83.23	71.85	84.28	88.25	77.21
Mean of calculated strain (10^{-3})	4.49	4.94	5.29	6.21	7.43	10.54
The standard deviation of calculated strain (10^{-3})	1.90	1.69	1.34	1.10	0.93	0.79

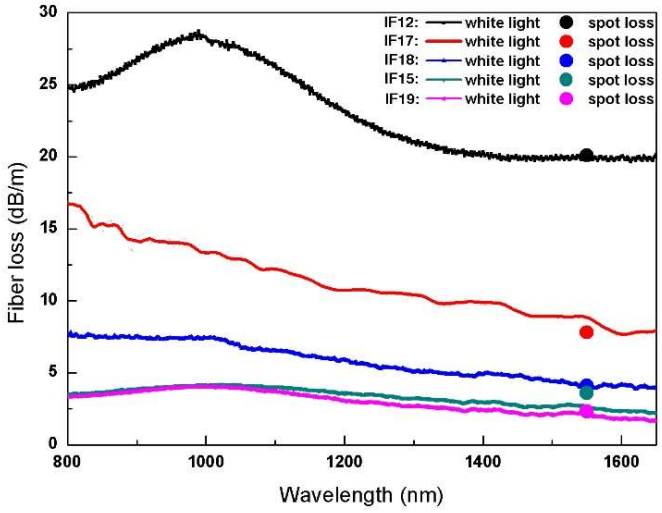

Figure 5. 9. Fibre loss spectra and spot loss measurement results at 1550 nm of IF12-6.

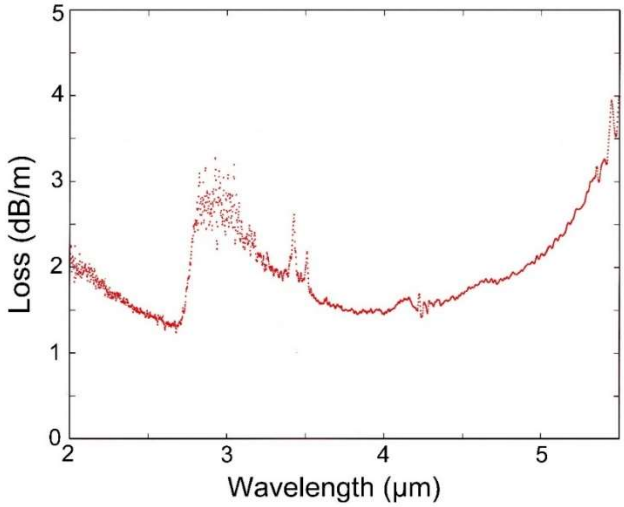

Figure 5. 10. FTIR loss spectrum of IF19 in the wavelength range of 2 – 5.5 μm (Alexander Hemming[4] measured).

[4] Affiliation: Cyber and Electronic Warfare Division, Defence Science & Technology Group, Edinburgh, SA 5111, Australia

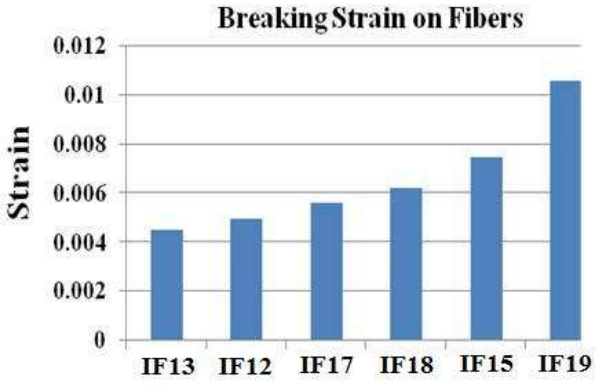

Figure 5. 11. Breaking strain of IF13, 12, 17, 18, 15 and19.

Figure 5.12 shows that the significant reduction in surface roughness of the fibres through improvement of various fabrication conditions led to a considerable decrease in fibre loss and increase in fibre strength (indicated by high bending strain).

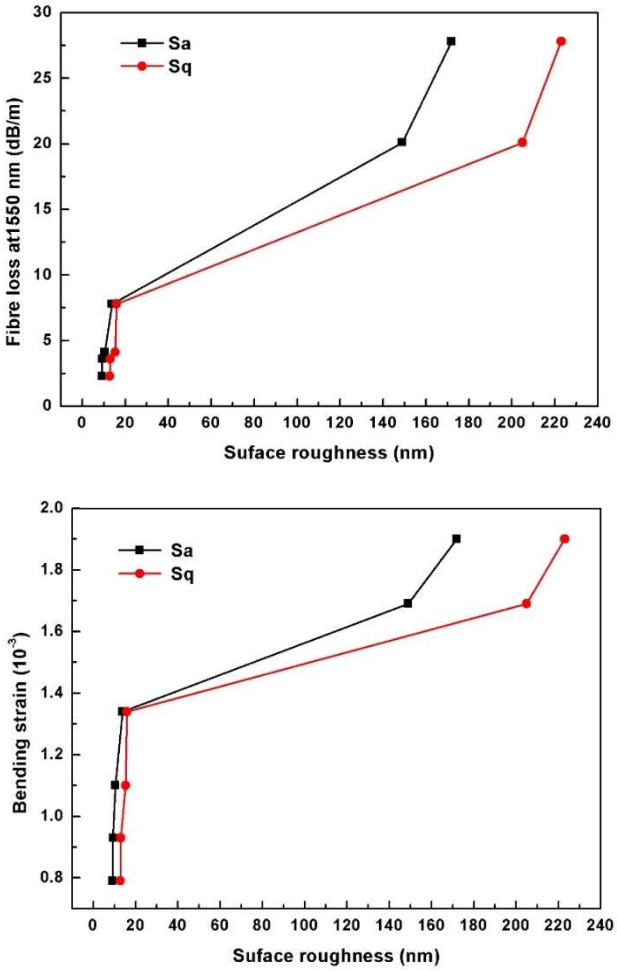

Figure 5. 12. Fibre loss and bend strain as a function of the surface roughness of the fibres.

5.3. Conclusions

Fibres drawn from preforms (prepared using the extrusion technique) had a lower fibre loss compared to the fibre drawn from the cast rod (IM6). This significant decrease in fibre loss is attributed to the better surface finish and reduced quantity of the bubbles in the extruded preforms. The absence of crystallisation in the preform extruded at 322 ˚C resulted in the lowest loss of the corresponding fibre. The formation of a white precipitate during etching procedure shows that 15 wt% $HCl_{(aq)}$ solution is not an effective etching method to improve the IZSBGC glass preform surface quality and hence reduce fibre loss. This Chapter described factors responsible for scattering loss in fluoroindate glass fibres. The results showed that this systematic refinement of the glass and fibre fabrication processes reduced the fibre loss by an order of magnitude: from 27.8 dB/m to 2.3 dB/m at 1550 nm. This improvement is attributed to the reduction in fibre surface roughness achieved by optimising the melting, preform and fibre fabrication conditions. The maximum fibre drawing temperature was reduced by expanding the length of the heating zone in the drawing furnace. The chemo-mechanical treatment of billets and preforms reduced the surface crystallisation observed on the preform neck-down and fibres at the elevated temperatures experienced during fibre drawing. Surface crystallisation was completely suppressed by using additional weight at the bottom of preforms.

In conclusion, a novel and feasible approach was achieved, for the first time, to fabricate fluoroindate glass rod preforms suitable for fibre drawing using the extrusion technique. The fibre surface roughness due to surface crystallisation was reduced by optimising the preform and fibre drawing conditions (including the extrusion temperature; chemo-mechanical treatment; expanding the heating zone length to decrease the maximum preform temperature; additional weight). This also reduced the loss of the fabricated fibres and increased fibre strength from trial IF13, 12, 17, 18, 15 and 19. Furthermore, the improved fibre drawing conditions significantly increased the yield of low-loss fibre (~1.5 dB/m at 4 μm wavelength in the mid-IR region) from a 2 m achieved in fibre drawn from IE1 to 38 m for IF19 in this work. However, the fluoroindate fibre IF19 has a significantly lower fibre loss of 1.8 dB/m at 4.7 μm because fluoroindate glasses have longer multi-phonon edge wavelengths (> 4.7 μm) [200] compared to ZBLAN (<4.7 μm) [114]. The fibre loss value of the lowest-loss fibre (the fibre drawn from IE1 with a fibre loss of 1.9 dB/m at 1550 nm) in this project is still higher than that of commercially available

fluoroindate glass fibre. This is potentially due to the purity of the commercially available raw materials (99.9~99.99%) used for fibre fabrications, which often contain transition metals and oxide impurities, limiting the reduction of extrinsic absorption loss in fibres. The impurity levels can be reduced by purification of commercial raw materials via sublimation and distillation [215].

Chapter 6

EXPERIMENTAL STUDY OF THE CHEMICAL DURABILITY OF FLUOROZIRCONATE AND FLUOROINDATE GLASSES IN DEIONIZED WATER[5]

The aim of this study was to investigate the chemical durability of both fluorindate (IZSBGC) bulk glasses and glass fibres against that of the widely studied fluorozirconate (ZBLAN) system. The chemical durability of glasses and fibres is an important parameter to examine, as glass/fibre samples are often exposed to moistures (i.e. H_2O) in air during application, and their properties, such as strength and optical transmission, may deteriorate over time. The glass durability was studied by investigating leaching of glass samples in deionized water, rather than in air, to ensure that appreciable reaction extents can be observed within a reasonable laboratory timescale. The leach process involves dissolution/release of certain components from a sample into a liquid. The chemical durability of IZSBGC fibres is particularly important, as poor chemical durability can limit their practical application. Therefore, it is essential to understand the corrosion process and chemical durability of these glasses to guide the development of improved fibre materials or methods for the protection of these fibre materials.

[5] The majority of this Chapter has been published in journal paper III in "Published papers".

A series of analyses were carried out using analytical techniques such as FTIR, XPS and SEM to study the sample surfaces (before and after leaching) and hydrated layer products, both of which reflected the nature of leaching (i.e. dissolution or corrosion) process.

6.1. Experimental details of leaching in deionized water

The preparation of IZSBGC glass (IM86) was carried out under the same conditions as those for IM68 (refer to Table 3.5 in Chapter 3). The preparation of fluorozirconate glass included batching, melting at 850 ˚C (2.5 h) and casting at 650 ˚C using high purity raw materials (5N for BaF_2 and AlF_3; 4N for LaF_3 and NaF; 3N for ZrF_4). The same glass melting facility with controlled dry atmosphere was used for preparation of both ZBLAN and IZSBGC glasses.

In this work, ZBLAN and IZSBGC (IF19) fibres drawn from preforms with 110 mm and 140 mm length, respectively, were used for leaching experiments. The fibre diameter was 156±8 μm for ZBLAN and 176±13 μm for IZSBGC. Both fibres were drawn with a preform feed rate at 1.6 mm/min. The draw tower furnace temperatures, which were higher than the glass temperatures [115], were maintained at 665 ˚C and 725 ˚C for ZBLAN and IZSBGC fibre drawing, respectively.

Leaching experiments were conducted in HDPE (high density polyethylene) containers using only deionized water (pH ~5.60) at the beginning of the leaching experiments at 25±2 ˚C. Fluoroindate and fluorozirconate glass samples were cut into ~2 mm thick slides which were then polished using ~3 μm diamond pastes and ~40 nm colloidal silica to obtain scratch-free surfaces [212].

A commercial FTIR spectrometer (refer to Chapter 2) was used to measure the IR transmission of glass slides after leaching in deionized water at various reaction times. The cross-sections of the glass slides after leaching were imaged by a scanning electron microscope described in Chapter 2. One glass slide for both ZBLAN and IZSBGC glasses was fractured in a glove box filled with N_2 (99.99 %). One part of the fractured glass slide was stored in an air lock container (filled with N_2) prior to analysis of the fractured surface using X-ray photoelectron spectroscopy (XPS). The second part of the fractured slide was immersed in deionized water for 30 min and then stored in an air lock container (filled with N_2), prior to XPS analysis on the fractured/leached surface. The Zr 3*d* spectrum was

fitted using the $3d_{3/2}$ and $3d_{5/2}$ doublet with a 2:3 ratio and an energy separation of 2.43 eV. The FWHM (full width at half maximum) for Zr $3d_{3/2}$ was set to the same value as that for Zr $3d_{5/2}$.

To determine the pH change of the deionized water during the course of leaching experiments, the pH was measured using a temperature-corrected pH Meter (Metrohm 827), with errors of ±0.05. Calibrations were carried out using standard buffers from Metrohm.

6.2. Results and Discussion

6.2.1. Infrared spectroscopic studies

The water-glass interaction for HMF glasses can be studied by IR absorption and assessed by the change in OH^- stretching (2.9 μm) and HOH bending (6.1 μm) vibrations [130]. The bending mode of HOH at 6.1 μm can be attributed to water molecules present within a thin hydrated layer on the surface [60]. The stretching mode of OH^- at 2.9 μm is thought to be due to OH^- in both bulk glass and glass surface [125, 216].

Figure 6.1 shows the absorption coefficients of ZBLAN and IZSBGC glasses exposed to water at 25± 2 ˚C for various reaction times. After reaction with water, both the ZBLAN and IZSBGC glass surfaces were found to be covered by opaque films to varying degrees, under which somewhat cloudy but still translucent surface layers could be discerned. Both OH^- stretching and HOH bending vibrations were observed with an increase in absorption for ZBLAN and IZSBGC glasses from ~30 mins leaching onwards (up to 90 min; Fig. 6.1a and 6.1b), indicating that hydrated layers formed in the leaching processes altered the glass surface properties [132]. The OH^- stretching vibration peak grew slightly faster than the HOH bending peak for both glass types after leaching. However, the absorption coefficient of IZSBGC glass at 2.9 and 6.1 μm increased more slowly than that of ZBLAN glass (Fig. 6.1c and 6.1d), suggesting that hydrolysis reaction of the former was slower. In previous studies [132, 160, 217, 218], incorporation of alkali glass modifiers into fluoride glasses such as Li and Na fluorides with high aqueous solubilities increased their leaching rates. For example, the high content of NaF in fluorozirconate glasses increased their glass corrosion rate for all glass components [74] compared to other fluorozirconate

glasses without NaF (e.g., ZBLA). As discussed above, the slower increase in absorption coefficient for IZSBGC glass at 2.9 and 6.2 μm in this work, compared to ZBLAN glass, is likely due to the absence of alkali glass modifiers (as opposed to 20 mol% NaF in the ZBLAN glass). Another possible reason is that ZrF_4 is an undesirable component from the viewpoint of glass durability, because of its higher solubility in water (1.32-1.39 g/100ml in water at room temperature; [136]) as compared to that of InF_3 (0.04 g/100ml in water at room temperature; [135]).

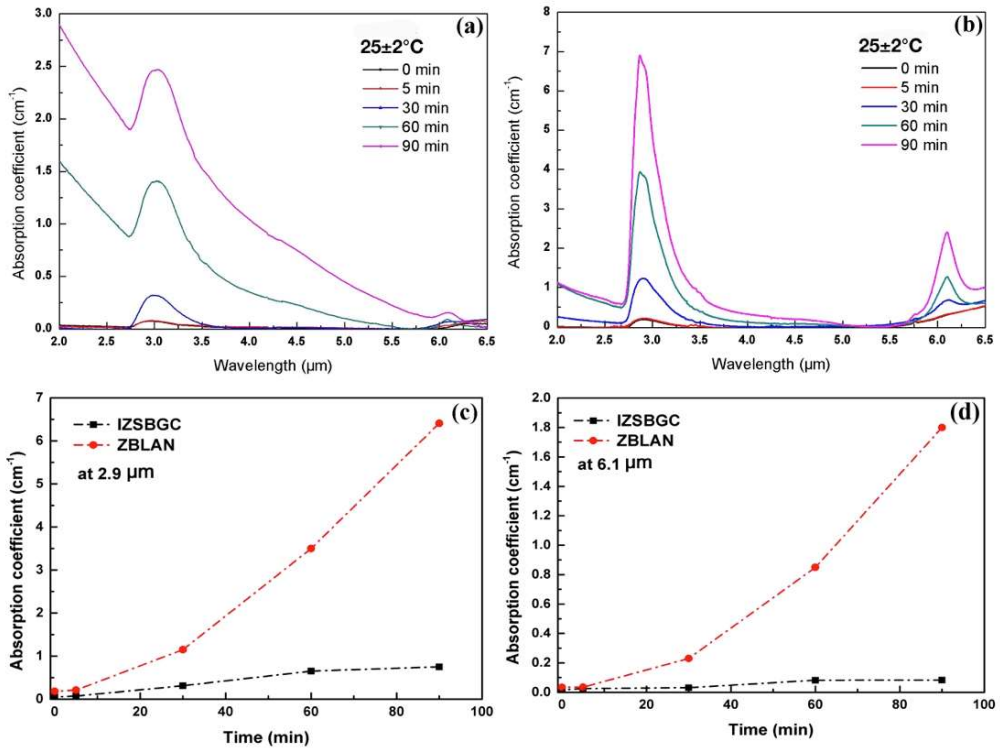

Figure 6. 1. Absorption coefficient of (a) IZSBGC and (b) ZBLAN after leaching in deionized water at 25±2˚C. Change of absorption coefficients for both glass types at (c) 2.9 μm and (d) 6.1 μm.

6.2.2. pH study of corrosion solution

During the course of the leaching experiments, the pH of the aqueous solutions (originally at ~5.60 for deionized water prior to leaching) all decreased (Fig. 6.2). The pH drift is attributed primarily to hydrolysis reactions [132]. In the very early stage of corrosion in stagnant solution (within 0.5 day), fluorides near the fresh glass surface undergo an appreciable hydrolysis associated with ion exchange between F^- and OH^- [132]. As a consequence, OH^- substitutes for F^- near the glass surface structure [132], leading rapidly to a pH decrease. In this work, after leaching for 0.5 day (Fig. 6.2), the pH drifted from

5.60 to 2.93 and 3.20 for leaching of ZBLAN and IZSBGC glasses, respectively, indicating that the pH decreased significantly into a more acidic range for both glass types after the initial leaching period (within 0.5 day). Similar results were found in an earlier study of hydrolysis reaction of fluorozirconate by Le Toullec et al. [125]. The reduced pH increased markedly the solubility of the fluoride glass components (i.e., metal fluorides), resulting in the leaching process occurring primarily via matrix dissolution as described in a study of dissolution of fluorozirconate glasses in Eq. (6-1) [60]:

$$MF_n(gl) \rightarrow MF_x^{(n-x)+}(aq) + (n-x)F^-(aq) \tag{6-1}$$

As the leaching proceeded to release cations and fluorine ions, leaching solutions became saturated with respect to the least soluble metal fluorides first, causing their precipitation on the fluoride glass surfaces and forming hydrated layers [130].

Leach experiments were run for 8 days for both ZBLAN and IZSBGC. pH for leaching of both glasses decreased significantly in the initial 12 h (0.5 day), after which the variations in pH were relatively small.

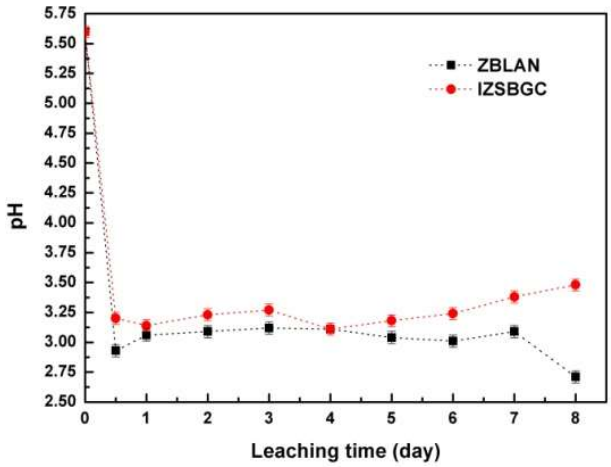

Figure 6. 2. pH values of deionized water solutions after different leaching time (error bars are smaller than data symbols).

6.2.3. Scanning electron microscopy study

The SEM images below (Figs. 6.3 and 6.4) show the formation of corrosion layers on ZBLAN and IZSBGC glasses after leaching in deionized water for different reaction times. The leached ZBLAN glass exhibit multi-layered products with different

compositions after leaching for > 0.5 day (Fig. 6.3). Spherical particles observed from 4 days onwards (Fig. 6.3) consisted of a multitude of thin platelets containing Zr and Ba, as confirmed by EDS analysis (Table 6.1). The spherical particles formed within Layer 1 were also found on the outermost surfaces after leaching for 4 and 6 days (Fig. 6.3). Polyhedral and spherical particles formed on the outermost surface were previously identified as $ZrF_4 \cdot XH_2O$ and $ZrBaF_6 \cdot XH_2O$ crystals, respectively [132], consistent with the compositions found in this work (Table 6.1). Compared to ZBLA glass after leaching in deionized water reported in [130], ZBLAN glasses studied in this work produced more porous hydrated layers (Fig. 6.3). In a previous study by Simmons et al. [132], it was proposed that a glass with high alkali content formed a thick and porous de-alkalized layer that can be easily dissolved. Similarly, a reduction in alkali content (e.g., ZBLA glass with no NaF vs. ZBLAN with high content of NaF) resulted in a decrease in the porosity of the hydrated layer [130]. In this work, the leach rate for IZSBGC without NaF slowed down compared to ZBLAN glass with high content of NaF. Clearly the variation in glass compositions after leaching resulted in different amounts of porosity formed in the leached samples, which in turn affected the leach rate.

Table 6. 1. Semi-quantitative analysis measured using EDS for multi-layer compositions for ZBLAN glass after 6 days corrosion in deionized water (in at.%) *.

	F	**Zr**	**Ba**	**La**	**Al**	**Na**
Spherical particles	29.10	24.37	40.39	3.50	1.10	1.54
Polyhedral particles	17.31	50.23	26.61	3.39	1.19	1.27
Layer1	25.42	31.80	21.96	16.41	0.86	3.55
Layer2	19.52	37.93	33.38	6.92	1.66	0.59
Layer3	28.80	34.94	24.34	8.61	1.06	2.25
Layer4	30.86	35.18	23.07	6.24	1.40	3.25
Bulk glass	30.97	39.45	16.23	3.74	2.42	7.19

*O content obtained from EDS analysis was excluded during normalisation in this Table to place emphasis on the metal and fluorine contents.

The hydrated layers formed in the IZSBGC glass (Fig. 6.4 and 6.5) had similar cation compositions to that of the original un-leached glass. Leaching for 2 days or longer resulted in an obvious gap between the formed layer and the reacted glass (e.g., 4 days in

Fig. 6.4). The size of this gap increased as the leaching progressed. The formed thin layers on IZSBGC glasses had numerous pores on the micron scale. The increased Ba content at Position 10 in Fig. 6.5 was probably due to the formation of a very thin Ba-rich layer (~1 μm) on the etched glass surface [129].

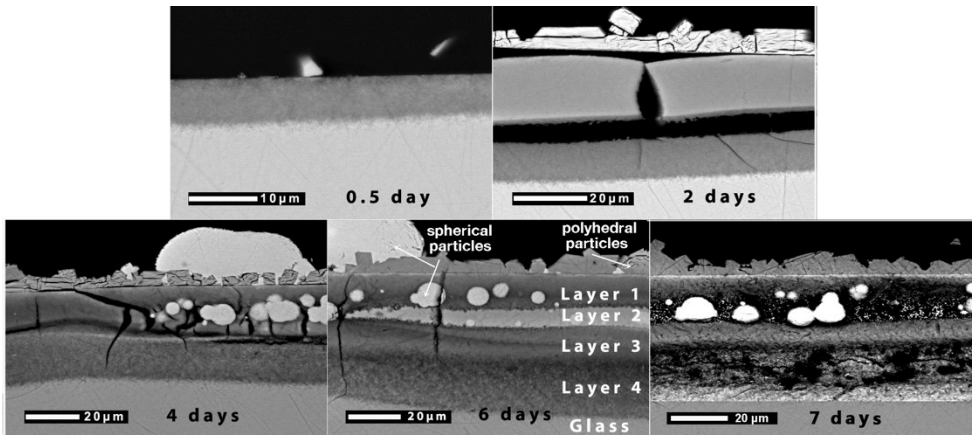

Figure 6. 3. Formation of multiple hydrated layers on ZBLAN glass during corrosion tests in deionized water.

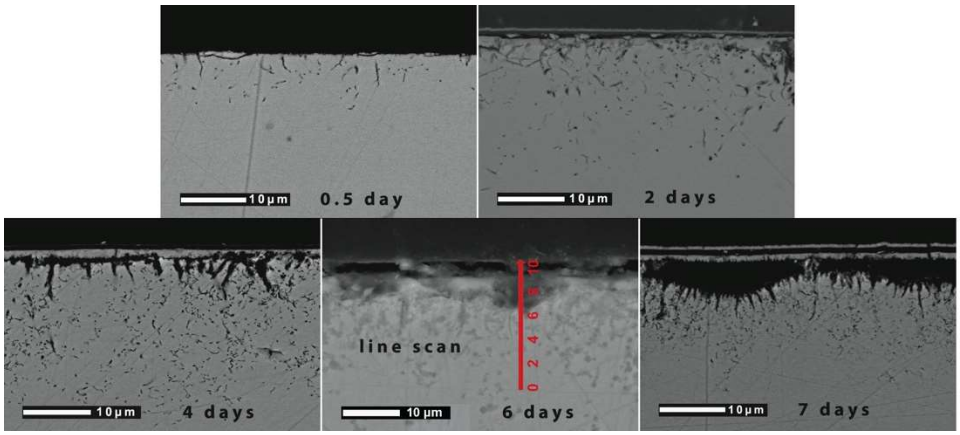

Figure 6. 4. Formation of multiple and hydrated layers of IZSBGC glass during corrosion test in deionized water.

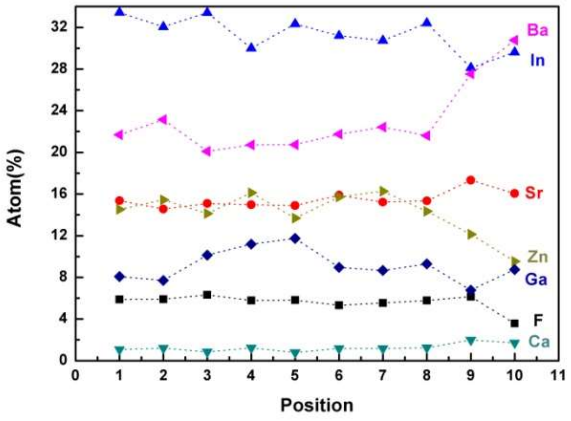

Figure 6. 5. EDS analysis for line scan (red line in Fig. 6.4) of the IZSBGC glass after leaching for 6 days in deionized water.

The thickness of the hydrated layer for both glass types generally increased with reaction time (Fig. 6.6). The results determined in a previous dissolution study of ZBLA glass [130] were employed in this study for comparison purpose. For all three glasses, the thickness increased rapidly at the beginning but much more slowly in the subsequent leaching. Within the experimental time scale investigated, no equilibrium state was reached for ZBLAN glass (i.e., thickness of the hydrated layer increased throughout the leaching in Fig. 6.6), suggesting that leaching was progressing, while equilibrium was almost established for IZSBGC and ZBLA glasses (i.e., thickness of the hydrated layer 'levelled off'). The leaching of IZSBGC glass slowed down from 4 days (Fig. 6.6), which may be partly due to the slight increases in pH (Fig. 6.2). In comparison, the relative large decreases (Fig. 6.2) in pH for the leaching of the ZBLAN glass at 7 days may result in the marked increase in its leach rate (a sharp increase in the hydrated layer thickness; Fig. 6.6). The porosity in the hydrated layer facilitated the leaching solution to pass through the layer to further react with the glass surface. However, the IZSBGC glass layers after leaching appeared to be less porous compared to the ZBLAN glass layers. This is possibly because the hydrated layers of IZSBGC glass may play a role in preventing the molecular water from diffusing through the layer into the unreached glass surface. This could also be another possible reason as to why the leaching of the IZSBGC glasses in deionized water occurred more slowly. Measurement of the thickness of the hydrated layers showed that the hydrated layer was less than 20 μm after leaching for 7 days for the IZSBGC glasses (Fig. 6.6), while the hydrated layer for ZBLAN was greater than 50 μm. Compared to ZBLA glass with no NaF, ZBLAN with a high NaF content had a much thicker hydrated layer (due to the higher solubility of NaF in water [219] than other

fluoride components), while IZSBGC glass had a slightly thinner porous hydrated layer structure. Therefore, the main difference in the hydrated layer between IZSBGC and ZBLAN glasses is likely attributed to the presence of NaF in ZBLAN glass.

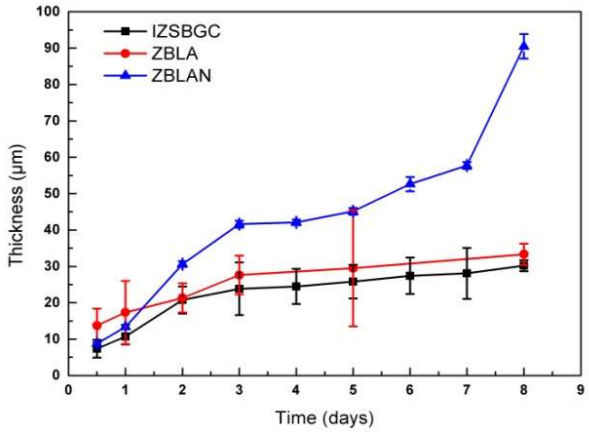

Figure 6. 6. Thickness of the hydrated layer of IZSBGC, ZBLA [130] and ZBLAN versus corrosion time in deionized water.

6.2.4. X-ray photoelectron spectroscopic study

Fractured surfaces of fluoroindate and fluorozirconate glasses before and after leaching in deionized water were studied using X-ray photoelectron spectroscopy. Analysis of high-resolution Zr 3*d* and In 3*d* spectra for fresh fractured surfaces of ZBLAN and IZSBGC glasses (Figs. 6.7 and 6.8), respectively, indicated that only zirconium or indium fluoride species existed on the glass surfaces, suggesting that the fractured glass surfaces were not oxidised. The high-resolution Zr and In 3*d* XPS spectra before and after leaching in deionized water (Figs. 6.7 and 6.8) revealed the most important aspects and variations of the glass surface chemistry. It can be seen that the Zr 3*d* peaks ($3d_{5/2}$ and $3d_{3/2}$) in Fig. 6.7 (top) observed on the reacted surface were broadened and somewhat shifted towards the lower binding energy, as compared to the fresh surface before leaching in deionized water. Fittings of the high resolution Zr 3*d* spectrum indicated formation of a new Zr(hydr)oxyfluoride species on the surface. The Zr 3*d* binding energy of this (hydr)oxyfluoride species was interpreted on the basis of its Pauling charge [127]. It is proposed that Zr(hydr)oxyfluoride is produced in aqueous solutions via attack of Zr-F bonds by molecular water. Similar to the Zr 3*d* peaks in ZBLAN glass, the In$3d_{5/2}$ peak was broadened and a shoulder peak appeared at the lower binding energy after leaching in the deionized water (Fig. 6.8). This shoulder peak was thought to be $In(OH)_3$ at a lower

bonding energy (444.9 eV [220]), a hydrolysis product from reaction with deionized water. The results in Figs. 6.7 and 6.8 further confirmed that hydrolysis reaction occurred in the leaching process, in good agreement with the FTIR and SEM findings. It is interesting to note that XPS analyses found no Na on the reacted surface of ZBLAN glass. Similarly, no Ca was found on the reacted IZSBGC glass surface. This is presumed to be due to the Na and Ca being preferentially dissolved during the leaching processes. The formation of hydroxide and oxyfluoride on the glass surfaces after leaching in deionized water for 30 mins also supports the concept of the ion exchange between F^- and OH^- in the initial stages of leaching (Section 6.2.2).

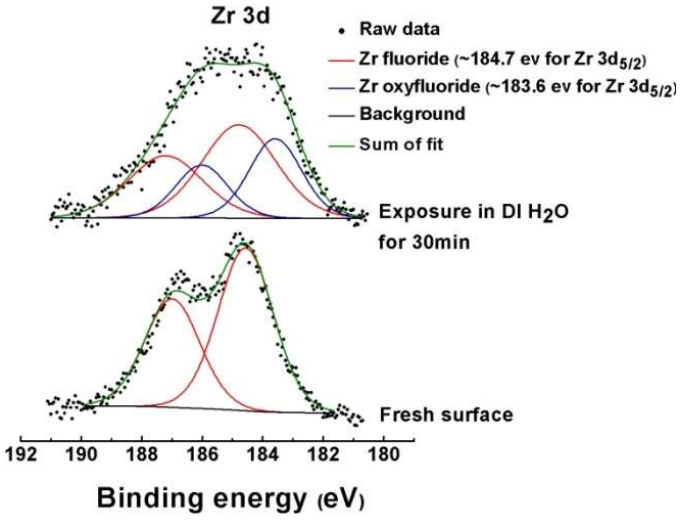

Figure 6. 7. High resolution Zr 3*d* spectra for a fresh fracture surface (bottom) and a hydrated surface (top).

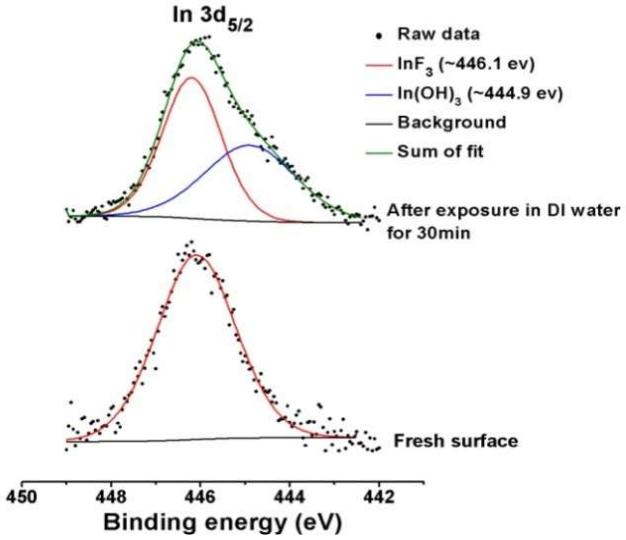

Figure 6. 8. High resolution In $3d_{5/2}$ spectra for a fresh fracture surface (bottom) and a hydrated surface (top).

6.2.5. ZBLAN and IZSGBG fibre strain and SEM study before and after corrosion

Chemical corrosion processes exert a strong influence on the strength and fracture behavior of fluoride glasses, not only in bulk samples but also in fibre forms. Previously published works have shown that surface and bulk crystal formation during fabrication of both preforms and fibres cause degradation in fibre strength [120, 129, 215].

Fibre breaking strain measurements were conducted before and after leaching in deionized water. It was found that the fibre breaking strain after leaching in deionized water only changed slightly after leaching for 30 mins and that the fibres were too fragile to allow breaking strain measurements due to the heavy surface crystals after leaching in deionized water for 90 mins. Therefore, the leaching time (in deionized water) was set to 45 mins for the fibre strain measurements. The ZBLAN fibres exhibited heavier opaque films on the surfaces than those on the IZSBGC fibre surfaces after leaching in deionized water. The fibre breaking strain results shown in Fig. 6.9 and Table 6.2 demonstrated that the average breaking strain of the IZSBGC fibre was reduced by 32%, which was lower than that of the ZBLAN fibre (39%). It suggests that the degradation in fibre strain for ZBLAN was greater than that for IZSBGC fibre, in agreement with the results in the preceding sections showing that ZBLAN has a relatively poor chemical stability.

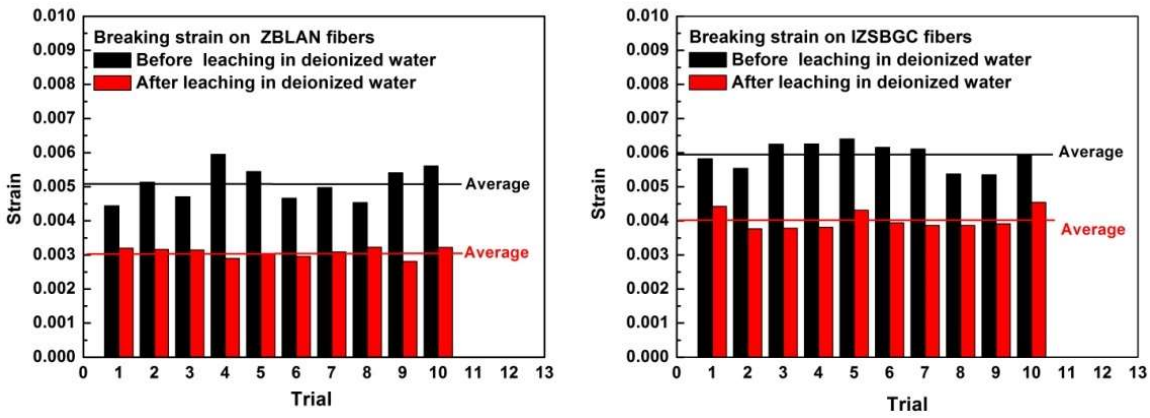

Figure 6. 9. Fibre breaking strains before and after leaching in deionized water for ZBLAN (left) and IZSBGC (right) fibres.

Table 6. 2. Comparison of fibre breaking strains before and after leaching in deionized water for ZBLAN and IZSBGC fibres.

Glass	Breaking strain on fibres				
	Before leaching in deionized water		After leaching in deionized water for 45 mins		Reduction (%)
	Average	σ	Average	Σ	
ZBLAN	0.0051	0.0005	0.0031	0.0001	39%
IZSBGC	0.0059	0.0004	0.0040	0.0003	32%

6.2.6. SEM study on cleaved fibre surface before and after corrosion

At a low fibre strength level, fracture surfaces of broken fibres with mirror-mist-hackle patterns have been observed [214, 221-223]. It is likely that this fracture pattern arises from surface defects and propagated rapidly when the fibre is fractured [214]. Compared to the fibre surface before leaching in deionized water, the obvious mirror-mist-hackle patterns occurred on both ZBLAN and IZSBGC fibre surface after leaching in deionized water for 45 mins, which suggested the formation of surface product layers or porous defects as reflected by the findings in Figs. 6.3 and 6.4. In Fig. 6.10, the fibre surfaces after leaching showed obvious defects, in contrast to the original glasses (Fig. 6.10a vs. Fig. 6.10b; Fig. 6.10c vs. Fig. 6.10d). These microscopic flaws led to the low breaking strains of the fibres, confirmed by the fibre breaking strain measurements.

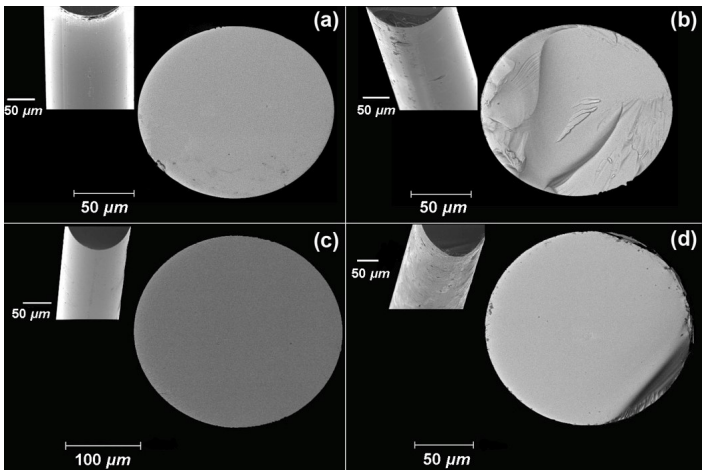

Figure 6. 10. Scanning electron microscopy images of fibre surfaces and cross-sections: (a) ZBLAN fibre before leaching in deionized water; (b) ZBLAN fibre after leaching in deionized water; (c) IZSBGC fibre before leaching in deionized water; (d) IZSBGC fibre after leaching in deionized water.

6.3. Conclusion

A comparison between absorption coefficients at 2.9 and 6.2 μm for both glass types after leaching in deionized water showed that the intensities of OH stretching and HOH bending vibration peaks of IZSBGC glass increased more slowly than those of ZBLAN glass. The results suggest that dissolution of the glasses occurred initially via an ion exchange between F^- and OH^-, decreasing the pH of the leaching solution. Subsequently, the solubility of metal fluorides increased dramatically due to the decreasing pH, leading to dissolution of the glass matrices. SEM studies suggested that the reactions occurred on the glass surfaces and that hydrated layers developed on both IZSBGC and ZBLAN glass surfaces. The NaF-free fluoride glass, IZSBGC, had thinner and less porous hydrated layers than the NaF-containing fluoride ZBLAN glass. This indicates that hydrolysis reaction of NaF-free fluoride glass was slower than NaF-containing fluoride glass, in agreement with previous findings on NaF-free ZBLA glasses [82]. Therefore, the fluoride glasses IZSBGC studied here were shown to be more stable against deionized water in comparison with NaF-containing glasses. The negative effect of NaF on the chemical durability was clearly demonstrated by the much more rapid leaching (thicker hydrated layers) of ZBLAN than that of ZBLA, which is supported by XPS observations with no Na found on the ZBLAN surfaces after leaching. XPS studies suggested that (hydr)oxyfluoride or hydroxide species were formed on the ZBLAN and IZSBGC glass surfaces after leaching in deionized water, respectively. FTIR, SEM and fibre breaking strain measurements showed that NaF-free fluoride glass IZSBGC presented better mechanical and chemical stability against water than NaF-containing ZBLAN glass. Although ZBLAN glass presented poorer stability against water than ZBLA glass due to the content of NaF, the former has been widely studied and used as fibre material because of its better crystallisation stability than ZBLA glass [82]. The NaF-free IZBSGC glass investigated here, however, exhibited not only extended IR transparency but also improved resistance against deionized water compared to the NaF-containing ZBLAN glass. This work advances the understanding of the corrosion behaviour of IZSBGC glass relative to the established ZBLAN glass in deionized water, and will assist with optimisation of the glass compositions to enable low-loss fibre with good chemical durability.

Chapter 7

STEP INDEX FIBRE FABRICATION

This chapter focuses on step index (core/clad) optical fluoroindate glass fibre fabrications. The fluoroindate glass in this study was doped with rare earth elements, with the aim of developing a fibre laser at ~4 μm. The doped fluoroindate glass composition is based on the base glass $32InF_3$-$20ZnF_2$-$20SrF_2$-$18BaF_2$-$8GaF_3$-$2CaF_2$ (in mol %) (IZSBGC). As lasers at transitions in mid-infrared range occurring in the rare earth ions Pr^{3+}, Dy^{3+}, Ho^{3+} and Er^{3+}, they were chosen as doping elements for investigation of their optical properties in fluoroindate glasses. Judd-Ofelt theory was applied to determine the Ω_t (t=2, 4, 6) parameters, lifetime and branching ratios of different emitting levels. Glass refractive indices were altered to produce two similar materials with slightly different indices of refraction for the core and cladding. Several fibre fabrication methods were tried, aiming at developing the capability to fabricate step index optical fibres from fluoroindate glasses for fibre laser application at ~4 μm.

7.1. Experimental procedures

All glasses in this study were melted in a platinum alloy crucible containing 5 % gold (internal volume: 100 ml). Rare earth (RE) ions were incorporated to substitute for InF_3 in samples IM47-50 (Table 7.1). These glasses were synthesised from commercial raw materials (5N for BaF_2 and InF_3, 4N for CaF_2, GaF_3, ErF_3 and HoF_3, 3N for SrF_2, ZnF_2, PrF_3 and DyF_3) using the same melting procedures as for IM18 (Table 3.1, Section 3.2.1, Chapter 3). These four samples were mainly used for Judd-Ofelt calculation. Besides, to create the higher refractive index required for the core and cladding glasses, IM95

($32InF_3$-$20ZnF_2$-$20SrF_2$-$16BaF_2$-$8GaF_3$-$2CaF_2$-$2PbF_2$) (Table 7.4) was synthesised from commercial raw materials (5N for BaF_2 and CaF_2, 4N for $InF_3 \cdot 3H_2O$ and SrF_2, 3N for PbF_2, 2N for ZnF_2, 1N for GaF_3) using the same melting procedure as for sample IM25 as per Table 3.3. All other samples of this study (Table 7.4) were synthesised using commercial raw materials (5N for and CaF_2, 4N for BaF_2, 3N for SrF_2, PrF_3 and PbF_2, 4N for InF_3, 2N for ZnF_2, 1N for GaF_3) with relatively high levels of impurities (4N) for InF_3, (2N) ZnF_2 and (1N) GaF_3 compared to raw materials with 5N purity used before. Therefore, a small amount of NH_4HF_2 (2.4 wt% of the batch weight) was used to fluorinate the impurities (refer to the melting condition for IM111 in Table 3.3, Section 3.2.2). Refractive index, differential scanning calorimetry, Raman spectroscopy measurements were conducted as described in Chapter 2.

7.2. Results and discussion

7.2.1. Selection of rare earth ions for 4 μm laser application

7.2.1.1. The composition of rare earth doped glasses

An ultimate goal of this study is to develop a fibre laser at ~4 μm. As a step towards this, spectroscopic measurements were carried out to select suitable rare earth ions for laser development with a medium concentration of 0.5 mol%, rather than a low (i.e., 0.1 mol%) or high (i.e., 1 mol%) concentration. As InF_3 is the main component (32 mol%) in the undoped glass, replacement of a small amount of InF_3 (0.5 mol%) by LnF_3 (Ln=Pr, Dy, Ho and Er) was expected to cause the least change in glass properties thus avoid crystallisation. As a result, except several small crystals in the doped glasses IM47-50 (Fig. 7.1), the glass quality was well suited for spectroscopic measurements. The intensity of white LED light was sufficient to excite green fluorescence in Er- and Ho-doped samples (Fig. 7.2).

Table 7. 1. RE ion doped IZSBGC glass blocks (30 g)*.

melt trial No.	RE / substitute
IM47 [e) f)]	0.5 mol% ErF_3 / InF_3
IM48 [e) g)]	0.5 mol% PrF_3 / InF_3
IM49 [e) g)]	0.5 mol% DyF_3 / InF_3
IM50 [e) f)]	0.5 mol% HoF_3 / InF_3

* The substitution is based on the basic glass composition $32InF_3$-$20ZnF_2$-$20SrF_2$-$18BaF_2$-$8GaF_3$-$2CaF_2$ (in mol %) with the InF_3 from Astron (~99.999% metal content). The melting condition for these four glasses was the same as for IM25 which can be found in Table 3.3 in Chapter 3 (glass prepared using the InF_3 from Astron).

Figure 7. 1. Photographs of IM47-50 glass samples.

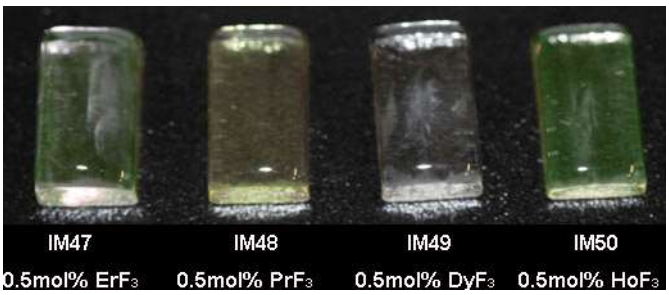

Figure 7. 2. Photographs IM47-50 glass samples under intense white light source (from left to right: IM47, IM48, IM49 and IM50).

7.2.1.2. Judd-Ofelt calculation

Judd-Ofelt calculation was applied in this study to determine the radiative decay rates of rare-earth ions (i.e., Pr, Dy, Ho and Er) in fluoroindate glass (i.e., the fundamental limit of radiative decay rates that can be achieved if there are no non-radiative processes). Since Judd and Ofelt proposed the Judd-Ofelt theory in 1962 [224, 225], it has been widely used to describe transition probabilities between different energy levels in rare earth ions doped materials, from which the radiative lifetimes and branching ratios of emission transitions can be determined. The procedure of the Judd-Ofelt analysis is represented in a simple

flow chart as in Figure 7.3 below, showing the major steps for the calculation of transition probabilities and branching ratios.

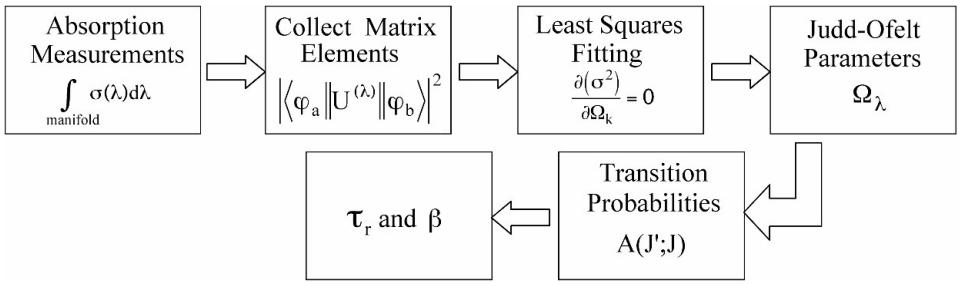

Figure 7. 3. Procedure of Judd-Ofelt analysis [226].

According to the Judd-Ofelt theory, the oscillator strength f_{exp} is related to the absorption spectrum [227]:

$$f_{\exp} = \frac{mc^2}{\pi e^2}\int \sigma_{abs}(\nu)d\nu \tag{7-1}$$

where σ_{abs} is the absorption cross section (cm^2), ν is the average wavenumber (cm^{-1}), m and e are the respective mass and charge of the electron, and c is the speed of light. The cross-section $\sigma_{abs}(\nu)$ of each band is defined by

$$\sigma_{abs} = \frac{\ln\left[I_0(\nu)/I(\nu)\right]}{Nt} = \frac{\ln\left[T_0(\nu)/T(\nu)\right]}{Nt} \tag{7-2}$$

where, T_0 is the transmission of un-doped glass, T is the transmission of doped glass, N is the number of ions per cm^3, and t is the absorption path length which is 10.0 mm in this study. Absorption coefficient $\alpha(\nu)$ can be defined by

$$\alpha(\nu) = \frac{\ln\left[T_0(\nu)/T(\nu)\right]}{t} \tag{7-3}$$

Note that the oscillator strength f_{exp}, absorption cross section (cm^2), σ_{abs} and absorption coefficient $\alpha(\nu)$ are for specific absorption bands/peaks, rather than the whole spectrum. The background for absorption spectrum was subtracted before the calculation.

Combining equations 7.1-7.3, the oscillator strength f_{exp} can be written as:

$$f_{\exp} = \frac{mc^2}{N\pi e^2}\int \frac{\ln\left[T_0(\nu)/T(\nu)\right]}{t} d\nu = \frac{mc^2}{N\pi e^2}\int \alpha(\nu) d\nu \tag{7-4}$$

A set of f_{exp} data for each glass serves as the basis for calculating the phenomenological parameters, Ω_t, using Eq. (7-5). To calculate the theoretical oscillator strength, both electron-dipole transition (f_{ed}) and magnetic-dipole transition (f_{md}) contributions should be taken into account [228]:

$$f_{cal}(a,b) = f_{ed}(a,b) + f_{md}(a,b)$$

$$= \frac{8\pi^2 m\nu}{3h(2J+1)}\left[\frac{\left[n^2+2\right]^2}{9n}\sum_{t=2,4,6}\Omega_t\left|\left\langle a\left\|U^{(t)}\right\|b\right\rangle\right|^2 + n\left(\frac{h}{4\pi mc}\right)^2 <\left\|L+2S\right\|>\right] \tag{7-5}$$

in which a and b are the initial and finial states of the dipole transition, h is the Planck constant, and n is the refractive index of the glass. As the refractive index measurements were not available for samples made before the Judd-Ofelt analysis was undertaken, n was assumed to be 1.52 in accordance with the literature reporting refractive indices from fluoroindate glasses with similar compositions as IZSBGC [229, 230]. Although refractive index is dependent on wavelength, the use of this estimated value of refractive index has a negligible effect (error < 4%) on the calculated oscillator strength. The values of squared reduced matrix elements of the transitions from a to b, $\left\langle a\left\|U^{(t)}\right\|b\right\rangle^2$, were taken from [231].

The Ω_t parameters were obtained by fitting the electric-dipole contributions of the experimental oscillator strengths of the observed transitions to the calculated ones by least-squares method.

According to the Judd-Ofelt theory, the Judd-Ofelt parameters can be used to calculate the probability of spontaneous emission, $A_{ba.}$ A_{ba}, referred to as spontaneous emission rate of a transition $J' \rightarrow J$, depends on the line strengths of the electronic and magnetic dipole contributions of this transition.

$$A_{ba}\left[b \rightarrow a\right] = \frac{64\pi^4}{3h} \times \frac{1}{2b+1} \times V_b^3 \times n^2 \times \left(\frac{\left(n^2+2\right)^2}{9n} \times S_{ed} + n \times S_{md}\right) \tag{7-6}$$

where the electric-dipole and magnetic-dipole line strengths, S_{ed} and S_{md}, are expressed as:

$$S_{ed}(a,b) = e^2 \sum_{t=2,4,6} \Omega_t \left| \langle a \| U^{(t)} \| b \rangle \right|^2 \tag{7-7}$$

$$S_{md}(a,b) = \frac{e^2}{4m^2c^2} \left| \langle a \| L + 2S \| b \rangle \right|^2 \tag{7-8}$$

The sum of spontaneous emission rates of all transition of an excited state (J') to lower energy states (I) designates the radiative lifetime, τ_{rad}, of the excited state.

$$1/\tau_{rad}[b] = \sum_i A_{bi} \tag{7-9}$$

Table 7.2 summarises the Judd-Ofelt parameters and R_{ms} (Root Mean Square) for the IZSBGC fluoroindate glasses IM47-50. Figures 7.4-7.7 show the absorption cross section spectra for RE-doped glasses in the wavelength range of 0.2-10 μm (50000-1000 cm^{-1}). Note that the scale for the cross section is the same for each glass. Good overlap between the UV-Vis-NIR and FTIR spectra was found. Those figures also illustrate the experimental and theoretical oscillator strength for each absorption band. The theoretical oscillator strength was calculated using the Judd-Ofelt parameter determined via fitting the experimental oscillator strength values. The majority of the absorption bands demonstrate good agreement between experimental and theoretical (calculated) oscillator strengths.

Table 7. 2. Judd-Ofelt parameters for IZSBGC fluoroindate glass.

	Ω_2 (10^{-20} cm^2)	**Ω_4 (10^{-20} cm^2)**	**Ω_6 (10^{-20} cm^2)**	**Rms (10^{-7})**
Pr^{3+}	1.35 ±0.49	3.21 ±0.62	5.16 ±0.19	2.37
Dy^{3+}	2.07 ±0.63	1.46 ±0.68	2.55 ±0.30	1.62
Ho^{3+}	0.85 ±0.36	2.89 ±0.52	1.61 ±0.20	2.03
Er^{3+}	1.63 ±0.16	1.36 ±0.22	1.46 ±0.08	2.37

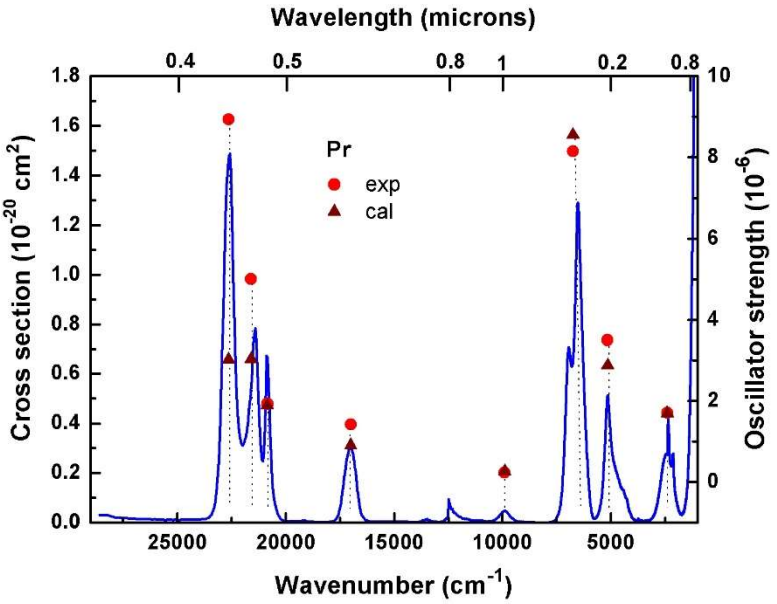

Figure 7. 4. Absorption cross-section spectrum and oscillator strengths for the various bands of Pr^{3+} in fluoroindate IZSBGC glass. The sharp peak at 2300 cm^{-1} (4.3 μm) is attributed to CO_2 absorption in the atmosphere. The red circles are the experimental oscillator strengths and the triangles are the calculated oscillator strengths, both of which are positioned at peak maximum values.

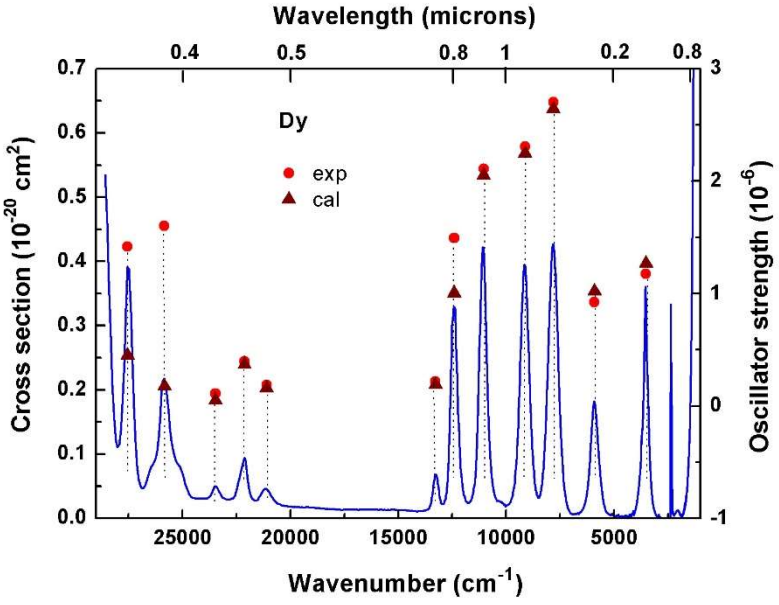

Figure 7. 5. Absorption cross-section spectrum and oscillator strengths for the various bands of Dy^{3+} in fluoroindate IZSBGC glass. The sharp peak at 2300 cm^{-1} (4.3 μm) is attributed to CO_2 absorption in the atmosphere. The red circles are the experimental oscillator strengths and the triangles are the calculated oscillator strengths, both of which are positioned at peak maximum values.

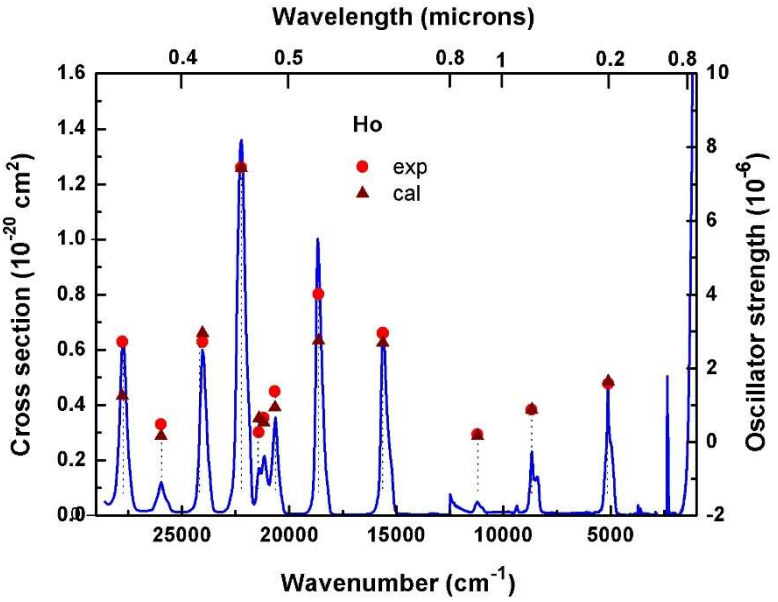

Figure 7. 6. Absorption cross-section spectrum and oscillator strengths for the various bands of Ho^{3+} in fluoroindate IZSBGC glass. The sharp peak at 2300 cm^{-1} (4.3 μm) is attributed to CO_2 absorption in the atmosphere. The red circles are the experimental oscillator strengths and the triangles are the calculated oscillator strengths, both of which are positioned at peak maximum values.

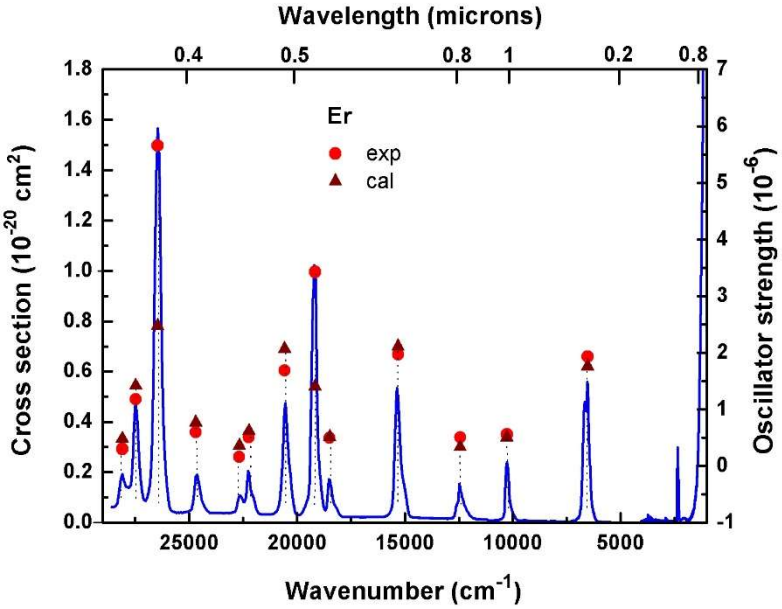

Figure 7. 7. Absorption cross-section spectrum and oscillator strengths for the various bands of Er^{3+} in fluoroindate IZSBGC glass. The sharp peak at 2300 cm^{-1} (4.3 μm) is attributed to CO_2 absorption in the atmosphere. The red circles are the experimental oscillator strengths and the triangles are the calculated oscillator strengths, both of which are positioned at peak maximum values.

Using the Judd-Ofelt parameters, the radiative decay rates for various emission transitions were calculated. Results for the low energy transitions with branching ratio ≥4% are

shown in Table 7.3. According to the exponential energy gap law [232], for a specific glass matrix the multiphonon relaxation rate (MPR) increases exponentially with decreasing energy gap as $W_{mp} \propto exp(-\alpha \Delta E)$. In this relationship, W_{mp} is MPR, ΔE is the energy gap between an excited state and the next lower state, α is a constant that only depends on host matrix [233]. For ZBLAN fluoride glass, the MPR rate at 300 K was predicted to be extremely high (i.e. $>10^6$ s^{-1}) at a small energy gap of < 2000 cm^{-1}, leading to negligible radiative transition, whereas at a large energy gap of >4000 cm^{-1}, the MPR rate is 10 s^{-1}, leading to negligible non-radiative transition [234]. For a given energy gap, the IZSBGC glass (phonon energy = 502 cm^{-1}; Chapter 7.2.2.2) has a lower MPR rate than ZBLAN glass (phonon energy = 580 cm^{-1} [235]) due to lower phonon energy. However, the MPR rate is still very high ($>10^6$ s^{-1}) at a small energy gap of < 2000 cm^{-1}, resulting in negligible radiative transition. Therefore, the radiative transitions from energy levels with energy gaps <2000 cm^{-1} are not shown in Table 7.3.

Using Judd-Ofelt analysis, the emission properties of rare earth ions in IZSBGC glass were evaluated (Table 7.3). Although Dy^{3+} and Ho^{3+} exhibit emission transitions at ~4μm (4.2 and 3.9 μm for Dy^{3+} and Ho^{3+}, respectively), they were not selected because the $^6H_{11/2} - {}^6H_{13/2}$ transition from Dy^{3+} at 4.2 μm and the $^5I_5 - {}^5I_6$ transition from Ho^{3+} at 3.9 μm have low branching ratios of ≤ 8% (Table 7.3). The Dy^{3+} transition ($^6H_{11/2} - {}^6H_{13/2}$) has the additional disadvantage of a larger radiative lifetime for the lower level than for the upper level. Hence, a significant population can accumulate in the lower level, which is not sufficiently rapidly depleted, resulting in the Dy^{3+} radiative transition $^6H_{11/2} - {}^6H_{13/2}$ being eventually hindered. Although rapid depletion can be achieved by suitable co-doping of rare earth ions, the aim of this study is to find a transition where no co-doping is required. Therefore, Dy^{3+} was not selected for study.

In contrast, the $^3H_5 \rightarrow {}^3H_4$ transition of Pr^{3+} at 4.2 μm has two distinct advantages over the transitions of Dy^{3+}, Ho^{3+} and Er^{3+} at ~4 μm.from the viewpoint of obtaining ~4 μm emission. Firstly, the $^3H_5 - {}^3H_4$ transition of Pr^{3+} has 100% branching ratio. Secondly, the absorption band of the $^3H_6$ level is relatively broad, with the peak around 1.9 μm. The absorption cross-section at 1.9 μm is 0.3×10^{-20} cm^2 (corresponding to 150 dB/m for 0.5mol% PrF_3 = 10^{20} Pr^{3+} ions/cm^3). Hence, the $^3H_5 \rightarrow {}^3H_4$ transition could be firstly excited into the $^3H_6$ state using the widely available 1.9 μm Tm^{3+}-doped fibre laser, the energy of which can be absorbed by Pr^{3+}-doped fluoroindate glass, followed by non-radiative decay to the upper laser level $^3H_5$. Four-level laser systems are ideal for

obtaining continuous light output with lower pump power compared with three-level laser system (e.g. the transition $^3H_5 \rightarrow {}^3H_4$ in Pr^{3+})[236], but there was no four-level laser system available in our rare earth ions doped fluoroindate glasses for 4 μm emission. Despite the fact that the transition $^3H_5 \rightarrow {}^3H_4$ in Pr^{3+} is a threee-level laser system, it has advantaes of 100% branching ratio and high absorption at a suitable pumping source (1.9 μm Tm^{3+}-doped fibre laser), which makes it a suitable tranistion for lasing at ~4 μm. Therefore, Pr^{3+}-doped was selected as a dopant for preparing fluoroindate glass fibre core material due to its transition $^3H_5 \rightarrow {}^3H_4$ in Pr^{3+} at 4 μm.

Table 7. 3. Radiative decay rates, A_{ba}, branching ratios, β_{ba}, radiative lifetime, $\tau_{rad,}$ and emission peak for the main emitting states of rare earth ions in IZSBGC glass.

RE	Initial state	Final state	A_{ed} (s^{-1})	A_{md} (s^{-1})	A_{total} (s^{-1})	β_{ba}	τ_{rad} (ms)	Emission peak (μm)
Pr^{3+}	$^3H_5$	$^3H_4$	11.24	1.08	12.32	1.00	81.89	4.2
	$^3H_6$	$^3H_5$	11.46	1.23	12.69	0.43		4
		$^3H_4$	16.94	0.00	16.94	0.57	33.76	2
Dy^{3+}	$^6H_{13/2}$	$^6H_{15/2}$	20.19	7.53	27.72	1.00	36.08	2.8
	$^6H_{11/2}$	$^6H_{13/2}$	3.19	4.44	7.62	0.09		4.2
		$^6H_{15/2}$	73.13	7.53	73.13	0.91	12.38	1.7
Ho^{3+}	$^5I_7$	$^5I_8$	57.90	20.47	78.38	1.00	12.76	1.9
	$^5I_6$	$^5I_7$	15.07	12.42	27.49	0.16		2.8
		$^5I_8$	140.59	0.00	140.59	0.84	5.95	1.2
	$^5I_5$	$^5I_6$	4.84	5.22	10.07	0.08		3.9
		$^5I_7$	69.80	0	69.80	0.53		1.6
		$^5I_8$	52.13	0	52.13	0.39	7.58	0.9
Er^{3+}	$^4I_{13/2}$	$^4I_{15/2}$	102.67	35.11	137.79	1.00	7.26	1.5
	$^4I_{11/2}$	$^4I_{13/2}$	18.50	10.47	28.97	0.18		2.7
		$^4I_{15/2}$	127.41	0	127.41	0.82	6.39	0.97

7.2.2. Selection of core and cladding glasses

For a step index optical fibre, the refractive index of the core glass is higher than that of the cladding glass. The difference in refractive index between the core and cladding glasses results in total internal reflection at the core/cladding interface. To select core and cladding glasses, the refractive indices of these glasses need to meet the requirement of sufficient numerical aperture (NA ≥0.1) up to 5.5 μm. PbF_2 and LnF_3 (Ln = La, Pr) were used as additional components to modify the glass composition to identify suitable core and cladding glass compositions and determine the impact of LnF_3 and PbF_2 on the thermal and optical properties of the glasses.

Various glass properties were measured including:

(a) refractive index over the wavelength range of 0.4-8 μm using spectroscopic ellipsometers;

(b) density using the buoyancy method;

(c) T_g and T_x using differential thermal calorimetry (DSC);

(d) Raman spectra using 785 nm pump wavelength.

The modified composition and properties of the glasses are described in Table 7.4.

Table 7. 4. Properties of 30 g glasses with modified glass composition.

glass No.	**composition**	**T_g (°C) ±2 °C**	**T_x (°C) ±2 °C**	**T_x-T_g (°C) ±2 °C**	**density (g/cm^3) ±0.002**	**n@1550nm ±0.006**	**n@4000nm ±0.006**
IM111	$32InF_3$-$20ZnF_2$-$20SrF_2$-$18BaF_2$-$8GaF_3$-$2CaF_2$	308	390	82	4.961	1.482	1.463
IM95	$32InF_3$-$20ZnF_2$-$20SrF_2$-$16BaF_2$-$8GaF_3$-$2CaF_2$–$2PbF_2$	304	384	80	4.995	1.488	1.471
IM120	$31.5InF_3$-$20ZnF_2$-$20SrF_2$-$16BaF_2$-$8GaF_3$-$2CaF_2$–$2PbF_2$–$0.5PrF_3$	--	--	--	4.941	1.485	1.447
IM127 (core)	31.5 InF_3–18 ZnF_2–20 SrF_2–16 BaF_2–8 GaF_3–2 CaF_2–$4PbF_2$–$0.5PrF_3$	299	379	80	4.828	1.489	1.457
IM128 (clad)	31.5 InF_3–20 ZnF_2–20 SrF_2–18 BaF_2–8 GaF_3–2 CaF_2–$0.5LaF_3$	308	394	86	4.600	1.481	1.445

7.2.2.1. Refractive index and density

As the base glass $32InF_3$-$20ZnF_2$-$20SrF_2$-$18BaF_2$-$8GaF_3$-$2CaF_2$ (IZSBGC) was found to be suitable for low-loss fibre fabrication (Chapter 5), the base glass was firstly considered as a suitable cladding glass candidate. To make a pair of core and clad glasses, a core glass containing Pr^{3+}, based on a previous selection of rare earth element for ~4 μm laser, should have a larger refractive index than the base glass. PbF_2 was demonstrated to be a suitable candidate to substitute for BaF_2 [36, 100]. Therefore, 2 mol% BaF_2 in the base glass was replaced by PbF_2 (IM95, 30 g), resulting in larger density and refractive index than those of a base glass sample (IM111, 30 g) which was made for comparison with modified glass compositions. The increase in density is due to replacement of 2 mol% of the lighter BaF_2 with the heavier PbF_2, while the increase in refractive index is due to both the increasing density and large polarisability of Pb^{2+} resulting from the fact that its lone 6s electron pair decreases the field strength [203]. Pr^{3+} was then doped into the PbF_2-containing glass (IM95) for the preparation of a core glass (IM120). However, even the small concentration of 0.5 mol% PrF_3 dopant reduced the refractive index and density compared with the undoped glass IM95, which can be attributed to an expansion of the glass network due to the large ionic radius of Pr^{3+} (Table 7.4). A larger amount of PbF_2 was then used for the preparation of IM127 core glass to compensate for the decrease in refractive index due to the introduction of 0.5 mol% PrF_3. Therefore, in the glass melt IM127, the amount of PbF_2 was doubled from 2 mol% (2 mol% of BaF_2 replaced by PbF_2 in IM95) to 4 mol% (2 mol% of ZnF_2 and 2 mol% of BaF_2 were replaced by 4 mol% PbF_2 in IM127). Note that we chose ZnF_2 for replacement by PbF_2 as the difference in ionic radius between Zn^{2+} and Pb^{2+} is larger than that between Ba^{2+} and Pb^{2+}, resulting in a larger increase in refractive index. As expected, the larger amount of PbF_2 increased the refractive index. However, relative to the base glass, the index increase was not sufficient for an NA ≥0.1. As 4 mol% doping of PbF_2 resulted in changes in thermal properties (refer to Section 7.2.2.3), a further increase in the amount of PbF_2 doping (> 4 mol%) would significantly alter thermal properties (glass transition temperature, T_g) and thus make the core glass incompatible with the cladding glass. Therefore, to further increase the difference in refractive index between the core and cladding glasses, it is required to further decrease the refractive index of the cladding glass without significant changes in glass properties compared to the core glass. Doping of Pr^{3+} has been shown to reduce the refractive index of IM120, but the reduction was not significant. Hence, an alternative

rare earth ion, La^{3+} (in the form of fluoride), was used to replace the glass network former, InF_3, of the base glass. The introduction of La^{3+} in IM128 (0.5 mol% InF_3 replaced by LaF_3) decreased the glass density and refractive index compared with the base glass IM111, possibly due to the expansion of the glass network resulting from the large ionic radius of La^{3+}. The refractive index reducing effect of La^{3+} is similar to that of Pr^{3+} (Pr-doped glass with 2mol% PbF_2 IM120 has a smaller refractive index than the corresponding undoped glass IM95). Compared with the Pr-doped core glass IM127, the decrease in index due to the introduction of La^{3+} into glass IM128 was found to be sufficient to enable NA≥0.1. Therefore, the IM127 and IM128 glasses were hereafter used for as core and cladding, respectively. The compositions of the two glasses are as follows:

Core: 31.5 InF_3 – 18 ZnF_2 – 20 SrF_2 – 16 BaF_2 – 8 GaF_3 – 2 CaF_2– 4PbF_2– 0.5PrF_3

Cladding: 31.5 InF_3 – 20 ZnF_2 – 20 SrF_2 – 18 BaF_2 – 8 GaF_3 – 2 CaF_2– 0.5LaF_3

The calculated NA values at different wavelengths for this core/cladding glass combination are listed in Table 7.5. The refractive index results are also shown in Fig. 7.8.

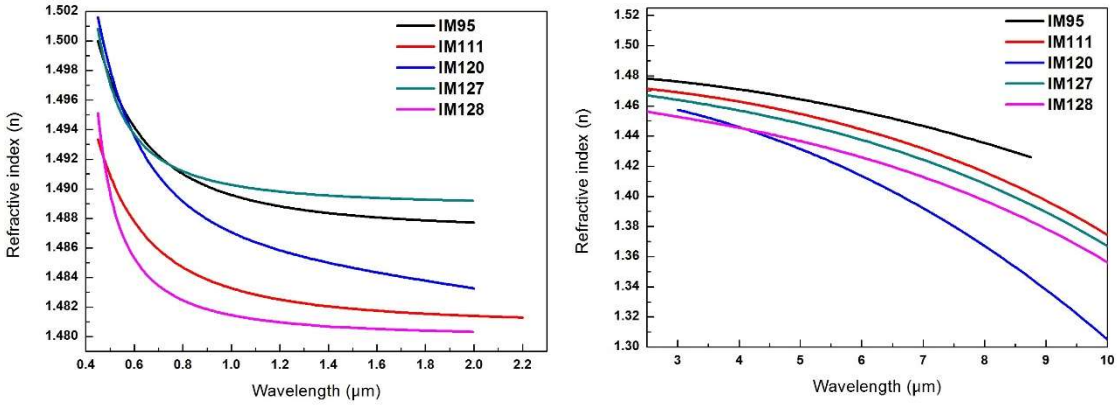

Figure 7. 8. Refractive index results for (left) 0.4-2.0 μm and (right) 3-12 μm wavelength range.

Table 7. 5. Comparison of refractive indices for IM127/IM128 and IE27 core/clad glass combination at 1550 nm (using J.A. Woollam Co., Inc. VASE Ellipsometer HS-190) and 3000~5500 nm (using J. A. Woollam Co., Inc. VASE Ellipsometer VB-400).

Glass	Refractive index			
	1550 nm	**3000 nm**	**4000 nm**	**5500 nm**
IM127 (core)	1.4794	1.4640	1.4573	1.4432
IM128 (clad)	1.4606	1.4515	1.4428	1.4290
Difference (IM127 *vs*. IM128)	0.0188	0.0125	0.0145	0.0142
Numerical Aperture	0.2351	0.1909	0.2051	0.2020
IE27 (core)	1.4728	1.4683	1.4622	1.4494
IE27 (clad)	1.4515	1.4470	1.4410	1.4285
Difference (IE27 core *vs* clad)	0.0290	0.0213	0.0212	0.02091
Numerical Aperture	0.2496	0.2492	0.2481	0.2452

*Numerical apertures of commercial InF_3-based glass fiber from Thorlabs (II-V) [237]: 0.17 to 0.35 for 0.4-5.5 μm.

7.2.2.2. Phonon energy

Raman spectra of different fluoroindate glasses are shown in Fig. 7.9. The Raman spectrum of base glass IM111 shows bands at 502 cm^{-1}, 288 cm^{-1}, and 224 cm^{-1}. These bands agree well with the Raman spectra of other fluoroindate glasses [29], and are attributed to the vibrations of octahedral [InF_6] groups [29, 238]. The peak position of the highest phonon-energy band of our fluoroindate glass is at 502 cm^{-1}, whereas that of ZBLAN glass is at 574 cm^{-1} [29]. These two bands correspond to In-F and Zr-F stretching vibrations, respectively [29]. The shift to shorter wavenumber for IZSBGC glasses, relative to ZBLAN, is consistent with the enhanced mid-IR transmission of the IZSGBC glasses [239] as described in Section 3.2.3.

Doping of LaF_3 into the base glass IM128 (with 0.5 mol% LaF_3) does not change the position, shape and intensity of the Raman spectral bands. All PbF_2-containing glasses exhibit significantly reduced intensities and flattened shapes for all three Raman bands.

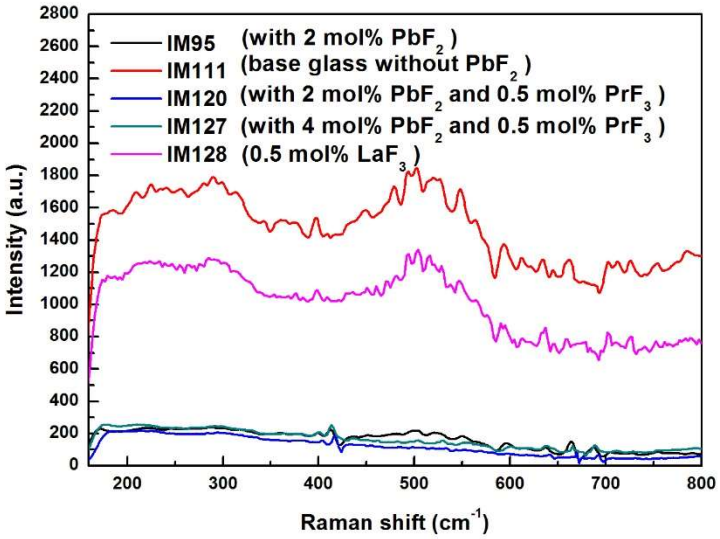

Figure 7. 9. Raman spectra for base and doped glasses.

7.2.2.3. Thermal properties

DSC results for base, core and cladding glasses are shown in Fig. 7.10. Relative to the base glass IM111, doping of LaF_3 into glass IM128 does not change T_g but slightly increases T_x, resulting in enhanced glass stability (T_x-T_g increases; Table 7.4). However, the larger amount of PbF_2 in the core glass IM127 results in a significant decrease in the T_g and a slight decrease in T_x-T_g and glass stability (Table 7.4).

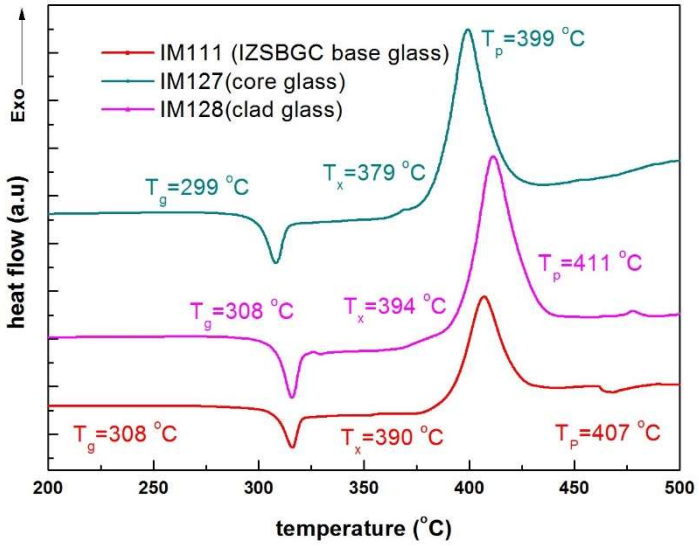

Figure 7. 10. DSC results of base, core and cladding glasses (experimental errors of ± 2 ˚C).

7.2.3. Fabrication of core/clad structures

7.2.3.1. Overview of methods

The objective was to investigate and evaluate methods for core/clad structure fabrication. The challenge is to obtain an interface free of bubbles and crystals between the core and clad glasses for the fabrication of low-loss fibres. The established methods for fluoride core and clad glass fabrication are rotational and suction casting [97, 99, 100]. The interface is formed during those casting processes, when the core glass melts are poured into a tube of cladding glass at a temperature near T_g. The advantage of rotational and suction casting is that the low viscosity of the core glass melt leads to a good fusion between the core and cladding glass. One drawback of these methods is the high demand on the fabricator's skill to perform the casting within a tight time schedule. Another disadvantage is that the cladding glass is reheated, which can induce crystallisation at the core/clad interface [240]. In addition, the reduced cooling rate of the core glass can lead to crystallisation in the centre of the core glass [203].

In my thesis, the fabrication of step-index fluoroindate fibres using the extrusion technique is investigated. The extrusion technique has been demonstrated to be a versatile and highly automated method to fabricate various soft glasses (including ZBLAN) with different preform shapes [200, 222, 241]. In this Chapter two different approaches to the fabrication of core/clad preforms using the extrusion procedure will be discussed: (1) the stacked billet extrusion, and (2) the rod/cane-in-tube method.

a) Stacked billet extrusion

In this method, a core/clad rod is extruded using a billet comprising a disk of core glass stacked on top of a disk of cladding glass (Fig. 11). This method has been used to fabricate low-loss infrared glass fibres (i.e., chalcogenide and fluoride fibres) [184, 242]. The challenge is to achieve good surface finish and flatness of the billet as this is critical to achieve a bubble-free interface. Two methods for the fabrication of stacked billet were investigated in my thesis (refer to Appendix for details).

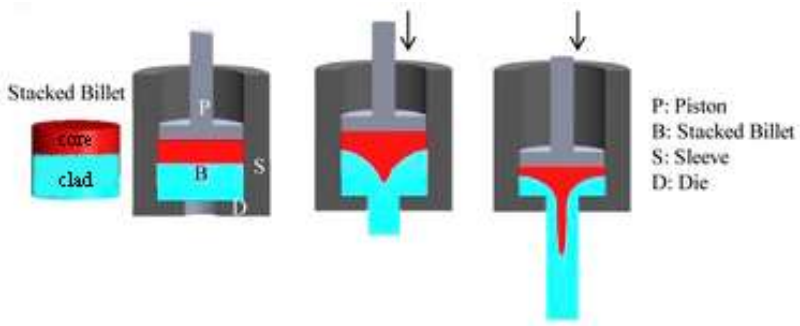

Figure 7. 11. A schematic diagram of stacked extrusion process for producing a simple core-clad structure.

b) Rod/cane-in-tube method.

For this method, a preform of a core glass rod inserted into a cladding glass tube is drawn down into a fibre. The cladding glass tube and core glass rod are made separately using the extrusion technique (Fig. 7.12). Either a smaller diameter rod was extruded and used directly for assembly with a cladding glass tube to draw a core/clad fibre, or a larger diameter rod was extruded, drawn into a smaller diameter rod, which was then used for assembly with a cladding glass tube. To distinguish the use of an extruded rod from the use of a drawn rod for drawing a core/clad preform, the latter is referred to as cane as this term is widely used for thin rods of one to a few millimeter diameter made via drawing of a preform with ≥10mm diameter.

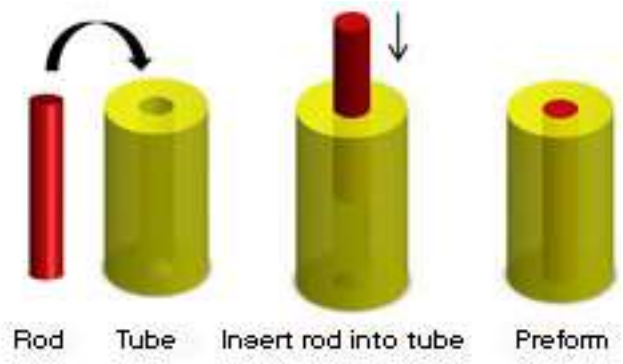

Figure 7. 12. Schematic of rod/cane-in-tube process for producing a simple core-clad structure.

7.2.3.2. Annealing tests

To explore whether surface crystallisation could occur under the extrusion conditions, annealing tests were conducted using thin polished glass slides. The polished glass slides were flatter and thinner than our extruded preforms. Therefore, it is easier to characterise

the glass slide under an optical microscope. A core glass (IM127) and cladding glass (IM128) slides were treated at elevated temperatures comparable to those used for extrusion. In IM127, there were isolated crystals visible after annealing at 315 ˚C, while significant crystallisation distributed on the wrinkles areas occurred on the edge after annealing at 318 ˚C (Fig. 7.13). The form of wrinkles may be attributed to the different thermal expansion coefficients between crystallisation areas and bulk glass. This suggests that a temperature of 318 ˚C for IM127 preform extrusion can cause potential surface crystallization. In contrast, 315 ˚C is suitable for core glass extrusion without potential surface crystallisation. For cladding glass IM128, there was no obvious crystallisation after annealing at a slightly higher temperature at 318 ˚C, while significant crystallisation distributed on the wrinkle areas occurred on the edge of the glass slide after annealing at 322 ˚C (Fig. 7.14), suggesting that a temperature of 322 ˚C for IM128 preform extrusion can cause potential surface crystallisation but 318 ˚C for extrusion is sufficiently low to prevent potential crystallisation. The annealing tests showed that to minimise potential crystallisation at a sufficiently low extrusion force, the core preform should be extruded at ≤ 315 ˚C while the cladding preform should be fabricated at about 318 ˚C. For stacked billet extrusion, both core and cladding glasses should be extruded at ≤ 315 ˚C.

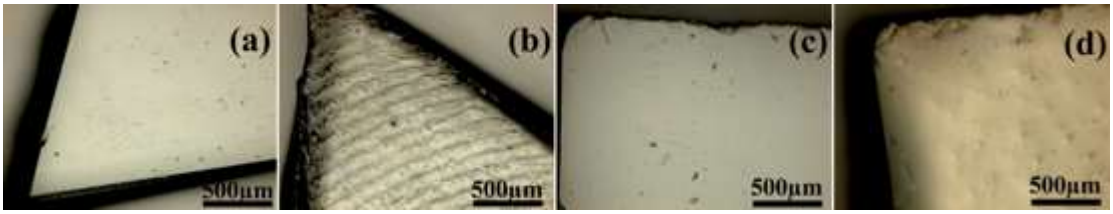

Figure 7. 13. IM127 glass surface images (core glass): (a) before annealing at 318 ˚C for 10 hours; (b) after annealing at 318 ˚C for 10 hours; (c) before annealing at 315 ˚C for 10 hours; (d) after annealing at 315 ˚C for 10 hours.

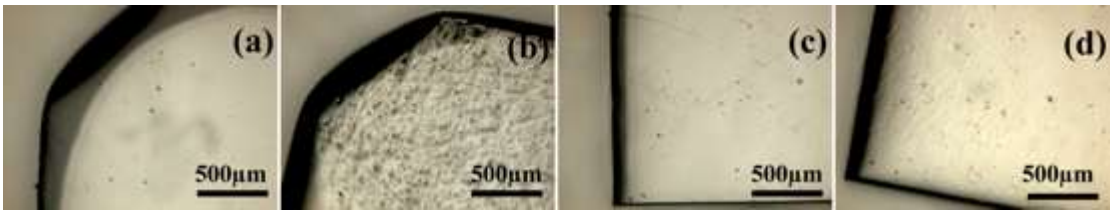

Figure 7. 14. IM128 glass surface images (cladding glass): (a) before annealing at 322 ˚C for 10 hours; (b) after annealing at 322 ˚C for 10 hours; (c) before annealing at 318 ˚C for 10 hours; (d) after annealing at 318 ˚C for 10 hours.

7.2.3.3. Extrusion of core/clad preform

(a) Extrusion trials using manually stacked billets

The core and cladding glass billets were successfully upscaled from 30 g to 60 g. The billets were prepared individually and then mechanically polished. The details for glass preparation can be found in Table 7.6. The cladding glass billet was placed directly onto a die, and the core glass billet was placed on top of the cladding glass billet. We conducted two extrusion trials (IE24 and IE25), using the same die design as that for rod extrusion of the base glass with a 10 mm diameter. Preform IE24 was first extruded at 322 ˚C, as this temperature results in the lowest loss of base glass fibre IF19, and the cladding glass has similar T_g to the base glass. However, crystallisation occurred in the core glass at this temperature, possibly due to the lower crystallisation stability compared with the base and cladding glasses (Fig. 7.15), and at the core/clad interface. Thus, a lower extrusion temperature of 318 ˚C was applied to the next extrusion trial IE25 (Fig. 7.15), which significantly reduced the extent of crystallisation in the core glass and at the interface (Fig. 7.16 and 7.17). However, a faint crystallisation pattern was still found at the interface of both ends of IE25.

Table 7. 6. Melting condition for different batch size*.

Raw materials	Melt example	Batch weight (g)	NH_4HF_2/batch weight (wt %)	Fluorination		Melting time / temp.	Time before casting (s)	Cast/Mould/Anneal temp. (˚C)	Usage
				Temp. (˚C)	Time (min)				
a	IM111	30	2.4	450	60	2h/900˚C	70	900/220/335	
b	IM95	30	6.8	235	45	3h/900˚C	65	900/270/330	
c	IM120	30	2.4	450	60	2h/900˚C	68	900/220/335	
d	IM127	30	2.4	450	60	2h/900˚C	68	900/200/330	
	IM131	60	2.4	450	70	2.5h/900˚C	103	900/200/330	IE24
	IM136	60	2.4	450	70	2.5h/900˚C	101	900/200/330	IE25
	IM148	100	2.4	450	60	3h/900˚C	115	900/190/330	IE28
	IM153	60	2.4	450	60	2.5h/900˚C	116	900/200/330	IE30
	IM158	100	2.4	450	60	3h/900˚C	114	900/190/330	IE35
e	IM128	30	2.4	450	60	2h/900˚C	68	900/200/335	
	IM147	100	2.4	450	60	3h/900˚C	120	900/200/335	IE29
	IM150	100	2.4	450	60	3h/900˚C	124	900/200/335	IE31
	IM152	60	2.4	450	60	2.5h/900˚C	115	900/200/335	

Table 7.6 (continued):

a: base glass, InF_3 (Synquest, 99.99% metal content), GaF_3 (Synquest, 96.3% metal content), other fluorides ≥99% metal content.

b: 32 InF_3–20 ZnF_2–20 SrF_2–16 BaF_2–8 GaF_3–2 CaF_2–2PbF_2, $InF_3 \cdot 3H_2O$ (Testbourne, 99.99% metal content), GaF_3 (Synquest, 96.3% metal content), other fluorides ≥99% metal content.

c: 31.5 InF_3–20 ZnF_2–20 SrF_2–16 BaF_2–8 GaF_3–2 CaF_2–2PbF_2–0.5PrF_3, InF_3 (Synquest, 99.99% metal content), GaF_3 (Synquest, 96.3% metal content), other fluorides 99% metal content.

d: Pr^{3+} doped core glass, InF_3 (Synquest, 99.99% metal content), GaF_3 (Synquest, 96.3% metal content), other fluorides 99% metal content.

e: clad glass, InF_3 (Synquest, 99.99% metal content), GaF_3 (Synquest, 96.3% metal content), other fluorides 99% metal content.

* The substitution is based on the basic glass composition 32InF_3-20ZnF_2-20SrF_2-18BaF_2-8GaF_3-2CaF_2 (in mol %) The melting condition for these four glasses can be referred to Chapter 3 (glass melting with InF_3 from Testbourne and Synquest).

For both IE24 and IE25, the core glass started to appear in the preform at about 3 cm from the tip of the preform (Fig. 7.16), although different extrusion temperatures were used. As the core and cladding glasses have different viscosities at the same extrusion temperature, the viscosity of the core glass is lower due to the lower T_g of the core glass as compared to the cladding glass. The preform diameter became much larger than the die exit diameter of 10 mm. The diameter of preform IE24 varied from 10.13 to 12.26 mm, while the diameter of preform IE25 changed from 10.16 to 11.82 mm. Compared with the maximum diameters of IE24 and IE25, the maximum diameter of the preform decreased when the extrusion temperature reduced. However, the preform surface roughness increased due to the increased friction between glass and die, as a result of the higher viscosity at the lower extrusion temperature.

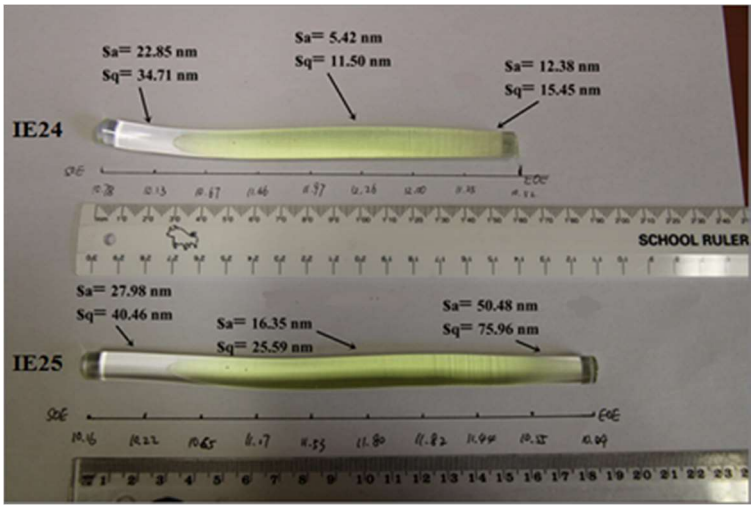

Figure 7. 15. Photographs of extruded preforms IE24 and IE25 made using stacked billets. Note the green glass is the core glass and the colourless glass is the cladding glass (SOE: start of extrusion; EOE: end of extrusion).

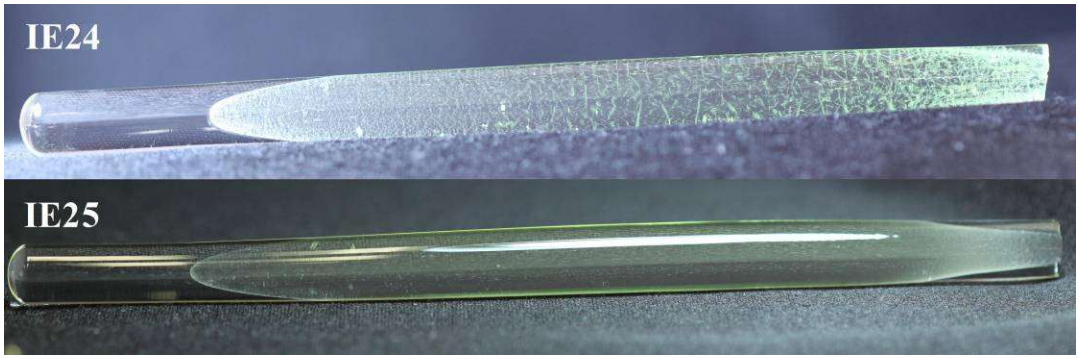

Figure 7. 16. Photographs of extruded rods IE24 and IE25. Note that the orientation and lighting of these preforms is different compared with the preforms shown in Figure 7.15 (Both extrusions started from left to right in the Figure).

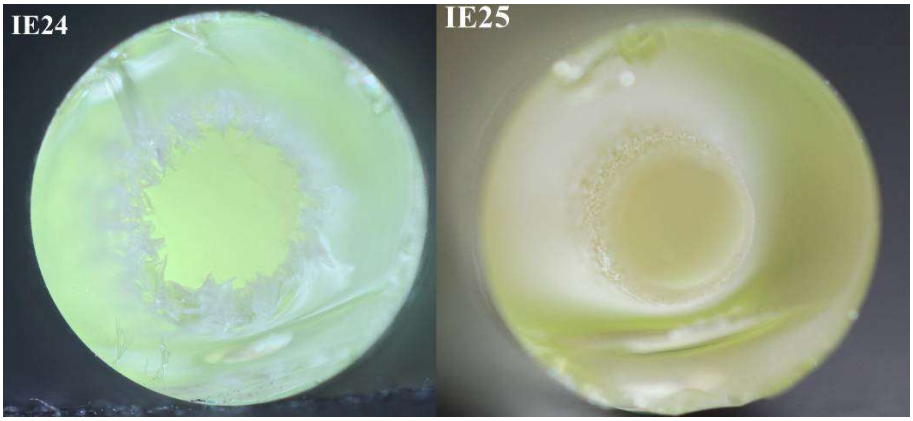

Figure 7. 17. Cross-sectional photographs of IE24 and IE25 preforms.

(b) Core/clad preforms via stacked billet extrusion

Extrusion trials IE24 and IE25 using manually stacked billets (IM131&136; Table 7.6) were conducted at 322 and 318 ˚C, respectively. Although a lower extrusion temperature was applied to IE25 compared with IE24, there was still a crystallisation pattern found at the interface of both ends of IE25. For extrusion trial IE27, the stacked billet IM139 was used, which was made by casting the cladding glass melt onto the core glass billet in a mould at the T_g~300 ºC of the core glass (see Appendix for the preparation of IM139). To prevent potential crystallisation between the core and cladding interface, the extrusion temperature of trial IE27 was further reduced to 315 ˚C. However, IE27 preform was not as straight as IE24 and IE25 due to the higher extrusion viscosity (lower extrusion temperature at 315 ºC) required for IE27 compared with IE24 (extrusion temperature at 322 ºC) and IE25 (extrusion temperature 318 ºC). During extrusion, bending of the extrudate may occur due to radial temperature gradient which may be caused by: 1) the extrusion part is not perfectly aligned to the furnace centre; 2) non-concentric radial temperature profile of the furnace; and 3) fluctuation in the flow of hot air between the heating elements and extrusion part.. IE27 preform was used to determine the core/clad ratio (Fig. 7.18) which was found to be up to 0.9. Although the annealing test showed that potential crystallisation occurred on the core preform after annealing at 318 ˚C for 10 h, stacked billets were still preferably extruded at about 318 ˚C to obtain a sufficient low force to prevent bending.

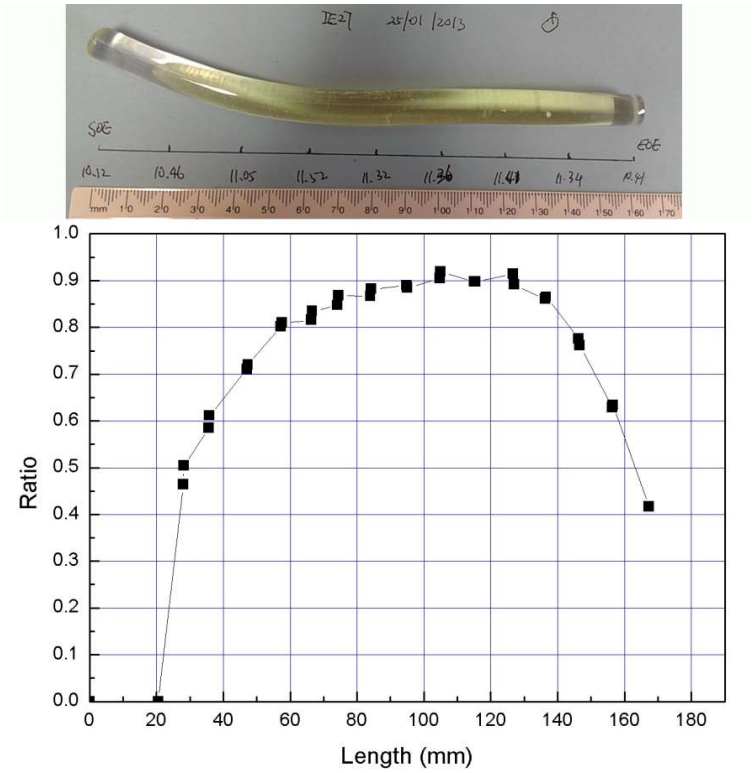

Figure 7. 18. Photograph of IE27 preform and the ratio of core/cladding in IE27.

Refractive index measurements showed that the glasses IM127 and IM128 are potential core and cladding glass candidates for step-index fibre fabrication (Table 7.5). The core glass (IM127, refractive index of 1.4894-1.4413 for the wavelength range 1550-5500 nm in Table 7.5) has a larger index than cladding glass (IM128, refractive index of 1.4805-1.4238 for the wavelength range 1550-5500nm). To confirm that core and cladding glasses have a sufficient index contrast after extrusion, core/clad preform IE27 was used for refractive index measurements in the range of 0.45-16 μm (Fig. 7.19). Table 7.5 compares the core and clad refractive indices and numerical aperture for IM127/IM128 and IE27 core/clad glass combination. A significant refractive index difference was found between the core and cladding glasses in preform IE27 (Table 7.5). In particular, the Numerical Aperture is larger for the extruded samples (i.e., core and clad glasses in IE27) than for the cast samples (i.e., IM127 & 128). This suggests that extrusion possibly influences glass refractive index due to changes in glass structure during the process of squeezing the glass through the die. As core and clad glass in IE27 were extruded at the same temperature but different viscosities, the extrusion effects on the refractive indices of core and clad glasses are different (i.e., refractive index of core glass increased at 3000~5500 nm while refractive index of clad glass decreased at 1550~5500 nm. In

addition, the Numerical Aperture for extruded core and clad glasses in IE27 is very similar at 1550~5500 nm but that for cast core and clad glasses at 3000~5500nm is larger than that at 1550 nm. The cause is yet to be explored. Future work is required to determine the major causes of the significant difference, possible including measurement errors (i.e., repeating measurements), extrusion (e.g., a measurement using one glass billet slide and one preform slide), and upscaling (e.g., a measurement using one glass billet slide and one glass billet slide).

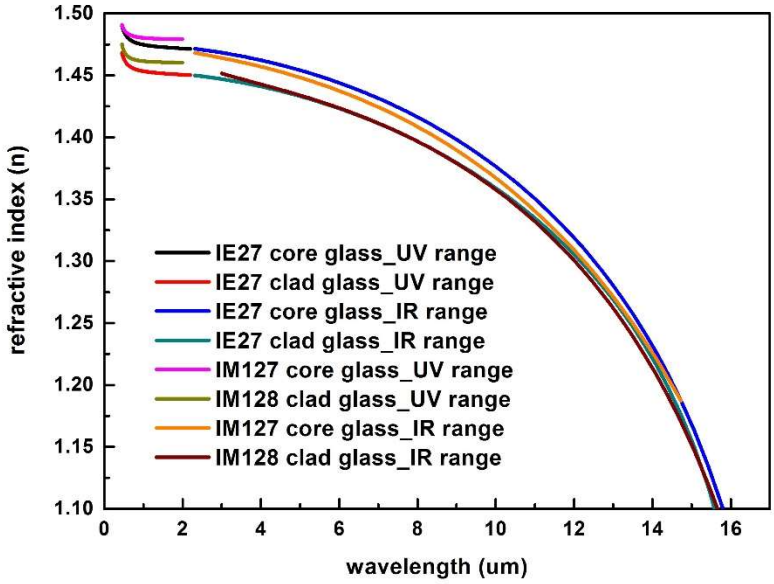

Figure 7. 19. Refractive index of core/cladding in IE27 and comparison with original core (IM127) and clad (IM128) glass.

(c) Core/clad preform extrusions

In this study, the extrusion experiments can be divided into extrusion of core glass rods and cladding glass tubes. Based on the annealing results, the core glass rods IE28, IE35 (10 mm in diameter) and IE30 (5 mm in diameter) were extruded at 315 ˚C. Apart from several graphite particles and extrusion marks, both preforms exhibited good optical quality.

Cladding glass tubes IE29 and IE31 were extruded at a temperature being 2 ˚C higher than that for stacked core/clad billet extrusion trial IE25, due to increased friction for tube extrusion. For IE29 extrusion trial, the billet was extruded through a die with 10 mm of die exit diameter and 2 mm of pin diameter. The internal design of the die is identical to the design of the dies used for IZSBGC base glass tube extrusion (see Appendix for

temperature profiling). The cladding glass tube IE29 exhibited good optical quality without cracking and crystallisation. All extrusion experiments carried out in this chapter are included in Table 7.7.

Table 7. 7. Extrusion condition for core and cladding glass.

No	Type	$T_{extrusion}$ (˚C)	diameter		Preform quality	Usage	Fibre surface	Loss at 980 nm (dB/m)
			Outer (mm)	Inner (mm)				
IE24	Stacked billet	322	10	---	Crystals on the interface of core and clad parts	IF25 and IF27 core/clad fibre	Bumps on fibre surface, fragile and unsmooth surface	180 (IF25), 153 (IF27)
IE25	Stacked billet	318	10	---	Reduced crystals on the interface of core and clad parts compared to IE24	IF24 core/clad fibre	Bumps on fibre surface, fragile and unsmooth surface	150
IE27	Stacked billet	315	10	--	Bend/Reduced crystals on the interface of core and clad parts as compared to IE25	index measurement	n/a	n/a
IE28	Core glass rod	315	10	---	Clear	IF23 core cane	Bumps on cane surface, fragile and unsmooth surface	70
IE29	Cladding glass tube	320	10	2	Clear	failed to draw a fibre (IF26) using cane(IF23)-in-tube(IE29) method	n/a	n/a

Table 7.7 (continued)

IE30	Core glass rod	315	5	---	Clear	Intent to make rod-in tube preform with IE33 tube; in stock		n/a
IE31	Cladding glass tube	320	12	6	failed due to die cracking	n/a	n/a	n/a
IE32	Core glass rod	315	10	---	Clear	IF28 core cane	Serious bumps on fibre surface due to the high drawing temperature without good control, fragile and unsmooth surface	cane was too fragile for loss measurements
IE33	Cladding glass tube	322	12	6	failed to be extruded with a 6 mm inner diameter	n/a	n/a	n/a
IE34	Cladding glass tube	320	10	2	Clear	failed to draw a fibre (IF29) using cane(IF28)-in tube(IE34) method	n/a	n/a
IE35	Core glass rod	315	10	---	Clear	IF30 core cane	Bumps on cane surface, fragile and unsmooth surface	~170
						IF31 core fibre		247

7.2.3.4. Fibre fabrication

The aim of this study is to undertake preliminary core/clad fibre fabrication trials as shown in Table 7.8 to assess the feasibility of preparation of core/clad glass and various fibre fabrication methods. The core/clad fibres were drawn, using preforms made from both the stacked billet extrusion and cane-in-tube methods (requiring drawing of a core cane for the latter method). However, the losses of the core/clad fibres were rather high. To gain insights into the cause of high losses in the core/clad fibres, a core glass fibre was drawn. This fibre was critical to the understanding of the results of the core/clad fibre drawing trials and will be discussed first in the following text.

(a) Fibre drawing of core unstructured fibre

To study the thermal stability of the core glass for fibre drawing, IE35 (extruded from IM158 core glass) was drawn into unstructured core glass fibre IF31 for loss and surface analysis. The surface of this fibre (IF31) was not smooth and covered with wrinkle patterns/bumps (SEM image; Fig. 7.20). Micro-XRD was also conducted on isolated clear and white part (with wrinkle patterns) of IF31 surface (Fig. 7.21a). Two sharp peaks in the XRD pattern (Fig. 7.21c), indicative of crystalline phase(s), were found on the white part. The loss of fibre IF31 was measured to be ~247 dB/m at 980 nm using spot loss measurement (Fig. 7.22). This loss is attributed to surface scattering arising from heavy surface crystallisation and roughness, which were confirmed by micro-XRD and SEM, and possibly undetectable nanocrystallisation in the volume of the core glass.

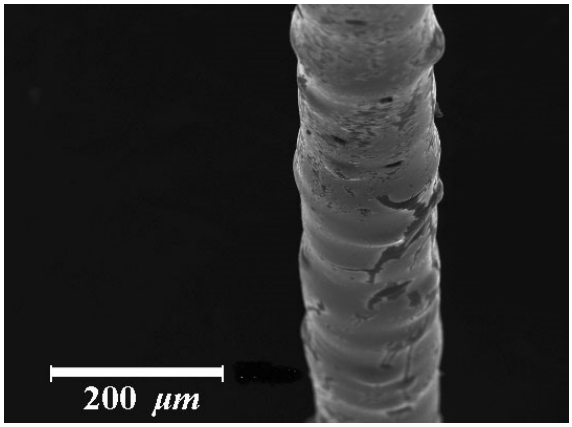

Figure 7. 20. SEM image of IF31 fibre drawn from IE35.

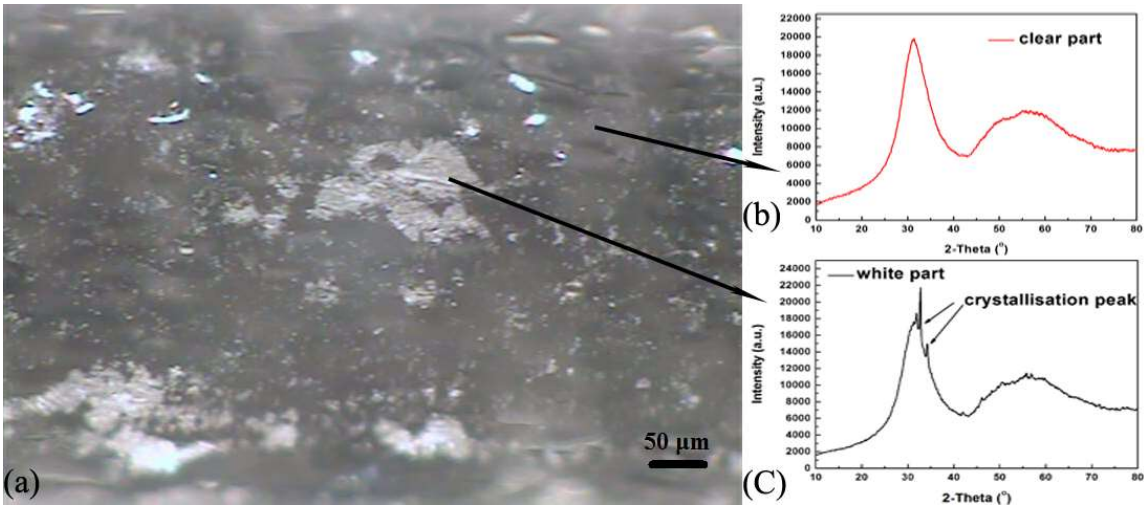

Figure 7. 21. Micro-XRD results of IF31 fibre drawn from IE35: (a) microscope image of the IF31 surface; (b) XRD pattern collected from a clear part in (a); and (c) XRD pattern collected from a white area in (a).

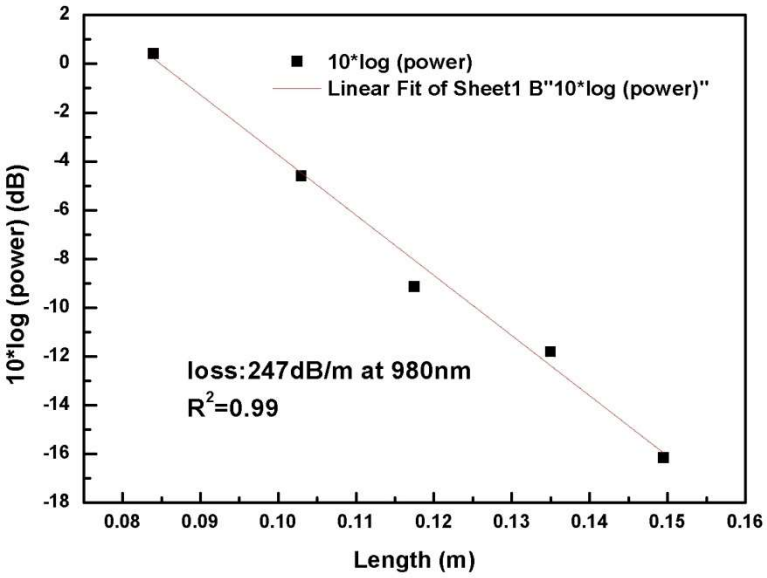

Figure 7. 22. Loss of IF31 at 980 nm using cutback measurement.

(b) Drawing of core glass canes

IF23 core glass cane with a diameter of 1.3 mm was drawn at about 740 ˚C and 6 mm/min feeding rate from IE28 extruded rod (Fig. 7.23). The loss measurement of the cane using white light source is shown in Fig. 7.24. The cane exhibits a high loss of ~70 dB/m at 980 nm. The high loss is attributed to high degree of surface scattering due to high cane surface roughness caused by surface crystallisation (Fig. 7.25 and Table 7.8), and/or high volume scattering loss due to the crystals formed as a result of the lower crystallisation stability of the core glass. IF30 cane has a higher loss of ~170 dB/m at 980 nm than IF23

cane, which is attributed to the higher surface scattering loss due to higher cane surface roughness of IF30 than that of IF23. It was also found that the loss of core glass fibre IF31 was higher than that of the corresponding core glass canes (e.g., IF23 with ~70 dB/m at 980 nm in Table 7.8). This can be explained by the higher glass viscosity (i.e., lower temperature) for cane drawing than that for fibre drawing as the drawing tension to enable drawing with a stable diameter control for the cane is an order of magnitude larger [243, 244] and the preform diameter drawing down ratio for the cane is an order of magnitude smaller (e.g., preform diameter drawing down ratio is 10 mm/1 mm = 10 for a cane and 10 mm/0.1 mm = 100 for a fibre). The lower drawing temperature for the cane resulted in less surface crystallisation of the cane compared with the fibre.

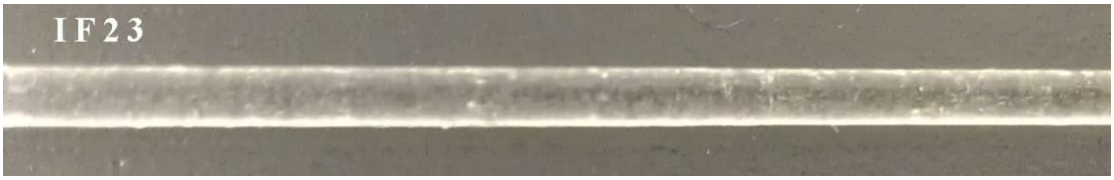

Figure 7. 23. Photograph of IF23 cane.

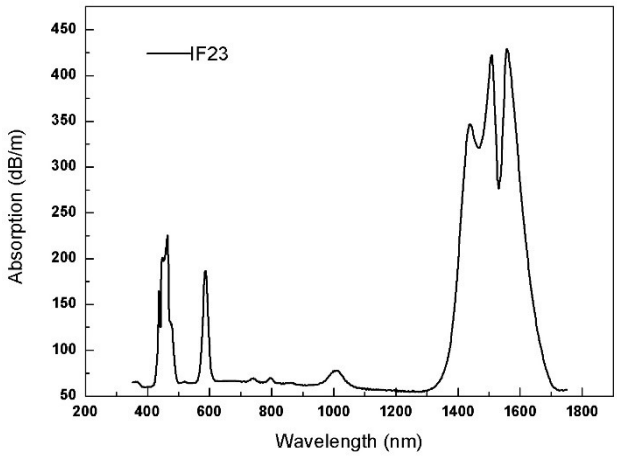

Figure 7. 24. Loss of IF23 cane using the cutback measurement. The high loss peaks are Pr^{3+} absorption bands.

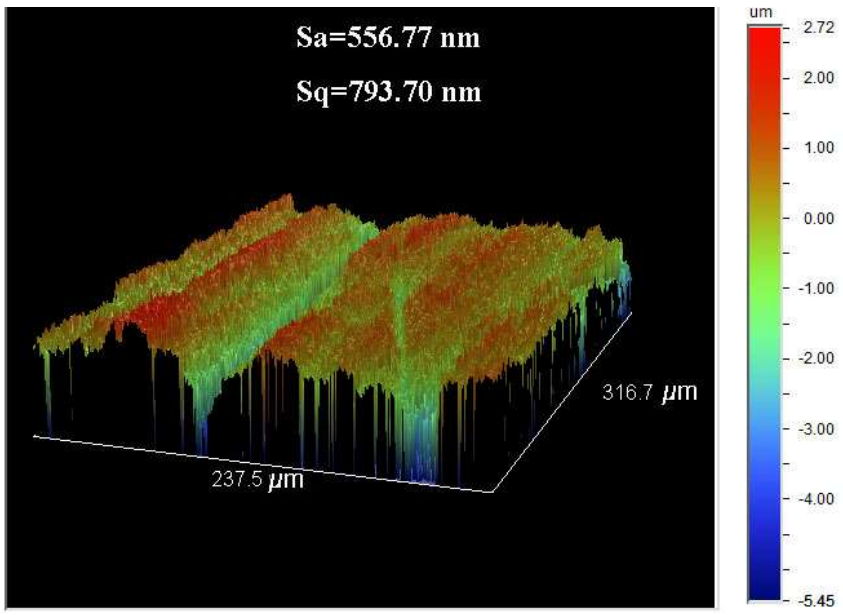

Figure 7. 25. Surface roughness measurement of cane IF23 cane using an optical profiler.

Table 7. 8. Surface roughness and fibre loss at 980 nm of fibres or canes*.

		IF19 (base glass fibre)	**IF23 (core glass cane)**	**IF25 (core/clad fibre)**	**IF27 (core/clad fibre)**	**IF30 (core glass cane)**	**IF31 (core glass fibre)**
Surface roughness	Sa (nm)	8.0	556.77	109.83	105.81	644.23	230.18
	Sq (nm)	12.0	793.70	148.16	135.48	930.82	479.77
Fibre loss*	dB/m	~4	~70	~180	~150	~170	247

* Fibre loss was measured using white loss measurement except for IF31 which was measured using spot loss measurement.

(c) Fibre drawing of core/clad fibres

(d) Fibre drawing of core/clad preforms were accomplished by two different methods: 1) made from stacked billets; 2) made using cane-in-tube method.

In the first method, IE24 and IE25 core/clad preforms (made using manually stacked billets) were used for fibre drawing trials IF25 and IF27, respectively. Note that IE24 preform showed relatively large amounts of crystals at the core/clad interface, whereas IE25 preform only exhibited several crystals at the interface. The stronger crystallisation for IE24 preform resulted in a higher viscosity of the glass around the core/clad interface compared to the glass in the other regions due to the presence of crystals, which increased the temperature required to form a preform drop. Hence, IF25 fibre resulting from the IE24 preform was drawn at a higher temperature than IF27 fibre (from IE25 preform). Only several pieces of fibres with length <5 m were obtained from IF25 fibre drawing trial, while IF27 fibre drawing trial yielded a ~46 m long fibre. Under the SEM, a smooth, clear core/clad interface of IF27 fibre was observed without any sign of crystallisation (Fig. 7.26), despite of several crystals or defects observed in the extruded preform.

Spot loss measurements were undertaken at 980 nm, where Pr^{3+} does not have absorption bands. The losses for IF25 and IF27 were measured to be ~180 dB/m and ~150 dB/m at 980 nm, respectively. Although the IE25 preform contained significantly smaller amounts of crystals in the core glass and at the core/clad interface compared with the IE24 preform, the fibre loss of IF27 was almost as high as that of IF25. As confirmed by micro-XRD in Fig. 7.27, the surfaces of both fibre IF25 and IF27 were covered with crystallisation on clad glass surface. As the core glass is less stable than clad glass, the impact of temperature on crystallisation is more significant on the core glass than on the clad glass during core/clad fibre drawing process. Although no obvious crystallisation was found in the core glass using both SEM and XRD measurements, there may be some nanocrystallisation occurring in the core region of IF25 and 27 below the detection limit of SEM and XRD, which contributes to the observed high loss in both IF25 and 27.

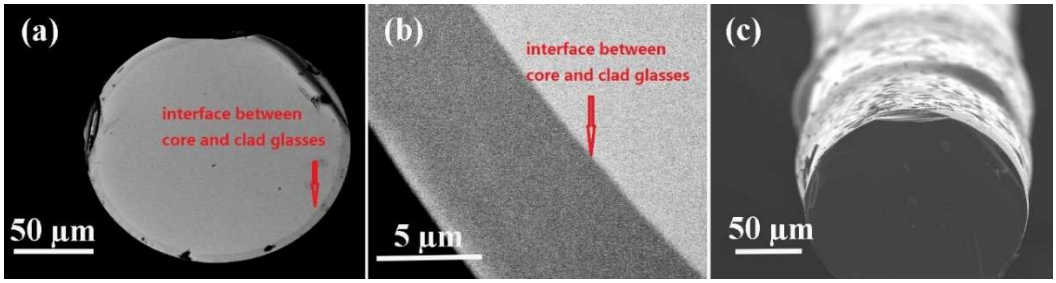

Figure 7. 26. SEM image of IF27 fibre drawn from IE25 core/clad preform: (a) fibre cross-section, (b) interface of core and clad region, (c) side view showing fibre surface roughness.

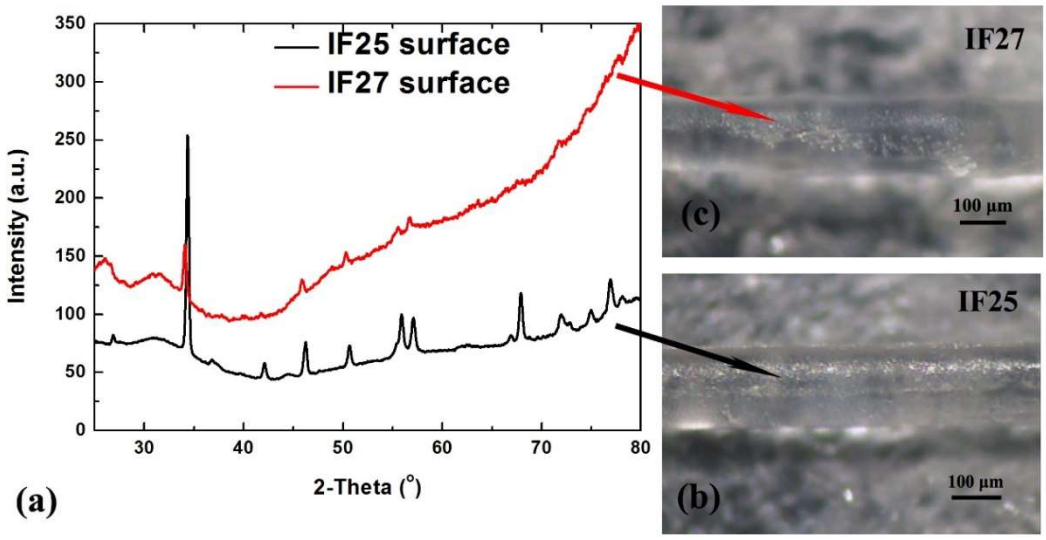

Figure 7. 27. Micro-XRD results of IF25 and 27 fibre drawn from IE24 and 25: (a) Crystallisation peaks found in micro-XRD spectrum collected from white areas on the surfaces from IF25 and 27 (b) white pattern on IF25 collected Micro-XRD measurement; and (c) white pattern on IF27 collected Micro-XRD measurement.

In the second method, he fibre drawing trials of the core/clad preform (i.e., IF26 and IF29) made using the cane-in-tube method failed and no fibre was produced. These two trials demonstrated that the core glass softened and dropped at a considerably lower temperature than the cladding glass. This behaviour is consistent with the significantly lower drawing temperature needed for core glass unstructured fibre (i.e., IF31 (735 ˚C)) and caning trials (i.e., IF23 and IF30 (685-750 ˚C)) compared with the fibre drawing trial of the cane-in-tube preform, IF26 and IF29 (750-800 ˚C (Table 7.7). Hence, the failure of the fibre drawing using core/clad preforms made by the cane-in-tube method is partly due to the large difference in glass softening temperatures (The higher the glass transition temperature (T_g), the higher the glass softening temperature) between core (T_g=299 ˚C) and cladding (T_g=308 ˚C) glasses for fibre drawing, which could be a

fundamental limitation. It is most likely that the lowest temperature at which a core and cladding fibre can be drawn is above the onset of crystallisation for the core glass. Another reason for the failure of fibre drawing using the cane-in-tube method is that under pressure could not be applied due to a problem with equipment thus suction, which can facilitate the fusion between core and clad parts, was not applied during fibre drawing. In contrast, two core/clad fibre trials (i.e., IF25 and IF27), using the stacked billet method (no suction applied), resulted in fibre pieces (i.e., IF25 and IF27) with measurable losses. The success of the stacked billet trials is due to the existing core and clad interfaces in IF25 and IF27 formed during stacked billet extrusions (i.e., IE24 and IE25). Future work is required to optimise the core glass composition and minimise the difference between core and clad glass temperatures (e.g., softening temperature and the onset of crystallisation temperature).

7.3. Conclusion

Individual rare earth ions of Er^{3+}, Pr^{3+}, Ho^{3+} or Dy^{3+}, was incorporated into fluoroindate glass for ~4 μm laser application. From the Judd-Ofelt calculation, Pr^{3+} is the most promising rare earth ion for 4 μm emission in fluoroindate glasses compared with Er^{3+}, Ho^{3+} and Dy^{3+}.

Results on glass characteristic temperatures and refractive indices showed that IM127 (core glass, (32-x) InF_3 – (20-y) ZnF_2 – 20 SrF_2 – (18-z) BaF_2 – 8 GaF_3 – 2 CaF_2– (y+z) PbF_2– xPrF_3, x=0.5, y=z=2) and IM128 (clad glass, (32-x) InF_3 – 20 ZnF_2 – 20 SrF_2 – 18 BaF_2 – 8 GaF_3 – 2 CaF_2– x LaF_3, x=0.5) were the best candidates for the step-index fibre fabrication from the viewpoint of refractive index contrast. Stacked billet extrusion and rod/cane-in-tube method using fluoroindate glasses were demonstrated to be feasible for step index fluoroindate glass fibre fabrications. The preforms extruded using stacked billet extrusion resulted in a large core/clad ratio up to 0.9. Compared to stacked billet extrusion, the rod/cane method allows the diameter of the core region to be defined by the diameter of the rod/cane made from a single material. However, both fibres and canes drawn from these preforms exhibited relatively high losses, which is attributed to both surface and volume crystallisation due to the high crystallisation tendency of the core glass.

Future work is needed to optimise core glass composition and doping concentration with better thermal stability (lower crystallisation tendency) for step-index fibre fabrications. The core glass candidate should also have similar onset crystallisation temperature (T_x) and glass softening temperature to those of the cladding glass in order to draw core and cladding fibre at a similar viscosity without crystallisation. In addition to the Judd-Ofelt calculation, spectroscopy studies of fluorescence and lifetime characterisation can further guide the pathway to the optimisation of core glass to achieve ~4 μm emission (e.g., optimisation of doping concentration for high luminescence). Furthermore, a new graphite die design is required to control the diameter ratio of a core and clad glass preform. The new graphite die design should also enable simultaneous extrusion of clad glass tube and core glass rod into a single die and fuse two glasses within the welding chamber due to the high pressure within the die.

Chapter 8

CONCLUSIONS AND FUTURE WORK

8.1. Conclusions

The PhD project contributes to the advancement of our knowledge in optimising the glass, and in developing preform and fibre fabrication processes to obtain low-loss fluoroindate glass fibres. In this work, the impact of melting conditions on the glass quality is studied. The extrusion of fluoroindate glass and drawing of fibers from extruded preforms has been demonstrated for the first time. Fibre fabrication processes have been improved via the optimisation of glass melting procedures, extrusion temperature, and application of an additional weight to the bottom of preform, etc., which minimised surface crystallisation and roughness. The reduced surface crystallisation resulted in increased mechanical strength of unstructured fibers and decreased fibre loss. The project improves our knowledge of chemical durability of fluoride glasses, particularly of the impact of alkali ions in glasses.

Different melting procedures and strategies (e.g., use of different amounts of NH_4HF_2) were developed to accommodate the variations of raw materials and batch sizes. Initially the absorption of OH groups at 2.9 μm in IZSBGC glasses was reduced by introducing a fluorination method with NH_4HF_2. To overcome the crystallisation issues due to the use of low purities of raw materials, different fluorination procedures/conditions were employed to include parameters such as temperature, NH_4HF_2 and compensation for impurities in different raw materials using different amounts of NH_4HF_2. The results of

reduced OH content also demonstrated that the glasses were successfully upscaled with minimum defects observed for billet extrusion.

The next research direction was to extrude the glass billets into unstructured preforms. Compared with the casting method for rod preparation, the extrusion method is found to be more suitable for the preparation of bubble-free preforms. Extruded rods typically exhibit a better surface finish than cast rods. The different surface finish between the extruded and cast rods can be understood by their different fabrication techniques; for instance, extruded preforms have fire polished surfaces as the hot glass cools down in free space, whereas the hot cast glass rod during casting procedure is in contact with the mould when cooling down. The use of extrusion, for the first time, also demonstrated that the preform surface properties including surface roughness and crystallisation essentially depended upon the extrusion temperature. A relatively high temperature was found to result in a smoother preform surface due to the reduced extrusion force. According to the results of annealing tests, 322 ˚C was sufficiently low to avoid potential surface crystallisation, and therefore was used for unstructured preform extrusion of the base glass.

While unstructured preforms have been prepared under optimised conditions such as melting and extrusion, crystallisation still occurred during the subsequent fibre fabrication due to a high maximum preform temperature and steep preform temperature gradient along the drawing axis using a short heating zone. Our experiments showed that the maximum preform temperature could be reduced by expanding the length of the heating zone in the drawing furnace and using additional weight at the bottom of a preform, resulting in a reduced fibre drawing temperature and surface crystallisation on both preform neck-down and fibre. The surface crystallisation observed on the preform neck-down and fibres was also significantly reduced through chemo-mechanical treatment of billets and preforms.

In addition, the study of the chemical durability and the evolution of hydrolysis reaction in deionized water has provided insight into the corrosion behaviour of IZSBGC glass relative to the established ZBLAN glass in deionized water. The reactions occurring on the glass surfaces and hydrated layers were found for both IZSBGC and ZBLAN glass surfaces. Our results suggest that the dissolution of glasses occurred initially via an ion exchange between F^- and OH^-, resulting in a decrease in pH of leaching solution.

Subsequently, the solubility of metal fluorides increased dramatically due to the decreasing pH, leading to dissolution of the glass itself. Our NaF-free IZSBGC glass has not only optimum optical properties but also good chemical durability in comparison with the NaF-containing ZBLAN glass.

Furthermore, preliminary work was carried out to prepare step index fibres for 4 μm laser application. To select a suitable rare earth element for 4 μm emission, 0.5 mol% InF_3 in IZSBGC base glass was substituted for PrF_3, ErF_3, HoF_3 and DyF_3, respectively. Judd-Ofelt calculation, reflecting the transition probabilities in doped IZSBGC glasses, demonstrated that doping of Pr^{3+} is the best choice for 4 μm emission compared with Er^{3+}, Ho^{3+} and Dy^{3+}. A pair of core and clad glasses with suitable index difference was developed by modifying the composition of the base IZSBGC glass, leading to NA>0.1 up to 5.5 μm. Although core and cladding preforms (stacked billet extruded preform and individual core and clad preforms for cane-in-tube fibre fabrication method) were successfully extruded without crystallisation, the obstacle was to reduce the surface roughness and bulk/surface crystallisation in/on the core glass during reheating in the fibre drawing process, which has been the most important transmission loss factor in step index fibres.

8.2. Future work

A research focus in the future will be to quantify the contributions of both extrinsic scattering and absorption to the loss of IZSBGC glass and fibre losses. Further understanding of the contributions of extrinsic and absorption will allow us to investigate and optimise fabrication conditions to reduce scattering and absorption losses. Further investigation of etching procedures is required to develop a suitable method for improving surface finish without colloidal silica polishing which currently limits its application to structured preforms. In addition, a better die material than the current graphite is required for extrusion. A more suitable die material needs to be inert (similar to graphite) in fluoride melts and also should have a fracture stability (similar to metals) higher than that of graphite.

Future work should also focus on development of new fluoride glass compositions with not only optimum optical property but also good durability, by decreasing the content of

alkali components (e.g., NaF) in the fluorozirconate glasses or alkaline earth components (e.g., CaF_2) in the fluoroindate glasses, both of which were found to be leached preferentially.

Our preliminary fabrication trials for step index fibre demonstrates that future work is required to improve the thermal compatibility between core and cladding glasses for successful fibre drawing. Further work is required to improve the thermal stability of both core/cladding glasses and their compatibility (e.g., a suitable difference in refractive index, similar softening temperature for fibre drawing), and optimise fibre drawing temperature to reduce the defects (i.e., high surface roughness and crystallisation of core glass during fibre drawing).

Finally, fluorescence and lifetime measurements are needed for the determination of RE dopant concentrations and fibre length to achieve ~4 μm emission for fibre laser application (e.g., high luminescence by optimisation of doping concentration). Judd-Ofelt calculation results were successful in understanding the fundamental limit of radiative decay rates (without considering non-radiative processes) of rare earth ions in IZSBGC glass in step index fibre experiments. Spectroscopy studies of fluorescence and lifetime characterisation may further determine the real radiative decay rates and compare with the calculated one using Judd-Ofelt theory.

Appendix A

An experimental study of directly cast core/clad glass billets

The established method for fluoroindate glass step-index fibre fabrication is rotational casting, whereby the interface is formed when the core glass is poured into a tube of clad glass with a temperature near the clad glass transition temperature [99]. The advantage of this method is that the core glass melt being in a liquid form enables complete fusion and wetting between the core and clad glass [245]. The good wetting behaviour prevents or reduces interface bubble formation [245] during the fabrication of a cast core/clad billet. Core/clad glass billets were made using the direct cast method and were extruded into preforms. The resulting preforms were compared with those prepared using the 'rod-in-tube' method (Chapter 7). It was found that the interface formed during casting using directly cast core/clad glass billet was similar to that resulting from the rotational casting technique. However, it is hard to prevent crystallisation between the core and clad glass interface using the direct cast method, and therefore, this method was not applied for fibre fabrication in this project.

I. Experimental details

Glass preparation procedures in this study were conducted under a dry N_2 atmosphere controlled furnace (described in Chapter 2.2) to prevent oxidation and reduce OH content in glass melting.

The first step of making a core/clad billet was to fabricate a casting glass billet (hereafter referred to as 1st glass, which could be either core or clad glass). In the next step, this 1st glass billet was placed into a cylindrical mould and pre-heated to a temperature close to or below the glass transition temperature. Simultaneously, the 2nd glass melt was prepared. Finally, the 2nd glass melt was cast onto the pre-heated 1st glass billet. The as-prepared billet can be extruded into a core/clad preform, similar to the extrusion of a stacked billet.

II. Results and discussion

The envisaged advantage of casting a core/clad billet (compared with rotational casting of a core/clad rod) is the flexibility in using the core or clad glass as the 1st glass which is reheated during the second casting step. In the rotational casting technique, the core glass (i.e. 2nd glass) needs to be cast within a tube of small inner diameter (~4 mm), requiring low viscosity for the core glass. In contrast, the core/clad billet casting technique has less stringent demand on the 2nd glass viscosity, as it is cast in a mould of 3 cm diameter. A possible challenge with the core/clad billet is to make the defect-free (no cyrstallisation, bubbles, or cracks) interface between the 1st and 2nd glasses.

To prepare a core/clad glass billet, the (clad glass billet IM133 (1st glass) was preheated to 160 ˚C, which is 40 ˚C lower than the mould temperature used for preparing individual clad glass billets. The core glass IM137 (2nd glass) was then cast onto the clad glassIM133 (Fig. A.1). At the beginning of the casting, the clad glass (1st glass) cracked instantly on a large scale, which is attributed to the low mould temperature of 160 ˚C. The core glass (2nd glass) showed serious crystallisation at the interface with the clad glass, which can be ascribed to the lower crystallisation stability of the core glass as compared to the base and clad glasses. (Section 7.3). Crystallisation occurred in the core glass, as the heat from the core glass melt could not be released from the core glass bottom (from the interface between core and clad glasses) sufficiently quickly to avoid crystallisation.

To prevent crystallization in the core glass, the clad glass melt (IM139) was cast onto the core glass billet for the next casting trial (IM138; Fig. A.1), using a mould temperature of 300 ˚C which is the T_g temperature of the core glass. In the core/clad billet, both core and clad glass exhibited a good quality except for the crystallisation at the interface between the two glasses.

The two casting trials described above suggested that the preheating mould temperature for core and clad glass should be between 160 ˚C and 300 ˚C to prevent both cracking and crystallisation. Thus, 230 ˚C was used as the mould temperature in a following trial. Again, the clad glass melt (IM142) was cast onto the core glass billet (IM141) (Fig. A.1). The core glass (1st glass) cracked slightly about 30 seconds after casting. Crystallisation still occurred at the interface between core and clad glasses.

For the subsequent two trials, a slightly higher mould temperature of 270 ˚C was used to prevent cracking of the bottom glass. Similar to the procedures described above, clad glass melts (IM145, IM146) were cast onto core glass billets (IM143, IM144) (Table A.1 and A.2). For these two trials, both the clad (2nd glasses) and core glasses (1st glasses) cracked. The difference between these two trials was the waiting time before casting.

In conclusion, direct casting of core/clad glass billets (casting 2nd glass on top of 1st glass) is limited by the restricted heat release during casting of the 2nd glass, due to close contact between the 2nd glass melt and the 1st glass billet. The reduced heat release, i.e. reduced cooling rate, can cause crystallisation at the interface of core and clad glass or in the centre of the 2nd glass. An alternative approach is to cast the clad glass around the core glass using a mould with a larger diameter. In this way, the clad glass (2nd cast glass) can be in contact with the mould with a large surface area, which may facilitate the release of the heat and thus prevent crystallisation.

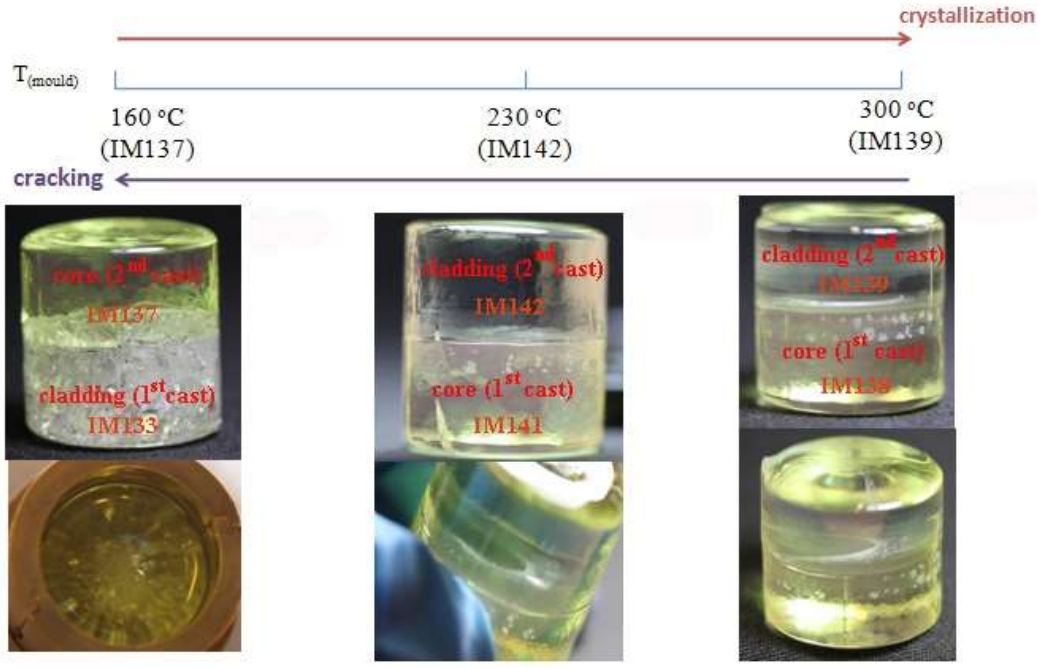

Figure A. 1. Photographs of directly cast core/clad glass billets.

Table A. 1. Results for IZSBGC clad glass melts*.

melt trial	batch weight	cast weight	yield	evaporative loss	fluorination time	melt time	time before casting	mould temp.
IM133	60g	54.1g	90%	1.9%	70mins	2.5h	101s	200˚C
IM139 (remelt IM133)	49g	43.8g	90%	0.3%	n/a	1.0h	94s	300˚C
IM142	60g	53.8g	90%	2.0%	60mins	2.5h	102s	230˚C
IM145 (remelt IM142)	58g	53.0g	92%	0.3%	n/a	1.0h	119s	270˚C
IM146 (remelt IM145)	58g	54.5g	95%	0.3%	n/a	1.0h	119s	270˚C

*: For all batch melts: fluorination was conducted at 450˚C using 2.4wt% excess NH_4HF_2, no use of excess InF_3 or GaF_3, 100mL Pt crucible, 900 ˚C melting and casting temperature.

Table A. 2. Results for IZSBGC Pr-doped glass melts including core glass melts*.

melt trial	batch weight	cast weight	yield	evaporative loss	fluorination time	melt time	time before casting	mould temp.
IM134	60g	55.7g	93%	2.20%	70mins	2.5h	100s	200˚C
IM135	60g	54.6g	91%	2.09%	70mins	2.5h	101s	200˚C
IM137	60g	54.8g	91%	2.8%	60mins	2.5h	106s	160˚C
IM138 (remelt IM137)	58g	53.0g	91%	0.4%	n/a	1.0h	93s	200˚C
IM141 (remelt IM134)	60g	56.5g	93%	0.2%	n/a	1.0h	95s	200˚C
IM143 (remelt IM135 and IM141)	58g	52.8g	92%	0.01%	n/a	1.0h	96s	200˚C
IM144 (remelt IM141)	56g	51.7g	93%	0.3%	n/a	1.0h	95s	270˚C

*: For all batch melts: fluorination was conducted at 450˚C using 2.4wt% excess NH_4HF_2, no use of excess InF_3 or GaF_3, 100mL Pt crucible, 900 ˚C melting and casting temperature.

Appendix B

Temperature profile study of a drawing tower furnace

This work is part of an interim report (by Heike Ebendorff-Heidepriem and me, 2013) to the project sponsor, Defence Science and Technology Group (DSTG), Adelaide, Australia [246]. In the DSTG report, I did all the experimental work, collected all analysis data, interpreted part of the data, and drafted part of the report, with extra data interpretation, writing, and collation of the report done by Heike (my PhD principal supervisor who was the project leader of the DSTG project).

In reality, a hot zone in a drawing tower furnace does not exhibit a constant temperature but rather an axial temperature gradient/profile with significant changes in temperature and a Gaussian-like distribution [115, 247, 248]. Furnace temperature profiles vary between drawing towers and furnace designs, depending on the particular setup of the furnace (susceptors and gas flows may be varied). In order to identify such fluctuations of temperature, it is necessary to understand the drawing process and identify the relevant parameters. In addition, to avoid crystallisation during fibre drawing, the glass temperature of the preform needs to be lower than the onset of the crystallisation temperature. During fibre drawing, the furnace temperature is controlled via a thermocouple placed inside the susceptor, which is heated via induction heating. However, the actual temperature of the glass preform within the susceptor cannot be monitored. Thus in order to determine the actual glass temperature of a preform at a certain susceptor temperature (hereafter referred to as furnace temperature), temperature profile of the

drawing furnace experiments were conducted to determine which susceptor was suitable for fluoroindate glass fibre drawing.

Sakaguchi et al demonstrated that extending the heating zone of the fibre drawing tower reduced surface crystallisation in the neck-down region [120]. In contrast, shorter susceptor length reduces the time the glass is exposed to elevated temperatures. To investigate the impact of heating zone length on IZSBGC glass temperature for our tower and ultimately on IZSBGC fibre loss and strength, two different susceptor lengths (2 cm and 4.5 cm) were used in this study.

I. Experimental details

An IZSBGC glass tube was fabricated prior to the temperature profile experiments. The tube preform was extruded at a temperature and speed, at which the force applied was predicted to be similar to that used for extrusion of an unstructured preform. The tube was extruded at 324 ˚C using an extrusion speed of 0.02 mm/min, resulting in a force of ~2 kN. This temperature was 2 ˚C higher than that of an unstructured preform extrusion (322 ˚C) as the friction between the glass and die increased due to the additional internal surface. This extrusion trial successfully yielded a tube with a good optical quality and structure.

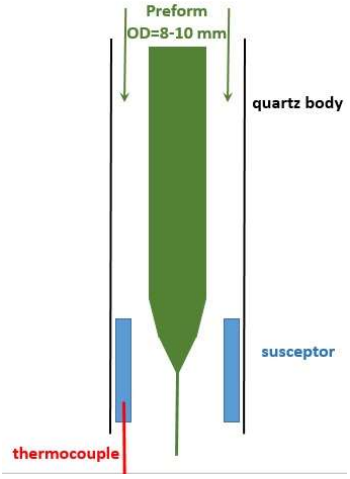

Figure B. 1. Sketch of fibre drawing furnace.

Table B.1 summarises the temperature profile conditions. In the temperature profile experiments, a thermocouple (accurate to 0.4 ˚C) (Fig. B.1) was inserted into the air hole of a tube with an outer and inner diameter of 10 and 2 mm, respectively. The temperature measured with this thermocouple is assumed to be equivalent to the glass temperature. The tube containing the thermocouple was placed into the tower furnace and moved axially (vertically) along the susceptor centre line. The thermocouple was in physical contact with the inner surface of the tube to ensure good thermal contact with the glass. The lower end of the tube was sealed via forming a drop using the drawing tower to prevent ingress of gas into the tube, which might result in glass cooling and would not happen during fibre drawing. Two different methods of profiling were conducted:

(1) static: The tube was placed to a certain axial position with 15 mm/min and the temperature was recorded after 5-10 min dwell time at this position. This method ensures thermal equilibrium.

(2) dynamic: The tube was continuously moved down using a preform feed speed of 1.4mm/min that is typically used for fibre drawing. The tube position and corresponding temperature was recorded in regular intervals.

Using these methods of profiling, the glass temperature has to be below the temperature where the glass starts to deform to allow re-usage of the tube. Similar profiling experiments for silica demonstrated that there is a linear relationship between the peak temperature of the axial temperature profile of the glass tube within the drawing tower furnace and the furnace temperature, enabling linear extrapolation to furnace temperatures used for fibre drawing [247].

II. Results and discussion

The peak glass temperatures and corresponding axial positions for the various furnace temperatures used are listed in Tables B.2 and B.3.

For example, Fig. B.2 shows the axial temperature profile for static and dynamic measurements at different furnace temperature. To compare the temperature profile of the two susceptors, the profiles with similar peak temperature (measured using dynamic

method) were plotted in Fig. B.3). It is obvious that the 2 cm susceptor yields a steeper temperature gradient and a shorter hot zone.

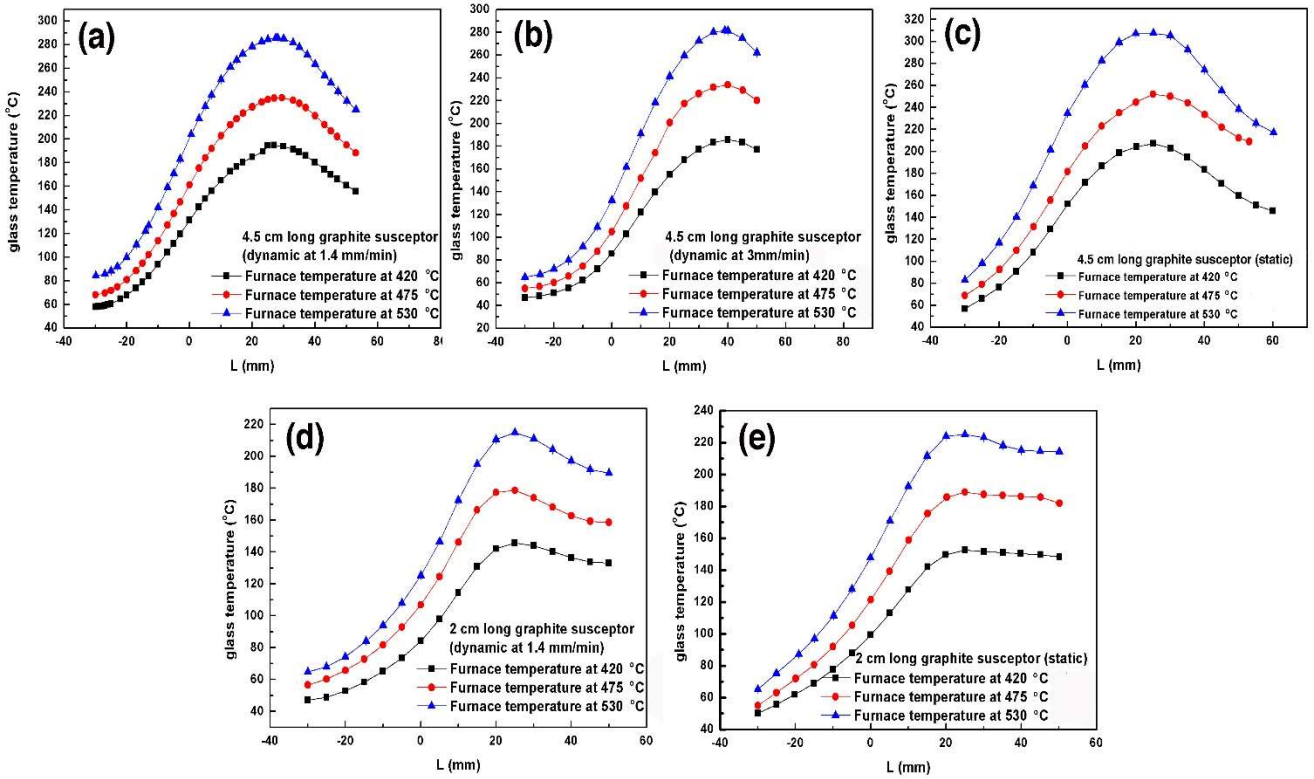

Figure B. 2. Measured glass temperature as a function of furnace temperature for static and dynamic measurement method using IZSBGC glass tube. For 4.5 cm long graphite susceptor (a) dynamic at 1.4 mm/min; (b) dynamic at 3 mm/min; (c) static. For 2 cm long graphite susceptor (d) dynamic at 1.4 mm/min; (e) static. The axial position L=0 coincides approximately with the top of the susceptor for both 2 and 4.5 cm susceptors; L=45 mm for 4.5 cm long susceptor and L=20 mm for 2 cm long susceptor coincide approximately with the bottom of the corresponding susceptor.

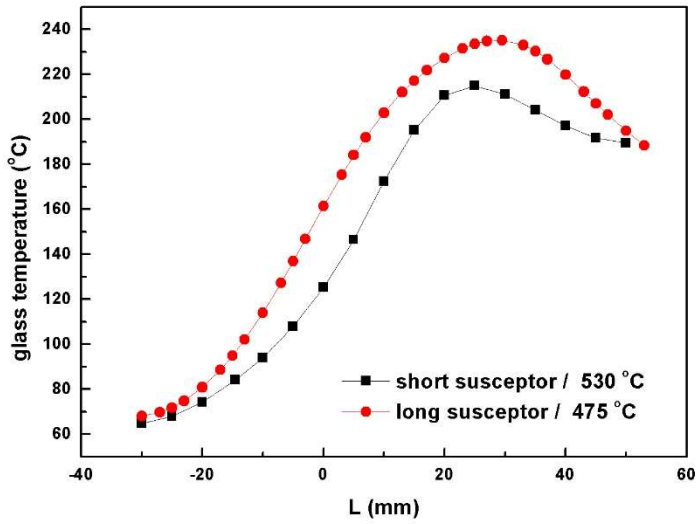

Figure B. 3. Glass temperature profile for dynamic (1.4mm/min) measurement method using IZSBGC glass tube and 4.5 cm and 2 cm susceptor. The axial positions L=0 and L=45mm coincide approximately with the top and bottom of the susceptor.

In an earlier study [247], furnace temperature profile measurements proved that there was a linear relationship between the specified furnace temperature and measured peak temperature. Since the furnace temperature measurements were conducted at lower temperatures, the measured values of peak temperatures and the specified peak temperature was compared by extrapolating temperatures to the range of interest (550~900 ˚C) (in Fig. B.4). For the 4.5 cm susceptor, the peak glass temperature of the dynamic method (1.4 mm/min) is 12-22 ˚C lower than that of the static (isothermal) method for all three furnace temperatures used (Fig. B.4, Tables B.2 and B.3). By comparison, for the 2 cm susceptor, the peak glass temperature of the dynamic method is only 7-10 ˚C lower than that of the static method. These results show that for the 4.5 cm susceptor the temperature difference between static and dynamic method is larger than for the 2 cm susceptor. Comparison of different preform feed rates of IZSBGC temperature profiling measurements suggests that the larger feed rate of 3 mm/min results only in 5-9 ˚C lower peak glass temperatures compared with the slower feed rate of 1.4 mm/min. The smaller temperature difference between the static and dynamic cases for the 2 cm susceptor compared with the 4.5 cm susceptor suggests that the IZSBGC glass is heated up faster using the 2 cm susceptor.

The glass viscosity range suitable for fibre drawing is 10^3-10^5 Pa.s. The viscosity range suitable for fibre drawing was found to correspond to a temperature range of 361-379 ˚C

by extrapolating the *Arrhenius* fit for the temperature-viscosity data given in Chapter 4. This temperature range is below the onset of glass crystallisation (T_x) for IZSBGC (389 ˚C in Chapter 3).

The furnace temperatures used for fibre drawing were 890 ˚C for IF12 using the 2 cm susceptor, 820 ˚C for IF17 using the 4.5cm susceptor and 725 ˚C for the low-loss fibre IF19 using 4.5 cm susceptor with an additional weight of 190 g applied. Note that for IF19, the relatively low furnace draw temperature of 725 ˚C relates to the draw regime where no surface crystallisation was found on the preform neck-down, i.e. enhanced furnace temperature due to surface hardening as a result of surface crystallisation did not play a role. Figure B.4 shows the corresponding peak glass temperatures for static and dynamic methods using both the 2 cm and 4.5 cm susceptors and linear extrapolation of measured values in Table B.2 and B.3. For both susceptors and methods, the furnace temperatures of fibre drawing correspond to peak glass temperatures considerably higher than the predicted drawing temperature range and T_x. This discrepancy may be due to the following possible reasons:

(1) extrapolation of measured temperature and viscosity data is not valid;
(2) the temperature profile from the tube method is different from that for a solid unstructured preform;
(3) in the temperature profiling experiment, only a single point in the cross section of a preform is measured, and the tube surface was not etched as for fibre drawing of rods.

Further profiling experiments are required to obtain a better understanding of the experimental conditions on the measured temperature values.

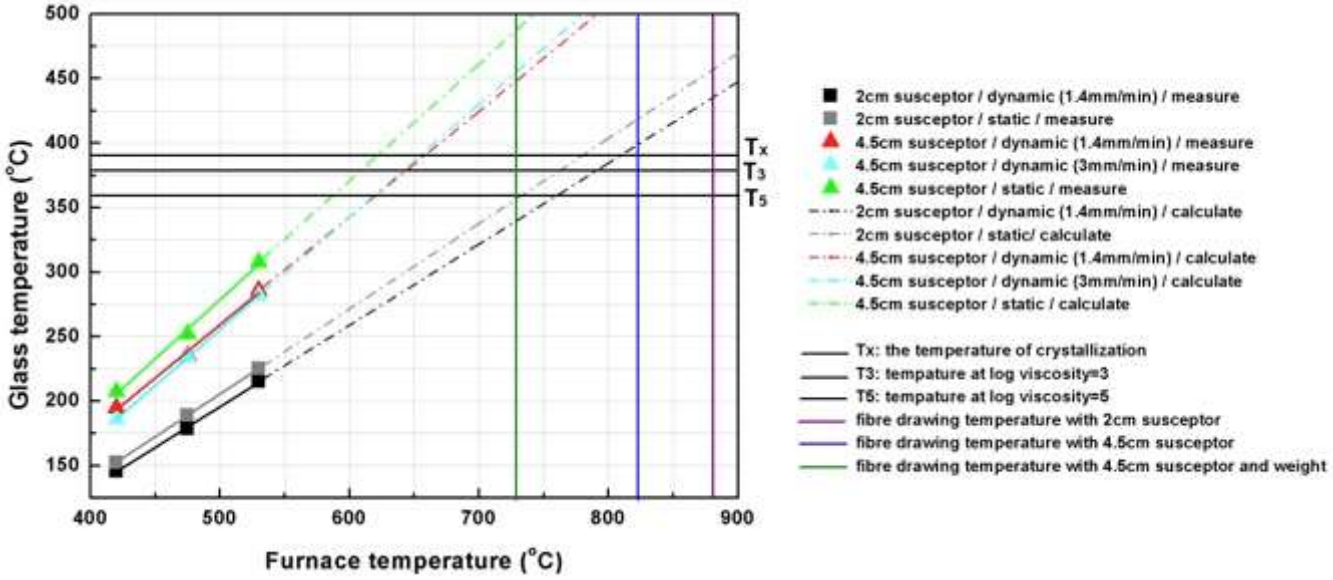

Figure B. 4. Peak glass temperature as a function of furnace temperature for dynamic and static measurements of IZSBGC glass using 4.5 cm and 2 cm graphite susceptors. ('dynamic' and 'dynamic*' refer to 1.4 and 3 mm/min feed rate, T_3 and T_5 are the temperatures at viscosities of 10^3 and 10^5 Pa.s and are the high- and low-temperature limit for fibre drawing, T_x is the onset temperature of glass crystallisation. Fibre drawing temperature vertical lines in blue and green were used for IF17 and IF19, respectively).

Table B. 1. Experimental details of IZSBGC glass profiling.

Glass	IZSBGC (base glass) tube (inner diameter: 2mm, outer diameter: 10mm)
Susceptor material	2cm or 4.5 cm graphite
Furnace temperatures	420 ˚C, 475 ˚C, 530 ˚C
N_2 flow	7L/min (top), 2L/min (bottom) (±0.1L/min)
Axial positions	0mm~95mm (±0.1mm)
Feed speed	static: 5mm/min (±0.01mm/min); dynamic: 1.4mm/min or 3.0mm/min (±0.01mm/min)
Day 1	420 ˚C (static)
Day 2	530 ˚C (static)
Day 3	475 ˚C (static)
Day 4	420 ˚C (static), 475 ˚C (dynamic), 530 ˚C (dynamic)

Table B. 2. Summary of peak glass temperature at different furnace temperatures for 4.5 cm susceptor.

Furnace temperature	420 ˚C	475 ˚C	530 ˚C	420 ˚C	475 ˚C	530 ˚C
Method	static	static	Static	dynamic (1.4mm/min)	dynamic (1.4mm/min)	dynamic (1.4mm/min)
Peak glass temperature	207.1 ˚C	252.1 ˚C	307.6 ˚C	194.8 ˚C	235.1 ˚C	285.7 ˚C
Position of peak glass temperature	25.1mm	25mm	25.1mm	27mm	29.5mm	28.1 mm

Table B. 3. Summary of peak glass temperature at different furnace temperatures for 2 cm susceptor.

Furnace temperature	420 ˚C	475 ˚C	530 ˚C	420 ˚C	475 ˚C	530 ˚C
Method	static	static	static	dynamic (1.4mm/min)	dynamic (1.4mm/min)	dynamic (1.4mm/min)
Peak glass temperature	152.5 ˚C	189.0 ˚C	225.2 ˚C	145.7 ˚C	178.7 ˚C	215.0 ˚C
Position of peak glass temperature	25mm	25mm	25mm	25mm	25mm	25 mm

BIBLIOGRAPHY

1. C. K. Kao, and H. G. A., "Dielectric-fiber surface waveguides for optical frequencies," in *Proc. IEE*(1966), pp. 1151-1158.
2. F. P. Kapron, D. B. Keck, and R. D. Maurer, "Radiation losses in glass optical waveguides," Appl. Phys. Lett. **17**, 423-425 (1970).
3. M. Horiguchi, and H. Osanai, "Spectral losses of low-OH-content optical fibres," Electron. Lett. **12**, 310-312 (1976).
4. R. Csencsits, P. J. Lemaire, W. A. Reed, D. S. Shenk, and K. L. Walker, "Fabrication of low-loss single-mode fibers," in *OFC'84* (1984), pp. 54-55.
5. H. Yokota, H. Kanamori, Y. Ishiguro, G. Tanaka, S. Tanaka, H. Takada, M. Watanabe, S. Suzuki, K. Yano, M. Hoshikawa, and H. Shimba, "Untra-low-loss pure-silica-core single-mode fiber and transmission experiment," in *OFC'86*(1986), pp. 11-18.
6. J. R. Taylor, "Infrared Optical Fibres," Journal of Modern Optics **36**, 1548 - 1549 (1989).
7. S. Shibata, M. Horiguchi, K. Jinguji, S. Mitachi, T. Kanamori, and T. Manabe, "Prediction of loss minima in infra-red optical fibres," Electron. Lett. **17**, 775-777 (1981).
8. J. R. Gannon, "Optical fibre materials for operating wavelengths larger than 2 μm," J. Non-Cryst. Solids **42**, 239-245 (1980).
9. J. A. Harrington, *Infrared fibers and their applications* (Technology & Engineering, 2004).
10. A. de, uacute, L. jo, iacute, E. E. s, A. S. L. Gomes, C. B. jo, Y. Messaddeq, A. Florez, and M. A. Aegerter, "Frequency upconversion of orange light into blue light in Pr^{3+}-doped fluoroindate glasses," Physical Review B **50**, 16219 (1994).
11. M. R. Oermann, H. Ebendorff-Heidepriem, Y. Li, T.-C. Foo, and T. M. Monro, "Index matching between passive and active tellurite glasses for use in microstructured fiber lasers: Erbium doped lanthanum-tellurite glass," Opt. Express **17**, 15578-15584 (2009).
12. H. T. Munasinghe, A. Winterstein-Beckmann, C. Schiele, D. Manzani, L. Wondraczek, S. Afshar V, T. M. Monro, and H. Ebendorff-Heidepriem, "Lead-germanate glasses and fibers: a practical alternative to tellurite for nonlinearfiber applications," Optical Materials Express **3**, 1488-1503 (2013).
13. A. Akella, E. A. Downing, and L. Hesselink, "New fluoroindate glass compositions," J. Non-Cryst. Solids **213-214**, 1-5 (1997).
14. D. G. Lancaster, S. Gross, H. Ebendorff-Heidepriem, M. J. Withford, T. M. Monro, and S. D. Jackson, "Efficient 2.9 μm fluorozirconate glass waveguide chip laser," Opt. Lett. **38**, 2588-2591 (2013).
15. G. Rault, J. L. Adam, F. Smektala, and J. Lucas, "Fluoride glass compositions for waveguide applications," J. Fluor. Chem. **110**, 165-173 (2001).
16. G. Tao, and A. F. Abouraddy, "Drawing robust infrared optical fibers from preforms produced by efficient multimaterial stacked coextrusion," (2014), pp. 89820F-89820F-89827.

17. A. A. Wilhelm, C. Boussard-Plédel, Q. Coulombier, J. Lucas, B. Bureau, and P. Lucas, "Development of Far-Infrared-Transmitting Te Based Glasses Suitable for Carbon Dioxide Detection and Space Optics," Advanced Materials **19**, 3796-3800 (2007).
18. H. Lin, K. Liu, E. Y. B. Pun, T. C. Ma, X. Peng, Q. D. An, J. Y. Yu, and S. B. Jiang, "Infrared and visible fluorescence in Er^{3+}-doped gallium tellurite glasses," Chemical Physics Letters **398**, 146-150 (2004).
19. H. Lin, X. Y. Wang, L. Lin, D. L. Yang, T. K. Xu, J. Y. Yu, and E. Y. B. Pun, "Spectral parameters and visible fluorescence of Sm^{3+} in alkali-barium-bismuth-tellurite glass with high refractive index," Journal of Luminescence **116**, 139-144 (2006).
20. Z. Pan, and S. H. Morgan, "Raman spectra and thermal analysis of a new lead–tellurium–germanate glass system," J. Non-Cryst. Solids **210**, 130-135 (1997).
21. R. Reisfeld, and J. Hormadaly, "Optical intensities of holmium in tellurite, calibo, and phosphate glasses," The Journal of Chemical Physics **64**, 3207-3212 (1976).
22. S. Q. Man, E. Y. B. Pun, and P. S. Chung, "Tellurite glasses for 1.3 μm optical amplifiers," Opt. Commun. **168**, 369-373 (1999).
23. X. Feng, W. H. Loh, J. C. Flanagan, A. Camerlingo, S. Dasgupta, P. Petropoulos, P. Horak, K. E. Frampton, N. M. White, J. H. Price, H. N. Rutt, and D. J. Richardson, "Single-mode tellurite glass holey fiber with extremely large mode area for infrared nonlinear applications," Opt. Express **16**, 13651-13656 (2008).
24. G. Ghosh, "Sellmeier Coefficients and Chromatic Dispersions for Some Tellurite Glasses," J. Am. Ceram. Soc. **78**, 2828-2830 (1995).
25. DM McPherson, and S. Murray, "Germanate glass for mid-infrared medical optical fiber," in *United States Patent*, U. S. Patent, ed. (1996).
26. J. Lucas, M. Chanthanasinh, M. Poulain, M. Poulain, P. Brun, and M. J. Weber, "Preparation and optical properties of neodymium fluorozirconate glasses," J. Non-Cryst. Solids **27**, 273-283 (1978).
27. A. Jha, S. Shen, and M. Naftaly, "Structural origin of spectral broadening of 1.5-mum emission in Er^{3+}-doped tellurite glasses," Physical Review B **62**, 6215 (2000).
28. J. A. Harrington, "Infrared fiber optics," OSA Handbook **3**, 1-13 (2001).
29. S. Kobayashi, Shibata, N., Shibata, S., and Izawa, T., "Characteristics of optical fibers in infrared wavelength region," Review of the Electrical Communication Laboratory **226**, 453-467 (1978).
30. V. S. Shiryaev, and M. F. Churbanov, "Trends and prospects for development of chalcogenide fibers for mid-infrared transmission," J. Non-Cryst. Solids **377**, 225-230 (2013).
31. J. S. Sanghera, L. B. Shaw, P. Pureza, V. Q. Nguyen, D. Gibson, L. Busse, I. D. Aggarwal, C. M. Florea, and F. H. Kung, "Nonlinear Properties of Chalcogenide Glass Fibers," International Journal of Applied Glass Science **1**, 296-308 (2010).
32. A. B. Seddon, "Chalcogenide glasses: a review of their preparation, properties and applications," J. Non-Cryst. Solids **184**, 44 (1995).
33. E. B. Ford, and J. A. SAvage, "A furnace for the synthesis of chalcogenide glasses," Journal of Physics E: Scientific Instruments **9**, 622 (1976).
34. K. Richardson, D. Krol, and K. Hirao, "Glasses for Photonic Applications," International Journal of Applied Glass Science **1**, 74-86 (2010).
35. M. Castillo, T. Steinberg, and T.-C. Ong, "ZBLAN glass synthesis in reduced gravity at the QUT Drop Tower Facility," in *40th COSPAR Scientific Assembly*(Moscow, Russia, 2014).

36. Y. Messaddeq, A. Delben, M. Boscolo, M. A. Aegerter, A. Soufiane, and M. Poulain, "New fluoroindate glass compositions," J. Non-Cryst. Solids **161**, 210-212 (1993).
37. G. Tao, H. Ebendorff-Heidepriem, A. M. Stolyarov, S. Danto, J. V. Badding, Y. Fink, J. Ballato, and A. F. Abouraddy, "Infrared fibers," Adv. Opt. Photon. **7**, 379-458 (2015).
38. T. I. M.R. Shahriari, G.H. Sigel, G. Merberg, "Synthesis and Characterization of Aluminum Fluoride-Based Glasses and Optical Fibers," Mater. Sci. Forum **32-33**, 99-105 (1985).
39. M. Poulain, M. Poulain, and J. Lucas, "Verres fluores au tetrafluorure de zirconium proprietes optiques d'un verre dope au Nd^{3+}," Mater. Res. Bull. **10**, 243-246 (1975).
40. J. Qui, K. Maeda, A. Konishi, R. Terai, and K. Kadono, "Influence of various divalent metal fluorides on the properties of glasses in the ZrF_4-AlF_3 system," J. Non-Cryst. Solids **184**, 109-113 (1995).
41. D. R. H. S-H. Ko, "Infrared Spectra and Structure of Fluorozirconate Glasses," Physics and Chemistry of Glasses **32**, 196-201 (1991).
42. L. N. Ignatieva, and V. M. Bouznik, "The quantum chemical study of the fluoride and oxyfluoride glass structure," J. Non-Cryst. Solids **258**, 131-139 (1999).
43. X. Zhu, and N. Peyghambarian, "High-power ZBLAN glass fiber lasers: review and prospect," Adv. Optoelectron. **2010**, article ID 501956 (2010).
44. C. Benhamidèche, A. Boutarfaia, and M. Poulain, "Fluoroaluminate glasses," Journal of Alloys and Compounds **366**, 233-240 (2004).
45. W. A. S. D.C. Yeh, "Upconversion Processes in Heavy Metal Fluoride Glasses," Mater. Sci. Forum **32 - 33**, 543-549 (1988).
46. Hong Hu, F. Lin, Y. Yuan, and J. Feng, "Effect of Rare Earth Fluoride on Properties of Fluoroaluminate Glass," Mater. Sci. Forum **67-68**, 239-244 (1991).
47. J. Yang, S. Dai, Y. Zhou, L. Wen, L. Hu, and Z. Jiang, "Spectroscopic properties and thermal stability of erbium-doped bismuth-based glass for optical amplifier," Journal of Applied Physics **93**, 977-983 (2003).
48. J.-J. Videau, J. Portier, and B. Piriou, "Raman spectroscopic studies of fluorophosphate glasses," J. Non-Cryst. Solids **48**, 385-392 (1982).
49. Y. Kawamoto, and A. Kono, "Raman spectroscopic study of AlF_3-CaF_2-BaF_2 glasses," J. Non-Cryst. Solids **85**, 335-345 (1986).
50. C. Haiyan, and G. Fuxi, "Vibrational spectra and structure of AlF_3-YF_3 fluoride glasses," J. Non-Cryst. Solids **112**, 272-276 (1989).
51. Y. Akasaka, T. Nanba, H. Inoue, T. Osuka, and I. Yasui, "Structural analysis of AlF_3-CaF_2-YF_3 glass by diffraction methods," J. Non-Cryst. Solids **140**, 249-254 (1992).
52. A. S. Oliveira, E. A. Gouveia, M. T. de Araujo, A. S. Gouveia-Neto, C. B. de Arau´jo, and Y. Messaddeq, "Twentyfold blue upconversion emission enhancement through thermal effects in Pr^{3+}/Yb^{3+}-codoped fluoroindate glasses excited at 1.064 μm," Journal of Applied Physics **87**, 4274–4278 (2000).
53. N. Rakov, G. S. Maciel, C. B. de Arau´jo, and Y. Messaddeq, "Energy transfer assisted frequency upconversion in Ho^{3+} doped fluoroindate glass," Journal of Applied Physics **91**, 1272 (2002).
54. P. P. Fedorov, and et al., "Fluoroindate glasses," Russian Chemical Reviews **69**, 705 (2000).
55. M. Saad, "Fluoride glass fiber: state of the art," in *Proc. SPIE*(2009), pp. 73160N-73161- 73160N-73116

56. J. J. Videau, B. Dubois, and J. Portier, " Verres a base de fluorure d'indium," C. R. Acad. Sci. Paris **297**, 483-485 (1983).
57. L. N. Ignatieva, N. V. Surovtsev, V. G. Plotnichenko, V. V. Koltachev, E. B. Merkulov, S. A. Polyshchuk, and V. M. Bouznik, "The peculiarities of fluoride glass structure. Spectroscopic study," J. Non-Cryst. Solids **353**, 1238-1242 (2007).
58. A. Boutarfaia, M. A. Poulain, M. J. Poulain, and S. E. Bouaoud, "Fluoroindate glasses based on the InF_3-BaF_2-YF_3 system," J. Non-Cryst. Solids **213-214**, 36-39 (1997).
59. A. Boutarfaia, M. Legouera, and M. Poulain, "Glass formation and crystallization kinetics in a multicomponent fluoride glass," J. Non-Cryst. Solids **291**, 176-180 (2001).
60. I. D. Aggarwal, and G. Lu, *Fluoride glass fiber optics* (Academic Press, 1991).
61. B. Szigeti, "Compressibility and Absorption Frequency of Ionic Crystals," Proceedings of the Royal Society of London A: Mathematical, Physical and Engineering Sciences **204**, 51-62 (1950).
62. P. W. France, *Fluoride glass optical fibres* (Blackie, 1990).
63. D. A. Pinnow, T. C. Rich, F. W. Ostermayer, and M. DiDomenico, "Fundamental optical attenuation limits in the liquid and glassy state with application to fiber optical waveguide materials," Applied Physics Letters **22**, 527-529 (1973).
64. H. Poignant, "Dispersive and scattering properties of a ZrF_4 based glass," in *Electron. Lett.*(Institution of Engineering and Technology, 1981), pp. 973-974.
65. Musikant, *Optical Materials* (Taylor & Francis, 1990).
66. J. Schroeder, R. Mohr, P. B. Macedo, and C. J. Montrose, "Rayleigh and Brillouin Scattering in K_2O–SiO_2 Glasses," J. Am. Ceram. Soc. **56**, 510-514 (1973).
67. D. C. Tran, K. H. Levin, R. J. Ginther, G. H. Sigel, and A. J. Bruce, "Light scattering in heavy-metal fluoride glasses in infra-red spectral region," Electron. Lett. **22**, 117-118 (1986).
68. D. C. Tran, C. F. Fisher, and G. H. Sigel, "Fluoride glass preforms prepared by a rotational casting process," Electron. Lett. **18**, 657-658 (1982).
69. D. C. Tran, K. H. Levin, C. F. Fisher, M. J. Burk, and G. H. Sigel, "Rayleigh scattering in fluoride glass optical fibres," in *Electron. Lett.*(Institution of Engineering and Technology, 1983), pp. 165-166.
70. J. S. V.G. Tsoukala, G.A. Floudas, David A. Thompson, "Intrinsic Rayleigh Scattering in Fluoride Glasses," Mat. Sci. Forum **19-20**, 637-646 (1987).
71. V. G. T. J. Schroeder, Allan J. Bruce, C. Staller, J.J. Hutta, Michael J. Suscavage, M.G. Drexhage, "Composition and Structural Relaxation Effects on the Intrinsic Rayleigh Scattering of Halide Glasses: Annealing Studies," Mat. Sci. Forum **6**, 561-570 (1985).
72. J. Schroeder, V. Tsoukala, C. O. Staller, M. A. Stiller, A. Bruce, C. T. Moynihan, J. J. Hutta, M. J. Suscavage, and M. Drexhage, "Heavy metal fluoride glasses with low intrinsic Rayleigh scattering," in *Electron. Lett.*(Institution of Engineering and Technology, 1984), pp. 860-862.
73. T. Kanamori, and S. Sakaguchi, "Preparation of Elevated NA Fluoride Optical Fibers," Jpn. J. Appl. Phys. **25**, 3 (1986).
74. J. Lucas, "Fluoride glasses," J. Mater. Sci. **24**, 1-13 (1989).
75. S. Mitachi, Y. Terunuma, Y. Ohishi, and S. Takahashi, "Reduction of impurities in fluoride glass fibers," J. Lightwave Technol. **2**, 587-592 (1984).
76. P. Kaiser, "Spectral losses of unclad fibers made from high-grade vitreous silica," Applied Physics Letters **23**, 45-46 (1973).
77. H. G. Lipson, J. J. Larkin, B. Bendow, and S. S. Mitra, "Molecular-impurity

absorption in KC1 for infrared laser windows," Journal of Electronic Materials **4**, 1-24 (1975).
78. M. Robinson, R. C. Pastor, R. R. Turk, D. P. Devor, M. Braunstein, and R. Braunstein, "Infrared-transparent glasses derived from the fluorides of zirconium, thorium, and barium," Mater. Res. Bull. **15**, 735-742 (1980).
79. Yasutake Ohishi, Shigeki Sakaguchi, and S. Takahashi, "Photoluminescence and Absorption of a Zirconium Fluoride Glass and ZrF_4 " J. Am. Ceram. Soc. **70**, c81-c83 (1987).
80. A. J. Drehman, "Viscous Flow vs Phase Separation During Calorimetric Analysis of Fluoride Glasses," J. Am. Ceram. Soc. **69**, c306-c307 (1986).
81. S. Varma, S. E. Prasad, I. Murley, and T. A. Wheat, "Use of microgravity for investigating phase separation and crystallization in a heavy metal fluoride glass," (1992), pp. 14-25.
82. R. Lebullenger, S. Benjaballah, C. Le Deit, and M. Poulain, "Systematic substitutions in ZBLA and ZBLAN glasses," J. Non-Cryst. Solids **161**, 217-221 (1993).
83. W. Vogel, "Phase separation in glass," J. Non-Cryst. Solids **25**, 170-214 (1977).
84. N. J. Kreidl, and M. S. Maklad, "Effect of Water Content on Phase Separation in Soda-Silica Glasses," J. Am. Ceram. Soc. **52**, 508-509 (1969).
85. S. Mitachi, T. Miyashita, and T. Kanamori, "Fluoride-glass-cladded optical fibres for mid-infra-red ray transmission," Electron. Lett. **17**, 672-673 (1981).
86. N. Norimatsu, Y. Noda, T. Nakaki, O. Shinbori, and Y. Mimura, "Scattering Characteristics of Fluoride Glass Fibers Prepared by Tubular-Crucible Technique," Mater. Sci. Forum **67-68**, 341-346 (1991).
87. U. Senapati, and H. S. Lee, "Graded index lens for fiber optic applications and technique of fabrication," (Google Patents, 2001).
88. J. Fan, J. R. Mitchell, and J. M. V. Blanshard, "A computer simulation of the dynamics of bubble growth and shrinkage during extrudate expansion," Journal of Food Engineering **23**, 337-356 (1994).
89. M. W. Moore, P. W. France, and S. F. Carter, "Scattering losses in fluoride glass fiber," Mater. Sci. Forum **32-33**, 457 (1988).
90. P. McNamara, and D. R. MacFarlane, "Bubbles in heavy metal fluoride glasses," J. Non-Cryst. Solids **95-96**, 625-632 (1987).
91. I. D. Aggarwal, J. S. Sanghera, B. B. Harbison, L. Busse, and P. Pureza, "Origin and Reduction of Scattering Losses in Fluoride Glasses and Fibers," Mater. Sci. Forum **67-68**, 443-452 (1991).
92. S. F. Carter, P. W. France, M. W. Moore, and J. R. Williams, "Extrinsic Scatter Losses In ZrF_4-Based Infrared Fibres," Mater. Sci. Forum **5-6**, 397-403 (1985).
93. A. Hruby, "Evaluation of glass-forming tendency by means of DTA," Czechoslovak Journal of Physics **12**, 1187 (1972).
94. M. P. Mohammed Saad, "Glass Forming Ability Criterion," Mater. Sci. Forum **19 - 20**, 11-18 (1987).
95. M. R. S. T. Iqbal, G.H. Sigel Jr., "A new Glass Forming Ability Criterion for Multicomponent Halide Glasses," Mater. Sci. Forum **67-68**, 225-232 (1991).
96. Lili. Hu, and Z. Jiang, "A New Criterion for Crystallization of Glass," Journal of the Chinese Ceramic Society **180**, 315-321 (1990).
97. Y. Nishida, T. Kanamori, T. Sakamoto, Y. Ohishi, and S. Sudo, "Development of PbF_2-GaF_3-InF_3-ZnF_2-YF_3-LaF_3 glass for use as a 1.3 μm Pr^{3+}-doped fiber amplifier host," J. Non-Cryst. Solids **221**, 238-244 (1997).
98. K. Itoh, H. Yanagita, H. Tawarayama, K. Yamanaka, E. Ishikawa, K. Okada, H.

Aoki, Y. Matsumoto, A. Shirakawa, Y. Matsuoka, and H. Toratani, "Pr^{3+} doped InF_3/GaF_3 based fluoride glass fibers and Ga-Na-S glass fibers for light amplification around 1.3 μm," J. Non-Cryst. Solids **256-257**, 1-5 (1999).

99. Y. Nishida, T. Kanamori, T. Sakamoto, Y. Ohishi, and S. Sudo., "Fluoride glass fiber," in *United States Patent*, U. S. Patent, ed. (1998), p. 25.
100. Y. Jestin, A. L. Sauze, B. Boulard, Y. Gao, and P. Baniel, "Viscosity matching of new PbF_2-InF_3-GaF_3 based fluoride glasses and ZBLAN for high NA optical fiber," J. Non-Cryst. Solids **320**, 231-237 (2003).
101. K. H. Sun, "Fluoride Glass," in *United States Patent* U. S. Patent, ed. (1946).
102. T. Nakai, Y. Mimura, H. Tokiwa, and O. Shinbori, "Dehydration of fluoride glasses by NF_3 processing," Lightwave Technology, Journal of **4**, 87-89 (1986).
103. S. Mitachi, Y. Ohishi, and T. Miyashita, "A fluoride glass optical fiber operating in the mid-infrared wavelength range," Lightwave Technology, Journal of **1**, 67-70 (1983).
104. J. C. Knight, T. A. Birks, P. S. J. Russell, and D. M. Atkin, "All-silica single-mode optical fiber with photonic crystal cladding," Opt. Lett. **21**, 1547-1549 (1996).
105. X. Jiang, N. Y. Joly, M. A. Finger, F. Babic, K. L. WongGordon, J. C. Travers, and J. RussellPhilip St, "Deep-ultraviolet to mid-infrared supercontinuum generated in solid-core ZBLAN photonic crystal fibre," Nat Photon **9**, 133-139 (2015).
106. D. Pysz, I. Kujawa, R. Stępień, M. Klimczak, A. Filipkowski, M. Franczyk, L. Kociszewski, J. Buźniak, K. Haraśny, and R. Buczyński, "Stack and draw fabrication of soft glass microstructured fiber optics," in *Bulletin of the Polish Academy of Sciences Technical Sciences*(2014), p. 667.
107. A. Ortigosa-Blanch, A. Diez, M. Delgado-Pinar, J. L. Cruz, and M. V. Andres, "Ultrahigh birefringent nonlinear microstructured fiber," IEEE Photonics Technology Letters **16**, 1667-1669 (2004).
108. P. Russell, "Photonic Crystal Fibers," Science **299**, 358-362 (2003).
109. G. Amouzad Mahdiraji, D. M. Chow, S. R. Sandoghchi, F. Amirkhan, E. Dermosesian, K. S. Yeo, Z. Kakaei, M. Ghomeishi, S. Y. Poh, S. Yu Gang, and F. R. Mahamd Adikan, "Challenges and Solutions in Fabrication of Silica-Based Photonic Crystal Fibers: An Experimental Study," Fiber and Integrated Optics **33**, 85-104 (2014).
110. H. Ebendorff-Heidepriem, and T. M. Monro, "Extrusion of complex preforms for microstructured optical fibers," Opt. Express **15**, 15086-15092 (2007).
111. H. Ebendorff-Heidepriem, and T. M. Monro, "Analysis of glass flow during extrusion of optical fiber preforms," Opt. Mater. Express **2**, 304-320 (2012).
112. E. Roeder, "Extrusion of glass," J. Non-Cryst. Solids **5**, 377-388 (1971).
113. H. Ebendorff-Heidepriem, Y. Li, and T. M. Monro, "Reduced loss in extruded soft glass microstructured fibre," Electron. Lett. **43**, 1343-1345 (2007).
114. H. Ebendorff-Heidepriem, T.-C. Foo, R. C. Moore, W. Zhang, Y. Li, T. M. Monro, A. Hemming, and D. G. Lancaster, "Fluoride glass microstructured optical fiber with large mode area and mid-infrared transmission," Opt. Lett. **33**, 2861-2863 (2008).
115. R. Kostecki, H. Ebendorff-Heidepriem, S. C. Warren-Smith, and T. M. Monro, "Predicting the drawing conditions for Microstructured Optical Fiber fabrication," Opt. Mater. Express **4**, 29-40 (2014).
116. T. M. Monro, S. Warren-Smith, E. P. Schartner, A. François, S. Heng, H. Ebendorff-Heidepriem, and S. Afshar V, "Sensing with suspended-core optical fibers," Optical Fiber Technology **16**, 343-356 (2010).
117. H. Ebendorff-Heidepriem, "Non-silica microstructured optical fibers for infrared

applications," presented at the 19th Optoelectronics and Communications Conference (OECC) and the 39th Australian Conference on Optical Fibre Technology (ACOFT), Barton2014.
118. K. Tajima, "Low water peak photonic crystal fibers," 29th European Conf. on Optical Commun., ECOC'03, (Rimini, Italy) (2003).
119. P. McNamara, D. G. Lancaster, R. Bailey, A. Hemming, P. Henry, and R. H. Mair, "A large core microstructured fluoride glass optical fibre for mid-infrared single-mode transmission," J. Non-Cryst. Solids **355**, 1461-1467 (2009).
120. S. Sakaguchi, Y. Terunuma, Y. Ohishi, and T. Kanamori, "Fluoride fibre drawing with improved tensile strength " J. Mater. Sci. Lett. **6**, 1063-1065 (1987).
121. "Editorial Board," J. Non-Cryst. Solids **161**, iii-iii (1993).
122. R. M. Almeida, and J. D. Mackenzie, "The effects of oxide impurities on the optical properties of fluoride glasses," J. Non-Cryst. Solids **56**, 63-68 (1983).
123. G. A. M. Amin, and A. F. Maged, "Compositional dependence of the physical properties of $Ge_1Se_{9-x}Tex$ amorphous system," Mater. Chem. Phys. **97**, 420 (2006).
124. M. Peng, X. Meng, and J. Qiu, "Bismuth doped germanium based optical glass," (SHANGHAI PRECISION OPTICAL INSTR INST (UYTJ) SHANGHAI INST OPTICS & PRECISION MECHANI (SHAN-Non-standard)).
125. M. Le Toullec, C. J. Simmons, and J. H. Simmons, "Infrared spectroscopic studies of the hydrolysis reaction during leaching of heavy-metal fluoride glasses," J. Am. Ceram. Soc. **71**, 219-224 (1988).
126. J. S. Wang, E. M. Vogel, and E. Snitzer, "Tellurite glass: a new candidate for fiber devices," Optical Materials **3**, 187-203 (1994).
127. C. G. Pantano, and R. K. Brow, "Hydrolysis reactions at the surface of fluorozirconate glass," J. Am. Ceram. Soc. **71**, 577-581 (1988).
128. S. Sakaguchi, Y. Terunuma, Y. Ohishi, and T. Kanamori, "Fluoride fibre drawing with improved tensile strength," J. Mater. Sci. Lett. **6**, 1063-1065 (1987).
129. H. W. Schneider, A. Schoberth, A. Staudt, and C. Gerndt, "Fluoride glass etching method for preparation of infra-red fibres with improved tensile strength," Electron. Lett. **22**, 949-950 (1986).
130. D. G. Chen, C. J. Simmons, and J. H. Simmons, "Corrosion layer formation of ZrF_4-based fluoride glasses," Mater. Sci. Forum **19-20**, 315-320 (1987).
131. C. T. Moynihan, and S. R. Loehr, "Chemical durability of fluoride glasses," Mater. Sci. Forum **32-33**, 243-253 (1988).
132. C. J. Simmons, and J. H. Simmons, "Chemical durability of fluoride glasses: I, reaction of fluorozirconate glasses with water," J. Am. Ceram. Soc. **69**, 661-669 (1986).
133. S. R. Loehr, A. J. Bruce, R. Mossadegh, R. H. Doremus, and C. T. Moynihan, "IR spectroscopy studies of attack of liquid water on ZrF_4-based glasses," Mater. Sci. Forum **5-6**, 311-322 (1985).
134. L. E. E. de Araújo, A. S. L. Gomes, C. B. de Araújo, Y. Messaddeq, A. Florez, and M. A. Aegerter, "Frequency upconversion of orange light into blue light in Pr^{3+}-doped fluoroindate glasses," Physical Review B **50**, 16219-16223 (1994).
135. http://us.vwr.com/store/catalog/product.jsp?catalog_number=AA40118-04.
136. http://en.wikipedia.org/wiki/Zirconium_tetrafluoride.
137. C. F. Kaminski, R. S. Watt, A. D. Elder, J. H. Frank, and J. Hult, "Supercontinuum radiation for applications in chemical sensing and microscopy," Appl. Phys. B **92**, 367-378 (2008).
138. C. Agger, C. Petersen, S. Dupont, H. Steffensen, J. K. Lyngs¯, C. L. Thomsen, J.

Th¯gersen, S. r. R. Keiding, and O. Bang, "Supercontinuum generation in ZBLAN fibers-detailed comparison between measurement and simulation," Journal of the Optical Society of America B **29**, 635-645 (2012).

139. V. V. Alexander, O. P. Kulkarni, M. Kumar, C. Xia, M. N. Islam, F. L. Terry Jr, M. J. Welsh, K. Ke, M. J. Freeman, M. Neelakandan, and A. Chan, "Modulation instability initiated high power all-fiber supercontinuum lasers and their applications," Optical Fiber Technology **18**, 349-374 (2012).
140. J. Wang, J. R. Lincoln, W. S. Brocklesby, R. S. Deol, C. J. Mackechnie, A. Pearson, A. C. Tropper, D. C. Hanna, and D. N. Payne, "Fabrication and optical properties of lead-germanate glasses and a new class of optical fibers doped with Tm^{3+}," Journal of Applied Physics **73**, 8066-8075 (1993).
141. J. R. Lincoln, C. J. Mackechnie, J. Wang, W. S. Brocklesby, R. S. Deol, A. Pearson, D. C. Hanna, and D. N. Payne, "New class of fibre laser based on lead-germanate glass," Electron. Lett. **28**, 1021-1022 (1992).
142. J. Wu, Z. Yao, J. Zong, and S. Jiang, "Highly efficient high-power thulium-doped germanate glass fiber laser," Opt. Lett. **32**, 638-640 (2007).
143. J. Geng, J. Wu, S. Jiang, and J. Yu, "Efficient operation of diode-pumped single-frequency thulium-doped fiber lasers near 2 μm," Opt. Lett. **32**, 355-357 (2007).
144. A. Mori, Y. Ohishi, and S. Sudo, "Erbium-doped tellurite glass fibre laser and amplifier," Electron. Lett. **33**, 863-864 (1997).
145. L. Gomes, M. Oermann, H. Ebendorff-Heidepriem, D. Ottaway, T. Monro, A. Felipe Henriques Librantz, and S. D. Jackson, "Energy level decay and excited state absorption processes in erbium-doped tellurite glass," Journal of Applied Physics **110**, - (2011).
146. C. B. Layne, and M. J. Weber, "Multiphonon relaxation of rare-earth ions in beryllium-fluoride glass," Physical Review B **16**, 3259-3261 (1977).
147. K. Hirao, S. Todoroki, and N. Soga, "CW room temperature upconversion lasing in Er^{3+}-doped fluoride glass fiber," J. Non-Cryst. Solids **143**, 40-45 (1992).
148. J. Y. Allain, M. Monerie, and H. Poignant, "Blue upconversion fluorozirconate fibre laser," Electron. Lett. **26**, 166-168 (1990).
149. E. W. J. L. Oomen, "Upconversion in Tm^{3+}-doped ZBLAN glasses," J. Non-Cryst. Solids **140**, 150-152 (1992).
150. K. Hirao, K. Tamai, S. Tanabe, and N. Soga, "Frequency upconversion and its new mechanism in Tm^{3+}-doped fluoroaluminate glasses," J. Non-Cryst. Solids **160**, 261-267 (1993).
151. K. Hirao, S. Tanabe, S. Kishimoto, K. Tamai, and N. Soga, "UV and blue upconversion in Tm^{3+}-doped fluoroaluminate glass by 0.655 μm excitation," J. Non-Cryst. Solids **135**, 90-93 (1991).
152. S. D. Jackson, "8.8 W diode-cladding-pumped Tm^{3+}, Ho^{3+}-doped fluoride fibre laser," Electron. Lett. **37**, 821-822 (2001).
153. R. A. Hayward, W. A. Clarkson, P. W. Turner, J. Nilsson, A. B. Grudinin, and D. C. Hanna, "Efficient cladding-pumped Tm-doped silica fibre laser with high power singlemode output at 2 μm," in *Electron. Lett.*(Institution of Engineering and Technology, 2000), pp. 711-712.
154. R. G. Smart, J. N. Carter, A. C. Tropper, and D. C. Hanna, "Continuous-wave oscillation of Tm^{3+}-doped fluorozirconate fibre lasers at around 1.47 μm, 1.9 μm and 2.3 μm when pumped at 790 nm," Opt. Commun. **82**, 563-570 (1991).
155. S. D. Jackson, T. A. King, and M. Pollnau, "Diode-pumped 1.7 W erbium 3 μm fiber laser," Opt. Lett. **24**, 1133-1135 (1999).
156. T. Sumiyoshi, H. Sekita, T. Arai, S. Sato, M. Ishihara, and M. Kikuchi, "High-

power continuous-wave 3 and 2 μm cascade Ho^{3+}:ZBLAN fiber laser and its medical applications," Selected Topics in Quantum Electronics, IEEE Journal of **5**, 936-943 (1999).
157. C. Carbonnier, H. Többen, and U. B. Unrau, "Room temperature CW fibre laser at 3.22 μm," in *Electron. Lett.*(Institution of Engineering and Technology, 1998), pp. 893-894.
158. H. TÖBBEN, "CW Lasing at 3.45 μm in Erbium-doped Fluorozirconate Fibres," Frequenz **45**, 250-252 (1991).
159. J. Schneide, C. Carbonnier, and U. B. Unrau, "Characterization of a Ho^{3+}-doped fluoride fiber laser with a 3.9 μm emission wavelength," Applied Optics **36**, 8595-8600 (1997).
160. F. Huang, Y. Ma, W. Li, X. Liu, L. Hu, and D. Chen, "2.7 μm emission of high thermally and chemically durable glasses based on AlF_3," Sci. Rep. **4** (2014).
161. S. Kishimoto, and K. Hirao, "Intense ultraviolet and blue upconversion fluorescence in Tm^{3+}-doped fluoroindate glasses," Journal of Applied Physics **80**, 1965-1969 (1996).
162. S. D. Jackson, "High-power and highly efficient diode-cladding-pumped holmium-doped fluoride fiber laser operating at 2.94 ?m," Opt. Lett. **34**, 2327-2329 (2009).
163. S. D. Jackson, "Towards high-power mid-infrared emission from a fibre laser," Nat Photon **6**, 423-431 (2012).
164. S. T. Davey, D. Szebesta, J. R. Williams, T. Whitley, and R. Wyatt, "Rare earth-doped, high NA fluoride fibre amplifiers," J. Non-Cryst. Solids **161**, 262-265 (1993).
165. H. M. T. Katsuyama, ed. *Infrared Optical Fibers* (Adam Hilger, 1978).
166. J. A. Savage, "Materials for infrared optics," Mater. Sci. R **2**, 99-137 (1987).
167. W. H. Dumbaugh, "Infrared Transmitting Glasses," OPTICE **24**, 242257-242257-(1985).
168. S. C. Warren-Smith, H. Ebendorff-Heidepriem, T. C. Foo, R. Moore, C. Davis, and T. M. Monro, "Exposed-core microstructured optical fibers for real-time fluorescence sensing," Opt. Express **17**, 18533-18542 (2009).
169. H. Ebendorff-Heidepriem, R. C. Moore, and T. M. Monro, "Progress in the Fabrication of the Next-Generation Soft Glass Microstructured Optical Fibers," AIP Conference Proceedings **1055**, 95-98 (2008).
170. J. S. Browder, and S. S. Ballard, "Low Temperature Thermal Expansion Measurements on Optical Materials," Applied Optics **8**, 793-798 (1969).
171. "https://en.wikipedia.org/wiki/Ellipsometry."
172. U. Rossow, "Depolarization/mixed polarization corrections of ellipsometry spectra," Thin Solid Films **313–314**, 97-101 (1998).
173. J. Lee, P. I. Rovira, I. An, and R. W. Collins, "Rotating-compensator multichannel ellipsometry: Applications for real time Stokes vector spectroscopy of thin film growth," Rev. Sci. Instrum. **69**, 1800-1810 (1998).
174. "Surface Roughness - Terminology - Part 1: Surface and Its Parameters," I. O. f. Standardisation, ed. (1984).
175. P. Y. Zavalij, S. Yang, and M. S. Whittingham, "Structures of potassium, sodium and lithium bis(oxalato)borate salts from powder diffraction data," Acta Crystallographica Section B **59**, 753-759 (2003).
176. F. Xia, J. Brugger, Y. Ngothai, B. O'Neill, G. Chen, and A. Pring, "Three-Dimensional Ordered Arrays of Zeolite Nanocrystals with Uniform Size and Orientation by a Pseudomorphic Coupled Dissolution−Reprecipitation

Replacement Route," Crystal Growth & Design **9**, 4902-4906 (2009).
177. J. Gal, D. Mogilanski, M. Nippus, J. Zabicky, and G. Kimmel, "Fast high-resolution characterization of powders using an imaging plate Guinier camera," Nuclear Instruments and Methods in Physics Research Section A: Accelerators, Spectrometers, Detectors and Associated Equipment **551**, 145-151 (2005).
178. http://www.aandd.jp/products/manual/balances/gx-13.pdf.
179. P. Roman, and J. M. Gutierrez-Zorrilla, "A quick method for determining the density of single crystals," J. Chem. Educ. **62**, 167-null (1985).
180. "Committees," J. Non-Cryst. Solids **161**, ix-ix (1993).
181. A. Boutarfaia, and M. Poulain, "Fluoride glasses in the InF_3-GaF_3-YF_3-PbF_2-CaF_2-ZnF_2 system," Journal of Physics and Chemistry of Solids **63**, 2129-2133 (2002).
182. "http://www.cardinalcorp.com/source/pdf/tsb/cg/CG07_01-2016.pdf."
183. "http://www.schott.com/advanced_optics/english/download/schott_tie-25_striae_in_optical_glass_eng.pdf."
184. K. Itoh, K. Miura, I. Masuda, M. Iwakura, and T. Yamashita, "Low-loss fluorozirco-aluminate glass fiber," J. Non-Cryst. Solids **167**, 112-116 (1994).
185. S. Takahashi., T. Kanamori., Y. Ohishi., K. Fujiura., and Y. Terunuma., "Reduction of Oxygen Impurity in ZrF_4-Based Fluoride Glass," Mater. Sci. Forum **32-33**, 87-92 (1988).
186. D. C. Tran, and C. Fisher, "SF6 Process for dehydration of fluoride glasses," (Google Patents, 1985).
187. P. W. France, S. F. Carter, J. R. Williams, K. J. Beales, and J. M. Parker, "OH-absorption in fluoride glass infra-red fibres," Electron. Lett. **20**, 607-608 (1984).
188. M. G. Drexhage, C. T. Moynihan, B. Bendow, E. Gboji, K. H. Chung, and M. Boulos, "Influence of processing conditions on IR edge absorption in fluorohafnate and fluorozirconate glasses," Mater. Res. Bull. **16**, 943-947 (1981).
189. M. Tomozawa, and R. H. Doremus, *Glass IV: Treatise on Materials Science and Technology* (Elsevier Science, 2013).
190. H. Yinnon, and D. R. Uhlmann, "Applications of thermoanalytical techniques to the study of crystallization kinetics in glass-forming liquids, part I: Theory," J. Non-Cryst. Solids **54**, 253-275 (1983).
191. N. P. Bansal, R. H. Doremus, A. J. Bruce, and C. T. Moynihan, "Kinetics of Crystallization of ZrF_4-Ba_2-LaF_3 Glass by Differential Scanning Calorimetry," J. Am. Ceram. Soc. **66**, 233-238 (1983).
192. S. Mitachi., and P. A. Tick., "Oxygen effects on fluoride glass stability," Mater. Sci. Forum **32-33**, 197-202 (1988).
193. K. Fujiura, Y. Nishida, K. Kobayashi, and S. Takahashi, "Oxygen Doping Effects on Thermal Properties of ZrF_4 -BaF_2 Glasses Synthesized by Plasma-Enhanced Chemical Vapor Deposition," Jpn. J. Appl. Phys. **30**, L2113 (1991).
194. M. Saad, "High purity fluoride glass synthesis: a review," IR photonics 2009 **http://www.iguide-irphotonics.com/pdf/Pwest2009.pdf.**
195. J. B. MacChesney, P. B. O. Connor, and H. M. Presby, "A new technique for the preparation of low-loss and graded-index optical fibers," Proceedings of the IEEE **62**, 1280-1281 (1974).
196. W. G. French, A. D. Pearson, G. W. Tasker, and J. B. MacChesney, "Low-loss fused silica optical waveguide with borosilicate cladding," Applied Physics Letters **23**, 338-339 (1973).
197. L. Němec, and V. Tonarová, "Glass melting and its innovation potentials: bubble removal under the effect of the centrifugal force," ceramics-silikaty **52**, 225-239

(2008).
198. C. A. G. Kalnins, N. A. Spooner, T. M. Monro, and H. Ebendorff-Heidepriem, "Surface Analysis and Treatment of Extruded Fluoride Phosphate Glass Preforms for Optical Fiber Fabrication," J. Am. Ceram. Soc. **99**, 1874-1877 (2016).
199. H. Ebendorff-Heidepriem, J. Schuppich, A. Dowler, L. Lima-Marques, and T. M. Monro, "3D-printed extrusion dies: a versatile approach to optical material processing," Optical Materials Express **4**, 1494-1504 (2014).
200. J. Bei, T. M. Monro, A. Hemming, and H. Ebendorff-Heidepriem, "Fabrication of extruded fluoroindate optical fibers," Opt. Mater. Express **3**, 318-328 (2013).
201. M. Braglia, S. Mosso, G. Dai, E. Billi, L. Bonelli, M. Baricco, and L. Battezzati, "Rheology of tellurite glasses," Mater. Res. Bull. **35**, 2343-2351 (2000).
202. R. E, "Flow behaviour of glass during extrusion," J. Non-Cryst. Solids **7**, 203-220 (1972).
203. J. E. Shelby, *Introduction to glass science and technology* (The Royal Society of Chemistry, 2005).
204. H. Ebendorff-Heidepriem, T. M. Monro, M. A. van Eijkelenborg, and M. C. J. Large, "Extruded high-NA microstructured polymer optical fibre," Opt. Commun. **273**, 133-137 (2007).
205. E. W. Deeg, C. G. Silverberg, and L. B. Martel., "Method for fire polishing optical glass," in *United States Patent*, U. S. Patent, ed. (1974), p. 6.
206. J. E. D. Jr, and B. R. Wheaton., "Processes for polishing glass and glass-ceramic surfaces using excimer laser radiation " in *United States Patent*, U. S. Patent, ed. (1998), p. 8.
207. P. A. Thompson, and S. M. Troian, "A general boundary condition for liquid flow at solid surfaces," Nature **389**, 360-362 (1997).
208. K. M. Reich, C. V. Gay, and J. A. Frangos, "Fluid shear stress as a mediator of osteoblast cyclic adenosine monophosphate production," J. Cell. Physiol. **143**, 100-104 (1990).
209. M. Chatzimina, G. C. Georgiou, K. Housiadas, and S. G. Hatzikiriakos, "Stability of the annular Poiseuille flow of a Newtonian liquid with slip along the walls," J. Non-Newton. Fluid Mech. **159**, 1-9 (2009).
210. A. Zhang, A. Lin, J.-S. Wang, and J. Toulouse, "Multistage etching process for microscopically smooth tellurite glass surfaces in optical fibers," Journal of Vacuum Science & Technology B **28**, 682-686 (2010).
211. Y. D. West, E. R. Taylor, R. C. Moore, and D. N. Payne, "Chemical etching of AlF_3-based glasses," J. Non-Cryst. Solids **256-257**, 200-206 (1999).
212. G. Qian, F. Xia, J. Brugger, W. M. Skinner, J. Bei, G. Chen, and A. Pring, "Replacement of pyrrhotite by pyrite and marcasite under hydrothermal conditions up to 220 °C: An experimental study of reaction textures and mechanisms," Am. Mineral. **96**, 1878-1893 (2011).
213. Y. Ahn, J.-Y. Yoon, C.-W. Baek, and Y.-K. Kim, "Chemical mechanical polishing by colloidal silica-based slurry for micro-scratch reduction," Wear **257**, 785-789 (2004).
214. P. C. Pureza, P. H. Klein, W. I. Roberts, and I. D. Aggarwal, "Influence of preform surface treatments on the strength of fluorozirconate fibres," J. Mater. Sci. **26**, 5149-5154 (1991).
215. D. R. MacFarlane, P. J. Newman, and A. Voelkel, "Methods of Purification of Zirconium Tetrafluoride for Fluorozirconate Glass," J. Am. Ceram. Soc. **85**, 1610-1612 (2002).
216. E. O. Gbogi, K. H. Chung, C. T. Moynihan, and M. G. Drexhage, "Surface and

bulk -OH infrared absorption in ZrF_4- and HfF_4-based glasses," J. Am. Ceram. Soc. **64**, c-51-c-53 (1981).
217. N. N. Sagamihara, "Fluoride glass," in *United States Patent* U. S. Patent, ed. (1982).
218. T. Iqbal, M. R. Shahriari, G. Merberg, and G. H. Sigel, "Synthesis, characterization, and potential application of highly chemically durable glasses based on AlF_3," J. Mater. Res. **6**, 401-406 (1991).
219. http://en.wikipedia.org/wiki/Sodium_fluoride.
220. C. Donley, D. Dunphy, D. Paine, C. Carter, K. Nebesny, P. Lee, D. Alloway, and N. R. Armstrong, "Characterization of Indium−Tin oxide interfaces using X-ray photoelectron spectroscopy and redox processes of a chemisorbed probe molecule: effect of surface pretreatment conditions," Langmuir **18**, 450-457 (2001).
221. S. Sakaguchi, and S. Mitachi, "Strength and fatigue of fluoride glass optical fibers," J. Am. Ceram. Soc. **66**, c151-c152 (1983).
222. J. Bei, T. M. Monro, A. Hemming, and H. Ebendorff-Heidepriem, "Reduction of scattering loss in fluoroindate glass fibers," Opt. Mater. Express **3**, 1285-1301 (2013).
223. T. Shibata, H. Takahashi, M. Kimura, T. Ijichi, K. Takahashi, Y. Sasaki, and S. Yoshida., "Fabrication of high-strength, low-loss fluorozirconate glass optical fibers," Mater. Sci. Forum **5-6**, 379-385 (1985).
224. B. R. Judd, "Optical Absorption Intensities of Rare-Earth Ions," Physical Review **127**, 750-761 (1962).
225. G. S. Ofelt, "Intensities of Crystal Spectra of Rare-Earth Ions," The Journal of Chemical Physics **37**, 511-520 (1962).
226. B. M. Walsh, "Judd-Ofelt theory: Principles and practices," in *Advances in Spectroscopy For Lasers and Sensing*(Springer, 2006), pp. 403-433.
227. W. Seeber, E. A. Downing, L. Hesselink, M. M. Fejer, and D. Ehrt, "Pr^{3+}-doped fluoride glasses," J. Non-Cryst. Solids **189**, 218-226 (1995).
228. H. Ebendorff-Heidepriem, D. Ehrt, M. Bettinelli, and A. Speghini, "Effect of glass composition on Judd–Ofelt parameters and radiative decay rates of Er^{3+} in fluoride phosphate and phosphate glasses," J. Non-Cryst. Solids **240**, 66-78 (1998).
229. A. Florez, S. L. Oliveira, M. Flórez, L. A. Gómez, and L. A. O. Nunes, "Spectroscopic characterization of Ho^{3+} ion-doped fluoride glass," Journal of Alloys and Compounds **418**, 238-242 (2006).
230. G. Maze, M. Poulain, J. Y. Carre, A. Soufiane, and Y. Messaddeq, "Indium fluoride, zinc fluoride and metal fluoride," (Google Patents, 1996).
231. A. A. Kaminskii, *Crystalline Lasers : Physical Processes and Operation Schemes* (CRC Press, 1996).
232. R. S. Quimby, and B. G. Aitken, "Multiphonon energy gap law in rare-earth doped chalcogenide glass," J. Non-Cryst. Solids **320**, 100-112 (2003).
233. M. Takahashi, M. Shojiya, R. Kanno, Y. Kawamoto, K. Kadono, T. Ohtsuki, and N. Peyghambarian, "Nonradiative decay processes and mechanisms of frequency upconversion of Er^{3+} in ZrF_4-BaF_2-LaF_3 glass," Journal of applied physics **81**, 2940-2945 (1997).
234. D. C. Yeh, W. A. Sibley, M. Suscavage, and M. G. Drexhage, "Multiphonon relaxation and infrared-to-visible conversion of Er^{3+} and Yb^{3+} ions in barium-thorium fluoride glass," Journal of Applied Physics **62**, 266-275 (1987).
235. M. Dejneka, E. Snitzer, and R. E. Riman, "Blue, green and red fluorescence and energy transfer of Eu^{3+} in fluoride glasses," Journal of Luminescence **65**, 227-245

(1995).
236. N. Subrahmanyam, B. Lal, and M. N. Avadhanulu, *A Text Book of Optics (m.e.)* (S. Chand Limited, 2004).
237. http://www.thorlabs.hk/newgrouppage9.cfm?objectgroup_id=7062.
238. T. Nanba, T. Miyaji, J. Takada, A. Osaka, Y. Miura, and I. Yasui, "Computer simulation on the structure and vibrational spectra in Ge□Pb□O□F glass," J. Non-Cryst. Solids **177**, 131-136 (1994).
239. X. Yu, X. Zhao, C. Li, and H. Lin, "Infrared spectrum estimation for maximum phonon energy in optical glasses," J. Dalian Polytechnic University **27**, 155-157 (2008).
240. J. Sanghera, and I. D. Aggarwal, *Infrared Fiber Optics* (Taylor & Francis, 1998).
241. H. Ebendorff-Heidepriem, D. G. Lancaster, K. Kuan, R. C. Moore, S. Sarker, and T. M. Monro, "Extruded fluoride fiber for 2.3 μm laser application," in *Proceedings of the International Quantum Electronics Conference and Conference on Lasers and Electro-Optics Pacific Rim 2011*(Optical Society of America, Sydney, 2011), p. C806.
242. G. Tao, S. Shabahang, E.-H. Banaei, J. J. Kaufman, and A. F. Abouraddy, "Multimaterial preform coextrusion for robust chalcogenide optical fibers and tapers," Opt. Lett. **37**, 2751-2753 (2012).
243. M. J. Chen, Y. M. Stokes, P. Buchak, D. G. Crowdy, H. T. C. Foo, A. Dowler, and H. Ebendorff-Heidepriem, "Drawing tubular fibres: experiments versus mathematical modelling," Optical Materials Express **6**, 166-180 (2016).
244. F. T. Geyling, "Basic Fluid-Dynamic Considerations in the Drawing of Optical Fibers," Bell System Technical Journal **55**, 1011-1056 (1976).
245. D. C. Tran, "Method of making low-temperature optical glass fibers free of defects," (Google Patents, 2009).
246. H. Ebendorff-Heidepriem, and J. Bei, "Developet of a low loss indium fluoride glass composition and optical fibre," (Defence Science and Technology Group, 2013).
247. C. Voyce, A. D. Fitt, and T. M. Monro, "Mathematical Modeling as an Accurate Predictive Tool in Capillary and Microstructured Fiber Manufacture: The Effects of Preform Rotation," J. Lightwave Technol. **26**, 791-798 (2008).
248. G. Yang, T. Rouxel, J. Troles, B. Bureau, C. Boussard-Plédel, P. Houizot, and J.-C. Sangleboeuf, "Viscosity of As2Se3 Glass During the Fiber Drawing Process," J. Am. Ceram. Soc. **94**, 2408-2411 (2011).

PUBLISHED PAPERS

I

Fabrication of extruded fluoroindate optical fibers

Jiafang Bei,[1],* Tanya M. Monro,[1] Alexander Hemming,[2] and Heike Ebendorff-Heidepriem[1]

[1]Institute for Photonics & Advanced Sensing and School of Chemistry & Physics, University of Adelaide, Adelaide, SA 5005, Australia

[2]Electro-Optic Technology Group, Electronic Warfare and Radar Division, Defence Science and Technology Organisation, Edinburgh, SA 5111, Australia

Fabrication of extruded fluoroindate optical fibers

Jiafang Bei,[1,*] Tanya M. Monro,[1] Alexander Hemming,[2] and Heike Ebendorff-Heidepriem[1]

[1]*Institute for Photonics & Advanced Sensing and School of Chemistry & Physics, University of Adelaide, Adelaide, SA 5005, Australia*
[2]*Electro-Optic Technology Group, Electronic Warfare and Radar Division, Defence Science and Technology Organisation, Edinburgh, SA 5111, Australia*
jiafang.bei@adelaide.edu.au

Abstract: Fluoroindate glasses are attractive materials for the fabrication of mid-infrared transmitting fibers with extended spectral range. Preparation of fluoroindate glasses under different melting conditions and preform fabrication using the billet extrusion technique were investigated in this study. Experimental results showed that the fluorination of the raw materials using ammonium bifluoride reduced OH content and oxide impurities, and enhanced the crystallization stability of the glasses. In addition, a shift of the IR absorption edge to longer wavelength was observed by using ammonium bifluoride. Casting and extrusion methods were compared for application to preform fabrication. In this work, the fiber with the lowest loss (~2 dB/m at 1.55 μm) was obtained using preform extrusion at 322 °C. The significantly reduced loss of the fiber made from the extruded preform compared to the fiber made using a cast preform is attributed to the suppression of scattering centers and the better surface quality of extruded rods compared with the cast rod.

OCIS codes: (160.2290) Fiber materials; (160.2750) Glass and other amorphous materials.

References and links

1. R. M. Almeida, "Fluoride glasses," in *Handbook on the Physics and Chemistry of Rare Earths*, A. G. Karl, Jr. and E. LeRoy, eds. (Elsevier, 1991), pp. 287–346.
2. X. Zhu and N. Peyghambarian, "High-power ZBLAN glass fiber lasers: review and prospect," Adv. Optoelectron. **2010**, 501956 (2010).
3. R. E. Slusher, G. Lenz, J. Hodelin, J. Sanghera, L. B. Shaw, and I. D. Aggarwal, "Large Raman gain and nonlinear phase shifts in high-purity As_2Se_3 chalcogenide fibers," J. Opt. Soc. Am. B **21**(6), 1146–1155 (2004).
4. J. S. Sanghera, I. D. Aggarwal, L. B. Shaw, C. M. Florea, P. Pureza, V. Q. Nguyen, F. Kung, and I. D. Aggarwal, "Nonlinear properties of chalcogenide glass fibers," J. Optoelectron. Adv. Mater. **8**, 2148–2155 (2006).
5. P. McNamara, D. G. Lancaster, R. Bailey, A. Hemming, P. Henry, and R. H. Mair, "A large core microstructured fluoride glass optical fiber for mid-infrared single-mode transmission," J. Non-Cryst. Solids **355**(28-30), 1461–1467 (2009).
6. J. M. Reau and M. Poulain, "Ionic conductivity in fluorine-containing glasses," Mater. Chem. Phys. **23**(1-2), 189–209 (1989).
7. D. Szebesta, S. T. Davey, J. R. Williams, and M. W. Moore, "OH absorption in the low loss window of ZBLAN(P) glass fiber," J. Non-Cryst. Solids **161**, 18–22 (1993).
8. L. E. E. de Araújo, A. S. L. Gomes, C. B. de Araújo, Y. Messaddeq, A. Florez, and M. A. Aegerter, "Frequency upconversion of orange light into blue light in Pr^{3+}-doped fluoroindate glasses," Phys. Rev. B Condens. Matter **50**(22), 16219–16223 (1994).
9. A. S. Oliveira, E. A. Gouveia, M. T. de Araujo, A. S. Gouveia-Neto, C. B. de Araujo, and Y. Messaddeq, "Twentyfold blue upconversion emission enhancement through thermal effects in Pr^{3+}/Yb^{3+}-codoped fluoroindate glasses excited at 1.064 μm," J. Appl. Phys. **87**(9), 4274–4278 (2000).
10. N. Rakov, G. S. Maciel, C. B. de Araujo, and Y. Messaddeq, "Energy transfer assisted frequency upconversion in Ho^{3+} doped fluoroindate glass," J. Appl. Phys. **91**(3), 1272–1276 (2002).

#182019 - $15.00 USD Received 18 Dec 2012; revised 30 Jan 2013; accepted 31 Jan 2013; published 1 Feb 2013

11. Y. Nishida, T. Kanamori, T. Sakamoto, Y. Ohishi, and S. Sudo, "Development of PbF_2-GaF_3-InF_3-ZnF_2-YF_3-LaF_3 glass for use as a 1.3μm Pr^{3+}-doped fiber amplifier host," J. Non-Cryst. Solids **221**(2-3), 238–244 (1997).
12. K. Itoh, H. Yanagita, H. Tawarayama, K. Yamanaka, E. Ishikawa, K. Okada, H. Aoki, Y. Matsumoto, A. Shirakawa, Y. Matsuoka, and H. Toratani, "Pr^{3+} doped InF^3/GaF^3 based fluoride glass fibers and Ga-Na-S glass fibers for light amplification around 1.3μm," J. Non-Cryst. Solids **256-257**, 1–5 (1999).
13. Y. Nishida, T. Kanamori, T. Sakamoto, Y. Ohishi, and S. Sudo, "Fluoride glass fiber," U.S. Patent No. 5,774,620 (dated Jun. 30, 1998).
14. Y. Jestin, A. L. Sauze, B. Boulard, Y. Gao, and P. Baniel, "Viscosity matching of new PbF_2-InF_3-GaF_3 based fluoride glasses and ZBLAN for high NA optical fiber," J. Non-Cryst. Solids **320**(1-3), 231–237 (2003).
15. M. Saad, "Fluoride glass fiber: state of the art," Proc. SPIE **7316**, 73160N, 73160N-16 (2009).
16. G. Rault, J. L. Adam, F. Smektala, and J. Lucas, "Fluoride glass compositions for waveguide applications," J. Fluor. Chem. **110**(2), 165–173 (2001).
17. H. Ebendorff-Heidepriem and T. M. Monro, "Analysis of glass flow druing extrusion of optical fiber preforms," Opt. Mater. Express **2**(3), 304–320 (2012).
18. E. Roeder, "Extrusion of glass," J. Non-Cryst. Solids **5**(5), 377–388 (1971).
19. H. Ebendorff-Heidepriem, Y. Li, and T. M. Monro, "Reduced loss in extruded soft glass microstructured fiber," Electron. Lett. **43**(24), 1343–1345 (2007).
20. H. Ebendorff-Heidepriem and T. M. Monro, "Extrusion of complex preforms for microstructured optical fibers," Opt. Express **15**(23), 15086–15092 (2007).
21. H. Ebendorff-Heidepriem, T. C. Foo, R. C. Moore, W. Zhang, Y. Li, T. M. Monro, A. Hemming, and D. G. Lancaster, "Fluoride glass microstructured optical fiber with large mode area and mid-infrared transmission," Opt. Lett. **33**(23), 2861–2863 (2008).
22. A. M. Mailhot, A. Elyamani, and R. E. Riman, "Reactive atmosphere synthesis of sol-gel heavy metal fluoride glasses," J. Mater. Res. **7**(06), 1534–1540 (1992).
23. S. Mitachi, Y. Terunuma, Y. Ohishi, and S. Takahashi, "Reduction of impurities in fluoride glass fibers," J. Lightwave Technol. **2**(5), 587–592 (1984).
24. S. Takahashi, T. Kanamori, Y. Ohishi, K. Fujiura, and Y. Terunuma, "Reduction of oxygen impurity in ZrF_4-based fluoride glass," Mater. Sci. Forum **32–33**, 87–92 (1988).
25. D. C. Tran and C. Fisher, "SF_6 Process for dehydration of fluoride glasses," U.S. Patent No. 4,539,032 (dated Sep. 3, 1985).
26. H. W. Schneider, A. Schoberth, A. Staudt, and C. Gerndt, "Fluoride glass etching method for preparation of infra-red fibers with improved tensile strength," Electron. Lett. **22**(18), 949–950 (1986).
27. P. C. Pureza, P. H. Klein, W. I. Roberts, and I. D. Aggarwal, "Influence of preform surface treatments on the strength of fluorozirconate fibers," J. Mater. Sci. **26**(19), 5149–5154 (1991).
28. A. Zhang, A. Lin, J. S. Wang, and J. Toulouse, "Multistage etching process for microscopically smooth tellurite glass surfaces in optical fibers," J. Vac. Sci. Technol. B **28**(4), 682–686 (2010).
29. Y. D. West, E. R. Taylor, R. C. Moore, and D. N. Payne, "Chemical etching of AlF_3-based glasses," J. Non-Cryst. Solids **256-257**, 200–206 (1999).
30. P. W. France, S. F. Carter, J. R. Williams, K. J. Beales, and J. M. Parker, "OH-absorption in fluoride glass infra-red fibers," Electron. Lett. **20**(14), 607–608 (1984).
31. M. G. Drexhage, C. T. Moynihan, B. Bendow, E. Gboji, K. H. Chung, and M. Boulos, "Influence of processing conditions on IR edge absorption in fluorohafnate and fluorozirconate glasses," Mater. Res. Bull. **16**(8), 943–947 (1981).
32. B. Bendow, "Transparency of bulk halide glasses," in *Fluoride Glass Fiber Optics*, I. D. Aggarwal and G. Lu, eds. (Academic Press, 1991), pp. 85–137.
33. M. G. Drexhage, "Heavy metal fluoride glasses," in *Treatise on Materials Science and Technology,* M. Tomozawa and R. H. Doremus, eds. (Academic Press, 1985), Vol. 26: Glass IV, pp. 228–229.
34. H. Yinnon and D. R. Uhlmann, "Applications of thermoanalytical techniques to the study of crystallization kinetics in glass-forming liquids, part I: theory," J. Non-Cryst. Solids **54**(3), 253–275 (1983).
35. N. P. Bansal, R. H. Doremus, A. J. Bruce, and C. T. Moynihan, "Kinetics of crystallization of ZrF_4-BaF_2-LaF_3 glass by differential scanning calorimetry," J. Am. Ceram. Soc. **66**(4), 233–238 (1983).
36. S. Mitachi and P. A. Tick, "Oxygen effects on fluoride glass stability," Mater. Sci. Forum **32-33**, 197–202 (1991).
37. K. Fujiura, Y. Nishida, K. Kobayashi, and S. Takahashi, "Oxygen doping effects on thermal properties of ZrF_4-BaF_2 glass synthesized by plasma-enhanced chemical vapour deposition," Jpn. J. Appl. Phys. **30**(Part 2, No. 12B), L2113–L2115 (1991).
38. R. M. Almeida and J. D. Mackenzie, "The effects of oxide impurities on the optical properties of fluoride glasses," J. Non-Cryst. Solids **56**(1-3), 63–68 (1983).
39. International Organisation for Standardisation, "Surface Roughness - Terminology - Part 1: Surface and Its Parameters," ISO 4287–1 (1984).

1. Introduction

Halide and chalcogenide glasses have attracted significant attention and experienced rapid developments due to their importance as infrared transmitting materials [1,2]. Current

#182019 - $15.00 USD Received 18 Dec 2012; revised 30 Jan 2013; accepted 31 Jan 2013; published 1 Feb 2013

applications of these materials include bulk optical components, and optical fiber for the near and mid infrared (IR) spectral regions. Chalcogenide glasses provide transparency further into the IR region than heavy metal fluoride glasses, and they are commonly investigated for nonlinear wavelength transfer due to their high nonlinearity [3,4]. However, chalcogenide glasses have higher refractive index and weaker mechanical strength than fluoride glasses, which limits their application for high power delivery devices [5]. In the heavy metal fluoride glass family, extensive previous research has focused on fluorozirconate glasses [6], which have been successfully drawn into low-loss fibers [7]. Other glass compositions of interest are fluoroindate systems, which present good optical quality, stability against atmospheric moisture, good mechanical stability [8] as well as low optical attenuation from 250 nm to 8 μm. Due to their low maximum phonon energy of ~510 cm^{-1}, they are characterized by transmittance further into the IR region, and significantly lower non-radiative decay rates in comparison to fluorozirconate glasses [9,10].

Several research studies have been published on the subject of fluoroindate glass fibers. Among these fluoroindate glass matrices, PbF_2-InF_3 based fluoride glass has good durability, high thermal stability against crystallization, and has been fabricated into a fiber with a minimum transmission loss of 0.043 dB/m at 3.33 μm [11]. In comparison, Itoh et al. have developed a single-mode fiber, using InF_3/GaF_3 glass as a core glass and ZBLAN glass as a cladding glass, with a low loss round 0.2 dB/m at 1.2 μm [12]. Nishida et al. systematically studied InF_3/GaF_3 glass fibers and obtained minimum loss of 0.025 dB/m at 3.3 μm [13]. Recently a multimode fiber with an optical loss of 0.85 dB/m at 1.3 μm was obtained from a preform made by rotational casting method, where the importance of fluorination with HF during glass melting was also discussed [14]. However, all these fibers have comparatively low InF_3 (~28 mol%) and high GaF_3 contents, which limits their IR transmittance.

Commercial fluoroindate glass fibers are now available with low loss in a wide spectrum (<1 dB/m for 1.5-5 μm) [15], but the glass composition is not available to the public. An earlier research study [16] showed that the glass composition $32InF_3$-$20ZnF_2$-$20SrF_2$-$18BaF_2$-$8GaF_3$-$2CaF_2$ (IZSBGC) with high InF_3 content was particularly promising for mid-infrared applications due to its high transmission and low rate of crystallization. Although short unstructured fibers (up to 5 m in length) were successfully drawn from a glass rod with a diameter of 9 mm from this IZSBGC glass, neither the approach used for glass rod fabrication (or preform preparation) nor the resulting fiber loss was given in their paper.

Casting techniques (e.g., rotational casting and suction casting methods) are widely used for fluoride glass preform fabrication, and have been used for making fluoroindate glass fibers [11,13,14]. Another promising alternative technique is billet extrusion, which can easily form long preforms with desired diameters and internal structures [17]. The extrusion technique has been demonstrated to be a versatile method for the production of optical fiber preforms for a wide range of soft glasses, (e.g., fluorozirconate glass) and the subsequent fabrication of low-loss microstructured optical fibers [17–21]. Itoh et al. successfully made their InF_3/GaF_3 core and ZBLAN cladding preform by stacked extrusion [12]. However, no details of the fabrication of fluoroindate glass preform using the extrusion technique have been reported.

The aim of this work was to explore the use of the extrusion technique to produce low-loss IZSBGC glass fiber preforms. To the best of our knowledge, for the first time, we demonstrate extrusion of fluoroindate glass and drawing of fibers from extruded preforms. In order to ensure good quality of the glass billets for the extrusions, we also studied the impact of the choice of melting conditions on the glass quality. More specifically, our aims were to reduce the hydroxyl (OH) group content in the glass and to explore the feasibility of fabricating glass billets with good optical quality.

#182019 - $15.00 USD Received 18 Dec 2012; revised 30 Jan 2013; accepted 31 Jan 2013; published 1 Feb 2013

2. Experimental procedure

All glass fabrication steps including batching, melting at 900 °C for 3 hours and casting were conducted in a controlled dry N_2 atmosphere (99.99%) melting facility. The glasses were prepared using commercially available fluorides as starting materials which were well mixed into 30~70 g batches and then melted in a platinum alloy crucible containing 5% gold (internal volume: 100 ml). It is well known that oxide and OH impurities in the raw fluoride starting materials can cause an increase in transmission loss, and that a fluorination process during fabrication can reduce the concentration of these impurities in the resulting glass [22,23]. Therefore, small glass blocks (30 g) (Table 1) were initially fabricated to optimize the melting conditions and investigate the effect of different fluorination techniques on the OH content in the glass blocks. Two approaches were considered; ammonium bifluoride (NH_4HF_2) was incorporated into the melting process as a fluorination reagent [24], and SF_6 was used as a secondary atmosphere to study the dehydration of the fluoride glasses [25]. The glass batches with excess NH_4HF_2 (6.7 wt% of the batch weight) were first heat-treated at 235 °C, and then melted at 900 °C, and the glass melts were cast into a pre-heated mold after melting. The SF_6 procedure included the application of an SF_6 reactive atmosphere at 700 °C for 15 minutes, followed by the melting process at 900 °C. SF_6 was introduced at 700 °C, rather than 900 °C, because we have observed that SF_6 can attack Pt metal to form black particles at the higher temperature. Table 1 summarizes the processes used to fabricate the glasses under investigation.

Table 1. Glass blocks melting conditions

Sample	Melting Conditions	Dwell Time @ 235 °C	Dwell Time @ 700 °C	Dwell Time @ 900 °C	Absorption co-efficient at ~2.9 μm (cm^{-1})	T_g (˚C)	T_x (˚C)	T_p (˚C)
A	N_2	45 min	15 min	3 h	0.00106(± 0.0012)	318	389	415
B	$N_2 + SF_6$	45 min	15 min with SF_6	3 h	0.0042(± 0.0004)	318	389	413
C	$N_2 + NH_4HF_2$	45 min	15 min	3 h	0.0023(± 0.0002)	310	389	419

Electron probe micro-analysis (EPMA) (CAMECA SX51) was carried out to determine the glass composition of sample C after melting. The analysis was undertaken using an accelerating voltage of 15 kV and a beam current of ~20 nA with wavelength-dispersive X-ray spectrometers (WDS).

To study the effect of the fluorination processes, glass blocks were cut into slides with a thickness of ~15 mm which were then polished for IR transmission measurements using a commercial spectrometer (PerkinElmer Spectrum 400). The absorption coefficients were calculated from the transmission data, where background absorption due to the Fresnel reflection at the interfaces was subtracted. The characteristic temperatures; glass transition temperature (T_g), the temperature of crystallization (T_x) and peak of glass crystallization (T_p) of samples A to C (Table 1), prepared under different melting conditions, were also measured using a Setaram Differential Scanning Calorimetry (DSC) 131 equipment with experimental errors of ± 2 °C.

For fiber fabrication, larger glass billets (up to 70 g) were prepared using fluorination with NH_4HF_2. One glass melt was cast into a rod mold with an inner diameter of 10 mm and a length of 120 mm. After annealing, this cast rod was directly used as a preform for fiber fabrication. The other two glass melts were cast into a billet mold with an inner diameter of 30 mm and a length of 30 mm, which were used for preform extrusion (Fig. 1).

#182019 - $15.00 USD Received 18 Dec 2012; revised 30 Jan 2013; accepted 31 Jan 2013; published 1 Feb 2013

Fig. 1. Fluoroindate glass in the form of: (Left) Cast billets. (Top) Cast rod. (Centre) Preforms cast from cast billets.

Graphite has been successfully used as a die material for fluorozirconate glass extrusion due to the relatively low friction between the die and glass surfaces [21]. Using a graphite die, fluorozirconate glass could be extruded at a relatively higher viscosity (~10^8 Pa·s), i.e. lower temperatures, which allows the fluorozirconate preforms to be extruded below the onset of glass crystallization temperature (T_x) [21]. Therefore, in this work, we chose a graphite die to extrude the glasses at temperatures within ~70 °C of T_x. Prior to extrusion the cylindrical billets were polished using 1 μm Al_2O_3 powders. The billets were then extruded into rod-shape (cylindrical) preforms of 8 mm in diameter at temperatures within 20 °C above the glass transition temperature (T_g = 310 °C) using graphite dies.

The quality of the surface of a glass preform has a significant impact on the loss and strength of a fiber drawn from the preform. For fluorozirconate glasses, chemical etching of the preforms can prevent surface crystallization during fiber drawing due to the removal of pre-existing surface defects, thereby reducing the loss and increasing the mechanical strength of fluorozirconate fibers [26,27]. HCl has been widely used as an etchant for soft glasses as it is a corrosive acid which can remove a surface layer from matrice [28,29]. In this work, preliminary chemical etching was performed by suspending Preform 2 (Fig. 1) in a 15 wt% $HCl_{(aq)}$ solution (stirring applied) at a reasonable etching rate and room temperature for about 25 min to remove a ~0.5 mm thick outer layer, followed by a short rinse with methanol in an ultrasonic bath. The glass surfaces before and after etching were probed by an Atomic Force Microscope (AFM) (NT-MDT Ntegra Solaris AFM) to determine their roughness, which allowed the quality of the etch to be quantified. During etching, some white precipitate was formed on the glass rod surface. Identification of this white precipitate will enable optimization of the etching components in future work (i.e., help to suppress the formation of the white precipitate). In this study, we employed a scanning electron microscope (SEM; Philips XL30 field emission SEM) equipped with an energy dispersive X-ray spectrometer (EDS) to study the microstructures and compositions of the white precipitate on the glass surface after etching.

The cast rod was polished using 1 μm Al_2O_3 powders, and Preform 1 was cleaned by isopropyl alcohol in an ultrasonic bath for 30 min prior to fiber drawing while Preform 2 was etched as described above. Both cast rods and extruded rods were then pulled into unstructured fibers with diameters of 130~180 μm.

To investigate the impact of extrusion and other fabrication conditions on fiber loss, we selected 1550 nm as the wavelength for loss measurements as both light source and detector are readily available for this wavelength compared with the mid-infrared >2 μm. The fiber losses were measured using the cutback method and 1550 nm laser as light source. The output powers of the fibers under tests were recorded by a power meter.

3. Results and discussions

Sample C (glass block) was selected for EMPA analysis to determine its final chemical composition (Table 2). Although we used 3 hours for glass melting at 900 °C, there was no significant difference between measured and calculated concentrations for each element, suggesting that evaporation loss during glass melting is negligible.

#182019 - $15.00 USD Received 18 Dec 2012; revised 30 Jan 2013; accepted 31 Jan 2013; published 1 Feb 2013

Table 2. Electron probe microanalysis of sample C (glass block)

	In	Zn	Sr	Ba	Ga	Ca	F
EMPA results (mol %)	9.74 ± 0.19	5.97 ± 0.28	6.05 ± 0.18	5.37 ± 0.32	2.88 ± 0.21	0.58 ± 0.09	67.74 ± 0.21
Glass batch composition (mol %)	9.41	5.88	5.88	5.29	2.35	0.59	70.60

Figure 2 shows the absorption coefficient spectra of the three glasses prepared under different conditions (Table 1). It is clear that fluorination of the raw materials using NH_4HF_2 significantly reduced the absorption of OH groups (at ~2.9 μm) from 0.00106 (± 0.0012) to 0.0023 (± 0.0002) cm^{-1} (Fig. 2a). The infrared absorption edges of our glass samples are shifted to longer wavelengths, compared to ZBLAN fluorozirconate glass (Fig. 2b). For example, at the wavelength where the absorption coefficient is 2.3 cm^{-1} (corresponds to ~10% transmission for 1cm sample thickness), IZSBGC glass (sample C) has a wavelength of 8.7 μm whereas ZBLAN has a wavelength of 7.4 μm. As the OH content increases, relatively strong hydrogen bonds between OH and fluorine ions can form, which shifts the OH resonance (~2.9 μm) to longer wavelengths [30]. In our IZBSGC glasses (Fig. 2b), additional absorption >7.5 μm is observed for samples A and B, which were made without NH_4HF_2. In particular, a shoulder at 7.8 μm and a shift of the IR edge to the shorter wavelengths is found. Similar IR absorption features were observed in ZrF_4-BaF_2-LaF_3 glasses (7.1 μm), and BaF_2-ZrF_4-YbF_3-ThF_4 glasses (9.1 μm) due to oxide impurities [31,32]. Therefore, the shoulder at 7.8 μm in the absorption spectrum in samples A and B is attributed to oxide impurities in the glasses caused by incomplete fluorination without NH_4HF_2. The absorption at 7.8 μm was suppressed using NH_4HF_2 for sample C, which indicates effective reduction of oxide and OH impurities in sample C. Drexhage [33] found that an incomplete conversion of the oxide starting materials by the fluorinating agent (NH_4HF_2) during glass melting could alter the slope of the IR multiphonon edge, which corresponds to a shift of the IR absorption edge. Hence, the significant shift of the IR absorption edge to shorter wavelengths for samples A and B compared to sample C (Fig. 2b) is also attributed to incomplete conversion of oxides to fluorides due to the lack of using NH_4HF_2 for samples A and B.

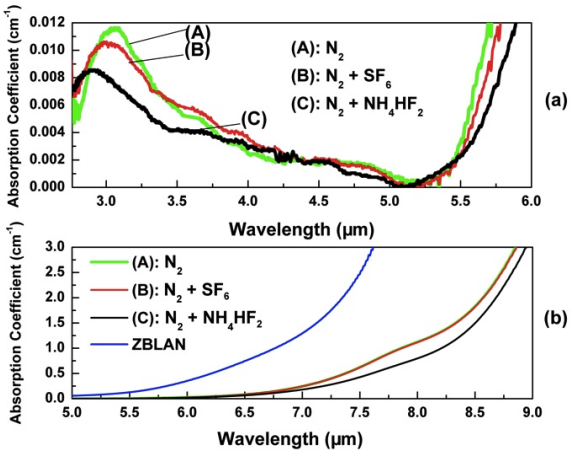

Fig. 2. Absorption coefficient for the glass samples prepared under the three different fabrication conditions (a) 2.75-6.00 μm; (b) 5.00-8.75μm.

DSC measurements showed that melting with NH_4HF_2 for sample C increased ΔT (T_x-T_g) and flattened the crystallization peak, suggesting a lower crystallization rate [16] compared

#182019 - $15.00 USD Received 18 Dec 2012; revised 30 Jan 2013; accepted 31 Jan 2013; published 1 Feb 2013

with samples A and B (Table 1 and Fig. 3). The crystallization peak of sample C shows a small shoulder at ~400 °C. Based on the crystallization theory by [34,35], the shoulder indicates a slight change in the crystallization behavior at this temperature.

It was found that oxide inclusions stimulated crystallization in zirconium fluoride-based glasses [36]. Therefore, we attribute the enhanced crystallization stability (reflected by increased ΔT and reduced crystallization rate) for sample C to a lower amount of oxide impurities in this sample as a result of the fluorination with NH_4HF_2. Sample C has a slightly lower glass transition temperature than the other two samples A and B, which we also attribute to the lower oxide impurity content of sample C. Similar results were observed when oxide impurities were present in ZrF_4-based ternary glasses [37,38].

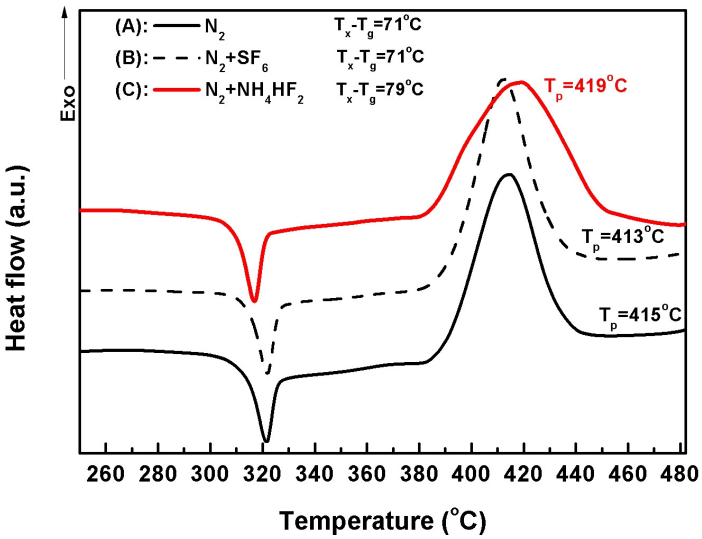

Fig. 3. DSC curves for the glass samples prepared under the three different fabrication conditions.

The cast rod contained relatively large bubbles (up to 1 mm in diameter) that formed during the rod casting procedure, while bubbles were not observed in preforms extruded from the glass billets (Fig. 1). This is consistent with our general observation that casting into long thin moulds leads to bubbles in the cast glass. This can probably be explained by the more turbulent flow of molten glass when it is poured into long thin moulds, which generates bubbles in the cast glass.

Our results show that the extrusion method is suitable for the preparation of bubble-free preforms, and that extruded rods typically exhibit a better surface finish than cast rods. The different surface finish between the extruded and cast rods can be understood by their different fabrication techniques: extruded preforms have a fire polished surface as the hot glass cools down in free space, whereas the hot cast glass rod during casting procedure is in contact with the mold when cooling down (Fig. 1).

The extrusions were conducted at 317 °C, 322 °C or 330 °C, requiring at least 8 hours. The higher viscosity at the relatively low temperature of 317 °C required higher extrusion force (~35 kN) compared with the other two higher temperatures, which caused the graphite die to crack. The extrusion force was greatly reduced by increasing the extrusion temperature, more specifically the force decreased to ~10 kN at 322 °C and 7-8 kN at 330 °C, respectively. The reduced extrusion force successfully prevented the graphite die cracking and decreased the friction between the glass surface and graphite die. Although no obvious crystallization was observed for the rods extruded at temperatures in the range of 322 °C to 330 °C under the optical microscope, we used thin polished glass slides made from the fluoroindate glass in

#182019 - $15.00 USD Received 18 Dec 2012; revised 30 Jan 2013; accepted 31 Jan 2013; published 1 Feb 2013

this study to explore whether surface crystallization could occur under such conditions. The polished glass slides had lower surface roughness and thickness than our extruded preforms. Therefore, it is easier to find crystallization on the glass slide under microscope. Two identical glass slides were treated at elevated temperatures comparable to those used for extrusion. There was no observable change before or after annealing at 322 °C, while significant crystallization in the form of wrinkles occurred on the edge of the glass sample after annealing at 330 °C (Fig. 4). This suggests that a temperature of 330 °C for preform extrusion can cause potential surface crystallization. By contrast, 322 °C extrusion temperature is sufficiently low to avoid potential surface crystallization while being sufficiently high to prevent graphite die cracking.

Note that the potential crystallization temperature of 330 °C is much lower than T_x measured by DSC due to the different thermal treatment during extrusion in comparison to the DSC measurement. In the extrusion process, the glass was kept at elevated temperature for about 8-10 hours, whereas during the DSC measurement the glass was heated at a rate of 10 °C/min. The long dwell time during extrusion can result in crystallization at temperatures below T_x.

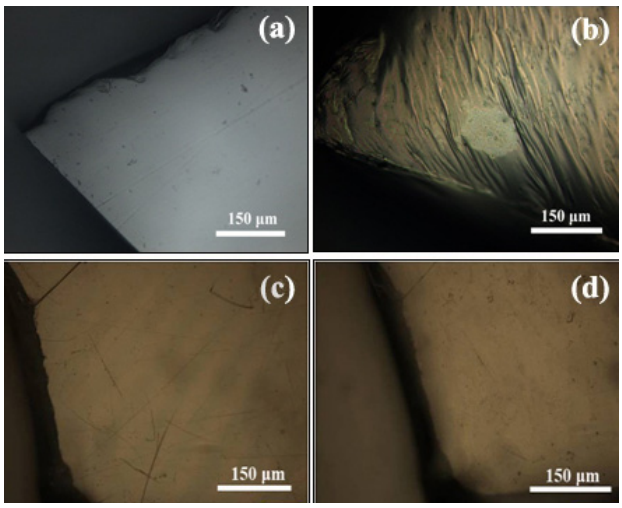

Fig. 4. Glass surface images: (a) before annealing at 330 °C less than 8 hours; (b) the edge of the glass after annealing at 330 °C less than 8 hours; (c) before annealing at 322 °C for 24 hours; (d) after annealing at 322 °C for 24 hours.

The annealing test showed that crystallization or nucleation were most likely to occur at 330 °C, even though no crystals were identified on the extruded Preform 2 on inspection with an optical microscope. The potential crystallization for the Preform 2 extruded at 330 °C would result in increasing amounts of crystals at the elevated temperature during the fiber drawing procedure, which would ultimately increase loss and decrease mechanical strength of the fiber made from this rod. To remove the potential crystallization outer layer, chemical etching was applied by suspending Preform 2 (Fig. 1) in a 15 wt% $HCl_{(aq)}$ solution (stirring applied) at room temperature for about 25 min to remove a ~0.5 mm thick outer layer.

To evaluate the efficacy of preform etching, we determined the surface roughness of the preform before and after etching using AFM (Fig. 5). AFM images of 50 × 50 µm^2 preform area were processed to determine the roughness parameters, S_a (Average Roughness), and S_q (Root mean square (RMS) Roughness) defined in Eqs. (1) and (2), respectively [39]:

$$S_a = \frac{1}{MN}\sum_{k=0}^{M-1}\sum_{l=0}^{N-1}\left|z(x_k, y_l)\right| \quad (1)$$

#182019 - $15.00 USD Received 18 Dec 2012; revised 30 Jan 2013; accepted 31 Jan 2013; published 1 Feb 2013

$$S_a = \sqrt{\frac{1}{MN}\sum_{k=0}^{M-1}\sum_{l=0}^{N-1}\left[z(x_k, y_l)\right]^2} \quad (2)$$

where M and N are the numbers of the measured points and $Z(x_k, y_l)$ is the distance from each measured point to the central plane on the surface of the tested preform sample. S_p is the maximum peak height. During the extrusion procedure, extrusion stripes, which can be seen on the preform surfaces (shown in inset optical micrograph of Fig. 5a), were most likely caused by the friction between the glass surface and graphite die. On the preform surface without white precipitate, the maximum roughness in the stripe regions dramatically decreased after etching, while the average roughness did not change obviously after etching (Fig. 5). SEM-EDS analysis (Fig. 6) showed that the white precipitate was composed of metal halides (F^- and Cl^-). EDS analysis also suggests that the chlorine ions from the etchant (i.e., $HCl_{(aq)}$) can co-precipitate with ions leached out from the glass matrix. Thus we can conclude that etching using solely 15 wt% $HCl_{(aq)}$ solution is not an effective way to improve the surface quality. However, the reduction of the surface roughness in the stripe regions (when no precipitate was present) indicates that etching will improve the surface quality and remove defects associated with preform extrusion once the etchant is further optimized, overcoming the issue of precipitate formation.

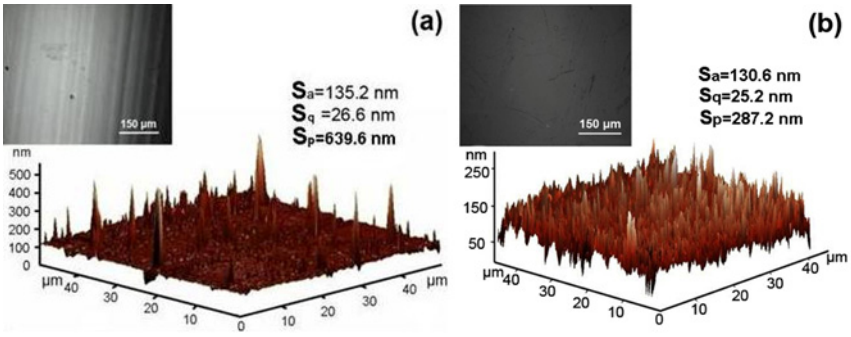

Fig. 5. AFM morphology of preform surface (a) before etching; (b) surface without white precipitate after etching by 15 wt% $HCl_{(aq)}$. Insets are optical microscope images of the preform surfaces before and after etching.

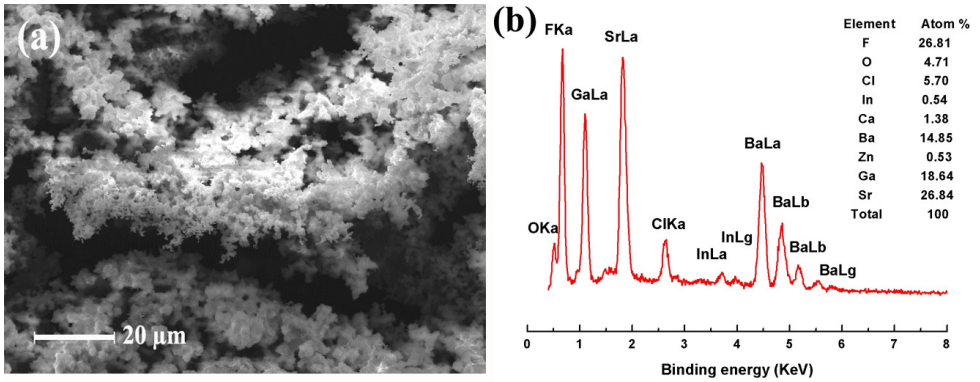

Fig. 6. (a) SEM secondary electron image and (b) EDS analysis of the white precipitate formed after 15 wt% $HCl_{(aq)}$ etch.

Fiber losses of the two unstructured fibers pulled from extruded preforms were lower than that of the fiber made from the cast rod (Table 3). This can be explained by reference to the improved surface finish and the lack of larger bubbles in the extruded preforms. The fiber

#182019 - $15.00 USD Received 18 Dec 2012; revised 30 Jan 2013; accepted 31 Jan 2013; published 1 Feb 2013

drawn from Preform 1, extruded at 322 °C, exhibited the lowest fiber loss of ~1.9 dB/m measured at 1550 nm (Fig. 7). This (un-etched) preform was successfully pulled into a bare unstructured optical fiber with a diameter of approximately 140 μm without any evidence of crystallization (Fig. 8). Both Preforms 1 and 2 were made using the extrusion technique. The lower loss of the fiber drawn from Preform 1 compared with the fiber drawn from Preform 2 is attributed to the lower extrusion temperature used for Preform 1, thus avoiding potential crystallization. Although chemical etching was applied to Preform 2 extruded at 330 °C to remove the potential crystallization surface layer, the resultant fiber exhibited a relatively high loss, which is attributed to the occurrence of the white precipitate on the etched preform. The precipitate produced an inhomogeneous surface crystallization during fiber drawing, which caused scattering centers on the fiber surface and is reflected by the relatively poor linear regression ($R^2 = 0.96$).

Table 3. Glass rod / preform preparation conditions and results of the fiber loss

Sample	Diameter of rod/preform (mm)	Fabrication Method	Surface Treatment	Fiber Loss at 1550 nm (dB/m)
Cast Rod	10	Direct Casting	Mechanical Polishing	42.3
Preform 1	8	Extruded @ 322 °C (± 1 °C)	Clean by Isopropyl Alcohol Ultrasonic Bath for 30 min	1.9
Preform 2	8	Extruded @ 330 °C (± 1 °C)	Etching by 15 wt% $HCl_{(aq)}$	31.2

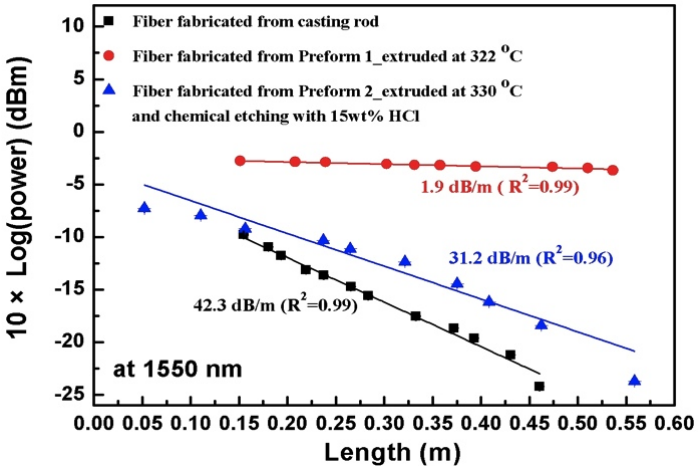

Fig. 7. Loss measurements at 1550 nm for fibers made using different conditions. Linear fits of the data are also shown in the figure.

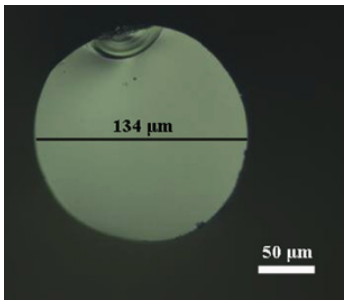

Fig. 8. Microscope image of the fiber drawn from the preform extruded at 322 °C.

#182019 - $15.00 USD Received 18 Dec 2012; revised 30 Jan 2013; accepted 31 Jan 2013; published 1 Feb 2013

4. Conclusions and future work

In summary, the absorption of OH groups at 2.9 μm in $32InF_3$-$20ZnF_2$-$20SrF_2$-$18BaF_2$-$8GaF_3$-$2CaF_2$ (IZSBGC) glasses was reduced by employing a fluorination method with NH_4HF_2. Fibers drawn from preforms (prepared using the extrusion technique) had a lower fiber loss (i.e., 1.9 dB/m), compared to the fiber drawn from the cast rod. This significant decrease in fiber loss is attributed to the better surface finish and reduced quantity of the bubbles in the extruded preforms. In contrast to 330 °C, 322 °C did not cause surface crystallization, which indicates that 322 °C is a suitable temperature for rod extrusion without crystallization. The absence of crystallization in the preform extruded at 322 °C resulted in the lowest loss of the corresponding fiber. The formation of the white precipitate during etching procedure shows that 15 wt% $HCl_{(aq)}$ solution is not an effective etching method to improve the IZSBGC glass preform surface quality and hence reduce fiber loss. The fiber loss value of our lowest-loss fiber is still higher than that of commercially available fluoroindate glass fiber. This is potentially due to the purity of the commercially available raw materials (99.9~99.99%) used for fiber fabrications. However, we provide a novel and feasible approach to fabricate fluoroindate glass rod preforms suitable for fiber drawing using the extrusion technique for the first time.

Future work will focus on the reduction of fiber loss, including further investigation of etching procedures to avoid surface precipitates and improve surface finish. Stacked extrusion of core and cladding billets [12] will also be investigated to prepare a glass-glass interface, which may further reduce loss by improving the quality of the guiding interface.

Acknowledgments

We acknowledge support from DSTO for funding this work. We also acknowledge the facilities, and the scientific and technical assistance (Mr Angus Netting and Mr Ken Neubauer) of the Australian Microscopy & Microanalysis Research Facility at Adelaide Microscopy Centre of The University of Adelaide. This work was performed in part at the Optofab node of the Australian National Fabrication Facility, a company established under the National Collaborative Research Infrastructure Strategy to provide nano and microfabrication facilities for Australia's researchers. We thank Dr. Guang Yang (University of Rennes, France) for DSC analysis, and Mr Roger Moore (University of Adelaide) for fiber drawing. Jiafang Bei acknowledges the International Postgraduate Research Scholarship (IPRS) supported by The University of Adelaide. H. Ebendorff-Heidepriem acknowledges the support of a DSTO Fellowship and T.M. Monro acknowledges the support of an ARC Federation Fellowship.

#182019 - $15.00 USD Received 18 Dec 2012; revised 30 Jan 2013; accepted 31 Jan 2013; published 1 Feb 2013

II

Reduction of scattering loss in fluoroindate glass fibers

Jiafang Bei,[1],* Tanya M. Monro,[1] Alexander Hemming,[2] and Heike Ebendorff-Heidepriem[1]

[1]*Institute for Photonics and Advanced Sensing and School of Chemistry and Physics, University of Adelaide, Adelaide, SA 5005, Australia*

[2]*Electro-Optic Technology Group, Electronic Warfare and Radar Division, Defence Science and Technology Organisation, Edinburgh, SA 5111, Australia*

Reduction of scattering loss in fluoroindate glass fibers

Jiafang Bei,[1,*] Tanya M. Monro,[1] Alexander Hemming,[2] and Heike Ebendorff-Heidepriem[1]

[1]*Institute for Photonics and Advanced Sensing and School of Chemistry and Physics, University of Adelaide, Adelaide, SA 5005, Australia*

[2]*Electro-Optic Technology Group, Electronic Warfare and Radar Division, Defence Science and Technology Organisation, Edinburgh, SA 5111, Australia*

**jiafang.bei@adelaide.edu.au*

Abstract: The current fluoroindate glass optical fiber loss is dominated by extrinsic absorption and scattering loss. Attempts were made to reduce fluoroindate glass fiber loss by optimizing glass melting conditions, preform extrusion process and fiber drawing conditions. Our results show that fluorination of the glass batches (with 99.99% InF_3) at 450 °C by addition of ammonium bifluoride reduced un-dissolved particles (potential scattering losses) in the glass. Glass flow analysis was carried out to provide insights into the glass temperature-viscosity behavior and the relationship between preform surface roughness and extrusion temperature, which enabled fabrication of preforms with low surface roughnesses and eventually reduced the fiber scattering loss. Fiber surface crystallization was reduced via conducting chemical etching and polishing (with colloidal silica) on both glass billets and preforms, extending the heating zone for fiber drawing, and applying additional weight at the bottom of preforms. As a consequence, the fiber surface roughness decreased, resulting in decreased fiber scattering loss and enhanced fiber strength.

OCIS codes: (160.2290) Fiber materials; (160.2750) Glass and other amorphous materials.

References and links

1. X. Zhu and N. Peyghambarian, "High-power ZBLAN glass fiber lasers: Review and prospect," Adv. Optoelectron. **2010**, 501956 (2010).
2. M. Saad, "Fluoride glass fiber: state of the art," Proc. SPIE **7316**, 73160N, 73160N-16 (2009).
3. S. Shibata, M. Horiguchi, K. Jinguji, S. Mitachi, T. Kanamori, and T. Manabe, "Prediction of loss minima in infra-red optical fibers," Electron. Lett. **17**(21), 775–777 (1981).
4. T. Kanamori and S. Sakaguchi, "Preparation of elevated NA fluoride optical fibers," Jpn. J. Appl. Phys. **25**(Part 2, No. 6), L468–L470 (1986).
5. J. Lucas, "Fluoride glasses," J. Mater. Sci. **24**(1), 1–13 (1989).
6. S. Mitachi, Y. Terunuma, Y. Ohishi, and S. Takahashi, "Reduction of impurities in fluoride glass fibers," J. Lightwave Technol. **2**(5), 587–592 (1984).
7. G. F. West and W. Höfle, "Spectral attenuation of fluoride glass fibers," J. Non-Cryst. Solids **213–214**, 189–192 (1997).
8. P. C. Pureza, P. H. Klein, W. I. Roberts, and I. D. Aggarwal, "Influence of preform surface treatments on the strength of fluorozirconate fibers," J. Mater. Sci. **26**(19), 5149–5154 (1991).
9. J. Bei, T. M. Monro, A. Hemming, and H. Ebendorff-Heidepriem, "Fabrication of extruded fluoroindate optical fibers," Opt. Mater. Express **3**(3), 318–328 (2013).
10. A. M. Mailhot, A. Elyamani, and R. E. Riman, "Reactive atmosphere synthesis of Sol-gel heavy metal fluoride glasses," J. Mater. Res. **7**(06), 1534–1540 (1992).
11. S. Takahashi, T. Kanamori, Y. Ohishi, K. Fujiura, and Y. Terunuma, "Reduction of oxygen impurity in ZrF_4-based fluoride glass," Mater. Sci. Forum **32–33**, 87–92 (1988).
12. R. M. Almeida and J. D. Mackenzie, "The effects of oxide impurities on the optical properties of fluoride glasses," J. Non-Cryst. Solids **56**(1-3), 63–68 (1983).
13. Y. Nishida, T. Kanamori, T. Sakamoto, Y. Ohishi, and S. Sudo, "Fluoride glass fiber," U. S. Patent 5 774 620, June 30, 1998.

#192346 - $15.00 USD Received 17 Jun 2013; revised 3 Aug 2013; accepted 4 Aug 2013; published 13 Aug 2013

14. Y. Nishida, T. Kanamori, T. Sakamoto, Y. Ohishi, and S. Sudo, "Development of PbF_2-GaF_3-InF_3-ZnF_2-YF_3-LaF_3 glass for use as a 1.3 μm Pr^{3+}-doped fiber amplifier host," J. Non-Cryst. Solids **221**(2-3), 238–244 (1997).
15. Y. Jestin, A. L. Sauze, B. Boulard, Y. Gao, and P. Baniel, "Viscosity matching of new PbF2-InF3-GaF3 based fluoride glasses and ZBLAN for high NA optical fiber," J. Non-Cryst. Solids **320**(1-3), 231–237 (2003).
16. H. Ebendorff-Heidepriem and T. M. Monro, "Analysis of glass flow during extrusion of optical fiber preforms," Opt. Mater. Express **2**(3), 304–320 (2012).
17. E. Roeder, "Extrusion of glass," J. Non-Cryst. Solids **5**(5), 377–388 (1971).
18. H. Ebendorff-Heidepriem, Y. Li, and T. M. Monro, "Reduced loss in extruded soft glass microstructured fiber," Electron. Lett. **43**(24), 1343–1345 (2007).
19. H. Ebendorff-Heidepriem and T. M. Monro, "Extrusion of complex preforms for microstructured optical fibers," Opt. Express **15**(23), 15086–15092 (2007).
20. H. Ebendorff-Heidepriem, T.-C. Foo, R. C. Moore, W. Zhang, Y. Li, T. M. Monro, A. Hemming, and D. G. Lancaster, "Fluoride glass microstructured optical fiber with large mode area and mid-infrared transmission," Opt. Lett. **33**(23), 2861–2863 (2008).
21. H. W. Schneider, A. Schoberth, A. Staudt, and C. Gerndt, "Fluoride glass etching method for preparation of infra-red fibers with improved tensile strength," Electron. Lett. **22**(18), 949–950 (1986).
22. I. D. Aggarwal and G. Lu, *Fluoride Glass Fiber Optics* (Academic Press, 1991), Chap. 5.
23. G. Qian, F. Xia, J. Brugger, W. M. Skinner, J. Bei, G. Chen, and A. Pring, "Replacement of pyrrhotite by pyrite and marcasite under hydrothermal conditions up to 220 °C: An experimental study of reaction textures and mechanisms," Am. Mineral. **96**(11-12), 1878–1893 (2011).
24. Y. Ahn, J.-Y. Yoon, C.-W. Baek, and Y.-K. Kim, "Chemical mechanical polishing by colloidal silica-based slurry for micro-scratch reduction," Wear **257**(7-8), 785–789 (2004).
25. H. Ebendorff-Heidepriem, T. C. Foo, R. C. Moore, W. Zhang, Y. Li, T. M. Monro, A. Hemming, and D. G. Lancaster, "Fluoride glass microstructured optical fiber with large mode area and mid-infrared transmission," Opt. Lett. **33**(23), 2861–2863 (2008).
26. G. Rault, J. L. Adam, F. Smektala, and J. Lucas, "Fluoride glass compositions for waveguide applications," J. Fluor. Chem. **110**(2), 165–173 (2001).
27. C. Voyce, A. D. Fitt, and T. M. Monro, "Mathematical modeling as an accurate predictive tool in capillary and microstructured fiber manufacture: the effects of preform rotation," J. Lightwave Technol. **26**(7), 791–798 (2008).
28. S. Sakaguchi, Y. Terunuma, Y. Ohishi, and T. Kanamori, "Fluoride fiber drawing with improved tensile strength," J. Mater. Sci. Lett. **6**(9), 1063–1065 (1987).
29. P. W. France, *Fluoride Glass Optical Fibers* (Blackie, 1990), Chap. 9.
30. M. Saad, "High purity fluoride glass synthesis: a review" (IR photonics 2009). *http://www.iguide-irphotonics.com/pdf/Pwest2009.pdf*.
31. M. Braglia, S. Mosso, G. Dai, E. Billi, L. Bonelli, M. Baricco, and L. Battezzati, "Rheology of tellurite glasses," Mater. Res. Bull. **35**(14-15), 2343–2351 (2000).
32. E. Roeder, "Flow behaviour of glass during extrusion," J. Non-Cryst. Solids **7**(2), 203–220 (1972).
33. J. E. Shelby, *Introduction to Glass Science and Technology* (The Royal Society of Chemistry, 2005), Chap. 6.
34. H. Ebendorff-Heidepriem, T. M. Monro, M. A. van Eijkelenborg, and M. C. J. Large, "Extruded high-NA microstructured polymer optical fiber," Opt. Commun. **273**(1), 133–137 (2007).
35. E. W. Deeg, C. G. Silverberg, and L. B. Martel, "Method for fire polishing optical glass," U. S. Patent 3 811 857, May 21, 1974.
36. Jr. J. E. Dickinson and B. R. Wheaton, "Processes for polishing glass and glass-ceramic surfaces using excimer laser radiation," U. S. Patent 5 742 026, April 21, 1998.
37. P. A. Thompson and S. M. Troian, "A general boundary condition for liquid flow at solid surfaces," Nature **389**(6652), 360–362 (1997).
38. K. M. Reich, C. V. Gay, and J. A. Frangos, "Fluid shear stress as a mediator of osteoblast cyclic adenosine monophosphate production," J. Cell. Physiol. **143**(1), 100–104 (1990).
39. M. Chatzimina, G. C. Georgiou, K. Housiadas, and S. G. Hatzikiriakos, "Stability of the annular Poiseuille flow of a Newtonian liquid with slip along the walls," J. Non-Newton. Fluid Mech. **159**, 1–9 (2009).
40. D. R. MacFarlane, P. J. Newman, and A. Voelkel, "Methods of purification of zirconium tetrafluoride for fluorozirconate glass," J. Am. Ceram. Soc. **85**(6), 1610–1612 (2002).

1. Introduction

Fluoride glasses have attracted much interest as potential materials for high power fiber delivery in the mid-infrared spectral region due to their unique optical properties [1]. They show a wide transmission range from the ultraviolet to the mid-infrared region, and have significantly lower theoretical optical loss than that of conventional silicate glass fibers [2]. Shibata et al. estimated the theoretical minimum fluoride fiber loss to be $<10^{-2}$ dB/km at 2-3 μm, one magnitude lower than that of silica fiber. This estimate was based on losses due to

#192346 - $15.00 USD Received 17 Jun 2013; revised 3 Aug 2013; accepted 4 Aug 2013; published 13 Aug 2013

Rayleigh scattering and IR edge absorption which are the dominant intrinsic loss factors in fluoride glasses [3]. However, the losses of fabricated fluoride fibers are higher than the theoretically estimated value. It is important to note that Rayleigh scattering, which ultimately determines the attainable loss, represents only a small contribution to the fiber loss for fibers fabricated to date, and elimination of many other extrinsic losses caused by absorptions and scatterings are challenging. The lowest fiber loss reported so far is 0.7 dB/km at 2.6 μm measured by Kanamori and Sakaguchi on a 30 m long fluorozirconate fiber [4], which is still higher than the theoretical loss. Since fluoride glasses have significantly lower crystallization stability than oxide glasses, impurities in the raw materials and moisture in the atmosphere during preparation of fluoride glasses can easily induce crystallization which leads to scattering centers and increases the loss [5]. Absorption of impurities such as transition metals and rare earth ions in the raw materials also contributes to the loss of the glass, resulting in absorption losses in the fibers [6].

Many researchers have reported efforts towards the development of low-loss fluoride glass fibers by reducing sources of extrinsic absorption and scattering. Hydroxyl ion, transition metals and rare earth elements in the raw materials, which result in absorption loss in glass fibers, are major problems to be overcome in the production of ultra-low loss fluoride glass fibers. Defects that cause scattering can be divided into volume and surface defects. Volume defects (e.g., contaminations from platinum crucible, bubbles, un-dissolved particles and crystals [7]) are imperfections within the glass matrices that are principally formed during glass melting. Surface defects (e.g., surface contaminations, micro-cracks, scratches [8] and surface crystallization) originate from the contact of the glass surfaces with molds or extrusion dies during casting and extrusion [9] and from the reaction of the glass surface with moisture in the atmosphere during fiber fabrication or storage.

The first step in reducing extrinsic losses in these glasses is to reduce oxide impurities in the starting materials used for the glass melts. This is achieved using a fluorination process during the glass melting, which can reduce the concentration of oxide impurities in the glasses [6,10], resulting in reduced scattering in the glasses. One traditional approach to fluorination is the use of ammonium bifluoride (NH_4HF_2) during glass synthesis to fluorinate all non-fluoride impurities in the raw materials [11]. In particular, this method plays a critical role in reducing the content of oxides and oxy-hydrides, which would otherwise increase the IR absorption or shorten the IR cut-off wavelength and result in substantial loss in the glasses [12].

In principle, by conducting all glass preparation under fluorination with ammonium bifluoride, the level of oxides and oxy-hydrides can be significantly reduced. However, other sources of extrinsic loss such as bubbles and poor surface quality (caused by e.g., surface crystallization) will cause an increase in fiber loss. Hence, it is critical to reduce loss in fluoride fibers by improving preform and fiber fabrication conditions. Casting techniques (e.g., rotational casting and suction casting methods) have been used successfully for preparation of fluoride glass preform and fluoroindate glass fibers [13–15]. An alternative technique is billet extrusion, which can be used to form long preforms of a desired diameter as well as a range of internal structures [16,17]. Compared to the casting method, the extrusion technique is a versatile method for the production of low-loss microstructured optical fibers with various shapes produced from different types of glasses [18–20]. It also has been demonstrated that the extrusion method is suitable for the preparation of bubble-free rods, which typically exhibit better surface finish and fewer bubbles than cast rods [9]. However, both casting and extrusion methods unavoidably introduce surface contaminations (i.e., metallic particles and graphite particles) and surface scratches (leading to high roughness) generated during contact with molds or dies. Poor surface quality associated with these surface contaminations and scratches will cause low fiber strength and high loss in air-clad (i.e., unstructured) fibers and air/glass microstructured fibers unless the contaminated layer can be removed [8]. The surface quality can be improved by chemical etching, which allows a uniform and rapid dissolution of surface

#192346 - $15.00 USD Received 17 Jun 2013; revised 3 Aug 2013; accepted 4 Aug 2013; published 13 Aug 2013

regions in fluoride glasses. The etching method can also smooth the fiber surface (i.e., reduce the surface roughness), which enables the preparation of fluoride fibers with low transmission loss and high fiber strength [21]. Although chemical etching prior to fiber drawing can effectively remove defects on the preform surface, fiber preform drawing presents a new set of challenges such as precise control of temperature and atmosphere. Since the viscosity of fluoride glasses shows a strong temperature dependence and sensitivity to surrounding atmosphere, an accurate control of the drawing temperature and atmosphere is critical to the preparation of long-length, low-loss and high-strength fibers [8,22].

In our previous study [9], the extrusion technique was demonstrated to be a suitable method for the production of low loss fluoroindate fibers made from $32InF_3$-$20ZnF_2$-$20SrF_2$-$18BaF_2$-$8GaF_3$-$2CaF_2$ (IZSBGC) glass. This fluoroindate glass composition is particularly promising for applications in the mid-infrared spectral region due to its high transmission and relatively low rate of crystallization compared to ZBLAN glass [9]. However, the presence of surface crystallization (e.g., white precipitates) and roughness on the preforms, which were major scattering centers, caused high fiber loss and low fiber strength in our previous work [9]. The aim of this study is therefore to reduce the fiber scattering loss and to improve mechanical strength of unstructured fibers by minimizing surface crystallization and roughness through optimization of fluorination processes, extrusion and fiber drawing conditions.

2. Experimental conditions and measurement techniques

2.1 Glass melting

All glass fabrication steps including weighing of the raw materials (batching), fluorination at 235 °C (45 min) or 450 °C (1 h), melting at 900 °C for 2 or 3 h, and casting were conducted in a controlled dry N_2 atmosphere (99.99%) melting facility. The temperature ramp speed was set to 5 °C/min. The glasses were prepared using commercially available fluorides as starting materials which were thoroughly mixed into 30-130 g batches and then melted in a platinum alloy crucible containing 5% gold (internal volume: 100 or 300 ml). We used two different InF_3 raw materials: 99.99% (metal purity) $InF_3{\cdot}3H_2O$ (labeled with a star '*' in Table 1), and anhydrous 99.99% (metal purity) InF_3 (labeled with double star '**' in Table 1). To fluorinate oxide impurities in the batch, NH_4HF_2 was added to the batch before melting. However, H_2O in $InF_3{\cdot}3H_2O$ reacts with InF_3, resulting in $In(OH)_3$ and gaseous HF. Hence, for glass batches using $InF_3{\cdot}3H_2O$, a higher amount of excess NH_4HF_2 (6.7 wt% of the batch weight) was used to compensate the loss of fluorine due to the formation and loss of HF, while for glass batches containing anhydrous InF_3 a lower amount of NH_4HF_2 was used (2.4 wt% of the batch weight) due to higher fluorine content in the raw material. The glass batches were first fluorinated at 235 °C or 450 °C, followed by melting at 900 °C. Finally, the glass melts were cast into a pre-heated mold. For basic glass characterization (samples A-C in Table 1), small melts of ~30 g were cast into rectangular glass blocks of dimensions of 15×10×30 mm^3. For preform extrusion, larger glass melts (up to 130 g) were prepared and cast into a cylindrical mold, resulting in glass billets of 30 mm diameter and 20-30mm height.

2.2 Chemical etching and mechanical polishing

To improve the surface quality of the cast billets and extruded preforms, mechanical polishing and/or chemical etching surface treatments were applied. More specifically, after glass melting, cylindrical billets were polished using 3 μm diamond pastes and then suspensions of 40 nm colloidal silica, which produced scratch-free surfaces [23,24]. For comparison purposes, some of the billets and/or preforms for chemical etching were suspended in a 1.36 M $ZrOCl_{2(aq)}$ solution (with stirring applied) at room temperature for about 30 min to remove a ~0.5 mm thick outer layer, followed by a rinse in methanol in an ultrasonic bath for 30 min and final hand polishing with 40nm colloidal silica solution (hereafter referred to as

#192346 - $15.00 USD Received 17 Jun 2013; revised 3 Aug 2013; accepted 4 Aug 2013; published 13 Aug 2013

chemo-mechanical treatment). The published etching solution recipe, i.e., 0.4 mol $ZrOCl_2 \cdot 8H_2O$ in 1L 1N HCl for ZBLAN glasses [21] resulted in the formation of a white layer on a glass preform during etching. However, when a 1.36 M $ZrOCl_{2(aq)}$ solution (optimized concentration) was used, white layer was not observed on the preform (immersed in etching solution) during the etching process. After etching, the preform was rinsed with methanol for 30 min and then was dried out using a N_2 gas gun. A few regions of light white layers were, however, found on the dried and etched billet or preform surface. Hence, we polished etched billets or preforms with a 40 nm colloidal silica suspension to remove white layer formed during etching. In comparison with our previous work, etching with 15 wt% $HCl_{(aq)}$ solution resulted in a significant white layer giving rise to a high loss [9].

2.3 Extrusion

Billet extrusion technique has been demonstrated as a suitable method for fluoroindate glass preform fabrication [9]. Extrusion conditions for fluorindate glasses were based on previous work on fluorozirconate glass extrusion [20]. Graphite has been successfully used as a die material for fluorozirconate glass extrusion due to the relatively low friction between the die and glass surfaces. Fluorozirconate glass could be extruded at a higher viscosities (~10^8 Pa·s), i.e., lower temperatures, using a graphite die compared with a stainless steel die. Extrusion with a graphite die allowed fluorozirconate preforms to be extruded below the onset of glass surface crystallization temperature (290 °C [25]) which is 62 °C lower than the glass crystallization temperature measured by DSC (T_x = 352 °C [26]). In this work, graphite was also used as the die material for the extrusion of IZSBGC glass at a temperature below the onset of glass crystallization temperature [9,20]. Surface crystallization of IZSBGC glass was observed for a 330 °C extrusion temperature, which is ~60 °C lower than T_x = 389 °C determined by DSC in our previous work [9]. Therefore, following polishing or chemo-mechanical treatment, the cylindrical billets were extruded into rod-shape (cylindrical) preforms of 5-10 mm in diameter at temperatures in the range of the glass transition temperature (T_g = 307 °C) (Fig. 2) to T_g + 23 °C under N_2 controlled atmosphere. Four types of graphite dies (a-d) with different die channel lengths and diameters (Table 2) were used to extrude unstructured rods. Die types (a) (8 mm die channel diameter) and (d) (5 mm die channel diameter) were used for the extrusion of 65 g (batch weight) glass billets, whereas die types (b) and (c) were used for extrusion of ≥100 g (batch weight) glass billets.

The extrusion trials were conducted at a fixed temperature and ram speed, while the extrusion force was varied. For the calculations described in Section 3.2, we used the extrusion force applied after the die was completely filled with glass, i.e., when the rod started to emerge from the extrusion die (Fig. 1). The other details of the extrusion set-up, die types and error analysis used in this work can be found in [16]. For analysis of the extrusion data in Table 2, errors for the viscosity values were obtained based on relative errors for the temperature measurements (0.90-0.95%) and ram force, *F* (3-17% in the region when a rod emerged from a die).

#192346 - $15.00 USD Received 17 Jun 2013; revised 3 Aug 2013; accepted 4 Aug 2013; published 13 Aug 2013

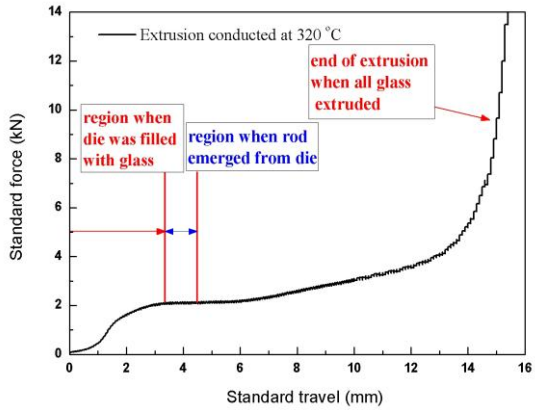

Fig. 1. Extrusion force profile for a fluoroindate extrusion trial using die (c) at 320 °C.

2.4 Fiber drawing

All preforms were pulled into unstructured fibers with diameters ranging from 130 to 180 μm under N_2 controlled atmosphere. The induction heating furnace used in the fiber drawing tower comprises a cylindrical graphite ring, which acts as the susceptor and therefore the heat source of the furnace. In a fiber-drawing furnace, the temperature that controls the furnace temperature is usually measured at a point close to the heat source (in our case the susceptor). However, earlier studies showed that the glass temperature varied significantly along the length of the furnace and also depended upon the heat source length [27,28], which corresponds to susceptor length for our fiber drawing furnace. Two types of graphite susceptors with the same inner and outer diameters but different heights (2 cm or 4.5 cm-long) were used to explore the impact of the furnace working temperature and the maximum preform temperature for fluoroindate glass fiber fabrications. For some preforms, an additional weight of ~190 g was applied to the bottom of the preforms during fiber drawing to decrease the temperature at which a drop is formed, thereby reducing the surface crystallization on the preform.

2.5 Measurements

The characteristic temperatures, i.e., glass transition temperature (T_g), glass crystallization temperature (T_x) and peak of crystallization temperature (T_p), of samples A and C (Fig. 2) were measured using a Setaram Differential Scanning Calorimetry (DSC) 131 equipment with experimental errors of ± 2 °C. This measurement was conducted from room temperature up to 530 °C at a heating rate of 10 °C /min under N_2 atmosphere.

For thermal dilatometric measurement, we used a piece of 5 mm diameter rod that was extruded at 320 °C. This measurement was conducted from room temperature up to 500 °C at a heating rate of 5 °C/min using a Dilatometer (Netzsch DIL 402, Germany), with experimental errors of ± 0.01 °C.

The surface roughness of preforms and fibers were measured using an optical interferometric profiler (model Contour GT-K1 Optical Profiler Stitching System from Veeco). From the optical profiler images, roughness parameters, S_a (average roughness), and S_q (root mean square (RMS) roughness) defined in Eqs. (4) and (5), respectively [9], were determined using the following expressions

$$S_a = \frac{1}{MN}\sum_{k=0}^{M-1}\sum_{l=0}^{N-1}\left|z(x_k, y_l)\right| \quad (1)$$

#192346 - $15.00 USD Received 17 Jun 2013; revised 3 Aug 2013; accepted 4 Aug 2013; published 13 Aug 2013

$$S_q = \sqrt{\frac{1}{MN}\sum_{k=0}^{M-1}\sum_{l=0}^{N-1}\left[z(x_k, y_l)\right]^2} \quad (2)$$

where M and N are the numbers of the measured points and $Z(x_k, y_l)$ is the distance from each measured point to the central plane on the surface of the tested preform sample. Three surfaces areas, each being ~120×160 μm^2, were probed in the preforms, while five areas, each being ~25×160 μm^2, were measured in the fibers.

To investigate the impact of fabrication conditions on fiber loss, we selected 1550 nm as a wavelength for spot loss measurements and broadband spectral range of 500-1750 nm for white light source measurements. The fiber losses were measured based on the cutback method using a 1550 nm laser (spot loss measurement) and a bulb (broadband loss measurement) as the light sources. The output power of the fiber under test during spot loss measurement at 1550 nm was recorded by a power meter and for broadband loss measurement with an optical spectrum analyzer. The relative errors for spot loss measurements varied from 2.2% to 5.9% of the average value. The uncertainties of the broadband loss measurements were up to 10% of measured values.

The mid-IR fiber transmission was measured from 2 to 8 μm using a fiber-coupled Bruker Vertex 70 FTIR spectrometer with a liquid nitrogen cooled HgCdTe detector. The fiber loss was determined via a cut-back measurement.

The cross-section and side surfaces of the fibers were imaged by a scanning electron microscope (SEM; Philips XL30 field emission SEM) to study the surface defects.

The mechanical strength of the fibers was determined by measuring the fiber bending radius at fiber breakage (minimum bending radius) [29]. Fiber pieces of approximately 15 cm length were bent and held between two vertically parallel plates as shown in Fig. 2. One of the plates was held stationary, while the other was mounted to a movable rail driven by a stepper motor. The latter plate was set to move at a speed of 0.3 mm/s towards the fixed plate until fiber breakage. Measurements were repeated to estimate the minimum bending radius at least 10 times. The calculation of the strain was based on Eq. (3):

$$\tau_s = r/0.42D \quad (3)$$

where τ_s is the breaking strain which can be measured from D, the minimum distance between the plates when the fiber fractures, and r is the fiber diameter.

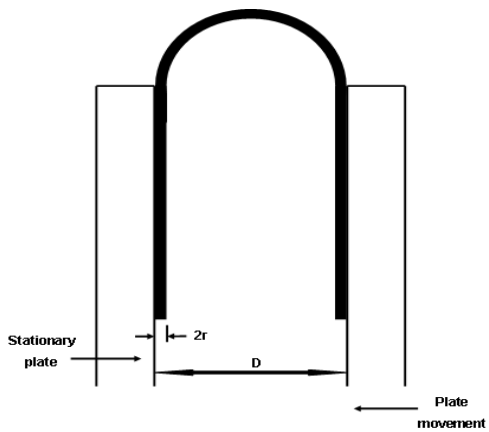

Fig. 2. Bending strength measurement approach.

#192346 - $15.00 USD Received 17 Jun 2013; revised 3 Aug 2013; accepted 4 Aug 2013; published 13 Aug 2013

3. Results and discussions

3.1 Optimization of glass melting

Table 1 lists the fluorination and melting conditions, and characteristic temperatures (T_g, T_x, and T_p) of samples A, B and C. The difference $\Delta T = T_x - T_g$ is used as a measure of glass stability.

Table 1. Melting conditions and properties of glass samples fabricated in this study.

Melting condition	Dwell Time @ 235 °C	Dwell Time @ 450 °C	Dwell Time @ 900 °C	T_g (°C)	T_x (°C)	T_p (°C)	ΔT (°C)
A*	45 min	---	3 h	307	385	409	78
B**	45 min	---	3 h	307	389	409	82
C**	---	1h	2 h	308	389	407	81

*raw material $InF_3 \cdot 3H_2O$ with~99.99% metal content
**raw material InF_3 with ~99.99% metal content

DSC measurements (Fig. 3, Table 1) show that different fluorination and melting conditions had negligible impact on T_g; the variations were within the temperature error of DSC measurements. However, it was found that Sample B contained a few un-dissolved particles. Mohammed [30] introduced 500 °C for elimination of NH_4HF_2 products prior to melting, for preparation of their fluoride glasses. Fluorination at 450 °C prior to melting in this work for Sample C may effectively reduce the remaining (i.e., non-reacted) NH_4HF_2 in the final glass. The un-dissolved particles in Sample B are attributed to possible residual products from NH_4HF_2 in the glass, which could not be eliminated by fluorination at 235 °C.

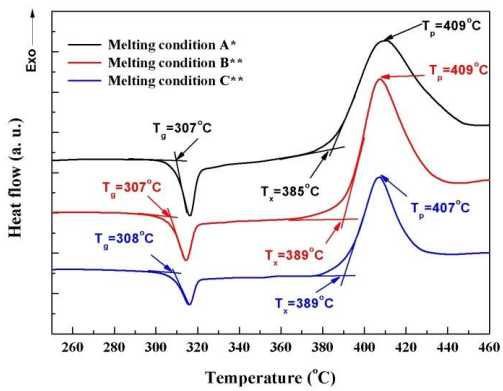

Fig. 3. DSC curves for glasses prepared under three different conditions.

Figure 4 shows the linear thermal expansion curve of the 5 mm diameter rod piece which was melted under the same condition as C** and extruded at 320 °C. The slope changes slightly at 308 ± 2 °C, which corresponds to the glass transition temperature (T_g). This value measured using a thermal dilatometer agrees well with the T_g value of the sample melted under condition C** (melted under the same conditions) obtained from DSC.

#192346 - $15.00 USD Received 17 Jun 2013; revised 3 Aug 2013; accepted 4 Aug 2013; published 13 Aug 2013

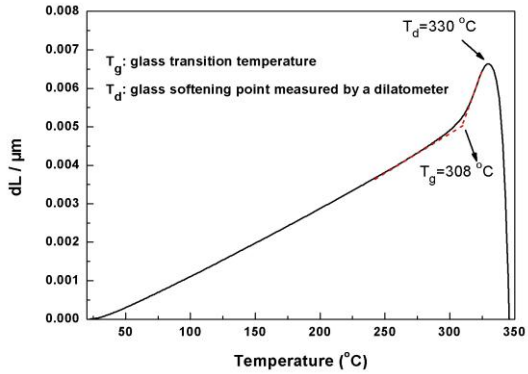

Fig. 4. Linear thermal expansion curve of IZSBGC sample obtained using 5 °C/min heating rate.

3.2 Extrusion

To achieve a good surface quality for glass items extruded through graphite dies, the extrusion force must be as low as possible while the temperature must be below the onset of glass surface crystallization temperature [9]. A low extrusion force minimizes shedding of graphite particles from the die onto the glass and reduces the chance of die breakage. Shedding can degrade the surface quality of extruded rods, whereas die breakage can lead to premature stopping of an extrusion trial. While higher temperatures decrease the extrusion force, they can increase the probability of the undesired surface crystallization. Therefore, the maximum temperature that can be used for extrusion of preforms with good surface quality will be limited by the onset of glass surface crystallization temperature.

For the IZSBGC fluoroindate glass, characteristic temperatures are around 307-308 °C for T_g and 385-389 °C for T_x (Table 1) depending on melting conditions. In our previous work [9], preliminary extrusion trials were conducted at 317 °C, 322 °C and 330 °C. In this work, to identify the best die design and advance our understanding of temperature-viscosity behavior and the impact of temperature on extrusion force and rod surface quality, we performed extrusion trials using different die designs and temperatures between 317 °C and 330 °C.

According to the previously published results [16,31,32], we can assume that the extrusion flow of fluoroindate glass follows the Poiseuille law, and that the glass can be regarded as a Newtonian fluid. Hence, the force or pressure required to extrude a glass through a circular die channel can be approximated by the following equation [16]:

$$P = \frac{128L_1}{\pi D_1^3 (D_1 + 8\alpha)} A_0 V_0 \eta \qquad (4)$$

where subscript '0' and '1' refer to the billet and die, respectively, $P = F/A_0$ is the pressure P calculated from the measured force F and billet cross section area A_0, L_1 is the die channel length, D_1 is the die channel diameter, V_o is the ram speed, η is the glass viscosity, and α is the slip coefficient at the glass/die boundary.

According to Eq. (4) and assuming a constant slip coefficient, the extrusion pressure is proportional to the die channel length and the inverse of the fourth exponent of the channel diameter. Metal dies made from stainless steel or nickel alloys were found to have no slip ($\alpha = 0$, i.e. constant slip coefficient) when they were used for the majority of oxide glass extrusions [16,32]. By contrast, graphite is a non-wetting material [32]. A slip at the glass/die boundary was observed previously by using graphite as an extrusion die material [16]. For extrusion of fluoroindate glass through graphite dies, we found that with the shorter die channel in die (c), compared to dies (a) and (b), the extrusion force did not decrease linearly

#192346 - $15.00 USD Received 17 Jun 2013; revised 3 Aug 2013; accepted 4 Aug 2013; published 13 Aug 2013

with the die channel length, L_1, which cannot be explained by Eq. (4) assuming a constant slip coefficient. Analysis of published data on extrusion of silicate glasses through graphite dies with different die channel length [16] revealed that the slip coefficient decreased linearly with decreasing die channel length, and can be approximated by:

$$\alpha(mm) = 0.5557 + 0.5652 L_1(mm) \quad (R^2 = 0.950) \tag{5}$$

Equation (5) indicates that α decreases with L_1. Therefore, the extrusion force decreases with L_1 in a nonlinear manner in Eq. (4), which explains our findings of the nonlinear decrease of the extrusion force with L_1 in the extrusion of fluoroindate glasses. Assuming that the dependence of die channel length on the slip coefficient for IZSBGC glass/graphite die interface is equal to that for silicate glass/graphite die interface, we used Eq. (5) to calculate the slip coefficients for different die channel length for our extrusion trials (Table 2).

Once the slip coefficient α is known, Eq. (4) can be used to calculate the viscosity from the measured extrusion force and other parameters in the extrusion trials conducted using different temperatures and graphite die geometries [16]. Table 2 shows the experimental parameters used for this calculation and the calculated viscosities. In Fig. 5, the calculated viscosity values are plotted as a function of the reciprocal of the glass temperature for fluoroindate glass extrusion trials, assuming die temperature is equivalent to glass temperature.

Table 2. Extrusion Parameters: Preform surface roughness, S_a and S_q, Extrusion temperature, T, Die Channel Diameter, D_1, Die Channel Length, L_1, Ram Speed, V_0, Ram Force, F, Ram pressure, P, Slip coefficient, α, Glass viscosity, η.[§]

Extrusion No	Preform surface roughness		Die Type	T (°C)	D_1 (mm)	L_1 (mm)	V_0 (μm/s)	F (kN)	α (mm)	log η (log Pa·s)
	S_a (nm)	S_q (nm)								
IE1	—	—	a	322	8	8	0.60	10.85	5.08	9.44 (± 0.06)
IE2	—	—	a	325	8	8	0.60	7.15	5.08	9.26 (± 0.04)
IE3	—	—	a	330	8	8	0.60	2.24	5.08	8.76 (± 0.03)
IE4	49.47 (± 5.68)	59.46 (± 10.83)	b	330	10	7	0.60	1.41	4.51	8.88 (± 0.04)
IE5	—	—	b	324	10	7	0.33	4.01	4.51	9.59 (± 0.05)
IE6	—	—	c	317	10	2	0.33	19.00	1.69	10.52 (± 0.03)
IE7	141.96 (± 14.22)	162.62 (± 6.96)	c	318	10	2	0.33	18.10	1.69	10.50 (± 0.03)
IE8	190.50 (± 10.90)	234.35 (± 21.65)	c	316	10	2	0.33	22.05	1.69	10.58 (± 0.03)
IE9	67.11 (± 7.20)	84.33 (± 7.61)	c	320	10	2	0.33	8.34	1.69	10.16 (± 0.05)
IE10	64.29 (± 1.88)	78.86 (± 0.96)	c	324	10	2	0.33	3.58	1.69	9.79 (± 0.04)
IE11	—	—	d	320	5	2	0.33	34.25	1.69	9.76 (± 0.06)

§: Note that only glass for IE11 was melted under condition C** and the glasses for IE1-10 were all melted under condition A*; the surface roughness S_a and S_q are the average values by repeating measurements 3 times.

#192346 - $15.00 USD Received 17 Jun 2013; revised 3 Aug 2013; accepted 4 Aug 2013; published 13 Aug 2013

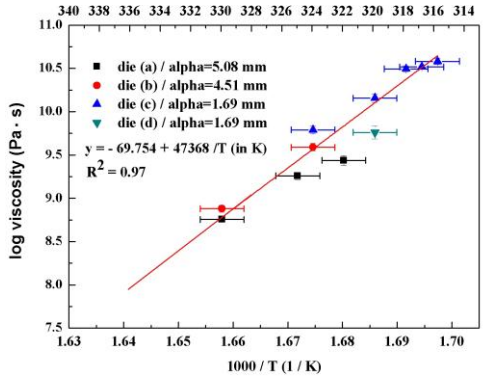

Fig. 5. Calculated viscosity values as a function of extrusion temperature.

For a limited viscosity range at the temperature between 317 and 330 °C, the experimental viscosity data can be well fitted with a two-parameter Arrhenius equation [31]:

$$log\eta = A + B / T \tag{6}$$

where η is the viscosity (in Pa·s), T is the temperature (in K) and A and B are empirical constants. For the fluoroindate glass reported in this work, we determined the Arrhenius equation of the temperature viscosity curve from glass viscosity calculated from extrusion trials. The linear fitting of Arrhenius equation for our fluoroindate glass yields $\log \eta$ (in Pa·s) = –69.754 + 47368/T (in K) (Fig. 5).

Using the dilatomer measurement (Fig. 3), the dilatometric softening temperature (i.e. the temperature, at which a sample reaches maximum expansion in a length versus temperature curve during heating of the sample [33]) was measured to be 330 °C for our fluoroindate glass. Note that the viscosity at this dilatometric softening temperature corresponds to 10^8-10^9 Pa·s [33], which is in agreement with the viscosity at 330 °C in Fig. 5, determined using the extrusion trials. This suggests the calculated viscosity results in Fig. 5 are reliable.

The surface roughness results for extruded preforms (Table 2) demonstrate that the roughness decreases with increasing extrusion temperature, which was also reported for extruded polymer preforms [34]. There are several reasons that possibly explain this observation. Firstly, the surface is smoothened by fire-polishing at elevated temperatures, i.e. at low glass viscosities [35]. The fire-polishing also occurs during extrusion. The glass preform is still hot when it emerges from the die exit and moves slowly out of the hot zone; this leads to fire-polishing of the preform surface. The fire-polishing process softens or melts the surface, which deliquesces and rounds sharp edges, and also fills pits (e.g., scratches) due to lower viscosity [36]. Consequently, the fire-polishing results in a smoothed preform surface and the surface roughness is reduced. The effects of fire-polishing will become more prominent with increasing temperature, thus leading to a smoother preform surface as the extrusion temperature increases.

Secondly, for a not completely wetted interface, a certain degree of slip occurs at the fluid/solid interface. For a Newtonian fluid, there exists a general nonlinear relationship between the amount of slip and the local shear rate at a solid surface [37]. The velocity gradient (shear rate) in viscous fluid flow generates a tangential force (mechanical shear stress) which is proportional to the viscosity when the fluid is under shearing [38]. When the temperature increases, the extrusion can be achieved at a lower viscosity with a lower shear stress. The lower shear stress, therefore, reduces the shearing at the graphite die surface, leading to reduced surface roughness and improved glass surface finish (e.g., less extrusion stripes). It also reduces the shearing of the graphite particles that can contaminate the glass surface, and therefore improves glass surface quality. Furthermore, higher extrusion forces can lead to

#192346 - $15.00 USD Received 17 Jun 2013; revised 3 Aug 2013; accepted 4 Aug 2013; published 13 Aug 2013

changes in the slip behavior at the fluid/die interface, which can result in melt fracture extrusion instabilities and increase the extruded preform's surface roughness [39]. Low extrusion forces at high extrusion temperatures are therefore desired to improve the surface roughness of extruded glass preforms.

Our recent work [9] on fluoroindate glass annealing tests demonstrated that a temperature of 330 °C for preform extrusion could cause potential surface crystallization, whereas 322 °C for extrusion was sufficiently low to avoid potential surface crystallization. Therefore, to achieve a low extrusion force and eliminate shear-induced surface roughness with no glass surface crystallization, we chose the extrusion temperatures of 320-322 °C for fiber drawing trials IF1-6 in the next section.

3.3 Fiber drawing

Table 3 summarizes the experimental details of fibers IF1-6 drawn under different conditions, and presents results of fiber surface roughness and fiber spot loss measurements at 1550 nm. To understand the surface roughness value of a fiber without surface crystallization, we also measured the surface roughness of an unstructured fiber made from commercial F2 lead-silicate glass for comparison (Schott Glass Co.) (Table 3). SEM analysis (Fig. 6) shows the features of the cross-sections and the surface of fibers IF1-6.

During fluoride fiber drawing, one of the most important aims is to minimize surface crystallization of the preform neck-down, because experiments have shown that this surface crystallization significantly correlates to degraded mechanical strength in the drawn fibers and increases fiber loss for air-clad (i.e., unstructured) fibers and air/glass microstructured fibers [28].

Chemical etching has been demonstrated to improve fluorozirconate glass surface quality and hence reduce surface crystallization [8]. Thus, we commenced with investigating the impact of etching on fluoroindate glass surface crystallization during fiber drawing. A preform extruded at 320 °C was cut into two pieces that were used for IF1 and IF2 fiber drawing trials using 2 cm heating zone. The difference between the two fiber drawing trials was that the IF2 preform was etched with 1.36 M $ZrOCl_{2(aq)}$ to remove a ~0.5 mm thick outer layer and then polished with 40 nm colloidal silica suspension, while the IF1 preform remained unetched. Surface roughness measurements of the IF2 preform before and after chemo-mechanical treatment revealed that the average roughness dramatically decreased from 70 to 7 nm (Fig. 7).

Table 3. Fiber drawing conditions, results of spot loss measurements and surface roughness of fibers IF1-6

Fiber No	Glass melting condition§	T (°C)	Surface treatment	Susceptor (cm)	Additional weight (g)	Fiber surface roughness		Spot loss at 1550 nm (dB/m)
						S_a (nm)	S_q (nm)	
IF1	A*	320	none	2	0	172.0 (± 77.0)	223.0 (± 103.0)	27.8
IF2	A*	320	Preform	2	0	149.0 (± 29.0)	205.0 (± 38.0)	20.1
IF3	C**	320	Preform	4.5	0	13.8 (± 4.1)	15.9 (± 4.4)	7.8
IF4	C**	320	Preform	4.5	190	10.5 (± 1.1)	15.2 (± 3.8)	4.1
IF5	C**	320	Billet/preform	4.5	190	9.3 (± 1.8)	12.9 (± 2.3)	3.6
IF6	C**	322	Billet/preform	4.5	190	9.1 (± 0.4)	12.8 (± 1.9)	2.3
F2† fiber	—	560	—	4.5	0	8.0 (± 0.8)	12.0 (± 1.2)	—

§: For glass melting conditions for IF1-6, please refer to Table 1.

†: Commercial F2 glass billet (outer diameter: 30 mm) was used to fabricate extruded preform and unstructured fiber.

#192346 - $15.00 USD Received 17 Jun 2013; revised 3 Aug 2013; accepted 4 Aug 2013; published 13 Aug 2013

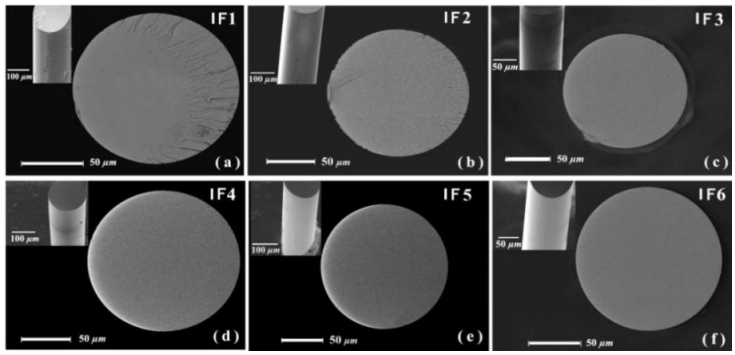

Fig. 6. Scanning electron microscopy images of fiber surfaces and cross-sections (IF1-6).

To investigate the effect of the chemo-mechanical treatment on the preform during fiber drawing, IF1 and IF2 preform neck-down surfaces were examined under an optical microscope (Fig. 8). During fiber drawing, re-heating of the IF1 preform resulted in the formation of corrugation patterns on the surface of the preform neck-down (Fig. 8(a)). This corrugation pattern is attributed to surface crystallization during glass re-heating. In contrast, no corrugation patterns were observed on the IF2 preform neck-down (Fig. 8(b)) except for several small crystal spots on the surface. The fiber surface roughness of IF2 was reduced to 149 ± 29 nm (S_a), as compared to 172 ± 77 nm (S_a) for IF1 (Table 3). This clearly indicates that the chemo-mechanical treatment applied to IF2 preform effectively reduced surface crystallization during fiber drawing.

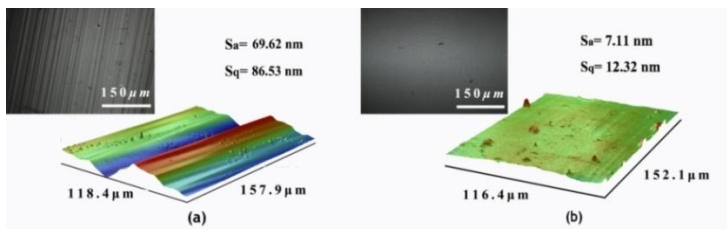

Fig. 7. Optical interferometric profiler images (colored images) of preform surface for IF2 fiber drawing (a) before chemo-mechanical treatment; the data in (a) is one of the measurements used for the surface roughness calculation of IE9 preform, Table 2; (b) after chemo-mechanical treatment. Images in grey scales in (a) and (b) are optical microscope images of the preform surfaces before and after chemo-mechanical treatment.

In Fig. 6, all the fibers from IF1 to IF6 were cleaved at a tension as low as possible to prevent a mirror-mist hackle pattern, which was otherwise observed to occur at high tensions. In addition, each fiber was cleaved at least 20 times to ensure that fiber surfaces (Fig. 6) were reproducible and representative. For all the cleaved surfaces of IF1, the fiber cross-section shows fracture patterns that resemble a mirror-mist hackle pattern (Fig. 6(a)). It is likely that this fracture pattern arises from surface crystallization and propagated rapidly when the fiber is fractured [8]. For IF2 fiber, its preform was chemo-mechanically treated before fiber drawing, resulting in significantly reduced mirror-mist hackle pattern (Fig. 6(b)).

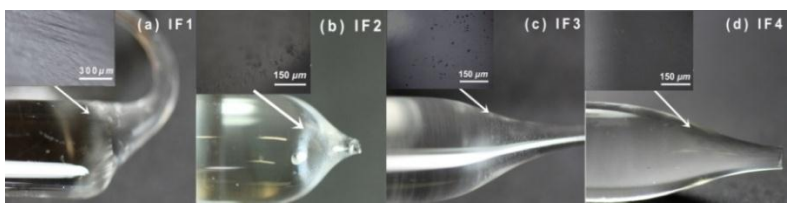

Fig. 8. Surface images of the fiber drop neckdown of IF1-4.

#192346 - $15.00 USD Received 17 Jun 2013; revised 3 Aug 2013; accepted 4 Aug 2013; published 13 Aug 2013

For the IF2 fiber, surface crystallization was reduced but not completely suppressed, as demonstrated by observation of crystal spots on the preform neck-down. Sakaguchi et al. [28] successfully minimized surface crystallization in the neck-down region of a fluorozirconate glass by extending the heating zone of the furnace used for fiber drawing. As fluoride glass has a steep temperature-viscosity dependence, small temperature fluctuations cause large variations in the glass viscosity. Thus, instabilities in drawing such as variations in diameter (± 30 μm for IF2) and drawing tension are caused by a shorter heating zone with a higher maximum preform temperature and steeper preform temperature gradient along the drawing axis [28]. The steeper temperature gradient requires higher maximum glass temperature to form a preform drop, which may lead to an increase in surface crystallization. In contrast, for a longer heating zone, the reduced temperature gradient and larger heat spread in axial direction allows the preform to drop at a lower maximum temperature, which reduces the probability of surface crystallization during fiber drawing. The neck-down shape using a longer heating zone is elongated, which indicates that the duration time for glass in the heating zone is increased compared to that of a shorter heating zone. The reduction of surface crystallization for a longer heating zone indicates that the impact of temperature on crystallization is more significant than the time the glass dwells in the hot zone [28].

For our fiber drawing furnace, we have confirmed that the susceptor length correlates with the length of the heating zone. To investigate the impact of increased heating zone length on surface crystallization for our fluoroindate glass fibers, we used a larger susceptor length of 4.5 cm for IF3 compared with 2 cm-long susceptor for IF2. IF3 was drawn at a furnace temperature being ~75 °C lower than that of IF2. This confirms that, for a longer heating zone, a lower maximum temperature can be used to form a preform drop. The length of neck-down of IF3 was observed to be elongated compared to that of IF2 (Fig. 8), consistent with results by Sakaguchi et al. [28], indicating lower maximum glass temperature. Although the neck-down surface of IF3 contained similar small crystal spots compared with those of IF2 (Fig. 8), the number of spots was significantly reduced. SEM images revealed that the mirror-mist hackle patterns of IF3 were greatly suppressed (Fig. 6(c)). In addition, the fiber surface roughness (S_a) was reduced from 149 ± 29 nm for IF2 to 13.7 ± 4.1 nm for IF3 (Table 3). These results demonstrate a decrease in surface crystallization for IF3, due to the reduced maximum preform temperature of IF3 combined with reduced temperature gradient along the drawing axis as a result of the longer heating zone used for IF3 than that for IF2.

For IF4, we applied an additional weight at the bottom of its preform to decrease the preform temperature required to form a drop during fiber drawing. The decreased preform temperature also reduced the surface crystallization rate (without wasting a significant length of the preform). The fiber drop temperature for IF4 decreased by 15 °C in comparison with IF3. No crystallization was found on the neck-down of IF4 on inspection with an optical microscope (Fig. 8 (d)). Both surface roughness of IF4 (Table 3) and mirror-mist hackle patterns of cleaved fiber cross-section (Fig. 6) were reduced due to the reduced crystallization of the fiber surface. Note that all billets for IF1-4 were polished mechanically.

For comparison, chemo-mechanical treatment was applied to IF5 and IF6 billets before extrusion. The only difference between IF5 and IF6 was that the preforms for these two fiber drawing trials were extruded at different temperatures (320 °C for IF5 and 322 °C for IF6). By comparing the fiber surface roughness of IF4 and IF5, we find that the chemo-mechanical treatment of IF5 billet before extrusion slightly improved the IF5 fiber surface quality and resulted in a reduced surface roughness relative to IF4 (Table 3). The improved fiber surface quality of IF5 is attributed to an improved billet surface quality after chemo-mechanical treatment, superior to use of only mechanical billet polishing before extrusion (for IF1-4). Chemo-mechanical treatment of the billet for IF5 removed surface micro-cracks and micro-scratches before extrusion, thereby enabling IF5 to have a lower fiber surface roughness. IF6, which was fabricated from a preform extruded at 322 °C, exhibits the lowest surface roughness (Table 3) of all fluoroindate fibers fabricated, and no mirror-mist hackle

#192346 - $15.00 USD Received 17 Jun 2013; revised 3 Aug 2013; accepted 4 Aug 2013; published 13 Aug 2013

patterns were found on this fiber cross-section (Fig. 6(f)). It is also the longest fiber obtained in this work with a length of 38 m. These results are attributed to the better surface quality of the IF6 preform by extruding the preform at 2 °C higher than those used for extrusion of IF1-5, resulting in a lower force for extrusion of IF6 preform. As discussed above, lower force results in an improved preform surface quality, which finally leads to improved fiber surface quality.

The spot loss measurement results at 1550 nm shown in Table 3 and Fig. 9 are consistent with the broadband fiber loss measurement results (Fig. 9). Note that no fiber of IF1 with adequate length was available for broadband loss measurements to be performed after spot loss measurement, due to low production yield of this fiber. The broad absorption band at 1000 nm of IF2 (Fig. 9) is thought to be due to absorptions from 3d transition metals (e.g., Fe^{2+}, Co^{2+}, Cu^{2+}) from the raw materials used for IF2. Both spot loss and broadband fiber loss results demonstrate that the loss is remarkably decreased from IF1 to IF6, which correlates with reduction of the fiber surface roughness. As IF1 and IF2 were made from the same billet and preform, the lower loss of IF2 compared with IF1 demonstrates that the loss is determined by surface scattering due to surface roughness caused by surface crystallization. Similar correlation is observed for IF3 to IF6 made from glass using C** melting condition. The reduction of surface crystallization from IF1 to IF6 resulted in a smooth fiber surface with low surface roughness, which effectively reduced light scattering and thus fiber loss.

IF6, which has the lowest loss in the near-infrared region of all fibers investigated in this work, also exhibited low loss in the mid-infrared region; the fiber loss of IF6 at 2, 4, 5 μm was measured to be 2.0, 1.5 and 2.2 dB/m, respectively. The lowest loss of 1.3 dB/m was located at 2.7 μm. In comparison, an unstructured ZBLAN fiber, which was made using commercial raw materials with comparable purity, fluorination with NH_4HF_2 at 235 °C, identical controlled atmosphere melting facility and the extrusion technique for preform fabrication, demonstrated a similar fiber loss of 1.1 ± 0.5 dB/m at 4.0 μm [20].

A 2 m-long fiber with 1.9 dB/m fiber loss at 1550 nm was drawn from an un-etched preform in our previous work [9], while IF6 with 2.3 dB/m was obtained with a length of 38 m. The significantly larger fiber yield for IF6 is attributed to the higher fiber drawing stability achieved. This is believed to be due to the improvements in the fiber fabrication conditions, resulting in the suppression of fiber surface crystallization during fiber drawing. Although chemical etching and additional weight were applied to prevent crystallization during fiber drawing in this work, IF6 exhibited a slightly higher fiber loss of 2.3 dB/m compared to the previously obtained fiber with 1.9 dB/m [9]. This can be explained by the relatively high levels of impurities in the raw materials used in this work: ZnF_2 - this work: 99%, work in [9]: 99.9%; and BaF_2 - this work: 99.99%, work in [9]: 99.999%. Those high purity raw materials used in our previous work are no longer available for purchase.

To further study the correlation between fiber loss and surface roughness, we also measured the fiber surface roughness of an unstructured F2 soft glass fiber. Ref [18]. demonstrated that the loss of air-clad and air/glass microstructured fibers was dominated by surface scattering associated with surface roughness compared with the loss of the bulk material, and that extruded F2 glass fibers showed the same loss as that of the F2 bulk glass within the measurement errors. This indicates that the surface roughness of unstructured F2 fiber is so low that it does not contribute to fiber loss. The indium fluoride fiber IF6 shows a surface roughness of 9.1 ± 0.4 nm (S_a), which is very close to the F2 fiber surface roughness of 8.0 ± 0.8 nm (S_a). This result confirms that the reduced surface roughness from IF1 to IF6, due to reduced surface crystallization, leads to a decrease in light scattering and hence reduces fiber loss both in spot loss and broadband fiber loss measurements.

The fiber breaking strains gradually increased from IF1 to IF6 (Table 4 and Fig. 10), which correlates with the observed decrease in fiber surface roughness (Table 3). A smooth fiber surface without defects (e.g. crystals) is, unsurprisingly, an important characteristic of high strength fibers [28]. The enhanced breaking strain of the fibers from trial IF1 to IF6 is

#192346 - $15.00 USD Received 17 Jun 2013; revised 3 Aug 2013; accepted 4 Aug 2013; published 13 Aug 2013

attributed to the reduced surface roughness due to the reduced crystallization on the fiber surfaces during fiber drawing via improvement of the preform and fiber fabrication conditions.

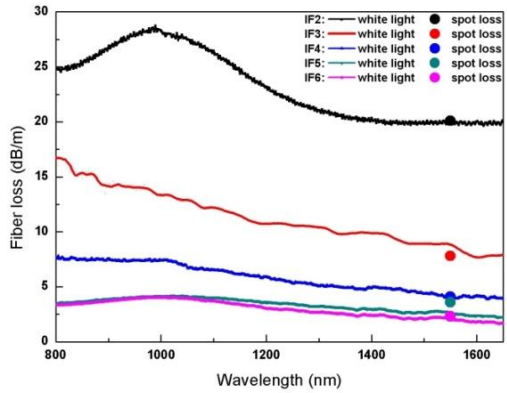

Fig. 9. Fiber loss spectra and spot loss measurement results at 1550 nm of IF2-6.

Table 4. Fiber strain of Trial IF1-6

	IF1	IF2	IF3	IF4	IF5	IF6
Mean of measured radius (μm)	62.34	83.23	71.85	84.28	88.25	77.21
Mean of calculated strain (10^{-3})	4.49	4.94	5.59	6.21	7.43	10.54
The standard deviation of calculated strain (10^{-3})	1.90	1.69	1.34	1.10	0.93	0.79

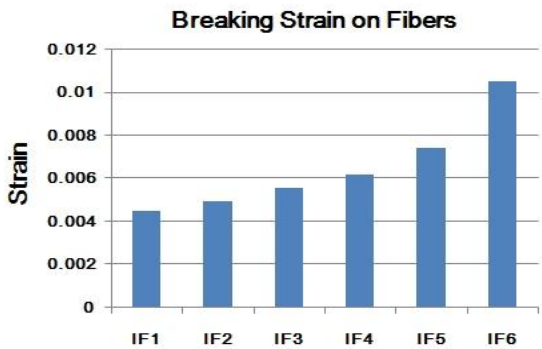

Fig. 10. Breaking strain of IF1-6.

4. Conclusions

We have presented a systematic characterization of factors responsible for scattering loss in fluoroindate glass fibers. The results showed that this systematic refinement of the glass and fiber fabrication processes reduced the fiber loss by an order of magnitude: from 27.8 dB/m to 2.3 dB/m. This improvement is attributed to the reduction in fiber surface roughness achieved by optimizing the melting, preform and fiber fabrication conditions.

Sample C melted using anhydrous InF_3 raw material with higher fluoride content demonstrated a higher glass crystallization stability compared to Sample A melted using $InF_3 \cdot 3H_2O$ raw material. High fluorination temperature of 450 °C for sample C enabled successful preparation of a crystal-free glass and eliminated the remaining NH_4HF_2 in the glass.

The preform surface properties including surface roughness and crystallization of extruded fluoroindate glass rods essentially depended upon the extrusion temperature. A relatively high temperature reduced the extrusion force, which minimized graphite shedding, cracking of dies and slip instabilities between glass and die surface. The fire-polishing effect became prominent

#192346 - $15.00 USD Received 17 Jun 2013; revised 3 Aug 2013; accepted 4 Aug 2013; published 13 Aug 2013

with increasing temperature, thus leading to a smoother preform surface as the extrusion temperature increased. Both these effects were found to be essential to minimizing rod surface roughness. However, even for rods with good surface finish, sufficiently high temperature eventually resulted in surface crystallization. In this study, the optimum temperature for extrusion was found to be around 322 °C.

The maximum fiber drawing temperature was reduced by expanding the length of the heating zone in the drawing furnace. The chemo-mechanical treatment of billets and preforms reduced the surface crystallization observed on the preform neck-down and fibers at the elevated temperatures experienced during fiber drawing. Surface crystallization was completely suppressed by using additional weight at the bottom of preforms.

In conclusion, the fiber surface roughness due to surface crystallization was reduced by optimizing the preform and fiber drawing conditions (including the extrusion temperature; chemo-mechanical treatment; expanding the heating zone length to decrease the maximum preform temperature; additional weight). This also reduced the loss of the fabricated fibers and the increased fiber strength from trial IF1-6. Furthermore, the improved fiber drawing conditions significantly increased the yield of low-loss fiber (~1.5 dB/m at 4 μm wavelength in the mid-IR region) from a 2 m achieved in our previous work [9] to 38 m for IF6 in this work. However, the fluoroindate fiber IF6 has a significantly lower fiber loss of 1.8 dB/m at 4.7 μm. This is because that fluoroindate glasses have longer multi-phonon edge wavelengths (> 4.7 μm) [9] compared to ZBLAN (<4.7 μm) [20].

In addition to extrinsic scattering loss in fluoroindate glasses discussed above, extrinsic absorption loss is another factor causing high fiber loss. As commercially available fluoride raw materials often contain transition metals and oxides impurities, it limits the reduction of extrinsic absorption loss in fibers [40]. Sublimation and distillation techniques are established methods of purification for high-purity fluorides [40]. In the future, we will aim to quantify the contributions of both extrinsic scattering and absorption to IZSBGC glass fiber loss to determine which one is the major contribution. This future work will guide us to the pathways for further improvement of the fabrication conditions.

Acknowledgment

We acknowledge support from Defence Science and Technology Organisation (DSTO) for funding this work. We also acknowledge the facilities, and the scientific and technical assistance of the Australian Microscopy & Microanalysis Research Facility at Adelaide Microscopy Centre of The University of Adelaide. This work was performed in part at the Optofab node of the Australian National Fabrication Facility, a company established under the National Collaborative Research Infrastructure Strategy to provide nano and microfabrication facilities for Australia's researchers. We thank Mr Roger Moore (University of Adelaide) for fiber drawing, Johann Troles (Université de Rennes 1) and Jonathan Campbell (The Flinders University of South Australia) for DSC measurements and Dr. Yinsheng Xu & Dr. Xunsi Wang (Ningbo University) for the thermal dilatometer measurement. Jiafang Bei acknowledges the International Postgraduate Research Scholarship (IPRS) and discipline of physics supplementary scholarship supported by The University of Adelaide. H. Ebendorff-Heidepriem acknowledges the support of a DSTO Fellowship and T.M. Monro acknowledges the support of an ARC Federation Fellowship.

#192346 - $15.00 USD Received 17 Jun 2013; revised 3 Aug 2013; accepted 4 Aug 2013; published 13 Aug 2013

III

Experimental study of chemical durability of fluorozirconate and fluoroindate glasses in deionized water

Jiafang Bei,[1],* Herbert Tze Cheung Foo,[1] Gujie Qian,[2] Tanya M. Monro,[1] Alexander Hemming,[3] and Heike Ebendorff-Heidepriem[1]

[1]Institute for Photonics and Advanced Sensing and School of Chemistry and Physics, University of Adelaide, Adelaide, SA 5005, Australia

[2] Materials and Minerals Science & Technology, Mawson Institute, Division of Information Technology, Engineering and the Environment, University of South Australia, SA 5095

[3]Electro-Optic Technology Group, Cyber and Electronic Warfare Division, Defence Science and Technology Organisation, Edinburgh, SA 5111, Australia

Experimental study of chemical durability of fluorozirconate and fluoroindate glasses in deionized water

Jiafang Bei,[1,*] Herbert Tze Cheung Foo,[1] Gujie Qian,[2] Tanya M. Monro,[1] Alexander Hemming,[3] and Heike Ebendorff-Heidepriem[1]

[1]*Institute for Photonics and Advanced Sensing and School of Chemistry and Physics, University of Adelaide, Adelaide, SA 5005, Australia*

[2] *Materials and Minerals Science & Technology, Mawson Institute, Division of Information Technology, Engineering and the Environment, University of South Australia, SA 5095*

[3]*Electro-Optic Technology Group, Cyber and Electronic Warfare Division, Defence Science and Technology Organisation, Edinburgh, SA 5111, Australia*

**jiafang.bei@adelaide.edu.au*

Abstract: This paper investigates the chemical durability of a fluoroindate (IZSBGC) glass (developed by our previous research for low-loss fluoroindate fiber production) compared to the widely studied fluorozirconate (ZBLAN) system via leaching of glass samples in deionized water. The chemical stability of both glass systems is probed using a series of analytical techniques such as FTIR, XPS and SEM to study the sample surfaces (before and after leaching) and hydrated layer products, both of which reflected the nature of the leaching process. Our experimental results suggest that IZSBGC glass presented better chemical stability in water than ZBLAN. The absorption due to both OH^- stretching and HOH bending vibrations for both glass types increased with increasing amounts of hydrated layers formed during the leaching. The investigation of hydrated layers using SEM suggests that the NaF content in fluoride glass accelerated the leaching significantly. XPS analyses suggest that (hydr)oxyfluorides and hydroxides formed on both fluorozirconate and fluoroindate glass surfaces after leaching, respectively. The degradation of fiber breaking strain in NaF-free IZSBGC glass is less than that of NaF-containing ZBLAN glass.

OCIS codes: (160.2290) Fiber materials; (160.2750) Glass and other amorphous materials.

References and links

1. J. Bei, T. M. Monro, A. Hemming, and H. Ebendorff-Heidepriem, "Fabrication of extruded fluoroindate optical fibers," Opt. Mater. Express **3**(3), 318–328 (2013).
2. J. Bei, T. M. Monro, A. Hemming, and H. Ebendorff-Heidepriem, "Reduction of scattering loss in fluoroindate glass fibers," Opt. Mater. Express **3**(9), 1285–1301 (2013).
3. X. Zhu and N. Peyghambarian, "High-power ZBLAN glass fiber lasers: review and prospect," Adv. Optoelectron. **2010**, article ID 501956, 23 pages (2010).
4. M. Le Toullec, C. J. Simmons, and J. H. Simmons, "Infrared spectroscopic studies of the hydrolysis reaction during leaching of heavy-metal fluoride glasses," J. Am. Ceram. Soc. **71**(4), 219–224 (1988).
5. J. S. Wang, E. M. Vogel, and E. Snitzer, "Tellurite glass: a new candidate for fiber devices," Opt. Mater. **3**(3), 187–203 (1994).
6. C. G. Pantano and R. K. Brow, "Hydrolysis reactions at the surface of fluorozirconate glass," J. Am. Ceram. Soc. **71**(7), 577–581 (1988).
7. S. Sakaguchi, Y. Terunuma, Y. Ohishi, and T. Kanamori, "Fluoride fibre drawing with improved tensile strength," J. Mater. Sci. Lett. **6**(9), 1063–1065 (1987).
8. H. W. Schneider, A. Schoberth, A. Staudt, and C. Gerndt, "Fluoride glass etching method for preparation of infra-red fibres with improved tensile strength," Electron. Lett. **22**(18), 949–950 (1986).
9. M. Saad, "Fluoride glass fiber: state of the art," Proc. SPIE **7316**, 73160N (2009).
10. D. G. Chen, C. J. Simmons, and J. H. Simmons, "Corrosion layer formation of ZrF_4-based fluoride glasses,"

#209189 - $15.00 USD Received 2 Apr 2014; revised 15 May 2014; accepted 17 May 2014; published 22 May 2014

Mater. Sci. Forum **19–20**, 315–320 (1987).
11. C. T. Moynihan and S. R. Loehr, "Chemical durability of fluoride glasses," Mater. Sci. Forum **32–33**, 243–253 (1988).
12. C. J. Simmons and J. H. Simmons, "Chemical durability of fluoride glasses: I, reaction of fluorozirconate glasses with water," J. Am. Ceram. Soc. **69**(9), 661–669 (1986).
13. A. J. Bruce, S. R. Loehr, R. Mossadegh, R. H. Doremus, and C. T. Moynihan, "IR spectroscopy studies of attack of liquid water on ZrF_4-based glasses," Mater. Sci. Forum **5–6**, 311–322 (1985).
14. A. S. Oliveira, E. A. Gouveia, M. T. de Araujo, A. S. Gouveia-Neto, C. B. de Arau'jo, and Y. Messaddeq, "Twentyfold blue upconversion emission enhancement through thermal effects in Pr^{3+}/Yb^{3+}-codoped fluoroindate glasses excited at 1.064 μm," J. Appl. Phys. **87**(9), 4274–4278 (2000).
15. L. E. E. De Araújo, A. S. L. Gomes, C. B. De Araújo, Y. Messaddeq, A. Florez, and M. A. Aegerter, "Frequency upconversion of orange light into blue light in Pr^{3+}-doped fluoroindate glasses," Phys. Rev. B Condens. Matter **50**(22), 16219–16223 (1994).
16. Y. Messaddeq, A. Delben, M. Boscolo, M. A. Aegerter, A. Soufiane, and M. Poulain, "New fluoroindate glass compositions," J. Non-Cryst. Solids **161**, 210–212 (1993).
17. http://us.vwr.com/store/catalog/product.jsp?catalog_number=AA40118-04.
18. http://en.wikipedia.org/wiki/Zirconium_tetrafluoride.
19. H. Ebendorff-Heidepriem, T.-C. Foo, R. C. Moore, W. Zhang, Y. Li, T. M. Monro, A. Hemming, and D. G. Lancaster, "Fluoride glass microstructured optical fiber with large mode area and mid-infrared transmission," Opt. Lett. **33**(23), 2861–2863 (2008).
20. T. Kanamori and S. Sakaguchi, "Preparation of Elevated NA Fluoride Optical Fibers," Jpn. J. Appl. Phys. **25**(Part 2, No. 6), L468–L470 (1986).
21. R. Kostecki, H. Ebendorff-Heidepriem, S. C. Warren-Smith, and T. M. Monro, "Predicting the drawing conditions for Microstructured Optical Fiberfabrication," Opt. Mater. Express **4**(1), 29–40 (2014).
22. G. Qian, F. Xia, J. Brugger, W. M. Skinner, J. Bei, G. Chen, and A. Pring, "Replacement of pyrrhotite by pyrite and marcasite under hydrothermal conditions up to 220 °C: An experimental study of reaction textures and mechanisms," Am. Mineral. **96**(11-12), 1878–1893 (2011).
23. I. D. Aggarwal and G. Lu, *Fluoride Glass Fiber Optics* (Academic, 1991).
24. E. O. Gbogi, K. H. Chung, C. T. Moynihan, and M. G. Drexhage, "Surface and bulk -OH infrared absorption in ZrF_4- and HfF_4-based glasses," J. Am. Ceram. Soc. **64**(3), c-51–c-53 (1981).
25. N. N. Sagamihara, "Fluoride glass," U. S. Patent 4 358 543, Nov 9, 1982.
26. F. Huang, Y. Ma, W. Li, X. Liu, L. Hu, and D. Chen, "2.7 μm emission of high thermally and chemically durable glasses based on AlF_3," Sci. Rep. **4**, 3604 (2014).
27. T. Iqbal, M. R. Shahriari, G. Merberg, and G. H. Sigel, "Synthesis, characterization, and potential application of highly chemically durable glasses based on AlF_3," J. Mater. Res. **6**(02), 401–406 (1991).
28. J. Lucas, "Fluoride glasses," J. Mater. Sci. **24**(1), 1–13 (1989).
29. http://en.wikipedia.org/wiki/Sodium_fluoride.
30. C. Donley, D. Dunphy, D. Paine, C. Carter, K. Nebesny, P. Lee, D. Alloway, and N. R. Armstrong, "Characterization of Indium–Tin oxide interfaces using X-ray photoelectron spectroscopy and redox processes of a chemisorbed probe molecule: effect of surface pretreatment conditions," Langmuir **18**(2), 450–457 (2002).
31. S. Sakaguchi and S. Mitachi, "Strength and fatigue of fluoride glass optical fibers," J. Am. Ceram. Soc. **66**(9), c151–c152 (1983).
32. T. Shibata, H. Takahashi, M. Kimura, T. Ijichi, K. Takahashi, Y. Sasaki, and S. Yoshida, "Fabrication of high-strength, low-loss fluorozirconate glass optical fibers," Mater. Sci. Forum **5–6**, 379–385 (1985).
33. P. C. Pureza, P. H. Klein, W. I. Roberts, and I. D. Aggarwal, "Influence of preform surface treatments on the strength of fluorozirconate fibres," J. Mater. Sci. **26**(19), 5149–5154 (1991).
34. R. Lebullenger, S. Benjaballah, C. Le Deit, and M. Poulain, "Systematic substitutions in ZBLA and ZBLAN glasses," J. Non-Cryst. Solids **161**, 217–221 (1993).

1. Introduction

Fluoride glasses are attractive for optical applications offering excellent transmission characteristics from visible to infrared wavelengths [1,2] and are of significant interest for a range of applications such as high power delivery fibers for mid-IR lasers [3]. However, fluoride glasses have relatively poor chemical durability when compared to oxide glasses (e.g., silicate [4] and tellurite glasses [5]), as they are reactive in aqueous environments. The presence of water or an acidic solution leads to dissolution of the fluoride glasses and subsequent formation of surface layers. In general, the corrosion of heavy metal fluoride (HMF) glasses in un-buffered water is extremely rapid compared to silicate glasses, with dissolution reactions more than 10-100 times faster than those for silicate glasses [6]. This is not surprising since the structure of fluoride glasses is quite different from that of the silicates. Chemical corrosion can result in high transmission losses in fluoride fibers as well as have a

#209189 - $15.00 USD Received 2 Apr 2014; revised 15 May 2014; accepted 17 May 2014; published 22 May 2014

significant negative impact on fiber strength [7,8], posing potential limitations to the application of fluoride fibers. Therefore, it is essential to understand the corrosion process and chemical durability of these glasses to guide the development of improved materials or methods for the protection of these materials.

To date many types of HMF glasses have been synthesized, of which the fluorozirconate glasses are most widely studied [9]. Leaching behaviors of HMF glasses (e.g., fluorozirconate) have been studied in earlier published work [10–12]. The chemical durability of these NaF-containing fluorozirconate glasses (e.g., ZBLAN) in aqueous environments was, however, found to be extremely poor and rather sensitive to water, while other fluoride glasses without NaF (e.g., ZBL and ZBLA [4,13]) are relatively stable in aqueous solutions. Similarly, Moynihan et al. [11] compared two fluorozirconate glasses (ZBLAN and ZBLA) and found that the ZBLA glass without NaF has better chemical durability in deionized water than the ZBLAN glass containing 20 mol% NaF.

Compared with the fluorozirconate glasses, fluoroindate glasses are characterized by transmittance extending further into the IR region due to their lower maximum phonon energy of ~510 cm^{-1} [14]. Fluoroindate glasses were said be relatively stable against atmospheric moisture, as compared to fluorozirconate glasses [15,16], possibly due to lower solubility of InF_3 (0.04 g/100ml in water at room temperature) [17] compared to ZrF_4 (1.32-1.39 g/100ml in water at room temperature) [18]. However, no actual experimental data are given in refs [15,16] regarding the stability of the fluoroindate glasses under atmospheric moisture conditions. Indeed, there are no research studies reported on the chemical durability of fluoroindate glasses.

Our previous study [19] and others [3,20] on low loss ZBLAN have shown that fluorozirconate glasses with a composition of $53ZrF_4$-$20BaF_2$-$4LaF_3$-$3AlF_3$-20NaF (in mol %) (fluorozirconate; ZBLAN) can be fabricated into low-loss fibers. Our recent work [2] has also shown another candidate of fluoride glass with a composition of $32InF_3$-$20ZnF_2$-$20SrF_2$-$18BaF_2$-$8GaF_3$-$2CaF_2$ (in mol %) (fluoroindate; IZSBGC) suitable for making low-loss fiber. Here we report recent results of the leaching of these two glasses in deionized water to gain insights into their corrosion behaviors. The reactions and possible formation of hydroxyl species on their glass surfaces during corrosion were studied by Fourier transform infrared spectroscopy, scanning electron microscopy and X-ray photoelectron spectroscopy. In addition, the fiber breaking strains of fibers before and after leaching for both glass types were also compared. The aim of this study was to test the chemical durability of both bulk glasses and glass fibers, the latter of which is particularly important as poor chemical durability of the fibers can limit its practical application.

2. Experimental procedure

IZSBGC and ZBLAN were chosen as starting materials for the leaching study in this work. These glasses were synthesized from high purity raw materials (5N for SrF_2, CaF_2, BaF_2 and AlF_3; 4N for $InF_3{\cdot}3H_2O$, LaF_3 and NaF; 3N for ZnF_2 and ZrF_4; 2N for GaF_3) that were thoroughly mixed into 30~60 g batches and then melted in a platinum alloy crucible containing 5% gold (internal volume: 100 ml). The glasses were melted using the conventional melting-quenching method in a controlled dry N_2 atmosphere (99.99%) melting facility. As H_2O in $InF_3{\cdot}3H_2O$ reacts with InF_3, producing $In(OH)_3$ and gaseous HF, a higher amount of excess NH_4HF_2 (3N, 6.7 wt% of the batch weight) was added into glass batches containing $InF_3{\cdot}3H_2O$ to fluorinate the oxide impurities produced from the raw materials and compensate for the loss of fluorine due to the formation and loss of HF. The fabrication of fluoroindate glass included batching, fluorination with NH_4HF_2 at 235 °C (52 mins), melting (3 h) and casting at 900 °C, while the preparation of fluorozirconate glass included batching, melting at 850 °C (2.5 h) and casting at 650 °C. All the melts were cast into preheated brass moulds.

#209189 - $15.00 USD Received 2 Apr 2014; revised 15 May 2014; accepted 17 May 2014; published 22 May 2014

In this work, the two preforms used for ZBLAN and IZSBGC fiber drawing were 110 mm and 140 mm long, respectively. The fiber diameter was 156 ± 8 μm for ZBLAN and 176 ± 13 μm for IZSBGC. Both fibers were drawn with a preform feed rate at 1.6 mm/min. The draw tower furnace temperatures, which are higher than the glass temperatures [21], were maintained at 665 °C and 725 °C for ZBLAN and IZSBGC fiber drawing, respectively.

Leaching experiments were conducted in HDPE (high density polyethylene) containers using only deionized water (pH ~5.60) at the beginning of the leaching experiments at 25 ± 2 °C. Fluoroindate and fluorozirconate glass samples were cut into ~2 mm thick slides which were then polished using ~3 μm diamond paste and ~40 nm colloidal silica to obtain scratch free surfaces [22].

IR transmission measurements were conducted using a commercial Fourier transform infra-red (FTIR) spectrometer (PerkinElmer Spectrum 400) before and after leaching in deionized water for various reaction times. The absorption coefficients were calculated from the transmission data, where background absorptions due to the Fresnel reflection at the interfaces were subtracted.

The cross-sections of the glass slides after leaching were imaged by a scanning electron microscope (SEM; Philips XL30 field emission SEM), equipped with energy dispersive spectrometers (EDS). One glass slide for both ZBLAN and IZSBGC glasses was fractured in a glove box filled with N_2 (99.99%). One part of the fractured glass slide was stored in an air lock container (filled with N_2) prior to analysis of the fractured surface using X-ray photoelectron spectroscopy (XPS). The second part of the fractured slide was immersed in deionized water for 30 mins and then stored in an air lock container (filled with N_2), prior to XPS analysis on the fractured/leached surface. XPS measurements were performed in an ultra high vacuum apparatus built by SPECS (Berlin, Germany) using a non-monochromatic Mg Kα X-ray source (1253.6 eV) and a hemispherical Phoibo100 energy analyser from SPECS. Charge compensation was performed by an electron flood gun SPECS FG20 at 1 eV and 1 μA. Calibrations of the XPS binding energies were made against adventitious carbon (284.8 eV). The Zr 3*d* spectrum was fitted using the $3d_{3/2}$ and $3d_{5/2}$ doublet which has a 2:3 ratio with an energy separation of 2.43 eV. The FWHM (full width at half maximum) for Zr $3d_{3/2}$ was set to the same value as that for Zr $3d_{5/2}$.

During the course of the leaching experiments, the pH of the deionized water solutions changed. pH measurements were performed using a temperature-corrected pH Meter (Metrohm 827), with errors of ~0.05. Calibrations were carried out using standard buffers from Metrohm.

To obtain the mechanical breaking strain of the fibers, we used an in-house fiber bending test setup shown in Fig. 1 (refer to [2] for detailed description). The mechanical breaking strain of each fluorozirconate and fluoroindate fiber piece under test (before and after leaching for 45 mins) (e.g., four sets of measurements) was determined by measuring the fiber bending radius at fiber breakage (minimum bending radius) and using Eq. (1),

$$\tau_s = r / 0.42D, \tag{1}$$

where τ_s is the breaking strain, D is the minimum distance between the two plates when the fiber fractures, and r is the fiber diameter. Each set of measurement was repeated 10 times to obtain the average strain. The fibers for this bending test were all cut into 150 ± 0.5 mm long pieces.

#209189 - $15.00 USD Received 2 Apr 2014; revised 15 May 2014; accepted 17 May 2014; published 22 May 2014

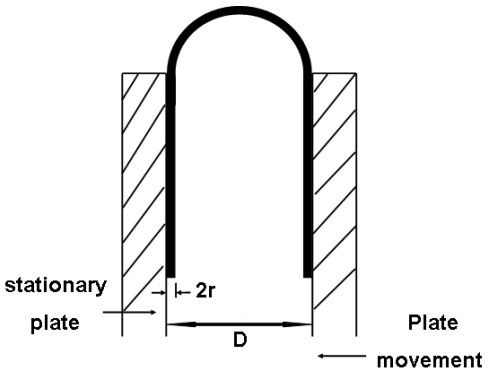

Fig. 1. Breaking strain measurement approach.

3.Results and discussion

3.1 Infrared spectroscopic studies

The water-glass interaction for HMF glasses can be studied by IR absorption and assessed by the change in OH^- stretching (2.9 μm) and HOH bending (6.1 μm) vibrations [10]. The bending mode of HOH at 6.1 μm can be attributed to water molecules present within a thin hydrated layer on the surface [23]. The stretching mode of OH^- at 2.9 μm is thought to be due to OH^- in both bulk glass and glass surface [4,24].

Figure 2 shows the absorption coefficients of ZBLAN and IZSBGC glasses exposed to water at 25 ± 2 °C for various reaction times. After reaction with water, both the ZBLAN and IZSBGC glass surfaces were found to be covered by opaque films to varying degrees, under which somewhat cloudy but still translucent surface layers could be discerned. Both OH^- stretching and HOH bending vibrations were observed with an increase in absorption for ZBLAN and IZSBGC glasses from ~30 mins leaching onwards (up to 90 mins) in Fig. 2a and 2b. This indicates that hydrated layers formed in the leaching processes and altered the glass surface properties [12]. The OH^- stretching vibration peak grew slightly faster than the HOH bending peak for both glass types after leaching. However, the absorption coefficient of IZSBGC glass both at 2.9 and 6.1 μm increased more slowly than that of ZBLAN glass (Fig. 2c and 2d), suggesting that hydrolysis reaction of the former was slower. In previous studies [12,25–27], incorporation of alkali glass modifiers into fluoride glasses such as Li and Na fluorides with high aqueous solubilities increased their leaching rates. For example, the high content of NaF in fluorozirconate glasses increased their glass corrosion rate for all glass components [28] compared to other fluorozirconate glasses without NaF (e.g., ZBLA). As discussed above, the slower increase in absorption coefficient for IZSBGC glass at 2.9 and 6.2 μm in this work, compared to ZBLAN glass, is likely due to the absence of alkali glass modifiers (as opposed to 20 mol% NaF in the ZBLAN glass). Another possible reason is that zirconium fluoride is an undesirable component from the viewpoint of glass durability, because of its higher solubility in water as discussed in the Introduction.

#209189 - $15.00 USD Received 2 Apr 2014; revised 15 May 2014; accepted 17 May 2014; published 22 May 2014

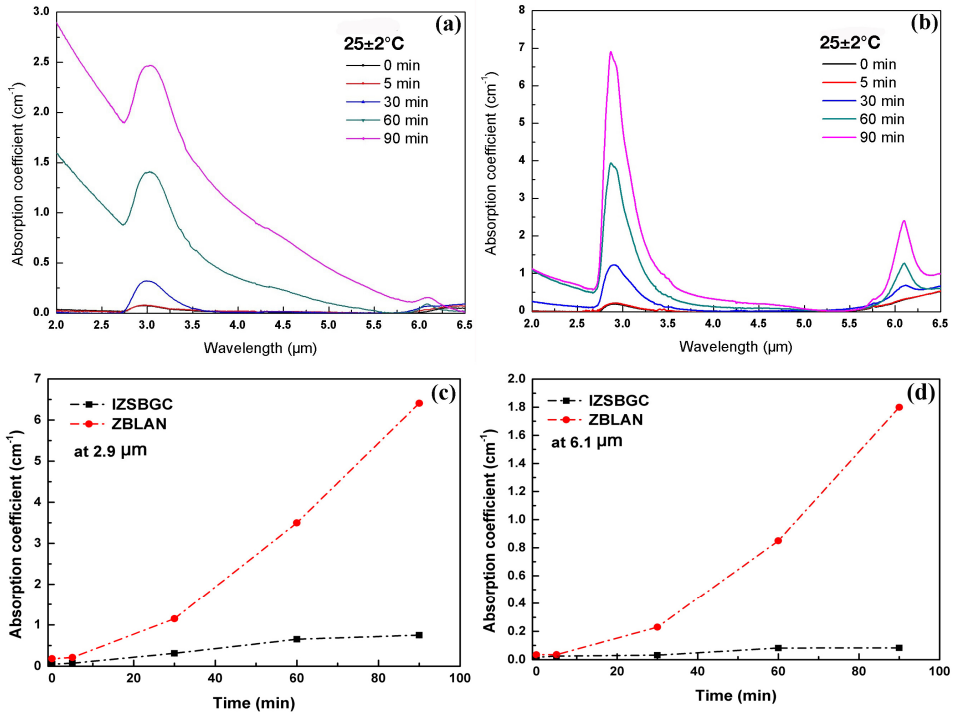

Fig. 2. Absorption coefficient of (a) IZSBGC and (b) ZBLAN after leaching in deionized water at 25 ± 2°C. Change of absorption coefficients for both glass types at (c) 2.9 μm and (d) 6.1 μm.

3.2 pH study of corrosion solution

During the course of the leaching experiments, the pH of the aqueous solutions (originally at ~5.60 for deionized water prior to leaching) all decreased (Fig. 3). The pH drifts were attributed primarily to hydrolysis reactions [12]. In the very early stage of corrosion in stagnant solution (within 0.5 day), fluorides near the fresh glass surface undergo an appreciable hydrolysis associated with ion exchange between F^- and OH^- [12]. As a consequence, OH^- substitutes for F^- near the glass surface structure [12], leading rapidly to a pH decrease. In this work, after leaching for 0.5 day (Fig. 3), the pH drifted from 5.60 to 2.93 and 3.20 for leaching of ZBLAN and IZSBGC glasses, respectively, indicating that the pH decreased significantly into a more acidic range for both glass types after the initial leaching period (within 0.5 day). Similar results were found in an earlier study of hydrolysis reaction of fluorozirconate by Le Toullec et al. [4]. The reduced pH increased markedly the solubility of the fluoride glass components (i.e., metal fluorides), resulting in the leaching process occurring primarily via matrix dissolution as described in a study of dissolution of fluorozirconate glasses in Eq. (2) [23]:

$$MF_n(gl) \rightarrow MF_x^{(n-x)+}(aq) + (n-x)F^-(aq) \qquad (2)$$

As the leaching proceeded to release cations and fluorine ions, leaching solutions became saturated with respect to the least soluble metal fluorides first, causing their precipitation on the fluoride glass surfaces and forming hydrated layers [10].

#209189 - $15.00 USD Received 2 Apr 2014; revised 15 May 2014; accepted 17 May 2014; published 22 May 2014

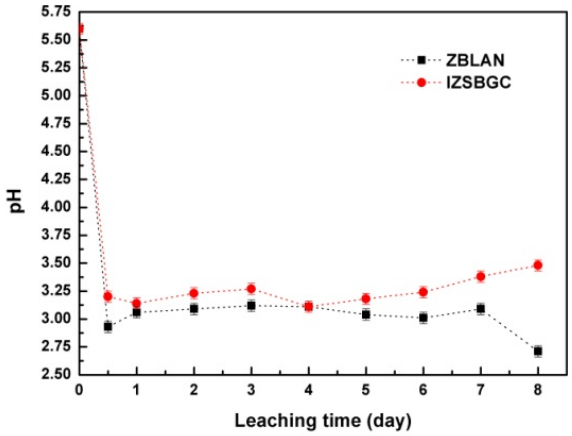

Fig. 3. pH values of deionized water solutions after different leaching time (error bars are smaller than data symbols).

3.3 Scanning electron microscopy study

The SEM images below (Figs. 4 and 5) show the formation of corrosion layers on ZBLAN and IZSBGC glasses after leaching in deionized water for different reaction times. SEM results showed that the leached ZBLAN glasses exhibited multi-layered products with different compositions after leaching for > 0.5 day (Fig. 4). Spherical particles observed from 4 days onwards (Fig. 4) were made up of a multitude of thin platelets containing Zr and Ba, as confirmed by EDS analysis (Table 1). The spherical particles formed within Layer 1 were also found on the outermost surfaces after leaching for 4 and 6 days (Fig. 4). Polyhedral and spherical particles formed on the outermost surface were previously identified as $ZrF_4 \cdot XH_2O$ and $ZrBaF_6 \cdot XH_2O$ crystals, respectively [12], consistent with the compositions found in this work (Table 1). Compared to ZBLA glass after leaching in deionized water reported in [10], ZBLAN glasses studied in this work produced more porous hydrated layers (Fig. 4). In a previous study by Simmons et al. [12], it was proposed that a glass with high alkali content formed a thick and porous de-alkalized layer that can be easily dissolved. Similarly, a reduction in alkali content (e.g., ZBLA glass with no NaF vs. ZBLAN with high content of NaF) resulted in a decrease in the porosity of the hydrated layer [10]. In this work, the leach rate for IZSBGC without NaF slowed down compared to ZBLAN glass with high content of NaF. Clearly the nature of the hydrated layers, depending on glass compositions, strongly affects the subsequent leach rate.

The hydrated layers formed in the IZSBGC glass (Fig. 5 and 6) had similar cation compositions to that of the original un-leached glass. Leaching for 2 days or longer resulted in an obvious gap between the formed layer and the reacted glass (e.g., 4 days in Fig. 5). This size of this gap increased as the leaching progressed. The formed thin layers on IZSBGC glasses had numerous pores on the micron scale. The increased Ba content at Position 10 in Fig. 6 was probably due to the formation of a very thin Ba-rich layer (~1 μm) on the etched glass surface [8].

#209189 - $15.00 USD Received 2 Apr 2014; revised 15 May 2014; accepted 17 May 2014; published 22 May 2014

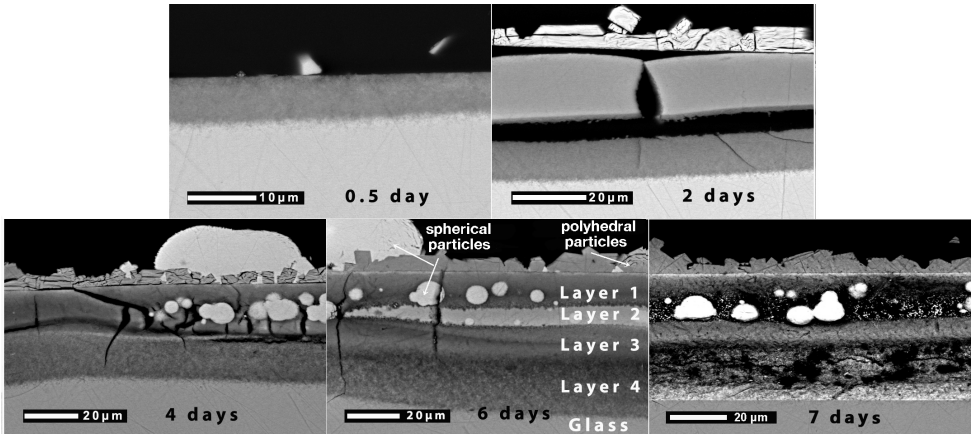

Fig. 4. Formation of multiple hydrated layers on ZBLAN glass during corrosion tests in deionized water.

Table 1. Semi-quantitative analysis measured using EDS for multi-layer compositions for ZBLAN glass after 6 days corrosion in deionized water (in at.%)*

	F	Zr	Ba	La	Al	Na
Spherical particles	29.10	24.37	40.39	3.50	1.10	1.54
Polyhedral particles	17.31	50.23	26.61	3.39	1.19	1.27
Layer1	25.42	31.80	21.96	16.41	0.86	3.55
Layer2	19.52	37.93	33.38	6.92	1.66	0.59
Layer3	28.80	34.94	24.34	8.61	1.06	2.25
Layer4	30.86	35.18	23.07	6.24	1.40	3.25
Bulk glass	30.97	39.45	16.23	3.74	2.42	7.19

*O content was normalized out in the EDS results.

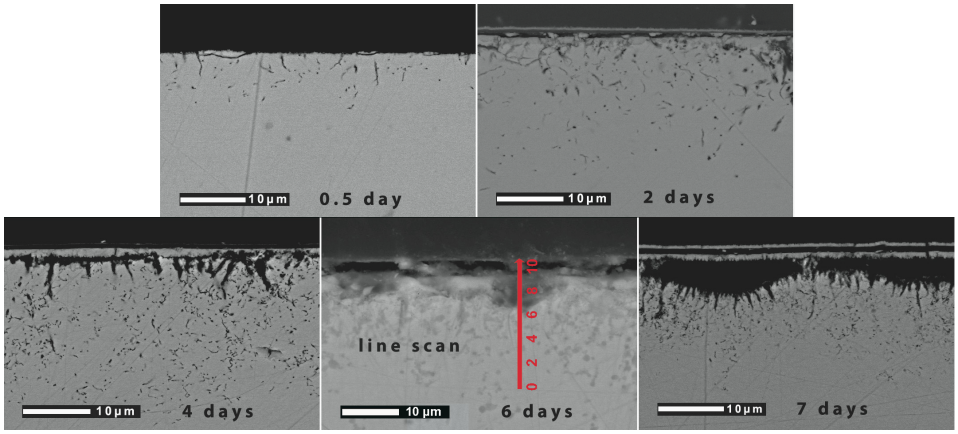

Fig. 5. Formation of multiple and hydrated layers of IZSBGC glass during corrosion test in deionized water.

#209189 - $15.00 USD Received 2 Apr 2014; revised 15 May 2014; accepted 17 May 2014; published 22 May 2014

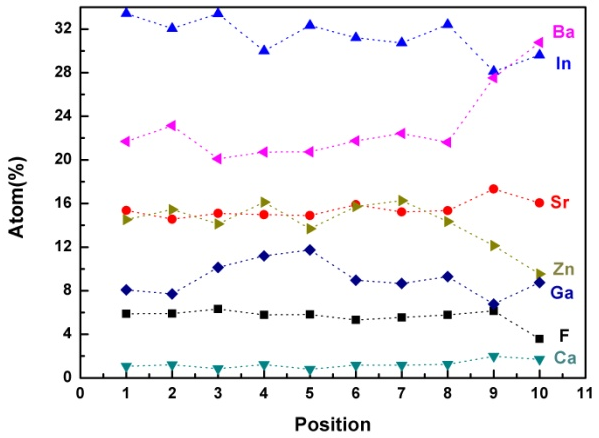

Fig. 6. EDS analysis for line scan (red line in Fig. 5) of the IZSBGC glass after leaching for 6 days in deionized water.

The thickness of the hydrated layer for both glass types generally increased with reaction time (Fig. 7). The results determined in a previous dissolution study of ZBLA glass [10] were employed in this study for comparison purpose. For all three glasses, the thickness increased rapidly at the beginning but much more slowly in the subsequent leaching. Within the experimental time scale investigated, no equilibrium state was reached for ZBLAN glass (i.e., thickness of the hydrated layer increased throughout the leaching in Fig. 7), suggesting that leaching was progressing, while equilibrium was almost established for IZSBGC and ZBLA glasses (i.e., thickness of the hydrated layer 'levelled off'). The leaching of IZSBGC glass slowed down from 4 days (Fig. 7), which may be partly due to the slight increases in pH (Fig. 3). In comparison, the relative large decreases (Fig. 3) in pH for the leaching of the ZBLAN glass at 7 days may result in the marked increase in its leach rate (a sharp increase in the hydrated layer thickness; Fig. 7). The porosity in the hydrated layer facilitated the leaching solution to pass through the layer to further react with the glass surface. However, the IZSBGC glass layers after leaching appeared to be less porous compared to the ZBLAN glass layers. This is possibly because the hydrated layers of IZSBGC glass may play a role in preventing the molecular water from diffusing through the layer into the unreached glass surface. This could also be another possible reason as to why the leaching of the IZSBGC glasses in deionized water occurred more slowly. Measurement of the thickness of the hydrated layers showed that the hydrated layer was less than 20 μm after leaching for 7 days for the IZSBGC glasses (Fig. 7), while the hydrated layer for ZBLAN was greater than 50 μm. Compared to ZBLA glass with no NaF, ZBLAN with a high NaF content had a much thicker hydrated layer (due to the higher solubility of NaF in water [29] than other fluoride components), while IZSBGC glass had a slightly thinner porous hydrated layer structure. Therefore, the main difference in the hydrated layer between IZSBGC and ZBLAN glasses is likely attributed to the presence of NaF in ZBLAN glass.

#209189 - $15.00 USD Received 2 Apr 2014; revised 15 May 2014; accepted 17 May 2014; published 22 May 2014

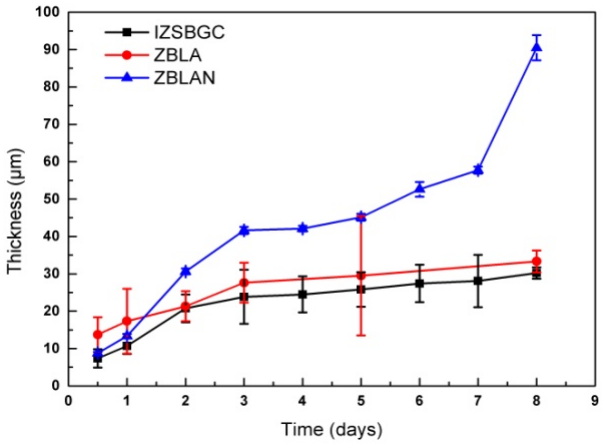

Fig. 7. Thickness of the hydrated layer of IZSBGC, ZBLA [10] and ZBLAN versus corrosion time in deionized water.

3.4 X-ray photoelectron spectroscopic study

Fractured surfaces of fluoroindate and fluorozirconate glasses before and after leaching in deionized water were studied using X-ray photoelectron spectroscopy. An attempt was made to fit the Zr oxyfluoride (for ZBLAN glass) and $In(OH)_3$ (for IZSBGC glass) peaks into the Zr 3*d* and In 3*d* spectra for fresh surfaces, but it was unsuccessful. This suggests the oxyfluoride/hydroxide content was negligible or not present on the fresh surfaces. The high resolution Zr and In 3*d* XPS spectra before and after leaching in deionized water (Figs. 8 and 9) revealed the most important aspects of the glass surface chemistry. It can be seen that the Zr 3*d* peaks ($3d_{5/2}$ and $3d_{3/2}$) in Fig. 8 (top) observed on the reacted surface were broadened and somewhat shifted towards the lower binding energy, as compared to the fresh surface before leaching in deionized water. Fittings of the high resolution Zr 3*d* spectrum indicated formation of a new Zr(hydr)oxyfluoride species on the surface. The Zr 3*d* binding energy of this (hydr)oxyfluoride species was interpreted on the basis of its Pauling charge [6]. It is proposed that Zr(hydr)oxyfluoride is produced in aqueous solutions via attack of Zr-F bonds by molecular water. Similar to the Zr 3*d* peaks in ZBLAN glass, the In$3d_{5/2}$ peak was broadened and a shoulder peak appeared at the lower binding energy after leaching in the deionized water (Fig. 9). This shoulder peak was thought to be $In(OH)_3$ at a lower bonding energy (444.9 eV [30]), a hydrolysis product from reaction with deionized water. The results in Figs. 8 and 9 further confirmed that hydrolysis reaction occurred in the leaching process, in good agreement with the FTIR and SEM findings. It is interesting to note that XPS analyses found no Na on the reacted surface of ZBLAN glass. Similarly, no Ca was found on the reacted IZSBGC glass surface. This is presumed to be due to the Na and Ca being preferentially dissolved during the leaching processes. The formation of hydroxide and oxyfluoride on the glass surfaces after leaching in deionized water for 30 mins also supports the concept of the ion exchange between F^- and OH^- in the initial stages of leaching (Section 3.2).

#209189 - $15.00 USD Received 2 Apr 2014; revised 15 May 2014; accepted 17 May 2014; published 22 May 2014

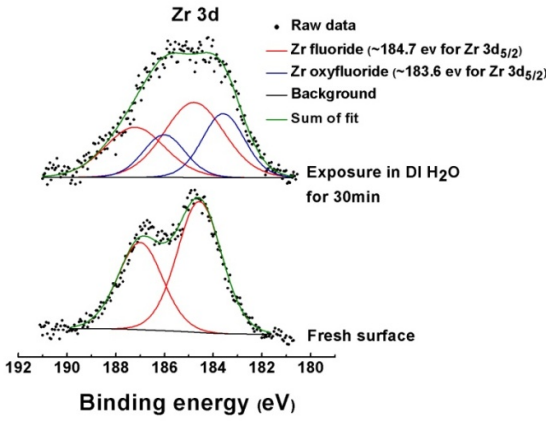

Fig. 8. High resolution Zr 3*d* spectra for a fresh fracture surface (bottom) and a hydrated surface (top).

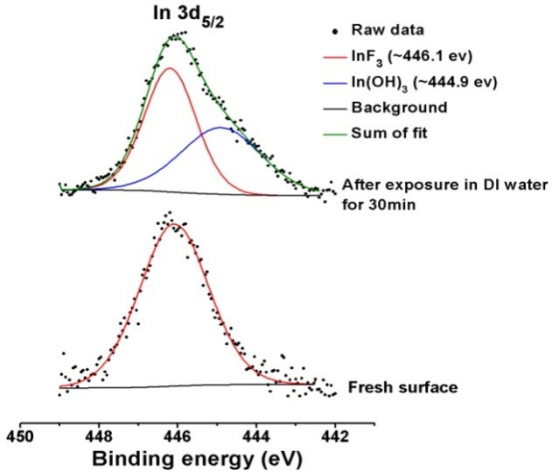

Fig. 9. High resolution In $3d_{5/2}$ spectra for a fresh fracture surface (bottom) and a hydrated surface (top).

3.5 ZBLAN and IZSGBG fiber strain and SEM study before and after corrosion

3.5.1 Fiber strain before and after corrosion

Chemical corrosion processes exert a strong influence on the strength and fracture behavior of fluoride glasses, not only in bulk samples but also in fiber forms. Previously published works have shown that surface and bulk crystal formation during fabrications of both preforms and fibers cause degradation in fiber strength [7,8,31].

Fiber breaking strain measurements were conducted before and after leaching in deionized water. We found that the fiber breaking strain after leaching in deionized water only changed slightly after leaching for 30 mins and that the fibers were too fragile for breaking strain measurements due to the heavy surface crystals after leaching in deionized water for 90 mins. Therefore, the leaching time (in deionized water) was set to 45 mins for the fiber strain measurements. The ZBLAN fibers exhibited heavier opaque films on the surfaces than those on the IZSBGC fiber surfaces after leaching in deionized water. The fiber breaking strain results shown in Fig. 10 and Table 2 demonstrated that the average breaking strain of the IZSBGC fiber was reduced by 32%, which was lower than that of the ZBLAN fiber (39%). It suggests that the degradation in fiber strain for ZBLAN was greater than that for IZSBGC

#209189 - $15.00 USD Received 2 Apr 2014; revised 15 May 2014; accepted 17 May 2014; published 22 May 2014

fiber, in agreement with the results in the preceding sections showing that ZBLAN has a relatively poor chemical stability.

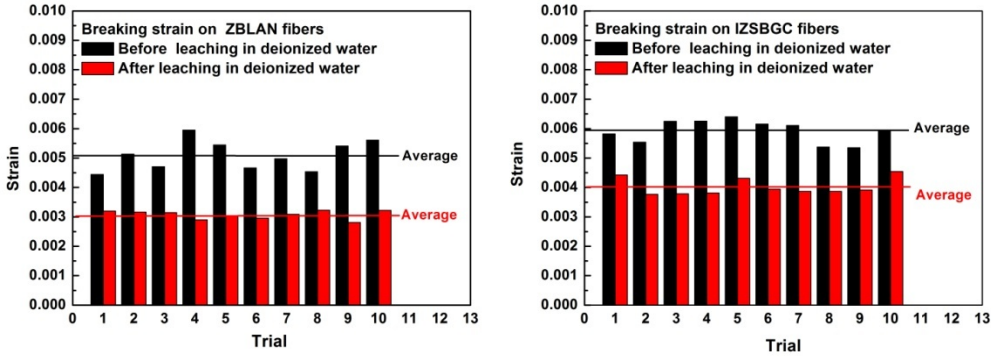

Fig. 10. Fiber breaking strains before and after leaching in deionized water for ZBLAN (left) and IZSBGC (right) fibers.

Table 2. Comparison of fiber breaking strains before and after leaching in deionized water for ZBLAN and IZSBGC fibers.

Glass	Breaking strain on fibers				Reduction (%)
	Before leaching in deionized water		After leaching in deionized water for 45 mins		
	Average	σ	Average	σ	
ZBLAN	0.0051	0.0005	0.0031	0.0001	39%
IZSBGC	0.0059	0.0004	0.0040	0.0003	32%

3.5.2 SEM study of fiber surfaces before and after corrosion

At a low fiber strength level, fracture surfaces of broken fibers with mirror-mist-hackle patterns have been observed [2,31–33]. It is likely that this fracture pattern arises from surface defects and propagated rapidly when the fiber is fractured [33]. Compared to the fiber surface before leaching in deionized water, the obvious mirror-mist-hackle patterns occurred on both ZBLAN and IZSBGC fiber surface after leaching in deionized water for 45 mins, which suggested the formation of surface product layers or porous defects as reflected by our findings in Figs. 4 and 5. In Fig. 11, the fiber surfaces after leaching showed obvious defects, in contrast to the original glasses (Fig. 11(a) vs. Fig. 11(b); Fig. 11(c) vs. Fig. 11(d)). These microscopic flaws led to the low breaking strains of the fibers, confirmed by our fiber breaking strain measurements.

#209189 - $15.00 USD Received 2 Apr 2014; revised 15 May 2014; accepted 17 May 2014; published 22 May 2014

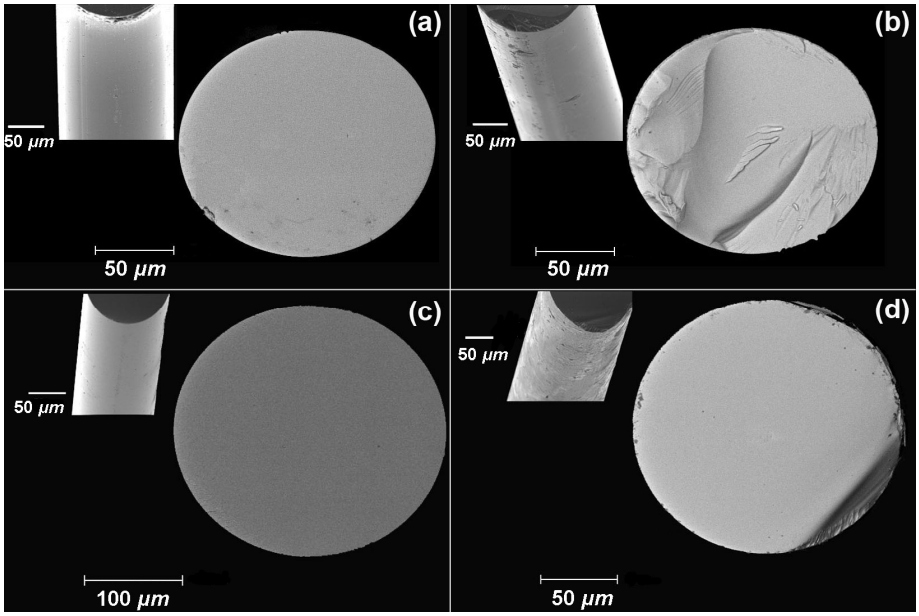

Fig. 11. Scanning electron microscopy images of fiber surfaces and cross-sections: (a) ZBLAN fiber before leaching in deionized water; (b) ZBLAN fiber after leaching in deionized water; (c) IZSBGC fiber before leaching in deionized water; (d) IZSBGC fiber after leaching in deionized water.

As a summary, the negative effect of NaF on the chemical durability was clearly demonstrated by the much more rapid leaching of ZBLAN compared to ZBLA (Fig. 7), supported by XPS observations where no Na was found on the ZBLAN surfaces after leaching. FTIR results (Fig. 2) showed that the increase in absorption due to OH^- was faster for ZBLAN than that for the IZSBGC glass, suggesting a more rapid leaching process for ZBLAN. This is consistent with the thickness measurements by SEM (Fig. 7), showing the thicknesses of the hydrated product layers for ZBLAN increased more rapidly. Both FTIR and SEM observations indicate that the IZSBGC glass and its fibers have a better chemical stability against deionized water compared to ZBLAN. For example, the stronger OH absorptions after leaching of the ZBLAN glass, compared to the IZSBGC glass, indicate a higher degree of hydrolysis reaction, consistent with the greater thicknesses of hydrated layers determined by SEM.

4. Conclusion

The chemical durability and the evolution of the hydrolysis reaction of IZSBGC and ZBLAN glasses in deionized water have been investigated by Fourier transform infrared spectroscopic, scanning electron microscopic and X-ray photoelectron spectroscopic analyses. A comparison between absorption coefficients at 2.9 and 6.2 μm for both glass types after leaching in deionized water showed that the intensities of OH stretching and HOH bending vibration peaks of IZSBGC glass increased more slowly than those of ZBLAN glass. Our results suggest that dissolution of the glasses occurred initially via an ion exchange between F^- and OH^-, decreasing the pH of the leaching solution. Subsequently, the solubility of metal fluorides increased dramatically due to the decreasing pH, leading to dissolution of the glass matrices. SEM studies suggested that the reactions occurred on the glass surfaces and that hydrated layers developed on both IZSBGC and ZBLAN glass surfaces. The NaF-free fluoride glass, IZSBGC, had thinner and less porous hydrated layers than the NaF-containing fluoride ZBLAN glass. This indicates that dissolution of NaF-free fluoride glass was slower than NaF-containing fluoride glass, in agreement with previous findings on ZBLA glasses [34]. Therefore, the fluoride glasses IZSBGC studied here were shown to be more stable against

#209189 - $15.00 USD Received 2 Apr 2014; revised 15 May 2014; accepted 17 May 2014; published 22 May 2014

deionized water compared to NaF-containing glasses. XPS studies suggested that (hydr)oxyfluoride or hydroxide species were formed on the ZBLAN and IZSBGC glass surfaces after leaching in deionized water, respectively, confirming the presence of OH^- on the glass surfaces; the resulting increases in absorption at both 2.7 and 6.2 μm observed in the FTIR spectra also supported XPS results. FTIR, SEM and fiber breaking strain measurements showed that NaF-free fluoride glass IZSBGC presented better mechanical and chemical stability against water than NaF-containing ZBLAN glass. Although ZBLAN glass presented poorer stability against water than ZBLA glass due to the content of NaF, the former has been widely studied and used as fiber material because of its better crystallization stability than ZBLA glass [34]. Our NaF-free IZBSGC glass investigated here, however, exhibited not only extended IR transparency but also improved resistance against deionized water compared to the NaF-containing ZBLAN glass. The work presented in this paper advances our understanding of the corrosion behavior of our IZSBGC glass relative to the established ZBLAN glass in deionized water, and will assist with optimization of the glass compositions to enable low-loss fiber with good chemical durability. In the future, we will explore new fluoride glass compositions with not only optimum optical properties but also good chemical durability. For example, fluorozirconate glasses with low content of alkali components (e.g., NaF) or fluoroindate glasses with low content of alkaline earth components (e.g., CaF_2) would be of interest.

Acknowledgments

We acknowledge support from DSTO for funding this work. We also acknowledge the facilities, and the scientific and technical assistance of the Australian Microscopy & Microanalysis Research Facility at Adelaide Microscopy Centre of The University of Adelaide. This work was performed in part at the Optofab node of the Australian National Fabrication Facility utilizing Commonwealth and SA State Government funding. We thank Associate Professor Gunther Andersson (The Flinders University of South Australia) for assistance with XPS measurements. Jiafang Bei acknowledges the International Postgraduate Research Scholarship (IPRS) and discipline of physics supplementary scholarship supported by The University of Adelaide. H. Ebendorff-Heidepriem acknowledges the support of a DSTO Fellowship and T.M. Monro acknowledges the support of an ARC Laureate Fellowship.

#209189 - $15.00 USD Received 2 Apr 2014; revised 15 May 2014; accepted 17 May 2014; published 22 May 2014

CONFERENCE PUBLICATIONS

1. ***Jiafang Bei,*** Heike Ebendorff-Heidepriem, Roger Moore and Tanya M. Monro. Influences of preform surface treatments on the properties of fluoroindate fibres. 8th International Symposium on Non-Oxide and New Optical Glasses ISNOG, 2012.7. (abstract)

2. ***Jiafang Bei,*** Heike Ebendorff-Heidepriem, Roger Moore and Tanya M. Monro. Fluoroindate Fibres with Reduced Loss in the Mid Infrared Spectral Region: A Study of the Glass Melting and Fibre Preparation Conditions. IQEC/CLEO Pacific Rim, 2011, 2011.8 (full-length paper).

3. ***Jiafang Bei,*** Heike Ebendorff-Heidepriem, Tanya M. Monro and Roger Moore. Fluoroindate glass optical fibre with improved loss in the mid-infrared. 9th International Meeting of Pacific Rim Ceramic Societies, 2011.7. (abstract)